FINAL REPORT

Airborne flux measurements of volatile organic compounds and oxides of nitrogen in California

Contracts 20RD003 and 20AQP012

Prepared for the California Air Resources Board

And Contract 20327 for the South Coast Air Quality Management District

Principal Investigators:

Allen Goldstein, University of California at Berkeley

E-mail: ahg@berkeley.edu

Ronald Cohen, University of California at Berkeley

E-mail: rccohen@berkeley.edu

Co-Principal Investigator:

Anthony Bucholtz, Naval Postgraduate School

Contributing Researchers:

Dr. Eva Y. Pfannerstill, Postdoc, UC Berkeley

Dr. Caleb Arata, Postdoc, UC Berkeley

Dr. Qindan Zhu, Postdoc, MIT/UC Berkeley

Clara Nussbaumer, PhD candidate, Max Planck Institute for Chemistry/UC Berkeley

August 13, 2023

Disclaimer

The statements and conclusions in this Report are those of the contractor and not necessarily those of the California Air Resources Board. The mention of commercial products, their source, or their use in connection with material reported herein is not to be construed as actual or implied endorsement of such products.

Acknowledgements

We thank our colleagues at the California Air Resources Board for useful collaboration on using the airborne fluxes for improvement of California NOx and VOC inventories.

We thank Dennis Baldocchi, Glenn Wolfe, Erin Delaria, and Tianxin Wang for insightful discussions about vertical flux divergence, Brian McDonald for help with SOA formation potentials, Matthew Coggon, Chelsea Stockwell, and Carsten Warneke for valuable discussions on PTR-ToF-MS VOC corrections, and the Regional Chemical Modeling Group of NOAA CSL for help with weather forecasting. Bryan Place and Paul Wooldridge led the measurements of NO, NO_2 and NO_y. We gratefully acknowledge Greg Cooper for excellent mission support, the pilots Bryce Kujat and George Loudakis for flight planning and execution, and Robert Weber and Erin Katz for logistical support.

Glossary of Symbols and Acronyms

a.g.l.	Above ground level
BEIS	Biogenic Emission Inventory System
BVOC	Biogenic Volatile Organic Compound
BDISNP	Berkeley Dalhousie Iowa Soil NO Parameterization
CARB	California Air Resources Board
CATEF	California Air Toxics Emission Factor
CWT	Continuous Wavelet Transformation
DFMR	Disaggregation combining Footprint analysis and Multivariate Regression
EMFAC	Emission Factor Mobile Source Inventory
EPA	United States Environmental Protection Agency
FIMR	Focusing ion-molecule reactor
FIVE-VCP	Fuel-based inventory for vehicle emissions
IVOC	Intermediate-volatility organic compound
LA	Los Angeles
MEGAN	Model of Emissions of Gases and Aerosols from Nature
m/z	Mass-to-charge ratio
NOAA	National Oceanic and Atmospheric Administration
NO_x	Nitrogen Oxides
O_3	Ozone
OH	Hydroxyl radical
OVOC	Oxygenated VOC
PBL	Planetary Boundary Layer
PM	Particulate Matter
PTR-ToF-MS	Proton Transfer Reaction Time of Flight Mass Spectrometer
RECAP-CA	Re-evaluating the Chemistry of the Atmosphere in California
RH	Relative Humidity
SIP	State Implementation Plan
SOA	Secondary Organic Aerosol
SoCAB	South Coast Air Basin
SJV	San Joaquin Valley
SVOC	Semi-volatile organic compound
TAS	True Air Speed
TD-LIF	Thermal dissociation-laser induced fluorescence
UCB	University of California Berkeley
USDA	United States Department of Agriculture
VCP	Volatile Chemical Product
VOC	Volatile Organic Compound
WRF	Weather Research and Forecasting Model
WRF-Chem	WRF coupled with Chemistry
z	Flight altitude above ground
z_i	Planetary Boundary Layer height

Table of Contents

Abstract

Despite declines in transportation emissions, air in the San Joaquin Valley and Los Angeles remains unhealthy. The formation of secondary air pollutants ozone and PM (particulate matter) are dependent on both volatile organic compounds (VOC) and oxides of nitrogen (NO_x = NO + NO_2). We performed 16 research flights to map emissions of NO_x and of an unprecedented range of VOCs using airborne flux measurements in the Los Angeles region (South Coast Air Basin) and the San Joaquin Valley. Emission inventories represented traffic emissions (both NO_x and VOC) better than biogenic or volatile chemical product emissions. In the San Joaquin Valley, we show mismatches of the observed fluxes with inventories, including an underestimation of soil NO_x fluxes, an underestimation of dairy and citrus processing VOC fluxes, and an overestimate of biogenic isoprene fluxes. In Los Angeles, the observations suggest that the inventory overestimates NO_x emissions near the coast and underestimates them inland, and underestimates biogenic VOC emissions for mono- and sesquiterpenes. We demonstrate that biogenic terpenoid emissions contribute on average 60% to ozone and secondary organic aerosol formation in summertime Los Angeles, that this contribution strongly increases with temperature, and that this emission is largely missing in the inventories.

Executive Summary

The South Coast Air Basin and the San Joaquin Valley of California are major hotspots of ozone and particulate matter air pollution in the United States. Ozone and $PM_{2.5}$ in these regions have not improved substantially for the last decade, despite a reduction in vehicular emissions of their NO_x and volatile organic compound (VOCs) precursors. This reduction in "traditional" sources results in more uncertainty in descriptions of the present-day emission mixture of air pollutant precursors. The RECAP-CA (Re-evaluating Chemistry of Air Pollutants in California) aircraft campaign was conducted to obtain VOC and NO_x flux datasets covering relevant areas of the San Joaquin Valley and South Coast Air Basin (Los Angeles area) and to use the measured fluxes to evaluate and thereby reduce the uncertainty of emission inventories for VOC and NO_x. Inventories that are used by the California Air resources Board (CARB) and other agencies in their predictions of O_3 and SOA were assessed. The study was intended to map emission sources and potentially find unknown or underestimated ones, to investigate magnitude and temperature dependence of the emissions, and to assess the extent of weekend effects on the emissions.

Airborne flux measurements were conducted using a Twin Otter aircraft flying out of the Burbank, CA, airport. The flight altitude was 300-400 m and flights were executed between June 1 and 22, 2021, under clear sky conditions between 11:00 and 17:00 local time. Flight legs were flown at constant altitudes with legs that were as long and straight as possible to ensure high quality flux measurements. The flight routes were designed to cover a wide range of representative emission sources – in the San Joaquin Valley, croplands, dairy farms, oil and gas production, oak forests, highway and urban areas; and in the Los Angeles area highways, residential areas, the port, the downtown and the warehouse region in the eastern San Bernardino Valley.

VOC and NO_x concentrations were measured at 10 and 5 Hz, respectively, along with vertical wind speed at 10 Hz. The covariance of wind and concentration measurements was calculated using continuous wavelet transformation to obtain fluxes at flight altitude. The fluxes were extrapolated to the ground to get surface emission and deposition fluxes by correcting for chemical and physical vertical flux divergence. Flux footprints were calculated by the KL04-2D model to determine the ground areas where the fluxes originated. Thus, the measured emissions could be matched with spatially and time resolved emission inventories.

In the Los Angeles area, we find that the NO_x fluxes have a pronounced weekend effect and are highest in the Eastern part of the San Bernardino valley. The comparison of the RECAP-CA and the modeled CARB NO_x fluxes suggest the modeled emissions are too high near the coast and in downtown Los Angeles and too low further inland in the Eastern part of the San Bernardino valley. VOC fluxes measured included tracers for source categories such as traffic, vegetation, and volatile chemical products (VCPs). In Los Angeles, mass fluxes were dominated by oxygenated VOCs, with ethanol contributing ~29% of the total. In terms of OH reactivity and aerosol formation potential, terpenoids contributed more than half. Observed VOC fluxes were compared with two commonly used emission inventories: the California Air Resources Board (CARB) inventory, and the combination of BEIS with the FIVE-VCP inventory. The comparison shows mismatches regarding the amount, spatial distribution, and weekend effects of observed

VOC emissions with the inventories. The agreement was best for typical transportation related VOCs, while discrepancies were larger for biogenic and VCP-related VOCs. We demonstrate that biogenic terpenoid emissions account for ~60% of ozone and secondary organic aerosol formation potential in summertime Los Angeles, and that this contribution strongly increases with temperature. We also show that some important anthropogenic VOC emissions increase with temperature, an effect which is not represented in current inventories. Because of the strong influence of temperature, efforts to mitigate urban air pollution need to consider that climate warming will strongly change emission locations, amounts and composition.

In the San Joaquin Valley, we combined footprint calculations and land cover statistics, and we disaggregated the observed fluxes into component fluxes characterized by three different land cover types. On average we find NO_x emissions of 0.95 mg N m^{-2} h^{-1} over highways, 0.43 mg N m^{-2} h^{-1} over urban areas and 0.30 mg N m^{-2} h^{-1} over croplands. The calculated NO_x emissions using flux observations are utilized to evaluate anthropogenic emission inventories and soil NO_x emission schemes. We show that two anthropogenic inventories for mobile sources, EMFAC (EMssion FACtor) and FIVE (Fuel-based Inventory for Vehicle Emissions), yield strong agreement with emissions derived from measured fluxes over urban regions. Three soil NO_x schemes, including MEGAN v3 (Model of Emissions of Gases and Aerosols from Nature), BEIS v3.14 (Biogenic Emission Inventory System) and BDISNP (Berkeley Dalhousie Iowa Soil NO Parameterization), show substantial underestimates over the study domain. Compared to the cultivated soil NO_x emissions derived from measured fluxes, MEGAN and BEIS are lower by more than one order of magnitude and BDISNP is lower by a factor of 2.2. Despite the low bias, observed soil NO_x emissions and BDISNP present a similar spatial pattern as well as temperature dependence. We conclude that soil NO_x is a key feature of the NO_x emissions in the SJV and that a state-of-the-science model of these emissions is needed to simulate emissions for modeling air quality in the region.

VOC mass fluxes in the San Joaquin Valley were dominated by alcohols, mainly from dairy farms, while oak isoprene emissions and citrus monoterpene emissions were important sources of reactivity. Comparisons with the CARB and BEIS+FIVE inventories showed that isoprene emissions in the croplands were overestimated, while dairy and highway VOC emissions were generally underestimated in the inventories, and important citrus and biofuel VOC point sources were missing from the inventories.

The results of this project thus present unprecedented insights into the VOC and NO_x sources in the San Joaquin Valley and South Coast Air Basin, and provide much needed information for the improvement of inventories, air quality predictions and regulations.

For future studies, we recommend repeating the flux measurements in both the San Joaquin Valley and South Coast Air Basin to establish seasonal patterns and longer-term trends in VOC and NO_x fluxes. It would be beneficial to explore establishing long term flux towers to supplement existing concentration measurement networks and to prepare to make routine and rapid use of the satellite remote sensing observations of NO_x, H_2CO and aerosol that will soon be available from TEMPO. Emission rates and source contributions will likely continue to evolve with climate change, transformation of the vehicle fleet towards electric power, and other

controls that may be implemented on anthropogenic sources. Thus, future measurements of fluxes both at fixed tower sites and through airborne measurements at regular intervals are needed for documenting future VOC and NO_x emissions in these evolving polluted regions.

Task summary and work described in this project

The major objective of this work was to obtain VOC and NO_x flux datasets covering relevant areas of the San Joaquin Valley and South Coast Air Basin, and using these to validate the CARB emission inventories for VOC and NO_x. The research included a field measurement planning exercise to optimize the amount of information to be gained from airborne flux observations, conducting field measurements, then comparing observed fluxes to modeled fluxes in order to assess and improve CARB's emission inventory.
The work done for each of the 5 tasks identified in the contract is briefly summarized below:

Task 1: Field campaign planning
The initial step of the project was field campaign planning. Informed by current emission inventories, peer-reviewed literature, and TROPOMI NO_2 data, and guided by discussion with CARB, we identified regions of particular interest. The flight routes were planned based on this information, the methodological necessities for airborne flux measurements (flying long straight legs low and slowly), and air traffic regulation. In the San Joaquin Valley we made sure to cover croplands, dairy farms, highway, oil and gas production, urban areas, and oak woodlands. In Los Angeles the terrain was a limiting factor, so that we covered mostly the valleys, but also made sure to include Environmental Justice Communities near Long Beach and the port area with waiting ships. The campaign time was chosen to be daytime in June to ensure a high planetary boundary layer and homogeneous mixing.

Task 2: Preparing for field campaign
Preparation included pre-installation instrument characterization, configuration, calibration, and safety review. It also included integration onto the aircraft, ground systems tests, and a 2-hour test flight based out of the NPS Twin Otter facility in Marina, CA prior to deployment.

Task 3: Airborne flux measurements
We performed a field campaign with a total of 80 flight hours distributed over 16 flights (9 in Los Angeles, 7 in the San Joaquin Valley) out of the airport in Burbank, CA between June 1 and June 23, 2021. 10 Hz VOC and wind data, and 5 Hz NO_x data were recorded for airborne eddy covariance. The same tracks were repeated during each individual San Joaquin Valley or Los Angeles flight, respectively. Flight days were chosen according to the weather forecast to ensure cloud free conditions and a certain variability of temperatures between flights. We also made sure to include both weekends and weekdays.

Task 4: Analyzing airborne flux data
Airborne eddy covariance fluxes were calculated using wavelet transformation. This method de-convolutes time series into frequency bins of covariance. The sum over all frequency bins gives the flux for each point of time. This results in spatially highly resolved airborne fluxes. Significant

fluxes were observed for more than 130 VOCs, out of more than 630 species with measurable concentrations. This includes tracers for traffic, VCPs, dairy emissions, oil and gas, biogenics, biomass burning, and more.

The area of origin for each flux varies according to wind conditions, flight altitude, surface roughness and other parameters. We evaluated footprint models to derive the one that most reasonably represented the observed flux variability.

The flux footprints were mapped and matched with inventory grid cells in space and time, and comparisons were performed spatially, by temperature, and by weekday. They were also overlaid with landcover data. Source attribution and quantification was performed via footprint disaggregation using this landcover information in each footprint for multivariate linear regression.

Task 5: Draft Final Report

This report is submitted in fulfilment of Task 5.

1. Introduction

Photochemical modeling is an essential tool used to develop State Implementation Plans (SIPs) for O_3 and PM. Models are sensitive to the spatial and temporal distribution and source strengths of VOCs, NO_x, meteorological fields, sinks, and chemical reactions. They are sensitive to VOCs because VOCs provide the fuel for atmospheric photochemical processes that produce O_3 and are the substance of secondary organic PM. They are sensitive to NO_x because NO_x affects hydroxyl radical (OH) concentrations, setting the rate of the photochemical engine leading to air pollution, catalyzing production of O_3 and setting the oxidation rate of VOCs and thus the rate of secondary organic aerosol formation. For example, changes in air pollution emissions from 2006 to 2013 in the Los Angeles Basin are estimated to have increased OH levels by ~35% in the city center, while decreasing OH levels by ~15% 100 km downwind (Figure 1). Temperature is also a major driver. High temperatures are correlated with stagnation and consequently higher concentrations of VOC and NO_x because of slowed removal to deposition and increased time for emissions to accumulate. High temperatures are also associated with the increase in the rate of reactions and most importantly with an increase in the emissions of many VOCs. These processes vary across air basins and control human exposure to air pollution and associated health effects.

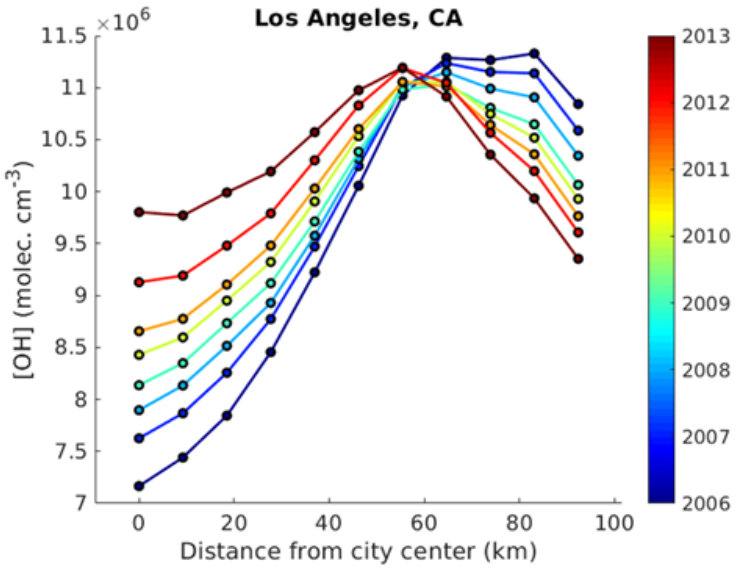

Figure 1.1: Model prediction of OH changes in the Los Angeles basin from 2006-2013. These changes are largely driven by decreases in NO_x. (Laughner, Zhu and Cohen, unpublished results)

1.1. Volatile Organic Compounds (VOCs)

A myriad of biogenic and anthropogenic sources can typically be identified by their VOC emission signatures (e.g. fossil-fuel based transportation, cooking, consumer products, industrial activities), but the mixture of sources and chemical composition of VOCs is rapidly changing. As shown in Figure 1.2, United States (US) vehicular VOC emissions have been dramatically decreasing due to successful efforts to control air pollution since the 1970s (e.g. Warneke et al., 2012). The Contractor recently completed a study funded by CARB investigating how organic compound emissions from light-duty vehicles are changing due to evolving emission control regulations and strategies (Goldstein et al., 2017). Detailed speciation of VOCs including intermediate and semi-volatile (IVOC/SVOC) emissions from a range of currently in-use vehicles demonstrated a rapid decline with improving emission controls as the on-road fleet transitions to newer vehicles (Drozd et al., 2019; Drozd et al., 2016; Saliba et al., 2017; Zhao et al., 2017). A critical take home message from these vehicle emission studies is that as emission control technologies improve, the fraction of total vehicular emissions from on-road driving is falling much faster than emissions from cold starts (when catalyst is cold). This must result in changing the urban spatial distribution of vehicular VOCs (and by implication also NO_x emissions), from on-road towards parking locations such as residential neighborhoods and urban parking locations, a pattern relevant to this project. Additional decreases are now also occurring due to a shift towards electric vehicles, especially in urban areas of California.

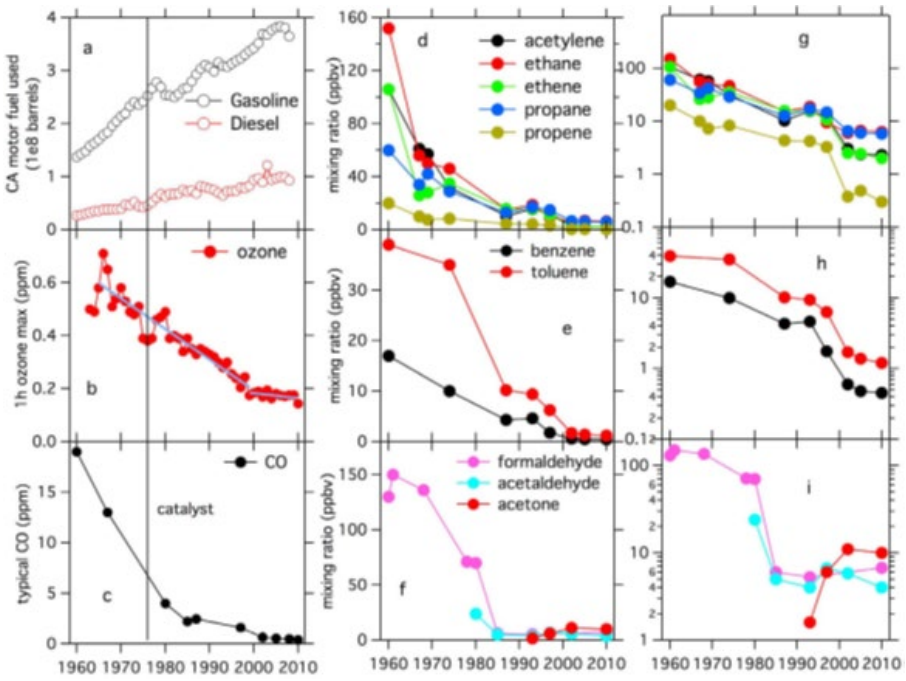

Figure 1.2: Trends since 1960: (a) California fuel (gasoline and Diesel) sales; (b) 1-h O_3 maximum mixing ratios in the LA basin. (c–f) Typical mixing ratios estimated from published data from various campaigns close to downtown LA. (g–i) Same as Figures 3d–3f on a logarithmic scale. Figure and caption adapted from Warneke et al. (2012).

On the other hand, the relative contribution of so-called volatile chemical products (VCPs), cooking emissions, and other indoor sources to urban VOC emissions is growing. A recent model (compared to measurements from 2010) estimates VCPs to contribute 50% of the petrochemical VOC sources in industrialized cities, as shown in Figure 1.3 (McDonald et al., 2018). Many important sources of VCPs are not targeted by air pollution regulation efforts, and VOC emission regulations and inventories have not been addressing the whole life cycle of the chemicals such as long-term off-gassing, volatilization of byproducts, etc. (Khare and Gentner, 2018). Even with the massive reductions in emissions from vehicles and other regulated sources, O_3 and PM levels still frequently exceed current air pollution standards in California. A better understanding of the complex evolving chemical cocktail of VOC emissions is required to yield further improvement in urban air pollution.

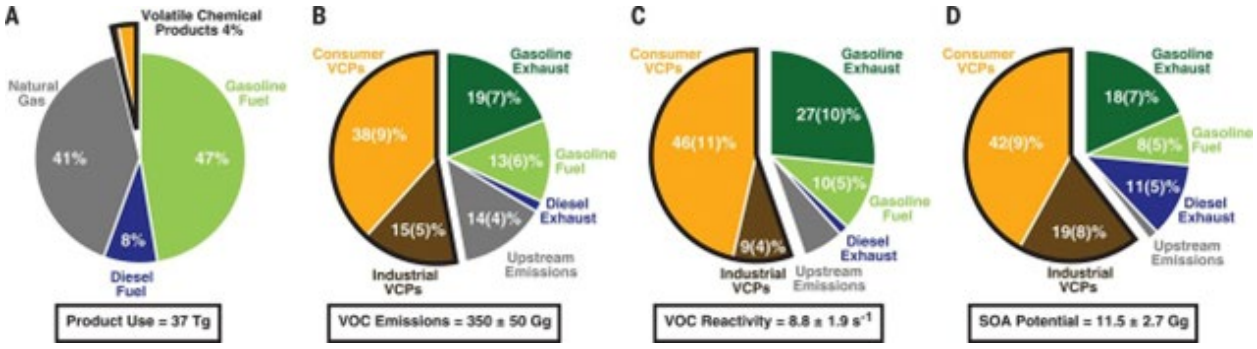

Figure 1.3: Anthropogenic contributors to ambient air pollution the role of VOC in Los Angeles air quality. (A to D) Distribution of (A) petrochemical product use, (B) anthropogenic VOC emissions, (C) anthropogenic VOC reactivity with OH, and (D) anthropogenic SOA formation potential across petrochemical sources only. Contributions from non-fossil sources are not shown. Uncertainties in source apportionment were determined by Monte Carlo analysis. From McDonald et al. (2018).

UC Berkeley has engaged in a series of research projects on the chemistry of indoor air, focusing mainly on indoor emission sources and chemical composition of gas and particle phase organic chemicals. A critical take home message from these studies relevant to this work is that VOC emissions indoors are substantial and a poorly understood source contributing to urban air pollution.

Studying a densely occupied university classroom, the highest emission rates of observed VOCs in the classroom were for cyclic volatile methyl siloxanes (cVMS), particularly decamethylpentasiloxane (D5), widely used in personal care products such as antiperspirants (Tang et al., 2015). These results have been cited in a series of new studies using cVMS compounds observed in urban air as indicators of VCP emissions. For example, Coggon et al. (2018) reported D5 emissions in Boulder, CO and Toronto, Canada as comparable to transportation emissions of benzene in those cities, clearly demonstrating that indoor emissions are relevant sources of outdoor air pollution.

Studying residential homes, ~50% of all indoor VOC species observed by Proton Transfer Reaction Time of Flight Mass Spectrometry (PTR-ToF-MS) were an order of magnitude higher than outdoors, ~80% of observed VOCs were at least twice as high as outdoors, and the dominant sources were continuous and temperature dependent (Liu et al. 2019). Episodic emissions due to human activities such as cooking and cleaning were also important (Liu et al. 2019). Ventilation rates were fast enough that in just a few hours the indoor air exchanged completely with outdoor air (Liu et al., 2019). Indoor oxidant concentrations were quite low (Arata et al., 2018). Together these results suggest indoor VOC emissions are typically transported to the outdoors providing a distinct VOC signature. Thus, transport of VOC/IVOC/SVOC emissions from indoors need further study as likely important sources of urban outdoor air pollution. Not yet published results indicate that the total flux of VOCs from a

normally occupied house are comparable to those measured from a dense pine forest (e.g., Bouvier-Brown et al., 2012) on a per ground area basis. Furthermore, monoterpene emissions, which come from cooking, cleaning, other household and personal care products, were also similar in magnitude to the emissions per area observed in the pine forest.

Tens of thousands of different VOCs are known, but many more remain so far unknown, largely because novel chemicals are created as secondary pollutants through atmospheric reactions of primary VOCs. Due to this complexity (and the technically challenging devices needed to observe this complex mixture), regulatory agency-operated urban monitoring stations typically do not measure a vast array of the VOCs present in the atmosphere. In the past, instrument limitations restricted VOC measurements to a few compounds, with mass spectrometers scanning one predefined molecular mass after the other. However, recently a new class of mass spectrometers became available which can quantify hundreds of VOCs at the same time - including detecting a vast array of secondary compounds that have not yet been isolated in the laboratory. These new measurement capabilities enable a far more comprehensive understanding of the complex VOC mixture in urban air. To determine the origin of anthropogenic emissions, VOC observations can provide crucial clues, as they provide "chemical fingerprints" of the different source types (e.g. transportation/vegetation/VCPs/residential/photooxidation, etc.). Once emitted to the atmosphere, VOCs react on timescales of minutes to weeks, depending on the specific compound. This changes their chemical and physical properties (e.g. vapor pressure / solubility). Depending on these properties, the VOCs either remain available for further chemical reactions, aggregate to form particulate matter, or are removed from the atmosphere by deposition (Goldstein and Galbally, 2007). Atmospheric losses must be accounted for when applying airborne flux measurements to estimate emissions of short-lived compounds.

1.2. Oxides of Nitrogen (NO_x)

NO_x in urban areas is primarily emitted from high temperature combustion sources—cars, trucks and other fossil fuel burning. Emissions can also result from lightning and from microbial metabolic pathways, often in association with fertilizer application. The latter are typically considered in agricultural regions—emissions from the urban biosphere have not been assessed in detail as vehicular emissions have historically and continue to dominate but there is speculation about the role of lawns, golf courses and agriculture at the urban rural boundary. Recently it has been shown with laboratory observations of California tree species at the branch scale and a column model, that stomatally controlled uptake of NO_x can be almost half the NO_x sink at concentrations above 10 parts per billion (ppb) (Delaria and Cohen, 2020; Delaria et al., 2018). Thus, fluxes can be to and from the landscape simultaneously.

Improvements in catalytic converters and their widespread implementation on passenger vehicles and new selective catalytic reduction (SCR) technologies implemented on heavy-duty diesel trucks have resulted in long-term NO_x reductions of about 7% year. These changes are important to setting the rate of chemistry in cities. Initially, reductions in NO_x led to an acceleration of chemistry, including more rapid oxidation of VOC and of NO_x. As a result, a 5% NO_x emission reduction might have been associated with a 7% NO_x concentration reduction. Separating the

two effects has been difficult and many analyses have implicitly assumed that concentration reductions can be directly mapped 1:1 to emission reductions. Recently, an extensive analysis of satellite observations of NO_2 confirmed that there have been decadal scale trends in the lifetime of NO_x and implying that these lifetime trends were coupled to trends in VOC and NO_x concentrations (Laughner and Cohen, 2019). As a consequence of this coupling, concentration of NO_x in Los Angeles decreased by less than the emissions decrease in Los Angeles as shown in Figure 1.4.

NO_x emissions from different sources are correlated with different VOCs and have unique ratios to CO and CO_2. The scientific design of this project, obtaining simultaneous observations of VOC and NO_x fluxes, aims at using these correlations to identify processes and sectors responsible for the different emissions.

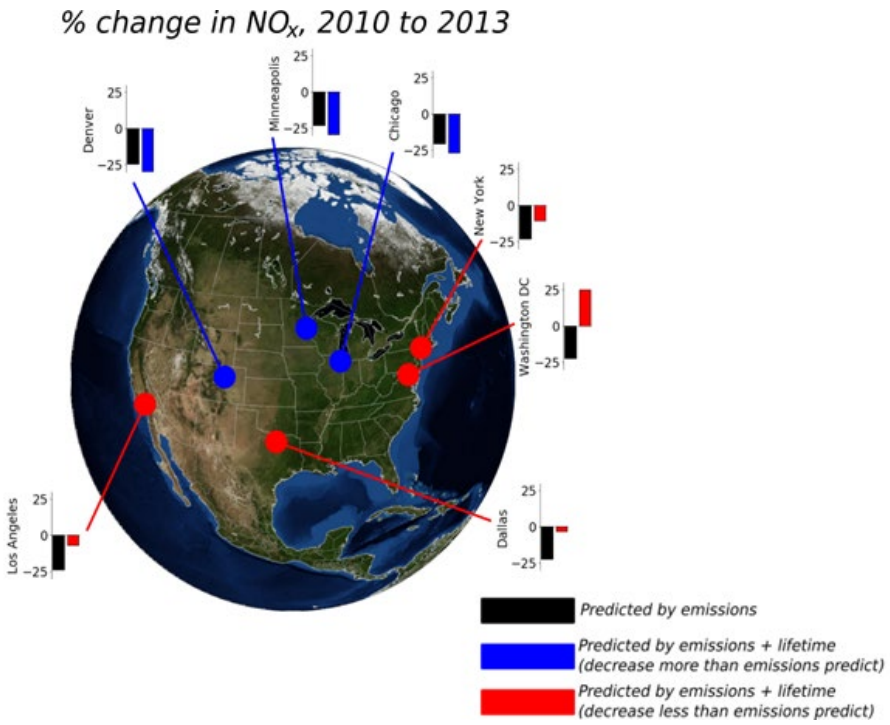

Figure 1.4. Relationship between NO_x emission reductions and NO_x concentration changes are different in different cities. Interpreting satellite observations of NO_2, Laughner and Cohen showed that concentration changes could be slower (red) or faster (blue) than emissions changes. The variations are assumed to be due to differences in the absolute NO_x concentration and to local VOC concentrations and reactivity (Laughner and Cohen, 2019).

2. Methods

2.1. Flight routes and study regions

A total of 16 flights was conducted in June 2021, seven of which in the San Joaquin Valley and nine in the Los Angeles region (South Coast Air Basin). Routes were selected to ensure a good coverage of the South Coast Air Basin (Fig. 2.1) and southern San Joaquin Valley (Fig. 2.2), while keeping individual flight legs as long and straight at a stable altitude of 300-400 m as possible (low, stable altitude and long legs assure good quality airborne flux measurements (Karl et al., 2013)). The aircraft flew slowly at an airspeed of 50-60 m/s to ensure a good spatial resolution. Each Los Angeles flight and every other San Joaquin Valley flight included a 12-15 km long stacked racetrack pattern (Karl et al., 2013) flown at 4-6 different altitudes within the planetary boundary layer. Adjustments to the routes were made according to requests from air traffic control both during planning and as necessary during flights. The aircraft took off at ~11:00-12:00 local time at Burbank Airport and landed at ~16:00-17:00.
Routes and flight days in Los Angeles were also designed to (i) cover a wide range of temperatures, (ii) include ships anchoring in front of the port of Los Angeles, (iii) the region with a high density of warehouses in the eastern San Bernardino Valley, and (iv) Environmental Justice Communities around refineries. Otherwise, routes in Los Angeles were repeated along the same tracks during each of the 9 flights, while alternating the flight direction (either first going into the San Bernardino Valley or to the south).

Routes in the San Joaquin Valley were planned to cover (i) agricultural areas, especially dairy farms, (ii) the highway I-99, (iii) oak woodlands in the Sierra Nevada foothills, (iv) the urban areas of Bakersfield and Fresno, and (v) the oil and gas fields northeast of Bakersfield.
Routes in the San Joaquin Valley were repeated along the same tracks during each flight, except that some flights were cut shorter towards the north and instead included a racetrack pattern at several altitudes, while others reached north up to Fresno.

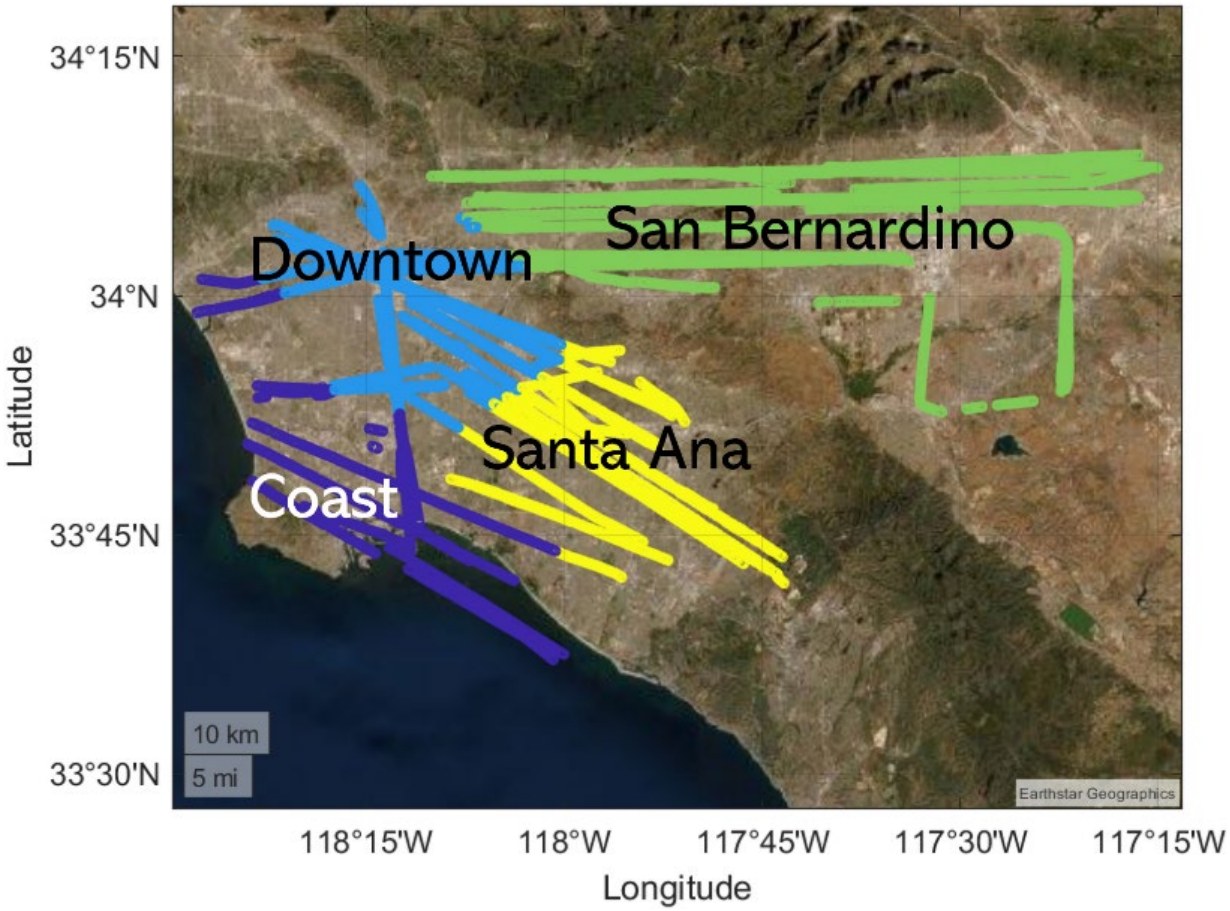

Fig. 2.1. Flight routes over Los Angeles (without segments that were removed for flux data quality reasons) and the four regions defined for the data analysis.

Fig. 2.2. Flight routes over the San Joaquin Valley.

2.2. Climatology during field campaign

Flights were performed between June 1 and 22, 2021, with average temperatures between 22 and 30°C in Los Angeles, and 23 to 36°C in the San Joaquin Valley. There was no precipitation. Flight days and routes were chosen so that no cloud cover was encountered. Table 2.1 and 2.2 provide overviews of the meteorological variables for each flight over Los Angeles and the San Joquin Valley, respectively. The flights were performed between 11:00 and 17:00 local time to ensure homogeneous turbulent conditions and a high planetary boundary layer (PBL). Average boundary layer heights in Los Angeles were around 500-700 m above ground, but often much lower at the coast, which made it at times challenging to stay within the PBL especially in that region, so that the flux data coverage is least dense at the coast of Los Angeles. In the San Joaquin Valley, PBL heights were 800-1300 m above ground.

Table 2.1. Average (± standard deviation) for meteorological variables and modeled OH for each flight (Los Angeles). OH was modeled using a box model that was trained using the flux gradients from stacked racetrack flights. RH: relative humidity, TAS: true air speed. w*: Deardorff velocity (convective velocity scale). "a.g.l.": above ground level.

Flight No	week-day	date	flight altitude a.g.l. (m)	TAS (m/s)	PBL height a.g.l. (m)	Wind speed (m/s)	wind direction (°)	RH (%)	Dewpoint temperature (°C)	Ambient temperature at 2 m a.g. l. (°C)	w* (m/s)	OH (molec/cm³)
LA1	week-day	01/06/2021	383 ± 77	56.2 ± 1.8	592 ± 71	3.1 ± 1.1	258 ± 20	66 ± 14	13.7 ± 0.7	26.6 ± 2.5	0.8 ± 0.3	3.0e+06 ± 4.5e+05
LA2	week-day	04/06/2021	347 ± 41	55.3 ± 2.0	515 ± 36	4.5 ± 1.6	235 ± 40	60 ± 18	12.3 ± 1.3	25.6 ± 3.4	0.8 ± 0.3	4.1e+06 ± 2.2e+06
LA3	week-end	06/06/2021	400 ± 55	56.0 ± 2.3	645 ± 15	4.9 ± 1.4	203 ± 55	74 ± 10	11.1 ± 0.5	22.6 ± 2.9	1.0 ± 0.3	5.9e+06 ± 2.4e+06
LA4	week-day	10/06/2021	395 ± 50	55.8 ± 2.1	694 ± 120	4.7 ± 1.4	249 ± 25	43 ± 7	4.5 ± 2.3	24.5 ± 1.4	1.1 ± 0.3	1.8e+06 ± 6.0e+05
LA5	week-day	11/06/2021	400 ± 61	57.0 ± 2.2	862 ± 258	3.9 ± 1.5	244 ± 50	40 ± 12	7.0 ± 2.8	28.7 ± 2.4	1.2 ± 0.4	3.8e+06 ± 1.2e+06
LA6	week-end	12/06/2021	366 ± 45	56.1 ± 1.8	572 ± 44	3.2 ± 1.2	256 ± 36	34 ± 9	6.4 ± 3.0	29.5 ± 2.8	0.9 ± 0.3	4.0e+06 ± 7.8e+05
LA7	week-day	18/06/2021	342 ± 35	56.5 ± 2.3	505 ± 58	3.1 ± 0.9	241 ± 44	68 ± 16	16.8 ± 0.6	29.1 ± 3.8	1.0 ± 0.3	3.3e+06 ± 1.1e+06
LA8	week-end	19/06/2021	345 ± 34	56.0 ± 1.9	477 ± 38	4.6 ± 1.6	247 ± 27	69 ± 13	17.2 ± 0.6	28.6 ± 2.9	0.8 ± 0.2	4.1e+06 ± 2.0e+06
LA9	week-day	21/06/2021	340 ± 52	55.1 ± 2.6	495 ± 84	4.1 ± 1.7	242 ± 43	63 ± 20	14.4 ± 1.9	28.0 ± 5.4	0.8 ± 0.3	3.4e+06 ± 8.7e+05

Table 2.2. Same as Table 2.1, but for San Joaquin Valley. "Fresno flight" indicates whether a flight included Fresno in the north (Y). If it did not (N), stacked racetrack patterns were flown at a suitable location in order to measure vertical flux gradients.

Flight No	**Fresno flight**	**date**	**flight altitude a.g.l. (m)**	**TAS (m/s)**	**PBL height (m a.g.l.)**	**Wind speed (m/s)**	**Wind direction (°)**	**RH (%)**	**Dewpoint temperature (°C)**	**Ambient temperature at 2 m (°C)**	**w* (m/s)**	**OH (molec/cm³)**
SJV1	N	03/06/2021	434 ± 126	57.1 ± 2.5	1303 ± 114	3.2 ± 1.3	335 ± 50	29 ± 4	9.7 ± 2.1	36.2 ± 1.9	1.1 ± 0.4	1.9e+06 ± 6.8e+05
SJV2	N	08/06/2021	430 ± 104	56.4 ± 2.3	1202 ± 52	3.1 ± 0.9	314 ± 45	40 ± 5	2.6 ± 1.2	22.8 ± 1.8	1.6 ± 0.4	2.9e+06 ± 9.7e+05
SJV3	Y	09/06/2021	424 ± 101	56.0 ± 2.7	1266 ± 20	3.5 ± 1.1	304 ± 33	41 ± 5	2.7 ± 0.7	22.6 ± 1.7	1.6 ± 0.4	3.0e+06 ± 8.3e+05

SJV4	Y	13/06/2021	439 ± 111	57.2 ± 2.5	1234 ± 73	2.8 ± 0.9	305 ± 38	48 ± 6	13.3 ± 1.6	31.2 ± 2.0	1.3 ± 0.4	2.6e+06 ± 8.3e+05
SVJ5	Y	15/06/2021	428 ± 114	57.1 ± 2.6	1193 ± 23	3.0 ± 1.2	323 ± 45	42 ± 6	8.3 ± 2.2	28.0 ± 2.0	1.3 ± 0.4	2.9e+06 ± 1.0e+06
SJV6	N	16/06/2021	421 ± 85	57.4 ± 3.2	899 ± 102	2.9 ± 1.1	307 ± 43	33 ± 4	9.4 ± 1.9	32.9 ± 1.3	1.1 ± 0.4	1.9e+06 ± 5.9e+05
SJV7	Y	22/06/2021	415 ± 94	56.9 ± 2.6	826 ± 126	2.6 ± 0.8	284 ± 35	36 ± 7	9.5 ± 2.2	31.6 ± 2.2	1.0 ± 0.3	2.4e+06 ± 9.2e+05

2.3. Aircraft

A two-engine UV-18A Twin Otter research aircraft (Fig. 2.3) was operated by the Naval Postgraduate School out of the Burbank airport, CA. The aircraft is equipped with micrometeorological sensors and is capable of flux measurements (Karl et al., 2013). The NPS Twin Otter payload during RECAP-CA included total temperature measured by a rosemount probe, dew point temperature (chilled mirror, EdgeTech Inc., USA), barometric, dynamic, and radome-angle pressures based on barometric and differential transducers (Setra Inc., USA), total air speed, mean wind, slip- and attack angles measured by a radome flow angle probe, GPS pitch, roll and heading (TANS Vector platform attitude, Trimble Inc., USA), GPS latitude, longitude, altitude, ground speed and track (NovAtel, Inc., USA), and latitude, longitude, altitude, ground speed and track, pitch, roll and heading measured by C-MIGITS-III (GPS/INS, Systron, Inc., Canada).

Air was drawn from a 3-inch isokinetic pipe inlet extending above the nose of the plane. Ambient air gets diffused from a 2.047 inch ID orifice at the tip (area ratio of about 2) to another diffuser with an area ratio of 5, resulting in a flow speed inside the tube of about 10% of the aircraft speed (~ 60 m s-1). Vertical wind speed was measured by a five-hole radome probe with 33º half-angles at the nose of the aircraft. The measured vertical wind speed is unaffected by the aircraft movement and flow distortion at the nose, as long as corrections based on “Lenschow maneuvers” are applied (Lenschow, 1986). More detailed descriptions of this particular aircraft can be found elsewhere (Hegg et al., 2005).
The aircraft payload included: 1) Airborne Vocus PTR-ToF-MS for VOC fluxes; 2) Laser-induced Fluorescence instrument for NO_x fluxes; 3) Picarro cavity-ringdown spectrometer for H_2O, CO, CO_2, and methane.

Fig. 2.3. Twin Otter aircraft with mounted inlet.

2.4. NO_x and VOC measurements

2.4.1. Laser Induced Fluorescence measurements of NO_x

Mixing ratios of NO_x were measured at 5 Hz frequency using a custom-built three-channel thermal dissociation-laser induced fluorescence (TD-LIF) instrument. The multipass LIF cells, fluorescence collection, long-pass wavelength filtering (for λ >700 nm), and photon counting details have been previously described (Thornton et al., 2000; Wooldridge et al., 2010; Da Day et al., 2002). Details specific to this implementation are described below.

Air was sampled from the aircraft community inlet through PFA Teflon tubing at a rate of ~6 L/min and split equally between the three instrument channels. Each measured NO_2 by laser-induced fluorescence utilizing a compact green laser (Spectra-Physics ExplorerOneXP 532 nm). The laser was pulsed at 80 kHz and the 1.7 Watt average power was split between the three cells. Earlier versions of the instrument used a dye laser tuned on and off a narrow rovibronic NO_2 resonance at 585.1 nm. Experience over a wide variety of conditions had demonstrated the off-line signal did not depend on the sample, other than from aerosol particles and that could be eliminated by adding a Teflon membrane filter. Moving to nonresonant excitation at 532 nm provided full-time coverage at 5 Hz along with lower complexity and more robust performance of the laser system. Maintaining the LIF cells at low pressure (~ 0.4 kPa) was no longer required to avoid line-broadening but was still desirable to extend the NO_2 fluorescence lifetime for time-gated photon counting to reject prompt laser scatter. Instrument zeros were run using ambient air scrubbed of NO_x every 20 minutes in flight to correct for any background drift during the flights. In addition, calibrations were performed in-flight every 60 minutes using a NO_2 in N_2 calibration cylinder (Praxair, 5.5 ppm, Certified Standard grade) diluted with scrubbed air.

NO_2 was measured directly in the first channel, with the sample passing only through a particle filter and a flow-limiting orifice before the cell. NO_x was measured in the second by adding O_3 (generated with 184.5 nm light and a flow of scrubbed and dried air) to convert NO to NO_2 before detection. A 122 cm length of 0.4 cm i.d. tubing served as the O_3+NO reactor, providing 4 seconds of reaction time before the orifice. The third channel was used to measure the sum of higher nitrogen oxides (e.g. organic nitrates and nitric acid) by thermal dissociation to NO_2 with an inline oven (~ 500 °C) before LIF detection.

2.4.2. Vocus-PTR-ToF-MS measurements of VOCs

2.4.2.1 Sampling and instrument operation

Ambient air was sampled via a 90 cm long heated (40°C) 1/4'' Teflon line through a Teflon filter from the abovementioned isokinetic inlet (flow speed approximately 6 m/s for 5 m length) with a mass flow controller at 1.5 L/min. The resulting lag time between the wind sensor and VOC detection was around 3 s.

The Vocus proton transfer reaction time of flight mass spectrometer (Vocus PTR-ToF-MS, Aerodyne Inc., Billerica, MA, USA, (Krechmer et al., 2018)) was operated at 60°C reactor temperature, 2.0 mbar reactor pressure, and an E/N of ≈130 Td. Mass resolution was 4805 ± 283 (average ± standard deviation). The potential gradient along the focusing ion-molecule reactor (FIMR) was 590 V. The gradient between skimmer 1 and skimmer 2 was changed once during the campaign from 6 to 9.1 V, which resulted in an improved sensitivity for some VOCs, but stronger fragmentation for others, both of which effects were taken into account for by calibrating. The reagent water flow was 20 sccm. With the resulting high water mixing ratio (10%v/v–20%v/v) in the FIMR, the instrument showed no humidity dependence for sensitivity, which is an advantage in flux measurements because it eliminates the necessity to correct for humidity differences between different eddies caused by water fluxes. The high water concentration causes a high primary ion (H_3O^+), whose signal is reduced by a big segmented quadrupole (BSQ) that decreases the transmission of low-mass ions in order not wear out the detector too quickly. However, we kept the voltage of the BSQ relatively low at 200 V so that signals for low-mass VOCs like methanol were not too strongly reduced.

Mass spectra were recorded at 10 Hz time resolution (or 2 Hz time resolution, for 3 flights out of 16: SJV6, LA7, LA8) for a mass range of 10-500 Da. Zero air measurements were conducted several times during each flight for 1-5 min, during direction changes of the aircraft, because data acquired during turns cannot be used for flux calculations. 2-4 times during each flight, the zero air measurement was followed by a pulse of calibration gas of approximately 1-5 min length. These calibration data were used to confirm that the instrument sensitivity after correction for the zero air background did not change significantly with the lower inlet pressure at our flight altitude and that, thus, the calibration factors acquired on the ground were applicable to the airborne data.

2.4.2.2 VOC data treatment and calibration

Raw PTR-ToF data were processed with Tofware 3.2.3. No dead time correction was applied in this step. 630 peaks were selected for peak fitting to derive ion counts per second. Ion counts

from in-flight zero air measurements were interpolated and subtracted from the ambient data. The instrument zero at flight altitude was different from the zero on the ground due to pressure effects that changed the pressure control valve position. Laboratory tests of pressure effects confirmed that after subtraction of the flight zero, the sensitivities at the altitudes we flew at were the same as on the ground.

Ground calibrations were conducted every 1-3 days (in total, 19 times) during the campaign using one of three different gravimetrically prepared multicomponent VOC standards (Apel-Riemer Environmental Inc., Colorado, USA). The following VOCs were included in the calibration gas standards: methanol, acetonitrile, acetaldehyde, ethanol, acrolein, dimethyl sulfide, isoprene, methacrolein + methyl vinyl ketone, benzene, toluene, xylene, p-cresol, 1-,3-,5-trimethylbenzene, D3 siloxane, D4 siloxane, D5 siloxane, D6 siloxane, propanol, butanol, acetone, furan, furfural, benzaldehyde, 6-MHO, monoterpenes (mixture of a- and b-pinene and limonene), nonanal, acrylonitrile, methyl ethyl ketone, b-caryophyllene. For most VOCs, the sensitivities were stable within 25% over the campaign.

For all m/z without a corresponding gas standard, the sensitivities were derived from a theoretical calibration, using a root function (the expected function of a ToF transmission) fitted to reaction rate normalized sensitivities of non-fragmenting and non-clustering gas-standard calibrated VOCs (Holzinger et al., 2019, Yuan et al., 2017). This approach accounts for transmission effects dependent on m/z. A commonly used default reaction proton transfer reaction rate of $k = 2\text{x}10^{-9}$ cm³ molecule s^{-1} was applied for the non-gas standard compounds. The uncertainties of this and the gas-standard calibration are based on typical estimates for the uncertainty of the theoretical calibration (50%) and the gas-standard calibration uncertainty (20%), which consists of the calibration standard uncertainty and the uncertainty of the mass flow controller. The resulting estimated uncertainty of the calibration for gas-standard calibrated VOCs was 20%, while it was 54% for all other VOCs (propagated from 20% and 50%).

2.4.2.3 VOC identification

Since the PTR-ToF-MS method provides exact masses that can be attributed to chemical formulas, but often not with certainty to molecular structures, measured ions can be mixtures of several isomers or originate from varying VOCs, depending on the dominant source type.

Gasoline vapor as well as oil and gas emissions include cycloalkanes that fragment on $C_5H_8H^+$ (m/z 69.0699), the ion that is usually attributed to isoprene in PTR-MS. E.g. Gueneron *et al.* (2015) show that several cyclohexanes fragment on $C_5H_8H^+$, especially at higher E/N, comparable to the instrument conditions in our study. Pfannerstill *et al.* (2019) reported in measurements of oil and gas emission-dominated air around the Arabian Peninsula that isoprene measured by GC-FID was substantially lower than the $C_5H_8H^+$ signal in PTR-ToF-MS. They therefore attributed the $C_5H_8H^+$ after isoprene subtraction to emissions from oil and gas extraction. Additionally, many of the longer-chain aldehydes, such as nonanal, fragment on $C_5H_8H^+$, too (Buhr et al., 2002). These aldehydes can be substantial in urban areas and in dairy

emissions (Rabaud et al., 2003). Both the long-chain aldehydes and the cycloalkanes also appear on $C_8H_{15}^+$ (m/z 111.117) and/or $C_9H_{17}^+$ (m/z 125.132).

In order to separate isoprene from interfering fragments of aldehydes and cycloalkanes, we used the following approach: From the (isoprene-free) nonanal calibration gas standard, the ratio of m/z 69.0699 vs (m/z 111.117 + m/z 125.132) was derived. This ratio was compared to that seen over oil and gas fields in the San Joaquin Valley, were the m/z 69.0699 is most likely dominated by cycloalkane fragments. Both ratios were the same at ~ 17 (for a gradient between skimmer 1 and skimmer 2 of 6 V) or ~ 45 (at a skimmer gradient of 9.1 V). This isoprene-free ratio of m/z 69.0699/(m/z 111.117 + m/z 125.132) was used to correct the isoprene signal:

$$Isoprene_{corr} = m69.0699 - [(m111.117 + m125.132) \cdot slope_{nonanal}] \qquad \text{(Eq. 2.1)}$$

For an accurate isoprene flux correction, this equation was applied to the fluxes of m/z 69.0699 and (m/z 111.117 + m/z 125.132) directly, not to the mixing ratios first. Since aldehydes are long-lived and represent a relatively high background in urban areas, the correction was rather large (factor of 2) when applied to the mixing ratios. However, the correction is small in the flux data (10%) since the fluxes of the aldehydes are small. We conclude that most of the observed flux (i.e. covariance with vertical wind) on m/z 69.0699 was an actual isoprene flux on top of a high constant background signal of aldehydes that did not covary with the vertical wind.

Similarly, acetaldehyde was corrected for ethanol fragments (Buhr et al., 2002). Benzene was calibrated on the O_2^+ product m/z 78.046 to avoid influence of benzaldehyde fragments.

The monoterpenes measured at m/z 137.13 may include fragments of monoterpenoids and monoterpene alcohols whose parents mass is m/z 155.14 ($C_{10}H_{18}O$, e.g. eucalyptol (Kari et al., 2018), linalool, cineole, terpineol (Tani, 2013)).

2.5. WRF-Chem model simulation

We conducted model simulations over the study period using the Weather Research and Forecasting-Chemistry model (WRF-Chem v 4.1). The model configuration is described in Li et al. (Li et al., 2021). We first performed a WRF-Chem simulation at 12 km horizontal resolution over the Continental US to provide the initial and boundary condition, and then performed a 4 km horizontal resolution nest run over California.

We utilized the RACM2_Berkeley2.0 chemical mechanism (Goliff et al., 2013; Browne et al., 2014; Zare et al., 2018) with the following updates: We incorporated the Madronich Photolysis (TUV) scheme for the calculation of photolysis and coupled SOA VBS scheme for better representation of SOA formation (Ahmadov et al., 2012). Isopropanol, propylene glycol, and glycerol are added as new species to represent the VOC chemistry from VCP emissions (Coggon et al., 2021).

The anthropogenic emissions are provided by the fuel-based inventory for vehicle emissions (FIVE-VCP), developed by McDonald et al. (McDonald et al., 2012) and updated by Harkins et al. (2021). The FIVE-VCP inventory was further updated to include emissions from volatile chemical products (Coggon et al., 2021). We also re-speciated the FIVE-VCP inventory to the updated RACM2_Berkeley2.0 mechanism. The biogenic emissions are provided by Biogenic

Emission Inventory System (BEIS) v3.14. It is the default scheme to estimate volatile organic compounds from vegetation and NO from soil developed by United States Environmental Protection Agency (EPA).

The WRF-Chem outputs used in this study were $J(O^1D)$, H_2O, and O_3 for the chemical vertical divergence correction (see below).

2.6. Airborne Eddy Covariance

2.6.1. Flight segment selection

Flight segments for flux calculation were chosen according to the following criteria: gap-free length of at least 10 km, stable aircraft roll and pitch (within 8°), stable altitude (within ±50 m). This is to reduce errors (Lenschow et al., 1994; Karl et al., 2013), which become large for short flight segments. Planetary boundary layer (PBL) height was derived by eye from stark drops in dew point, water concentration, toluene concentration and temperature during aircraft soundings. Soundings were conducted at least at the beginning and end of each flight and before each stacked racetrack, but sometimes much more frequently when the aircraft accidentally left the low PBL near the LA coast. Datapoints outside the PBL were disregarded for flux calculation. In the remainder of this section, we offer a detailed description of application of our methodology to VOC. Nearly identical procedures were applied to NO_x.

2.6.2. Continuous wavelet transformation

Lag times were determined for each VOC and each segment by calculating the covariance and searching for the maximum covariance in a window of 4 s (covariance peak, see Fig. 2.5 A). Different VOCs have different levels of stickiness, which causes lag times to differ between compounds (Taipale et al., 2010). Because of our use of a mass flow controller in front of the inlet pump, pressure changes additionally influenced the lag time. Moreover, as Taipale et al. (2010) describe, lag times can vary because pumping speed varies over time, so a variable lag time assures that the flux is not underestimated. When there was no covariance peak above the noise, a constant lag time (the lag time of isoprene) was applied for the respective VOC and segment. The reason for this approach is that it is possible that there was a positive flux during half of the segment and a negative flux during the other half of the segment, which can be resolved with wavelet transformation.

Lag times were determined for NO_x following the same procedures as VOCs. However, for NO_x measurement, the time lag is assumed to be due to differences in the clocks of the two instruments and the transit time of air through the TD-LIF instrument, we assume that the lag time for each flight is constant. We use the median lag time from each flight for all segments collected on the same day to calculate the NO_x flux.

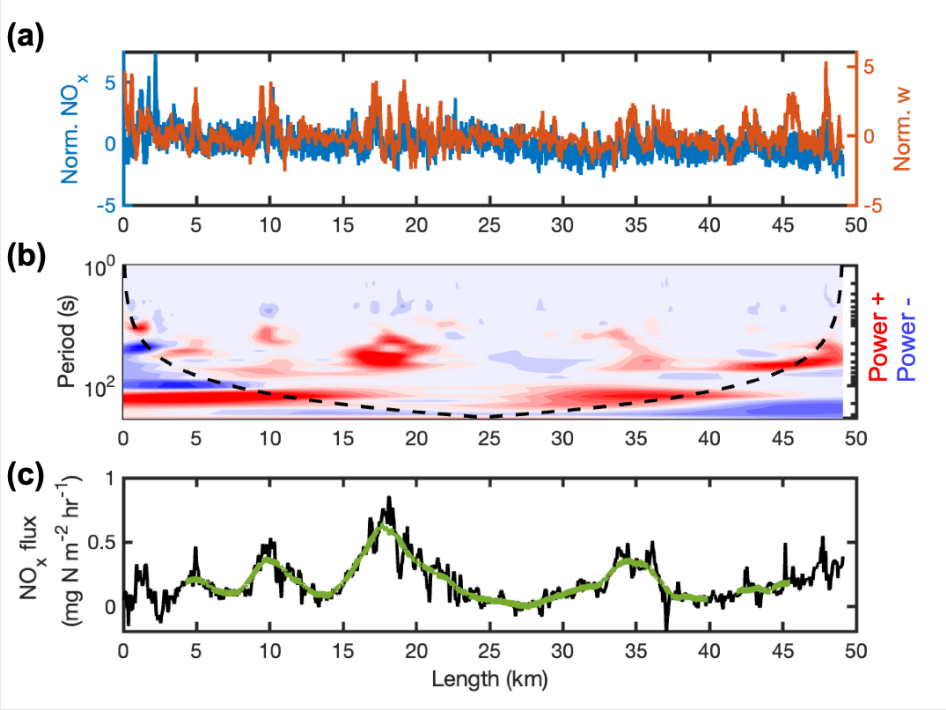

Fig. 2.4. Illustration of the steps from raw 5 Hz timeseries to the flux timeseries. a) Variance of NO_x and vertical wind speed, b) frequency and time resolved wavelet power spectrum with cone of infuence shown as black dotted line, c) the integrated fluxes from the raw data points are shown in black, the fluxes after moving averaging and COI filtering are shown in green.

Aircraft fluxes for each VOC were determined by continuous wavelet transformation (Torrence and Compo, 1998), which de-convolutes the variance within a timeseries along both the frequency and time (distance) domains (Fig. 2.5). 10 Hz wind and VOC data were aligned using the lag times determined as described above. Wavelet transformation of the data yielded the local wavelet co-spectra for each data point along the flight track. Integration over all frequencies generates the flux timeseries. A quality filter removed points containing > 80% spectral power within the cone of influence, the region in which edge-effects can lead to spectral artifacts. A moving average of 2 km was applied to the 10-Hz fluxes to remove artificial emission and deposition that are effects of turbulence, and sub-sampled to 200 m. All flux data points have associated systematic and random uncertainties. For the three flights where data was recorded only in 2 Hz resolution, disjunct Airborne Eddy Covariance was applied. Otherwise, these data were treated the same as the 10 Hz data. A comparison between results of 10 Hz fluxes and the same data averaged to 2 Hz before doing the wavelet transformation showed a very minor high frequency loss, with an overall reduced average flux of e.g. 0.5 % for isoprene and 0.4% for benzaldehyde. As the cumulative cospectrum (Fig. 2.5) shows, almost 100% of all flux is at frequencies below 1 Hz (the Nyquist frequency which can be resolved by 2 Hz sampling, Fig. 2.5). This indicates that the eddies were sufficiently large at our flight altitude that no significant information was lost by 2 Hz sampling. Previous aircraft campaigns operated at an even lower 0.7 s time resolution (Misztal et al., 2014; Karl et al., 2013) without a need for correction for high-frequency losses. The Nyquist frequency for 10 Hz measurements is 5 Hz (Fig. 2.5).

We note that polar VOCs such as long-chain OVOCs or siloxanes are prone to losses in the inlet system, leading to a dampened covariance peak and thus, a potential underestimation of their flux. However, the cumulative cospectra for most OVOCs compared well with the modeled complete cospectra, including sticky ones like cresol, ethanol or methanol. The stickiest among the gas-standard-calibrated VOCs was nonanal, for which the cospectrum suggests around 50% spectral loss.

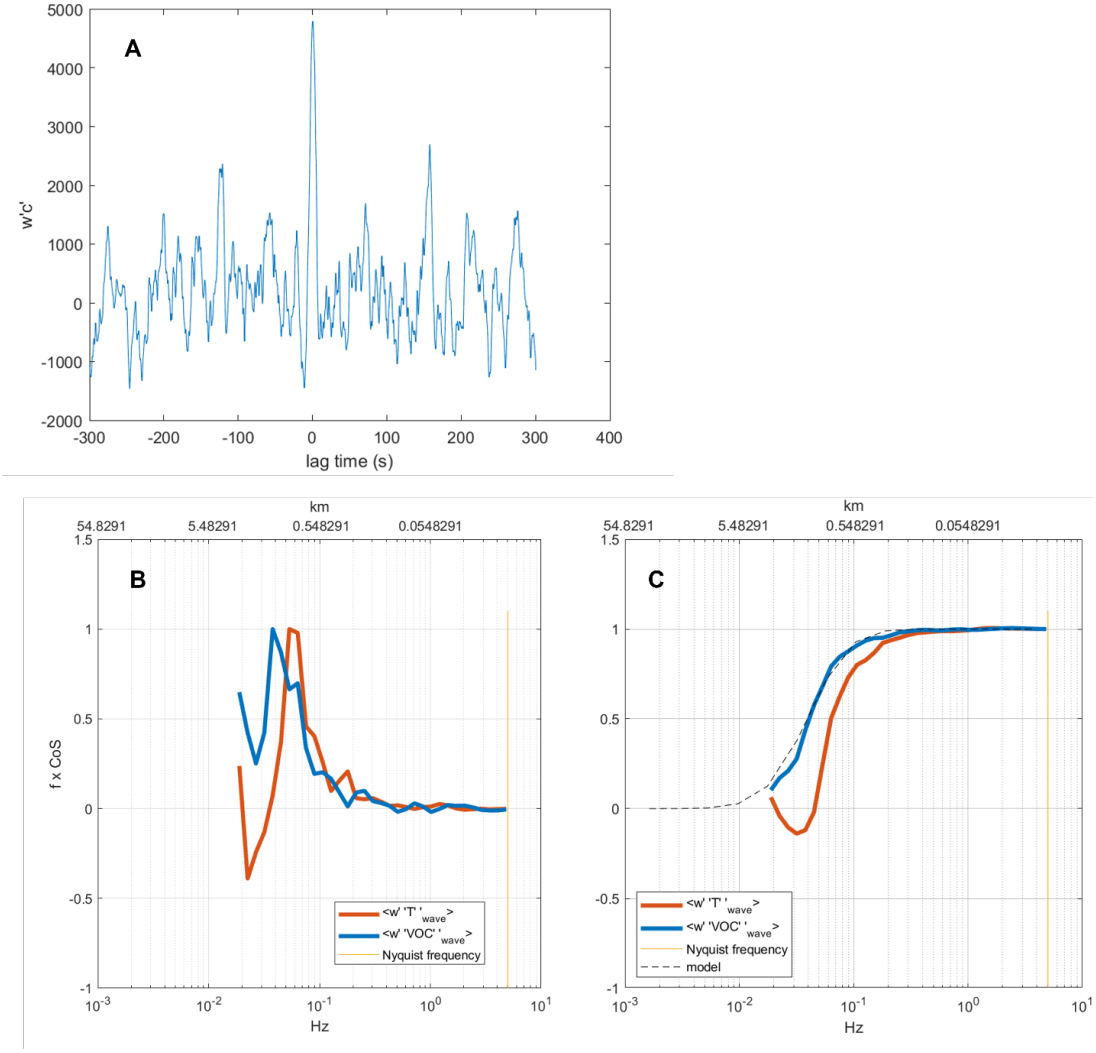

Fig. 2.5. Spectral quality control. (A) Covariance peak for D5 siloxane as an example for a VOC that is sticky and has low emissions. The covariance peak was resolved nonetheless. (B) Cospectra of toluene flux (w'VOC') and heat flux (w'T') for one example segment of flight LA3. (C) Cumulative cospectrum for toluene (w'VOC') and heat (w'T') fluxes for the same example segment of flight LA3. The cospectral model was derived by optimizing transfer functions from Lee *et al.* (2005) following Misztal *et al.* (2014).

2.6.3. Vertical flux divergence correction

2.5.3.1 Chemical vertical flux divergence correction for reactive VOCs

Reactive VOCs are partly lost between emission on the ground and observation at 300-400 m due to reaction with OH and ozone. In order to correct for this loss, gradients of fluxes of isoprene, trimethylbenzene, and dimethylfurane were used to derive approximate OH concentrations. The resulting OH for each of these three VOCs and their isomers covers a certain range. In order to get OH concentrations for the whole flight track, and not just the racetrack locations, we use the steady state box model described in the Supplement of Laughner and Cohen (Laughner and Cohen, 2019). Input parameters include the measured NO_x concentrations, VOC reactivity (calculated from all measured VOCs, CO, and methane, multiplied by 1.3 to account for unmeasured species), an organic nitrate branching yield of 0.056 based on the measured VOC composition, and OH production rates calculated using simulated $J(O^1D)$, H_2O and O_3 from WRF-Chem (see 2.5). The performance of the model was verified with data from the CalNex campaign, where direct OH and total OH reactivity measurements are available (Griffith et al., 2016).

The VOCs were then corrected using the OH concentration following:

$$\frac{dF}{dz} = k_{OH+VOC} * [OH][VOC] \qquad \text{(Eq. 2.2)}$$

$$F_s = z * \frac{dF}{dz} + F_z \qquad \text{(Eq. 2.3),}$$

where F_s is the flux at the surface and F_z the flux at flight altitude, z is the flight altitude, k_{OH+VOC} is the OH reaction rate of the respective VOC, and [OH] and [VOC] are the concentrations of hydroxyl radicals and VOC, respectively. The ozone correction was done the same way. OH and ozone reaction rates used and references are listed in Supplementary Table 1 and 2. Reaction rates for NO_x are too slow for its fluxes to be significantly affected by OH.

The speciation of monoterpenes measured as $C_{10}H_{16}H^+$ was assumed to be comparable to the afternoon Los Angeles monoterpene composition in van Rooy *et al.* (2021). The resulting reaction rate was verified and adjusted to represent (i) the ratios of inferred surface flux (after O_3 and OH correction) to measured aircraft flux at altitude, with the gradient observed in stacked racetracks, and (ii) the monoterpene oxidation product/monoterpene ratio with expected yields according to the reaction rate used. Both methods showed that the assumed combination of monoterpenes with 44% a-pinene, 8% camphene, 1% sabinene, 5% b-pinene, 5% b-myrcene, 1% 3-carene, 14% limonene, 10% eucalyptol, 1% phellandrene, 10% ocimene causing an average OH reaction rate coefficient of 8.52e-11 $cm^3\ molec^{-1}\ s^{-1}$ and an ozone reaction rate coefficient of 1.9e-17 $cm^3\ molec^{-1}\ s^{-1}$ are reasonable. Eucalyptol was included here despite being a $C_{10}H_{18}O$ monoterpenoid since ~90% of it is expected to fragment on $C_{10}H_{16}H^+$ (Kari et al., 2018). The monoterpenoid parent masses measured as $C_{10}H_{16}O$ and $C_{10}H_{18}O$ contributed only 0.06% and 2% of the total monoterpene flux, respectively, and therefore the choice of their reaction rate coefficients (here based on the average of citral and camphor reaction rates for $C_{10}H_{16}O$, and on the average of terpineol, linalool, and citronellal for $C_{10}H_{18}O$) did not significantly impact the result.

Even though there is uncertainty in the monoterpene composition and in the resulting chemical vertical divergence correction, a sensitivity analysis showed that the next step in the analysis – physical vertical divergence correction – removes most of the bias caused by an over- or underestimation of the monoterpene OH reaction rate coefficients, since it is based on the remaining vertical gradient in the oxidation-corrected data (see below). In the sensitivity analysis, a factor of 2 change in monoterpene reaction rate coefficients led to only a 12% change in average monoterpene flux.

2.5.3.2 Physical vertical flux divergence correction for VOCs

Physical vertical flux divergence is caused by horizontal advection and entrainment (Pigeon et al., 2007). Entrainment causes the flux divergence to be different for each chemical species. The vertical racetrack data did not show conclusive vertical gradients in non-reactive VOCs. We attribute this to impacts of local emissions and the larger uncertainty of the fluxes on the short (10 km) racetrack legs. Therefore, we used data from complete flights to determine the vertical flux divergence. Since the boundary layer heights varied strongly across the study domain and from day to day, we covered a wide range of z/zi (flight altitude normalized by boundary layer height) from 0.2-1. Due to the generally low, marine-influenced boundary layer in Los Angeles, 95% of the data was between z/zi = 0.5 and z/zi = 1 here. In the San Joaquin Valley, 95% of the data was between z/zi = 0.2 and z/zi = 0.66, causing a much smaller physical vertical divergence. The aggregation of data from multiple time periods caused uncertainty in the determination of the slopes, which is why we use the day-to-day-variation in the slopes as a basis for the Monte Carlo error propagation to determine the uncertainty of the vertical divergence correction (see chapter 2.6.4).

Vertical flux divergence was determined for each VOC and each of the four regions of Los Angeles separately. At first, for quality reasons, any data points with a random error > 30% or with a horizontal wind speed > 8 m/s or with a $z/z_i > 0.8$ were excluded. Data above z/zi 0.8 gets so close to the entrainment layer that the correction is more uncertain here, and in addition, the correction would become very large (and thus more uncertain) since it exponentially increases when approaching the top of the boundary layer.

Fluxes for each VOC and region were binned into eight different z/zi bins at regular intervals between $z/z_i = 0$ and $z/z_i = 0.8$, removing any bins that contain less than 3% of the data and any data points that do not have a counterpart in the other bins within 6 km distance (~ footprint size). The vertical divergence slope (s) is determined from a linear regression of the median flux of each altitude bin vs. z/z_i (Fig. 2.6 shows x and y axis inverted). The linear equation for a flux at altitude z (F_z) can be expressed as:

$$F_z = F_0 + s\frac{z}{z_i} \qquad \text{(Eq. 2.4)}$$

The slope is normalized by the intercept F_0 (which corresponds to the surface flux), and we call the normalized slope: $s/F_0 = C$. The slope needs to be normalized to get the relative loss due to vertical divergence, which can be applied to each surface flux (Wolfe et al., 2018; Druilhet and Durand, 1984).

$$\frac{F_z}{F_0} = 1 + C\,\frac{z}{z_i} \qquad \text{(Eq. 2.5)}$$

Rearranging the equation, the surface fluxes (F_0) can be calculated from the fluxes at altitude z as:

$$F_0 = \frac{F_z}{1 + C \cdot \frac{z}{z_i}} \qquad \text{(Eq. 2.6)}$$

C is negative for VOCs that are emitted at the surface. However, C can be positive when VOCs are deposited at the surface, or for OVOCs that are being formed (through oxidation) while the air moves from the surface to the point of observation.

Data points where the vertical divergence correction was larger than 3 times the median correction factor of the respective VOC were replaced with "NaN" in order to not introduce very high uncertainties. The vertical divergence correction in Los Angeles amounted to a factor of 2.1 ± 1.8 (average ± standard deviation), and in the San Joaquin Valley to a factor of 1.0 ± 1.3.

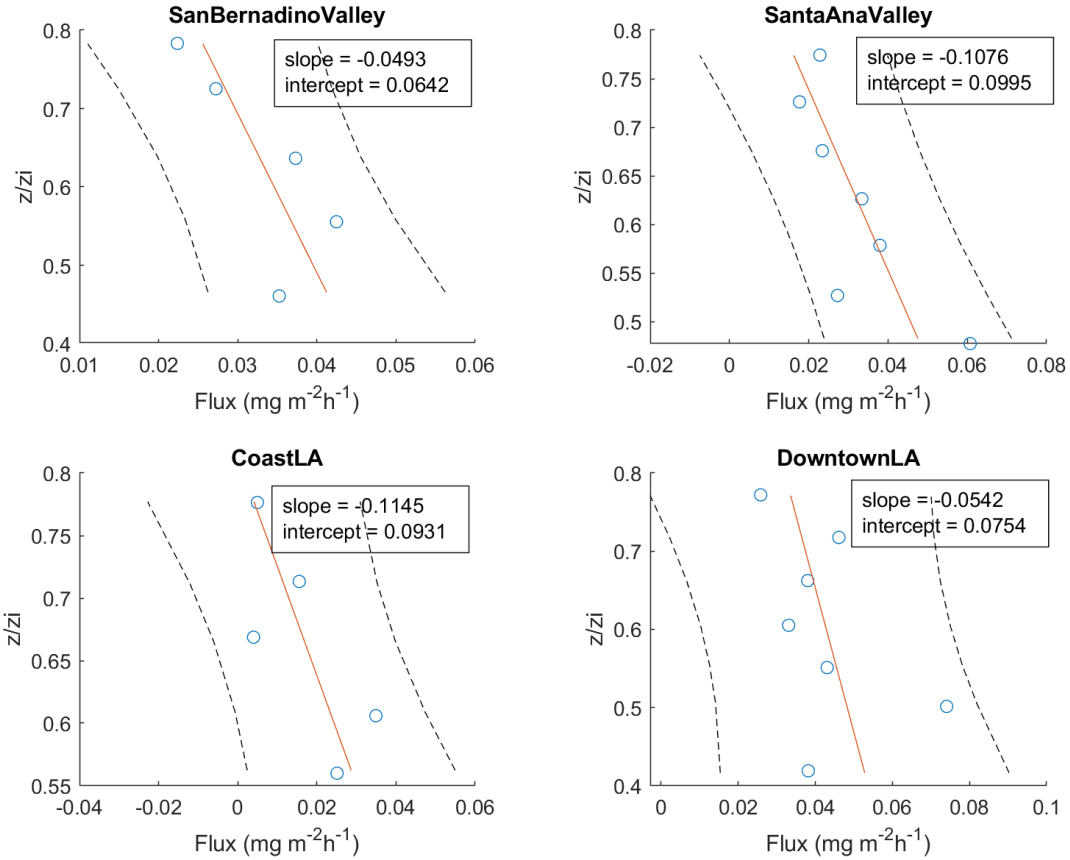

Fig. 2.6. Vertical divergence for benzene for each region of Los Angeles. The dashed lines denote the 95% confidence interval of the linear regression, and the orange lines the linear fit (where y= Flux, x = z/zi). z/zi is the flight altitude normalized by the boundary layer height.

2.5.3.3 Physical vertical flux divergence correction for NO_x

To investigate the impact of vertical divergence, the flight route includes three vertically stacked racetracks, during which the segments are close to each other in space but vary in height. After removing the legs that fail the quality control, only one racetrack measurement carried out between 14:20 to 15:10 on June 8th presented qualified flux segments, and the vertical distribution of fluxes is shown in Fig. S2.1. No consistent increase or decrease of fluxes with increasing height is detected during the racetrack in this study because the vertical divergence is hampered by emission heterogeneity. The footprint map for each segment at various altitudes covers regions with high heterogeneity.

Therefore, we use an alternative approach to calculate the vertical divergence. Instead of extracting racetrack measurements, we collect a subset of flux measurements during the whole field campaign based on the footprint coverage. Only fluxes with footprints covering croplands exclusively are included to avoid emission heterogeneity. We calculate the ratio of measurement heights relative to the PBL height (z/z_i) and 98% of selected fluxes are located within 70% of the PBL height and they are divided into 7 bins of z/z_i with uniform width. We then perform a linear fit for the binned median fluxes versus z/z_i to calculate the vertical correction factor (C = slope/intercept) (Figure 2.7). This correction factor is used to linearly extrapolated the fluxes at the measurement height (F_z) to fluxes at the surface (F_0) (Eqn. 2.6). After vertical divergence correction, the surface fluxes are on average 26% higher than the fluxes at the measurement heights.

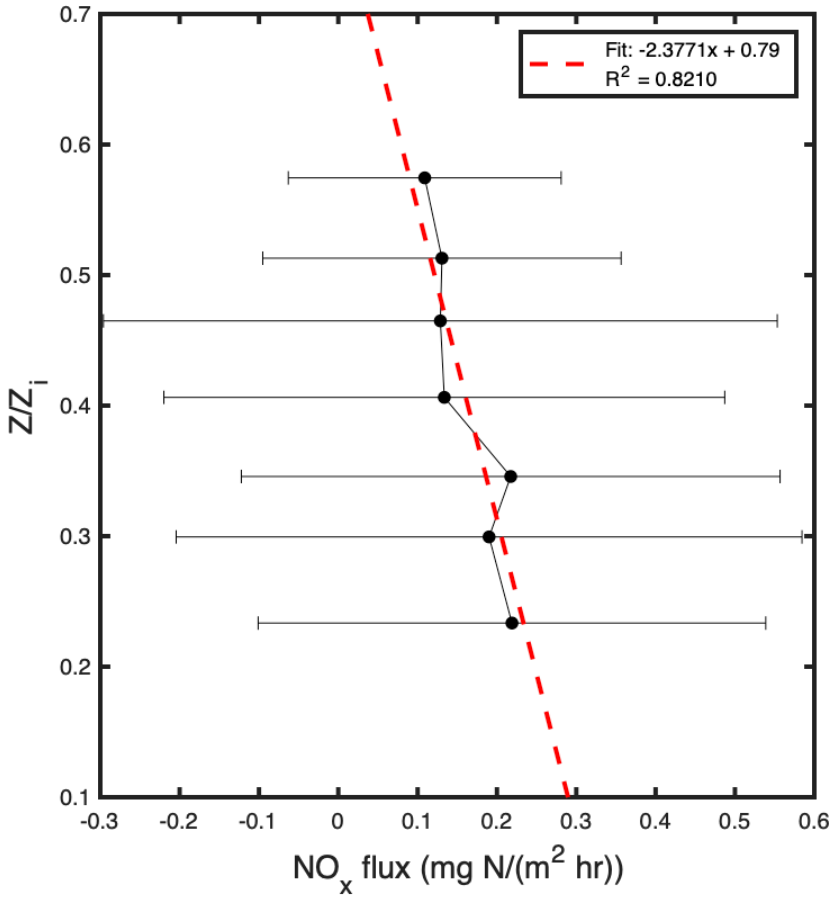

Fig. 2.7. Vertical profiles of measured fluxes above croplands during RECAP-CA field campaign binned by the ratio of measurement height and PBL height (z/z_i). The points represent the median flux within each bin, and the error bars represent the standard deviation. The red dashed line shows a linear fit for median fluxes versus relative height.

2.6.4. Flux detection limit and uncertainty for VOCs

The flux detection limit was calculated for each VOC and for each flight segment. The uncertainty due to instrument noise was propagated along with the uncertainty due to random sampling of the fluxes: First, a VOC white noise time series was created following Langford *et al.* (Langford et al., 2015), and then wavelet fluxes were caluclated using this white noise time series and the measured wind. If the resulting random flux was below the random covariance (i.e., covariance at ± 220-240 s lag time), the random covariance of the respective segment was used. The overall precision was propagated from the 2σ detection limit and the random uncertainty of the flux calculation which was calculated following Lenschow *et al.* (Lenschow et al., 1994; Karl et al., 2013). The accuracy was propagated from the uncertainty of the calibration, the systematic uncertainty of the flux calculation (Lenschow et al., 1994), and the uncertainties of divergence corrections. The uncertainty of the chemical vertical divergence correction was estimated to be 20% of the correction applied (a numerical calculation of this uncertainty is

difficult since the sequence of applying this correction before the physical vertical divergence correction means that any over- or undercorrection of the oxidative loss should be approximately eliminated by the physical vertical divergence correction). The uncertainty of the physical vertical divergence correction was estimated using a Monte Carlo uncertainty propagation, assuming a 17% uncertainty each for the slopes and boundary layer heights, since 17% was the average day-by-day variability in the vertical divergence slopes of benzene. The resulting average uncertainty of the vertical divergence correction was in Los Angeles ~70% for the VOCs tested, and in the San Joaquin Valley it was typically lower with a median of 17% and an average of 51%. The resulting uncertainties depend on the VOC, ranging for Los Angeles data from 19% to 67% precision, and from 73% to 100% accuracy. Resulting average total uncertainties range from 75%-86% for gas-standard calibrated VOCs, and 90-170% for the more than 400 VOCs that were calibrated using the theoretical approach. The average total uncertainty for each species is listed in Supplementary Table 1 (Los Angeles) and 2 (San Joaquin Valley). For the San Joaquin Valley data, precision ranged from 4%-220% (for gas standard calibrated VOCs 4-150%), accuracy from 7-400% (for gas standard calibrated VOCs 7-120%), and total uncertainty from 33% to 136% (for gas standard calibrated VOCs 33-87%).

As a quality filter, any data points with a random error > 30% (indicating that the corresponding legs were too short) or with a horizontal wind speed > 8 m/s were excluded. The latter criterion aimed at accommodating the range of wind speeds from the vertical divergence correction. Since only few data points have such high wind speeds, we assume that the physical vertical divergence correction would be larger for these data points, and we do not have enough data to determine a suitable correction.

2.6.5. Postprocessing, flux detection limit and uncertainty for NO_x

It is worth noting that cropland includes not only soil NO_x emissions but the off-road vehicle emissions. Erroneously attributing the NO_x from off-road vehicle emissions to soil NO_x emissions leads to a high bias. While trimethylbenzene was observed during RECAP-CA field campaign, the trimethylbenzene fluxes are interpolated to match the NO_x fluxes in time and are utilized as an indicator of off-road vehicle emissions over croplands (Tsai et al., 2014). The trimethylbeneze fluxes are categorized into two groups; the first group presents footprints covering croplands exclusively and the second group presents footprints with mixed land cover types. Shown in Fig. S2.2, the trimethylbeneze flux is much lower over croplands, a median of 0.003 mg m^{-2} h^{-1} compared to a median of 0.009 mg m^{-2} h^{-1} over mixed land cover types including highway and urban areas. Among all observations over cropland, we identify those with the trimethylbeneze flux larger than 0.02 mg m^{-2} h^{-1}, which consists of 7% of the total data points, are impacted by the off-road vehicle emissions, and then filter out them in the later analysis. We also vary the threshold of the trimethylbeneze flux between 0.005 mg m^{-2} h^{-1} and 0.04 mg m^{-2} h^{-1} and conclude that the choice of the threshold does not influence the results.

The flux detection limit does not only depend on the signal-to-noise ratio of the NO_x measurement, but also varies with wind speed and atmospheric stability. Following Langford et al., 2015, we calculate the detection limit of flux (LoD) before the moving and spatial average

are applied. For each segment, the observed NO_x is replaced with a white noise time series and is then feed into the CWT to yield the corresponding time series of ``noise'' flux. The random error affecting the flux ($\sigma_{NO_x,noise}$) is defined as the standard deviation of this noise-derived flux, and LoD is defined as $2 \times \sigma_{NO_x,noise}$(95th confidence level). Among 142 segments, Fig. 2.8 (a) shows the distribution of flux LoD among 142 segments. The LoDs range from 0.02 mg N m^{-2} h^{-1} to 0.30 mg N m^{-2} h^{-1}, and the average LoD is 0.10 mg N m^{-2} h^{-1}. To obtain a better constraint on the flux quality, we compare the LoD against the time series of flux in each segment and filter out 18 segments in which the whole time series is below the LoD.

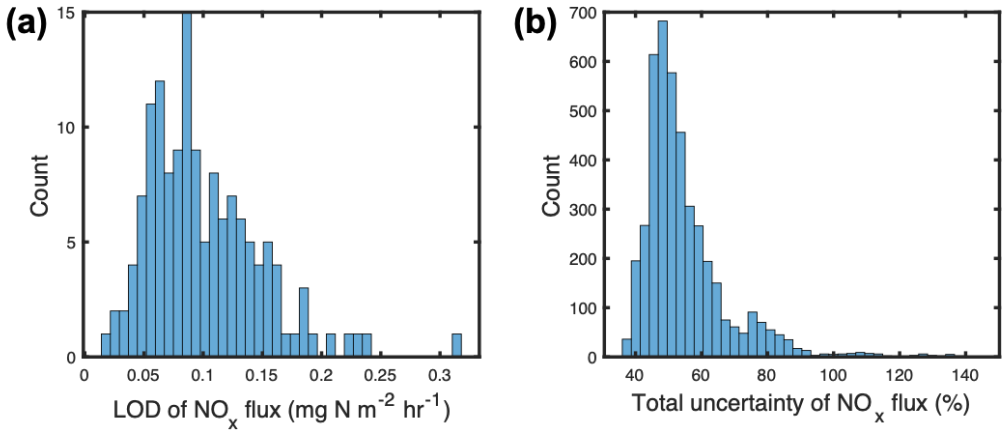

Fig. 2.8: a) The distribution of segment-based NO_x flux detection limit (LoD). b) The distribution of total uncertainty of NO_x flux.

The flux calculation using CWT introduces uncertainty from a variety of sources. We describe systematic errors and random errors following Wolfe et al., 2018. Systematic errors arise from the under-sampling of high-frequency and low-frequency ranges. The CWT algorithm fails to resolve a frequency higher than the Nyquist frequency. Due to the high temporal resolution (5 Hz), we expect a minimal loss at the high-frequency limit. The upper limit of systematic error associated with low frequency is calculated using Eqn. 2.7 (Lenschow et al., 1994).

The flux calculation using CWT introduces uncertainty from a variety of sources. We describe systematic errors and random errors following Wolfe et al., 2018, and quantify the uncertainty introduced from the constant lag correction.

The systematic errors arise from the under-sampling of high frequency and low frequency ranges. The CWT algorithm fails to resolve frequency higher than the Nyquist frequency. Due to the high temporal resolution of data points (5 Hz), we expect a minimal loss of high frequency limit. The upper limit of systematic error associated with low frequency is calculated using Eq. 2.7 (Lenschow et al., 1994).

$$SE \leq 2.2\left(\frac{z}{z_i}\right)^{0.5}\frac{z_i}{L} \qquad \text{(Eq. 2.7)}$$

z and L are the measurement heights and the length of segments, respectively. z_i are the boundary layer heights from HRRR. We estimate the low frequency error ranges from 1%-5%.

Random errors arise from the noise in the instrument (RE_{noise}) as well as the noise in turbulence sampling (RE_{turb}), which are calculated using Eqn. 2.8 and Eqn. 2.9 (Wolfe et al., 2018, Lenschow et al., 1994).

$$RE_{noise} = \frac{\sqrt{\sigma_{NO_x,noise}^2 \sigma_w^2}}{N} \qquad (Eq. 2.8)$$

$$\frac{RE_{turb}}{F} \leq 1.75 \left(\frac{z}{z_i}\right)^{0.25} \left(\frac{z_i}{L}\right)^{0.5} \qquad (Eq. 2.9)$$

z, L and z_i are the same as Eqn. 2.7, σ_w^2 is the variance of vertical wind speed. Note that RE_{noise} assumes the noise in each time step is uncorrelated, therefore, we ignore the moving average step in the uncertainty calculation and N denotes the number of points used to yield each 500m spatially averaged flux.

Utilizing a constant lag time introduces an additional source of uncertainty. We estimate the uncertainty by comparing the calculated fluxes using segment-specific and constant lag times across all segments that specific lag times are available. Shown in Fig. S2.4, the difference is less than 25% for 90 percent of the data. Therefore, we attribute an uncertainty of 25% due to the lag time correction (RE_{lag}). While we believe this error is unphysical and that a single lag time is more appropriate, we include it to be conservative in our estimate of the uncertainties.

Estimating the uncertainty caused by the correction of vertical divergence is tricky. While we conclude that the influence of vertical divergence is non-negligible, it is ignored in some previous airborne flux studies (e.g. Vaughan et al., 2016; Vaughan et al., 2021; Hannun et al., 2020; Drysdale et al., 2022). While the flux is scattered in each vertical intervals in our divergence calculation, we first bootstrap the flux observations and calculate the uncertainty of correction factor (σ_c) to 40%. As we see a significant difference in vertical correction factor on racetrack measurements versus a selected subset of flux observations, we tentatively set the uncertainty of C to 100%, in order to account for the case of no vertical divergence. Besides, we account for a 30% uncertainty in the PBL heights.

We propagate the total uncertainty from each component using Eqn. 2.11and the distribution of total uncertainty is shown in Fig. 2.8 (b). The average uncertainty is 60% and the interquartile of total uncertainty are 48% and 68%. The random error and the vertical divergence correction dominate the uncertainty and the uncertainty is consistent with previous studies (Wolfe et al., 2018; Vaughan et al., 2016).

$$\sigma_{F_z} = \sqrt{SE^2 + RE_{noise}^2 + RE_{turb}^2 + RE_{lag}^2} \quad (Eq. 2.10)$$

$$\sigma_{F_0} = \sqrt{\frac{\sigma_{F_z}^2}{(1 + C\frac{z}{z_i})^2} + \sigma_C^2 (\frac{z}{z_i})^2 (\frac{F_z}{(1 + C\frac{z}{z_i})^2})^2 + \sigma_{z_i}^2 (\frac{Cz}{{z_i}^2})^2 (\frac{F_z}{(1 + C\frac{z}{z_i})^2})^2} \qquad (Eq. 2.11)$$

2.6.6. Flux footprints and land cover

The footprint describes the contribution of surface regions to the observed airborne flux. We used an updated version of the KL04+2D footprint (Metzger et al., 2017; Vaughan et al., 2021; Metzger et al., 2013) algorithm to derive 90% footprint contours. The code is accessible on GitHub (Zhu and Pfannerstill, 2022). This KL04+2D parameterization is developed from a 1-D backward Lagrangian stochastic particle dispersion model (Kljun et al., 2004). Metzger et al. (2012) implemented a Gaussian cross-wind distribution function to resolve the dispersion, perpendicular to the main wind direction. The input parameters include height of the measurements, standard deviation of horizontal and vertical wind speed, horizontal wind direction, boundary layer height, surface roughness length and the friction velocity. The obtained footprints were typically 3-6 km long and 2-6 km wide at their widest point.

Fig. 2.9 shows the resulting footprints along the flight track in Los Angeles, and Fig. 2.10 for the San Joaquin Valley. The roughness lengths for the San Joaquin Valley were taken from HRRR, and for Los Angeles they were derived from land cover using the relationship between Los Angeles land use and roughness lengths described in Burian *et al.* (2002). 2019 Landcover data for Los Angeles were obtained from the National Land Cover Database (Multi-Resolution Land Characteristics (MRLC) Consortium, 2019). High-resolution tree cover data were obtained from Alex Guenther (UC Irvine), and population density data was acquired from the US census database (U. S. Census Bureau, 2020). CropScape 2018 (National Agricultural Statistics Service, 2018) was used as land cover data for the San Joaquin Valley. In both regions, additional emission sources were taken from the Vista-CA methane inventory (Hopkins et al., 2019). For the San Joaquin Valley, we found high monoterpene emissions over citrus processing facilities (such as juice factories and citrus packaging warehouses) and high ethanol emissions from an ethanol biofuel plant. Using Google Maps, we derived our own inventory of citrus processing and packing facilities for the study area (Pfannerstill, 2022).

The KL04+2D footprint algorithm was compared with the half-dome footprints (Weil and Horst, 1992) applied for airborne VOC fluxes by Misztal et al. (2014), and with the Kljun et al. (2015) algorithm applied for airborne fluxes by Hannun et al. (2020). Matches with known point sources and VOC flux increases observed (dairy farms, methanol) were used to check whether an algorithm's result explained the observed VOCs. From this comparison, the KL04+2D algorithm showed the best match.

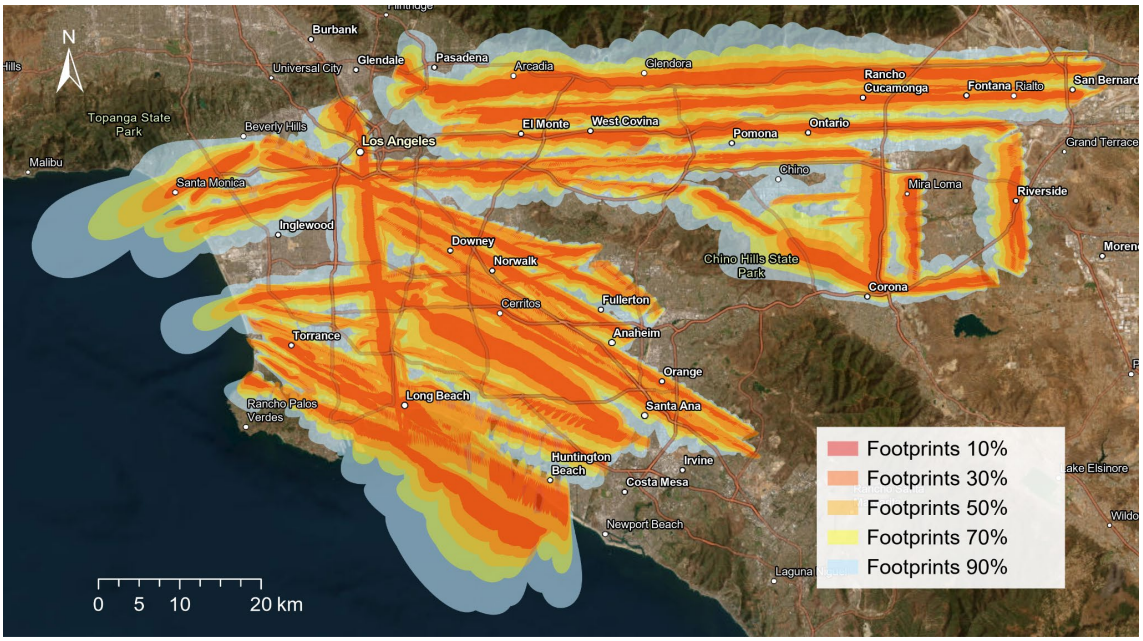

Fig. 2.9. Flux footprints along the flight tracks in Los Angeles. The different colors show the areas where the 10th, 30th, 50th, 70th, and 90th percentiles of the measured fluxes originated.

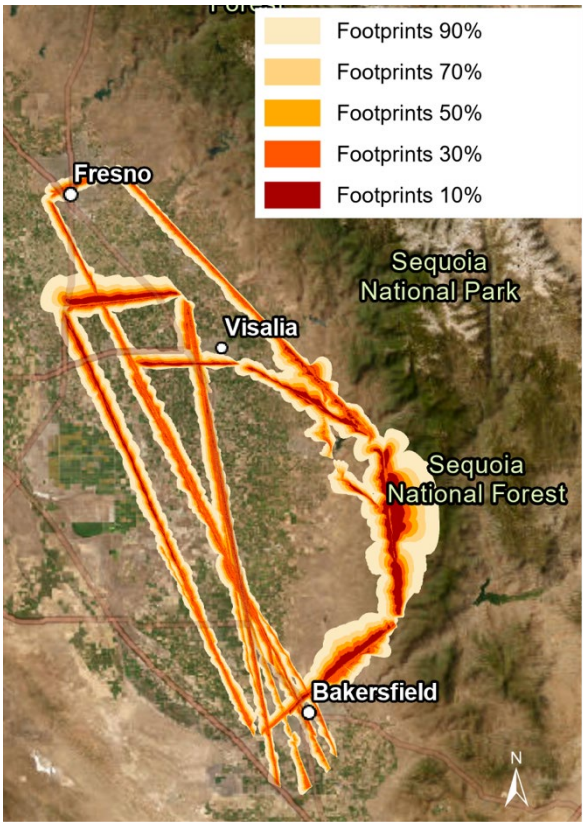

Fig. 2.10. Flux footprints along the flight tracks in the San Joaquin Valley. The different colors show the areas where the 10th, 30th, 50th, 70th, and 90th percentiles of the measured fluxes originated.

2.7. Inventory comparison method

We compare our observations to commonly used inventories. First, we use the inventory developed by the California Air Resources Board (CARB). The anthropogenic emissions of NO_x and VOCs consist of mobile sources, stationary sources and other emissions from miscellaneous processes such as residential fuel combustion and managed disposal. In the State of California inventory, the mobile sources are estimated from EMission FACtor (EMFAC) v1.0.2 and OFFROAD mobile source emission models. The stationary sources are estimated based on the reported survey of facilities within local jurisdiction and the emission factors from California Air Toxics Emission Factor (CATEF) database. An alternative anthropogenic emission inventory is the FIVE-VCP emission inventory described in the section "2.5 WRF-Chem simulations". The FIVE-VCP inventory (anthropogenic) and the BEIS inventory (biogenic) were summed up to obtain the complete inventory that is used for WRF-Chem by NOAA.

Biogenic inventories include both biogenic VOC emissions and soil NO_x emissions and they vary nonlinearly with meteorological conditions, soil conditions and agricultural activities. The Model of Emissions of Gases and Aerosols from Nature v3 (MEGAN) (Guenther et al., 2012) is the most commonly used scheme and is capable of providing biogenic VOC and soil NO_x emissions in the CARB emission inventory. It is gridded at 4 km spatial scale and has hourly time steps. Biogenic Emission Inventory System (BEIS) is the default scheme to estimate volatile organic compounds from vegetation and NO from soil developed by United States Environmental Protection Agency (EPA). We obtained the hourly BEIS v3.14 biogenic VOC and soil NO_x emission at 4 km during the study period from the Weather Research and Forecasting-Chemistry model (WRF-Chem, described in the section "2.5 WRF-Chem simulations"). For soil NO_x emissions, we also obtained a third scheme named Berkeley Dalhousie Iowa Soil NO Parameterization (BDISNP) (Hudman et al., 2012; Sha et al., 2021). The BDISNP scheme is the most recent soil NO_x scheme with modifications to better represent the soil moisture and temperature, the response to meterological parameters and fertilizer N emissions. Using the WRF-Chem setup described in (Sha et al., 2021) (2021), we also calculate the BDISNP soil NO_x emissions during the study period at the spatial resolution of 2 km and re-grid them to 4 km.

For VOC flux comparison with the inventory, each footprint (corresponding to a measured flux) was matched to the inventory grid cells that it overlapped with, weighted by the percentage of the overlap, if the overlap was > 10% of the area of the grid cell and the sum of all overlaps amounted to at least 100%. The measured and inventory data for each grid cell were matched in time. Only for the purpose of plotting maps, an average of all flyovers was calculated for each grid cell.

3. NO_x fluxes in Los Angeles

*A version of this chapter is under review at Atmospheric Chemistry and Physics under the title "**Measurement report: Airborne measurements of NO_x fluxes over Los Angeles during the RECAP-CA 2021 campaign**", with the following authors: Clara M. Nussbaumer, Bryan K. Place, Qindan Zhu, Eva Y. Pfannerstill, Paul Wooldridge, Benjamin C. Schulze, Caleb Arata, Ryan Ward, Anthony Bucholtz, John H. Seinfeld, Allen H. Goldstein, and Ronald C. Cohen, https://doi.org/10.5194/egusphere-2023-601*

3.1. Overview of observed NO_x fluxes

NO_x concentrations and NO_x fluxes over Los Angeles were separated into four different geographical regions, as shown in Figure 4.1. We analyze the effects of temperature and the planetary boundary layer height, as well as differences between weekend and weekday data. Figure 3.1 shows the temperature for the different sections, measured on the research aircraft (380 ± 63 m altitude).

Lowest temperatures were observed in the coastal section with a median value of 17 ˚C. Temperatures measured over Santa Ana and Downtown were slightly higher with median values around 19 ˚C. Further inland, observed temperatures were highest with a median value of 24 ˚C. Significant differences between the four sections were also observed regarding the boundary layer height (BLH) as presented in Figure 3.1(b). The lowest BLH was found for the coastal section with a median value of 470 m, followed by Santa Ana with 490 m and a median value of 540 m for Downtown. The BLH in the San Bernardino valley was highest with a median value of 590 m. Figure 3.1(c) shows NO_x concentrations and Figure 3.1(d) shows the corresponding fluxes over Los Angeles, separated into the geographical sections and into weekdays and weekends. Neither NO_x concentrations nor NO_x fluxes were found to be temperature dependent (see Figure S3.1 in the appendix).

Median mixing ratios were highest in Downtown with 6.5 ppbv on weekdays and 3.4 ppbv on weekends. In the San Bernardino valley, median concentrations were 5.8 ppbv and 4.1 ppbv on weekdays and weekends, respectively. The observed levels of NOx reductions from weekdays to weekends are consistent with previous results based on ground-based measurements across Los Angeles, which, for example, we have investigated in Nussbaumer and Cohen (2020). The median measured fluxes in Downtown Los Angeles were 0.27 and 0.12 mg N m^{-2} h^{-1}, respectively for weekdays and weekends. In the San Bernardino valley the median fluxes were 0.31 mg N m^{-2} h^{-1} on weekdays and 0.15 mg N m^{-2} h^{-1} on weekends. In all of these locations weekend emissions decreased by 50 - 60% from weekday values.

Mixing ratios were lower near the coast. Median NOx mixing ratios were similar for the coastal section and Santa Ana with 2.8–3.0 ppbv on weekdays. The weekend values were smaller with 2.0–2.3 ppbv. However, no significant differences could be observed between weekday and weekend fluxes in these regions. Much of the coastal region is over water and the median values of fluxes are near zero on both weekdays and weekends and approximately 0.1 mg N m^{-2} h^{-1} on both weekdays and weekends in the Santa Ana region.

While NO_x concentrations were observed to be highest over Downtown Los Angeles, NO_x fluxes were found to be highest in the San Bernardino valley. This effect could be partly caused by the observed differences in the boundary layer height. While highest emissions occurred in the San Bernardino valley, the increased planetary BLH (as shown in Figure 3.1(b)) should lead to a ~ 15% lower mixing ratio. The differences in concentrations are likely also due to chemistry and advection.

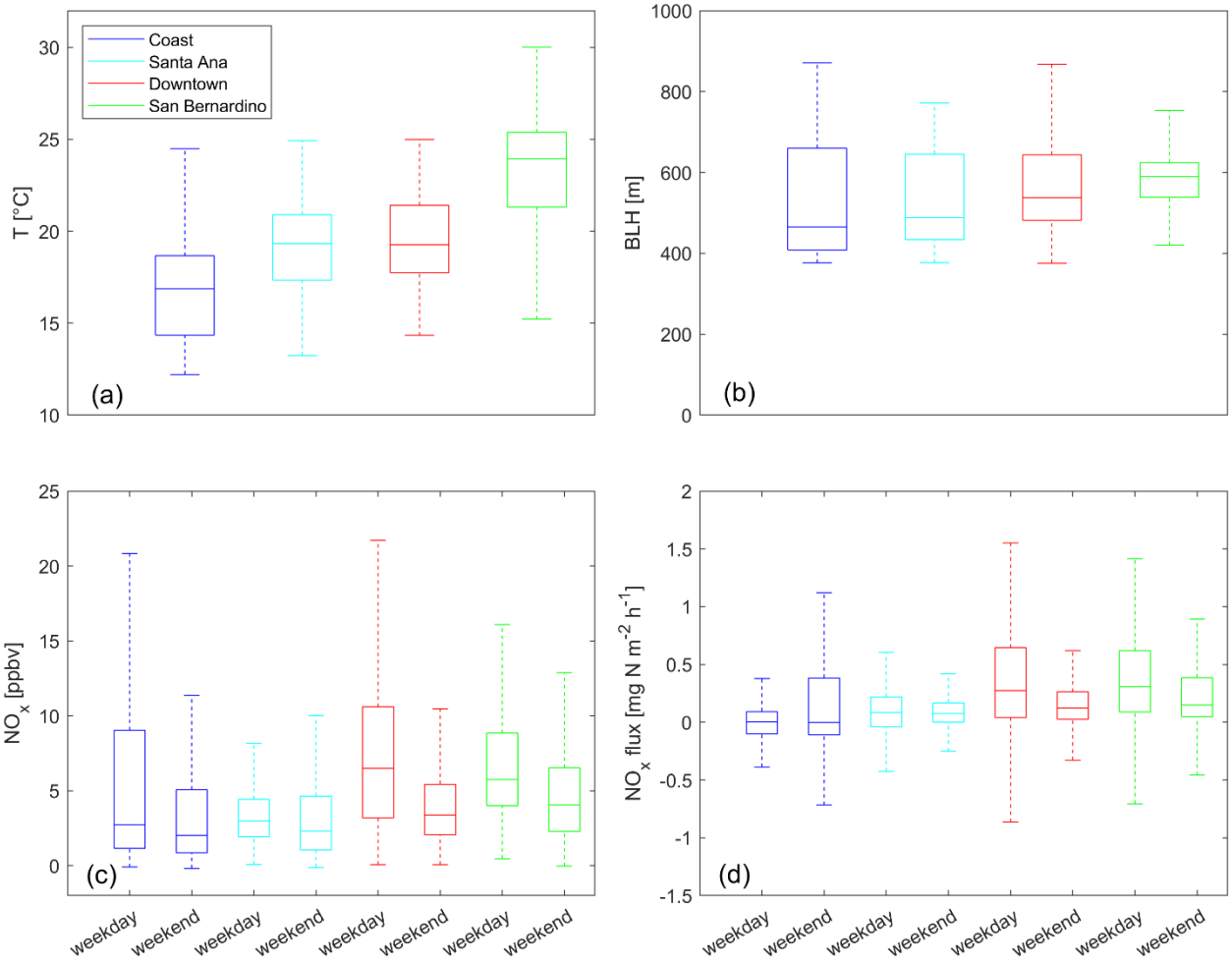

Figure 3.1. Boxplots for (a) the temperature, (b) the boundary layer height, (c) NO*x* concentrations and (d) NO*x* fluxes subdivided into four geographical sections according to Figure 1b and into weekday and weekend data. Please note that outliers are not shown.

Figure 3.2 presents NO_x fluxes along the flight tracks.

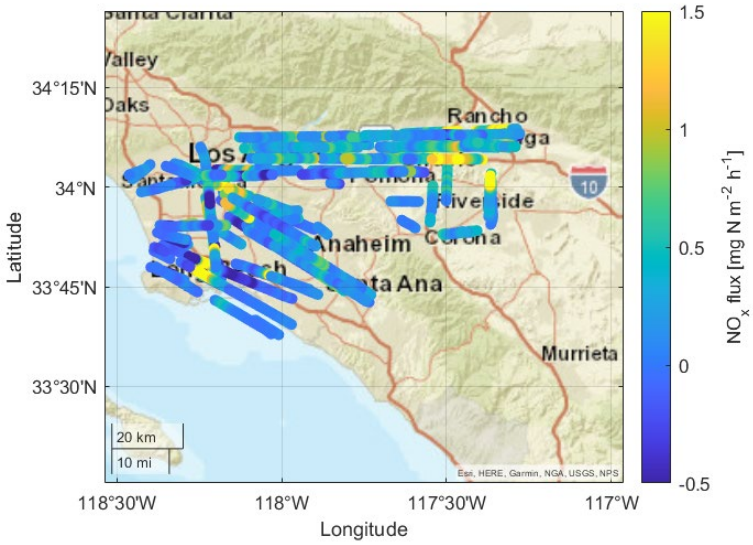

Figure 3.2. NO_x fluxes along the flight tracks across Los Angeles.

Using the highway information by the California Department of Transportation (2015), we separated NOx fluxes into emissions from highway and non-highway grid cells. A 500m x 500m grid cell is considered a highway emission when it is crossed by a highway. The resulting boxplots for highway and non-highway emissions on weekdays and weekends can be seen in Figure 3.3. For weekdays, NOx fluxes from highway grid cells were on average 0.27±0.48 mg N m^{-2} h^{-1}, approximately 25% higher than NOx fluxes from non-highway grid cells with an average of 0.22±0.42 mg N m^{-2} h^{-1}. Weekend NOx fluxes from highways were on average 0.19±0.31 mg N m^{-2} h^{-1}. Weekend NOx emissions from non-highway areas were 0.15±0.32 mg N m^{-2} h^{-1}. Note the large 1σ standard deviations, indicating the large variability of the fluxes. The median values were lower compared to the mean values (0.18 and 0.10 mg N m^{-2} h^{-1} for highway and non-highway, respectively, on weekdays and 0.09 and 0.13 mg N m^{-2} h^{-1} for highway and non-highway, respectively, on weekends), but showed a similar qualitative result with higher emissions from highway compared to non-highway areas.

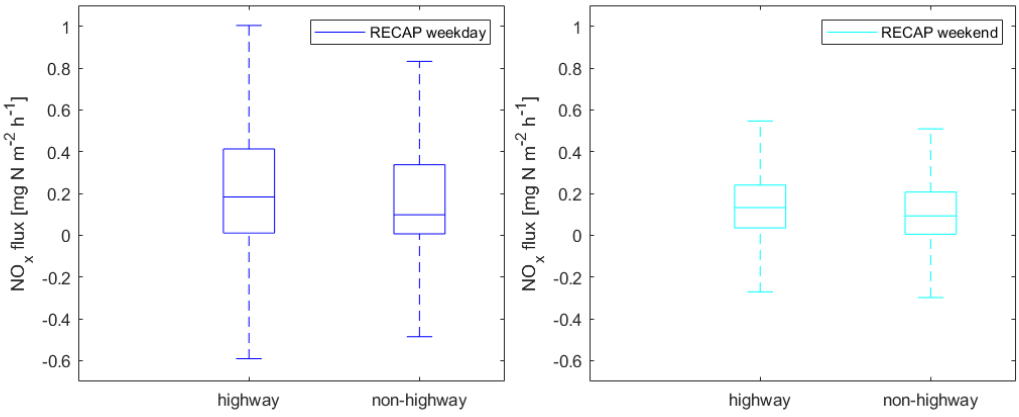

Figure 3.3. Boxplots for (a) weekday NO_x fluxes and (b) weekend NO_x fluxes subdivided into fluxes originating from highways and from non-highway areas.

3.2. Comparison to the CARB emission inventory

The comparison between the emission inventory and the calculated NO_x fluxes is shown in Figure 3.4. We present the weekday data here and show the weekend data in Figure 3.5. Panel (a) shows the RECAP-CA NO_x fluxes at 4 km × 4 km, panel (b) presents the CARB emission inventory and in panel (c) we show the difference between the RECAP-CA and the CARB data. Red colors indicate higher fluxes from the emission inventory and blue colors show higher fluxes from the RECAP-CA airborne measurements.

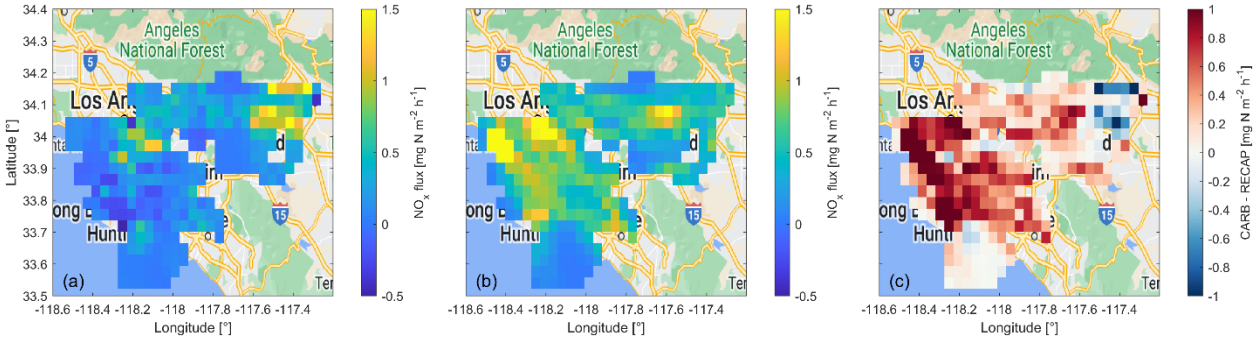

Figure 3.4. Weekday averages of NO*x* emissions without vertical divergence correction across Los Angeles with a 4 km × 4 km spatial resolution (a) during the RECAP-CA campaign, (b) from the CARB emission inventory and (c) the difference between RECAP-CA and CARB NO_x fluxes.

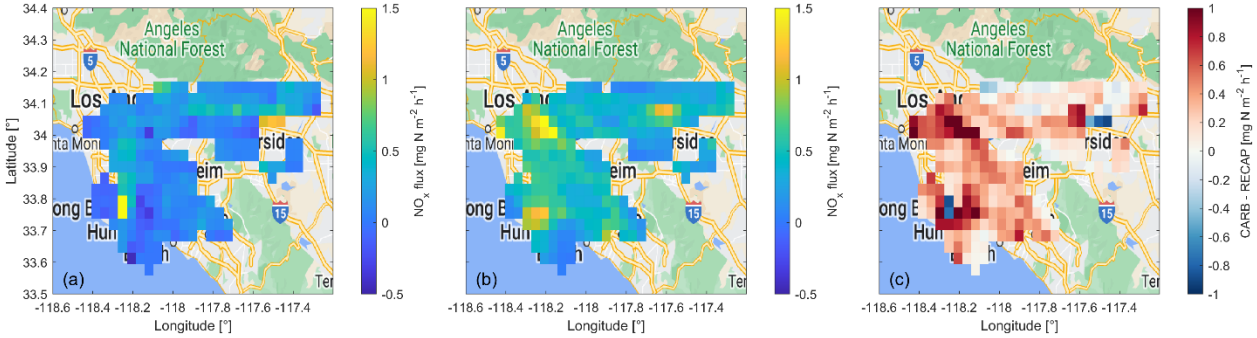

Figure 3.5. Weekend averages of NO*x* emissions without vertical divergence correction across Los Angeles with a 4 km × 4 km spatial resolution (a) during the RECAP-CA campaign, (b) from the CARB emission inventory and (c) the difference between RECAP-CA and CARB NO_x fluxes.

As expected from the results presented in Section 3.1, the highest NO_x fluxes were observed in the San Bernardino valley which is characterized by several heavily trafficked highways and warehouses that cause dense diesel truck traffic (Uranga, 2023). Elevated NO_x emission also occurred in the region around Downtown Los Angeles. The average weekend RECAP-CA NO_x fluxes (Fig. 3.4a) showed a similar emission distribution over Los Angeles compared to the weekday data, but with smaller values. This is in line with the findings presented in Section 3.1.

Figure 3.4(b) shows average weekday NO_x fluxes as predicted by the CARB emission inventory. The large NO_x flux in proximity to the coast (~ 34.0 ° N, 118.4 ° W) with a value close to 3.5 mg N m^{-2} h^{-1} was associated with aircraft emissions, as well as ground handling equipment and vehicle traffic, from and around Los Angeles International Airport (LAX). Additionally,

emissions from aircraft not only at the surface but also at elevated altitudes could contribute to the observed value. We show the NO_x fluxes as predicted by CARB separated into (a) on-road emissions, (b) aircraft emissions, (c) area sources and (d) emissions from ocean going vessels in Figure S3.2 of the Appendix. Aircraft NO_x emissions can also be observed in the San Bernardino valley (~34.1˚N, 117.6 ˚ W) from Ontario International Airport which is illustrated in Figure S3.2b. High NO_x fluxes in this area were also associated with on-road emissions, shown in Figure S3.2a. The Downtown Los Angeles area (~ 34.0 ˚ N, 118.2 ˚ W) also showed high fluxes which originated from on-road and area sources. Elevated NO_x fluxes around Long Beach (~ 33.8 ˚ N, 118.2 ˚ W) were associated with shipping and port emissions. Average weekend NO_x fluxes predicted by the emission inventory are presented in Figure 3.4b which showed a similar qualitative distribution compared to the weekday data but were generally lower.
Figure 3.3c presents the difference between the NO_x fluxes from the RECAP-CA campaign and the CARB emission inventory. Blue colors represent higher values for the RECAP-CA campaign compared to the emission inventory. Red colors indicate higher fluxes from the emission inventory. In most places, the NO_x fluxes predicted by the emission inventory were higher compared to the values from the RECAP-CA campaign. This difference was particularly pronounced in the area around Downtown Los Angeles and along the coast. Due to lively air traffic, the research aircraft could not approach the airport closely and the footprints only covered a minor area of the airport which we show in Figure 3.6.

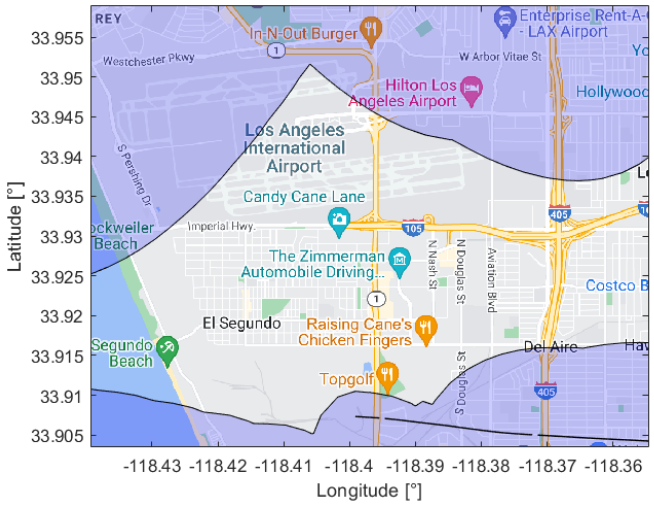

Figure 3.6. The majority of Los Angeles international airport (LAX) was not covered by the footprints during the RECAP-CA campaign.

As a result, the differences in the vicinity of the airport should not be interpreted as meaningful. NO_x fluxes around Downtown Los Angeles are dominated by area sources and on-road emissions.

We observed higher NO_x fluxes during the RECAP-CA campaign compared to the emission inventory in the San Bernardino valley. A possible explanation could be the accumulation of distribution and fulfillment centers which are accessible to delivery trucks via multiple highways in this area (Uranga, 2023; Schorung and Lecourt, 2021). Over the past two decades net sales via

distribution centers have grown exponentially (Statista, 2022a). In the U.S., the number of delivered orders by the online retailer amazon has increased by nearly a factor of 6 between 2018 and 2020 (Statista, 2022b). NO_x emissions in proximity to warehouses have likely increased to a similar extent in recent years which might not yet be incorporated in the CARB 2020 emission inventory. Additional research is needed to examine more details of these differences and connect them to specific processes in the inventory and observations.

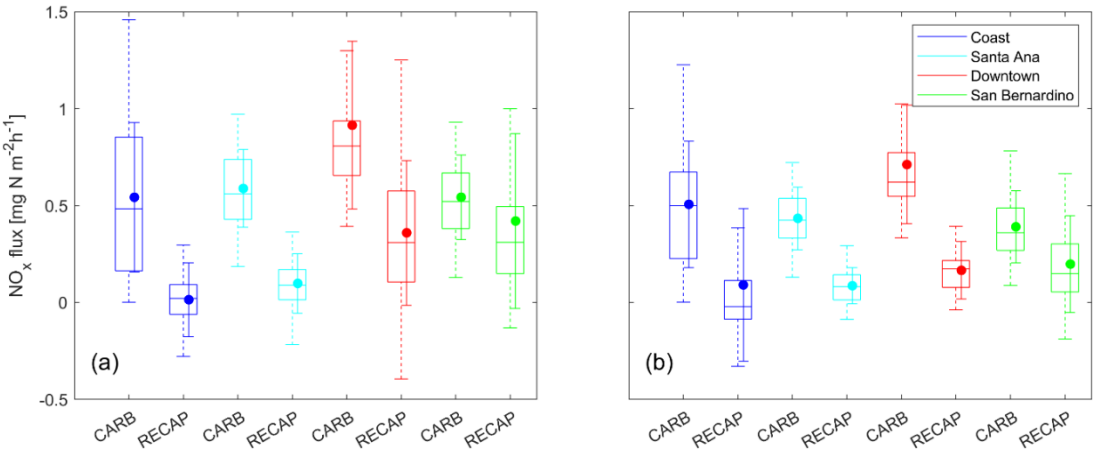

Figure 3.7. Boxplots for (a) weekday NO_x fluxes and (b) weekend NO_x fluxes subdivided into four geographical sections and into RECAP-CA campaign and CARB emission inventory data. Filled circles and solid line error bars represent means and 1σ variabilities, respectively.

Figure 3.7 shows weekday (3.7a) and weekend (3.7b) NO_x fluxes separated into the four geographical segments and into RECAP-CA campaign and CARB emission inventory data, as boxplots. The vertical lines represent the medians and the boxes show the 25th and 75th percentiles. Please note that the values for the RECAP-CA NO_x fluxes presented here can slightly deviate (quantitatively) from the values shown in Figure 3.1, as we used the 4 km x 4 km spatial grid in Figure 3.7 allowing for a comparison with the CARB emission inventory, while we used the data along the flight tracks in Figure 3.1. For all areas, the median NO_x flux from the CARB emission inventory was higher compared to the NO_x flux from the RECAP-CA campaign. The difference was smallest for the San Bernardino valley with a median weekday flux of 0.31 and 0.52 mg N m^{-2} h^{-1} for RECAP and CARB, respectively. The median weekend flux was 0.15 and 0.36 mg N m^{-2} h^{-1}, respectively. This is likely a counteracting effect from higher RECAP fluxes in the more Eastern part and higher CARB fluxes in the more Western part of the geographic segment. The differences were more significant for the remaining three areas. The RECAP median flux for the coast was close to zero, while it was close to 0.5 mg N m^{-2} h^{-1} for the emission inventory. For Santa Ana, the RECAP median fluxes were 0.09 and 0.08 mg N m^{-2} h^{-1} for weekdays and weekends, respectively, while the CARB fluxes were 0.42 and 0.56 mg N m^{-2} h^{-1}, respectively. For Downtown Los Angeles we observed a difference between RECAP and CARB fluxes of 0.50 mg N m^{-2} h^{-1} for weekdays and 0.45 mg N m^{-2} h^{-1} for weekends.
In Figure 3.8 and 3.9 we show the NO_x fluxes corrected for vertical divergence as presented in Section 2.6.3 in comparison to the CARB emission inventory for weekdays and weekends,

respectively. The emission features shown in Figure 3.4 for the RECAP-CA campaign are more pronounced after applying the factor for vertical correction. High emissions are observed over Downtown Los Angeles and the inland highways in San Bernardino, while the coastal region and Santa Ana show lower, and even negative fluxes. As a result, CARB emissions remain dominant over RECAP-CA fluxes in the coastal region, but are lower around Downtown Los Angeles and in San Bernardino. The median values of the corrected fluxes are around a factor of 3 higher compared to the non-corrected fluxes. The interquartile range increases by even more as a result of the large scatter induced by the correction. This sensitivity analysis emphasizes how important the characterization of the vertical flux divergence is and should be subject to future studies.

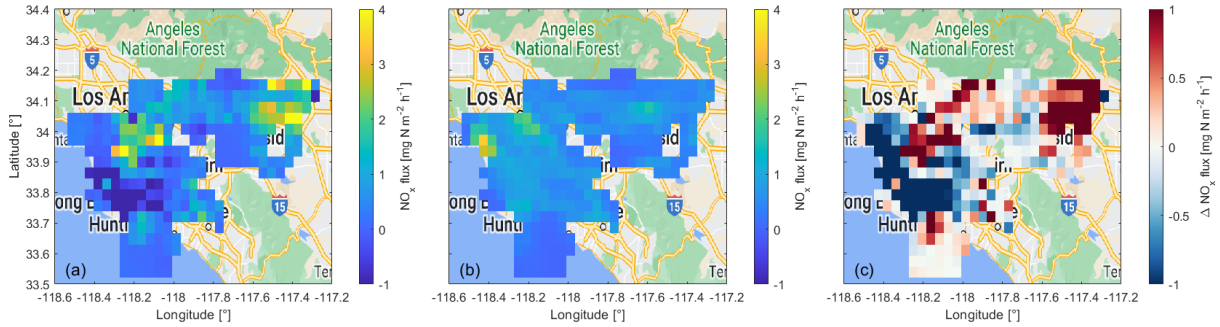

Figure 3.8. Weekday averages of vertical divergence corrected NO_x emissions across Los Angeles with a 4 km × 4 km spatial resolution (a) during the RECAP-CA campaign, (b) from the CARB emission inventory and (c) the difference between RECAP-CA and CARB NO_x fluxes.

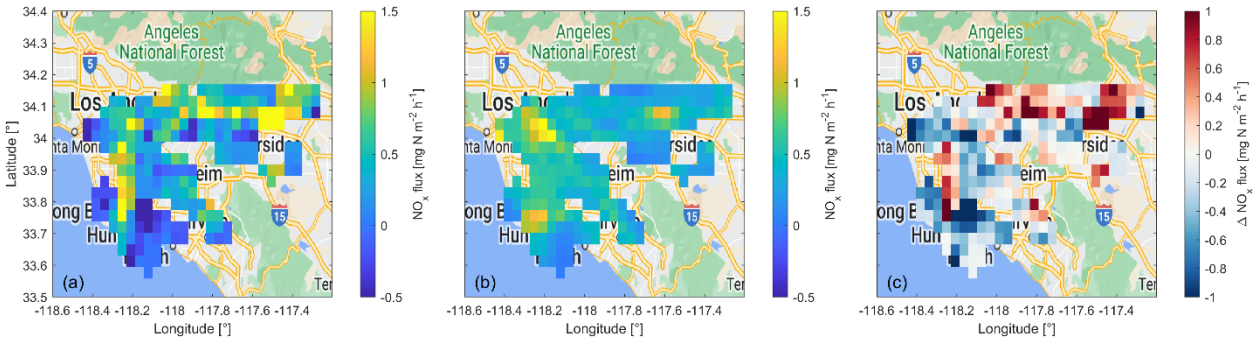

Figure 3.9. Weekend averages of vertical divergence corrected NO_x emissions across Los Angeles with a 4 km × 4 km spatial resolution (a) during the RECAP-CA campaign, (b) from the CARB emission inventory and (c) the difference between RECAP-CA and CARB NO_x fluxes.

4. VOC fluxes in Los Angeles

*A version of this chapter is under review in Environmental Science & Technology under the title "**Mismatches between inventories and spatially resolved airborne flux measurements of volatile organic compounds in Los Angeles**", with the following authors: Eva Y. Pfannerstill, Caleb Arata, Qindan Zhu, Benjamin C. Schulze, Roy Woods, Colin Harkins, Rebecca H. Schwantes, John H. Seinfeld, Anthony Bucholtz, Ronald C. Cohen, and Allen H. Goldstein*

4.1. Overview of observed VOC fluxes

The spatial distribution of VOC fluxes measured along flight tracks is shown in Fig. 4.1 for example species that were highly relevant for mass flux, OH reactivity and/or SOA formation potential (see Fig. 4.3). Spatial distributions of the fluxes differed strongly between VOCs, reflecting source distribution. E.g., isoprene emissions were highest on the outskirts of the city, on the less- or non-urbanized hillslopes. This distribution and the observed emission range agrees with a high-resolution BVOC emission inventory for the region (Scott and Benjamin, 2003). Monoterpene and sesquiterpene fluxes were higher in downtown Los Angeles than in the San Bernardino Valley, potentially reflecting fragrance-related sources and the distribution of terpene-emitting, non-native trees like e.g. eucalyptus (McPherson et al., 2013). Ethanol and acetone had a few strong point sources and were, as has been shown previously for OVOCs (Niinemets et al., 2014), deposited in some areas (negative fluxes). Benzene was especially high over highways, while the distribution of toluene was more similar to that of PCBTF (para-chlorobenzotrifluoride), potentially reflecting their similar sources in solvent use (Stockwell et al., 2020). D5 (decamethylcyclopentasiloxane), a personal care product tracer (Coggon et al., 2018), showed a distribution most similar to that of ethanol, reflecting that they both vary with population density.

Measured emissions were in the ranges of direct flux observations performed previously in other cities (Fig. 4.2). Note that we compared only with stationary tower urban flux studies. We refrained from comparing with previous urban airborne eddy covariance observations, since currently available published studies did not correct for vertical divergence.

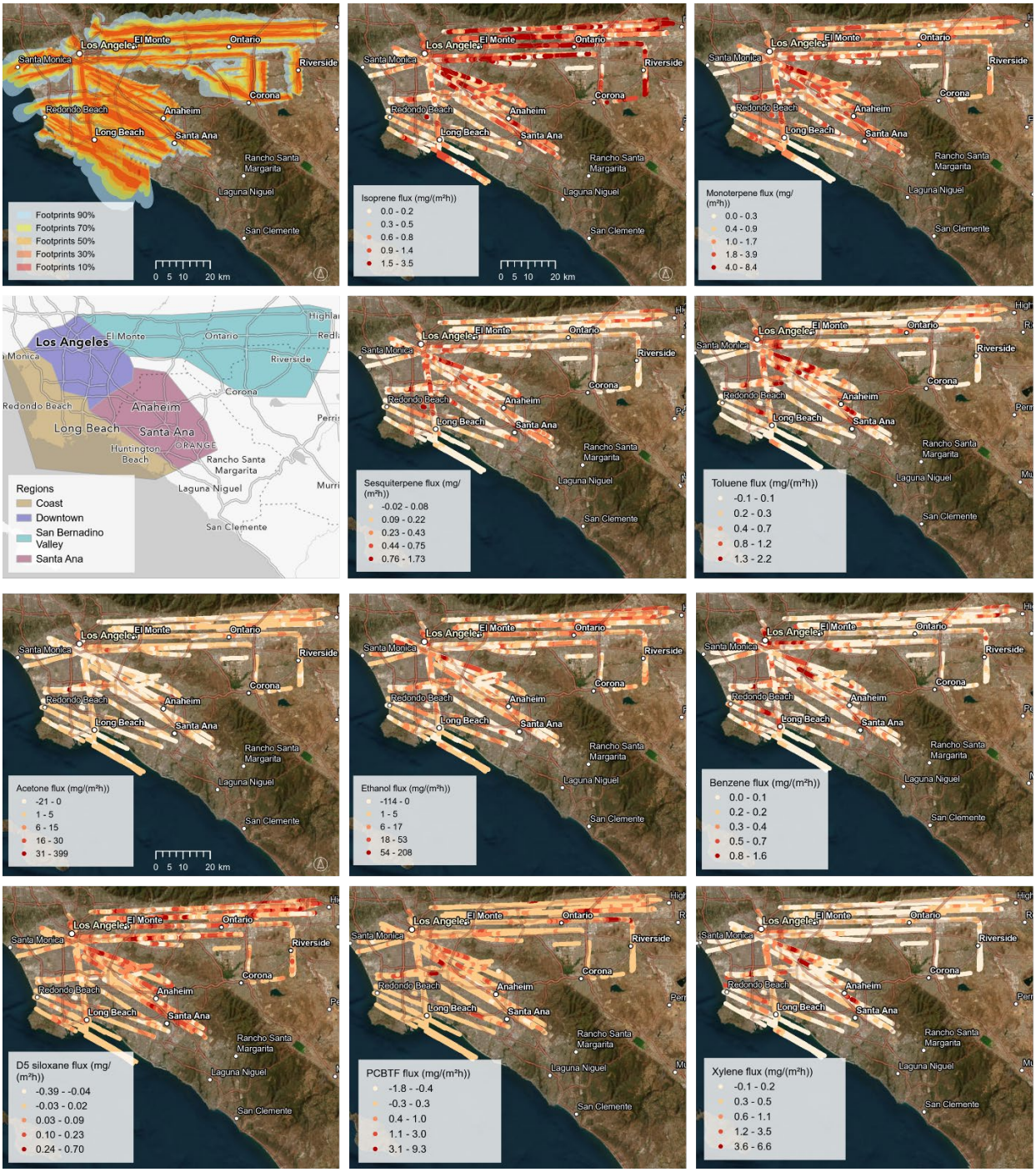

Figure 4.1. Maps showing flux footprints, regions defined for the analysis, and fluxes for ten example VOCs along the flight track. Data from all nine flights is shown here. Flux values are 2 km running averages (to remove influence of small-scale turbulence on the flux values) downsampled to 100 m (for easier data handling and display). Satellite maps from ESRI ArcGis Pro.

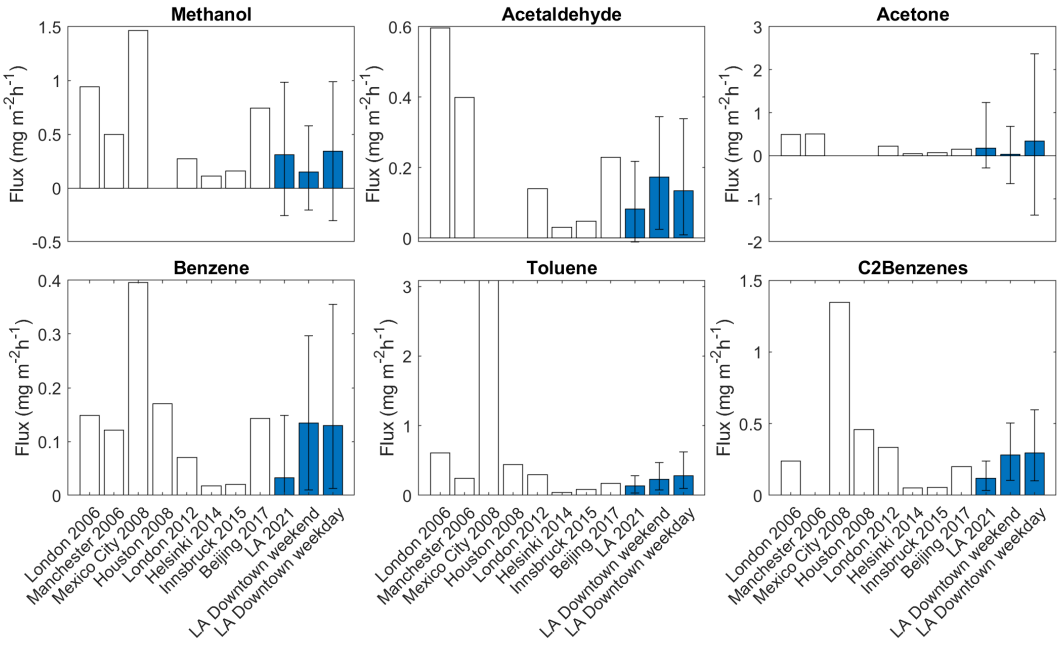

Figure 4.2. Comparison of median flux observations from this airborne study (blue) with previous stationary tower urban flux observations. Error bars show the 25th to 75th percentiles. C2-benzenes include xylenes and ethylbenzene. References: Langford et al., 2009; Langford et al., 2010; Velasco et al., 2009; Park et al., 2010; Valach et al., 2015; Rantala et al., 2016; Karl et al., 2018; Acton et al., 2020. Note that the Houston study measured fluxes using relaxed eddy accumulation, not eddy covariance.

In the domain, the VOC with the highest observed individual net mass flux was ethanol with 3.8 ± 12.9 mg m^{-2} h^{-1} (~29% of the total mass flux) (Fig. 4.3). The next highest emissions by mass were the sum of acetone and propanal (C_3H_6O, 0.8 ± 7.2 mg m^{-2} h^{-1}), monoterpenes ($C_{10}H_{16}$, 0.8 ± 0.8 mg m^{-2} h^{-1}), and isoprene (0.7 ± 0.7 mg m^{-2} h^{-1}). The large standard deviations reflect the high spatial variability in emissions, where some areas have emissions close to zero, while other areas or point sources emit large amounts. In terms of contribution to OH reactivity, isoprene was the largest single contributor, followed by monoterpenes and ethanol. The SOA formation potential of the emissions is highest for VOCs with low-volatility oxidation products, which is why monoterpenes and sesquiterpenes were the most important constituents by a wide margin, followed by toluene. Notably, a coating VCP, PCBTF (Stockwell et al., 2020), which is not traditionally among surveyed VOCs, appeared in the top 10 both for mass flux and SOA formation potential.

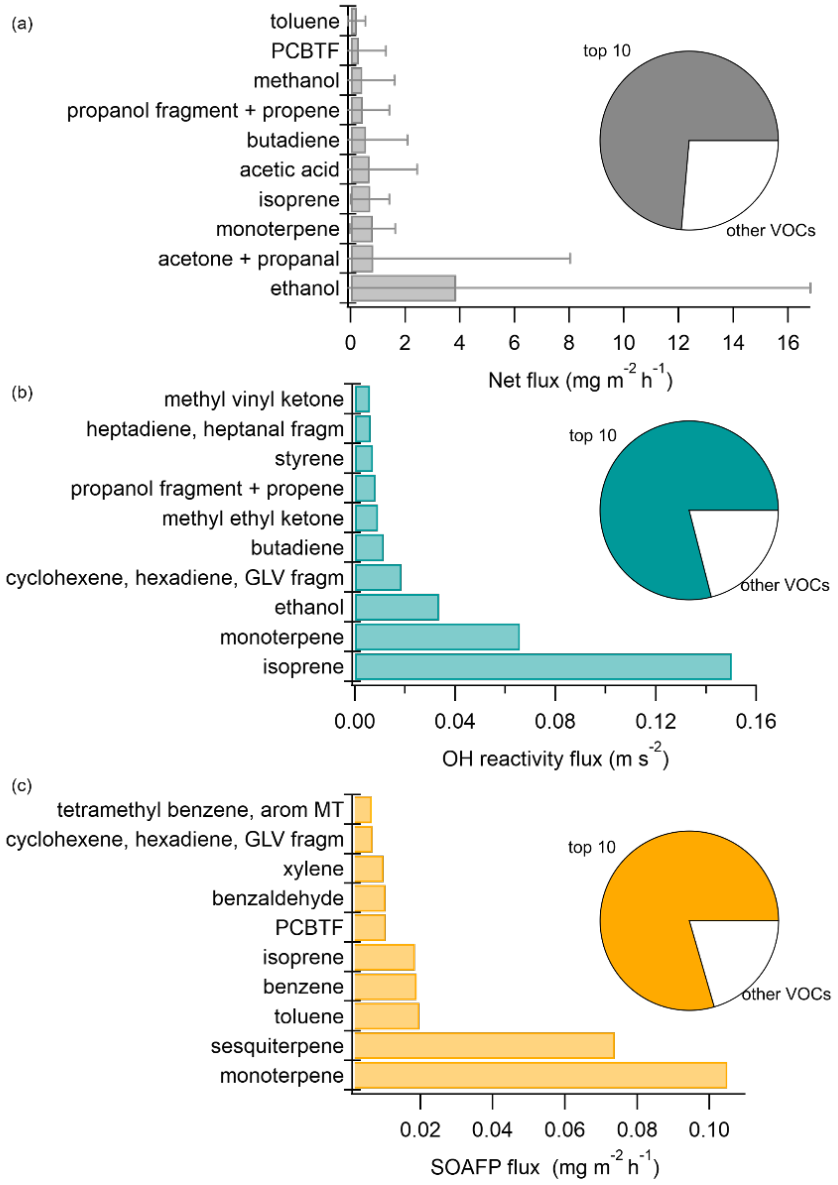

Figure 4.3. The top ten measured ions (labeled as attributed VOCs) contributing to the VOC mass flux, OH reactivity flux, and SOA formation potential of flux. "arom MT": aromatic monoterpenes, "fragm": fragment, "GLV": green leaf volatile, "PCBTF": p-chlorobenzotrifluoride. Values shown are averages of the whole campaign. For the net fluxes, standard deviations are shown as error bars. The pie charts show how much of the summed respective flux is explained by the top 10 VOCs.

In downtown Los Angeles, we observed an average toluene/benzene ratio of 1.7 (weekend) or 2.2 (weekday). The downtown toluene/benzene emission ratios here were thus very similar to those reported from tunnel measurements in California with 1.99 (weekend) and 2.24 (weekday) (Warneke et al., 2013) and to direct gasoline exhaust measurements with ~1.5 (Drozd et al., 2016). This indicates that vehicle emissions dominate toluene and benzene emissions in downtown Los Angeles. When the whole study area (not just downtown) is included in the average, our flux measurements result in a much larger toluene/benzene ratio of 4.1. This is close to the

toluene/benzene ratio of 4.2 found in emissions from solvent use (Wang et al., 2022c), and higher than the emission ratios derived from VOC concentration measurements in Los Angeles in 2010 (Gouw et al., 2017), where the toluene/benzene ratio was 2.9. Potentially, this reflects a growing relative influence of non-traffic (solvent) sources for toluene, while the likely almost exclusively traffic-related benzene emissions (Drozd et al., 2016) have decreased since 2010. This is supported by the differing spatial distributions of toluene and benzene emissions (Fig. 4.1), and by inventory timelines which predict that solvent VOC emissions (part of the VCPs) have not decreased as strongly as traffic emissions over the last few decades (Kim et al., 2022).

4.2. Emission inventory comparison

Figure 4.4a displays a comparison of the sum of measured molar VOC emissions with those included in the inventory from medians of the whole campaign. The most striking difference here is that observed alcohol emissions (dominated by ethanol) were much higher than both the inventories predicted – more than a factor of 2 compared to the BEIS+FIVE-VCP inventory, and more than a factor of 5 compared to the CARB inventory. The sum of observed acid emissions was also substantially (more than a factor of 5) underestimated by the inventories. The summed carbonyl emissions were higher than observations in the BEIS+FIVE-VCP, and lower than observations in the CARB inventory. Overall, the total of observed oxygenated VOC emissions was substantially underestimated by the inventories. A similar observation was made in the comparison of VOC flux measurements with a regional inventory in London, where the biggest discrepancies were in oxygenated VOCs (Langford et al., 2010).

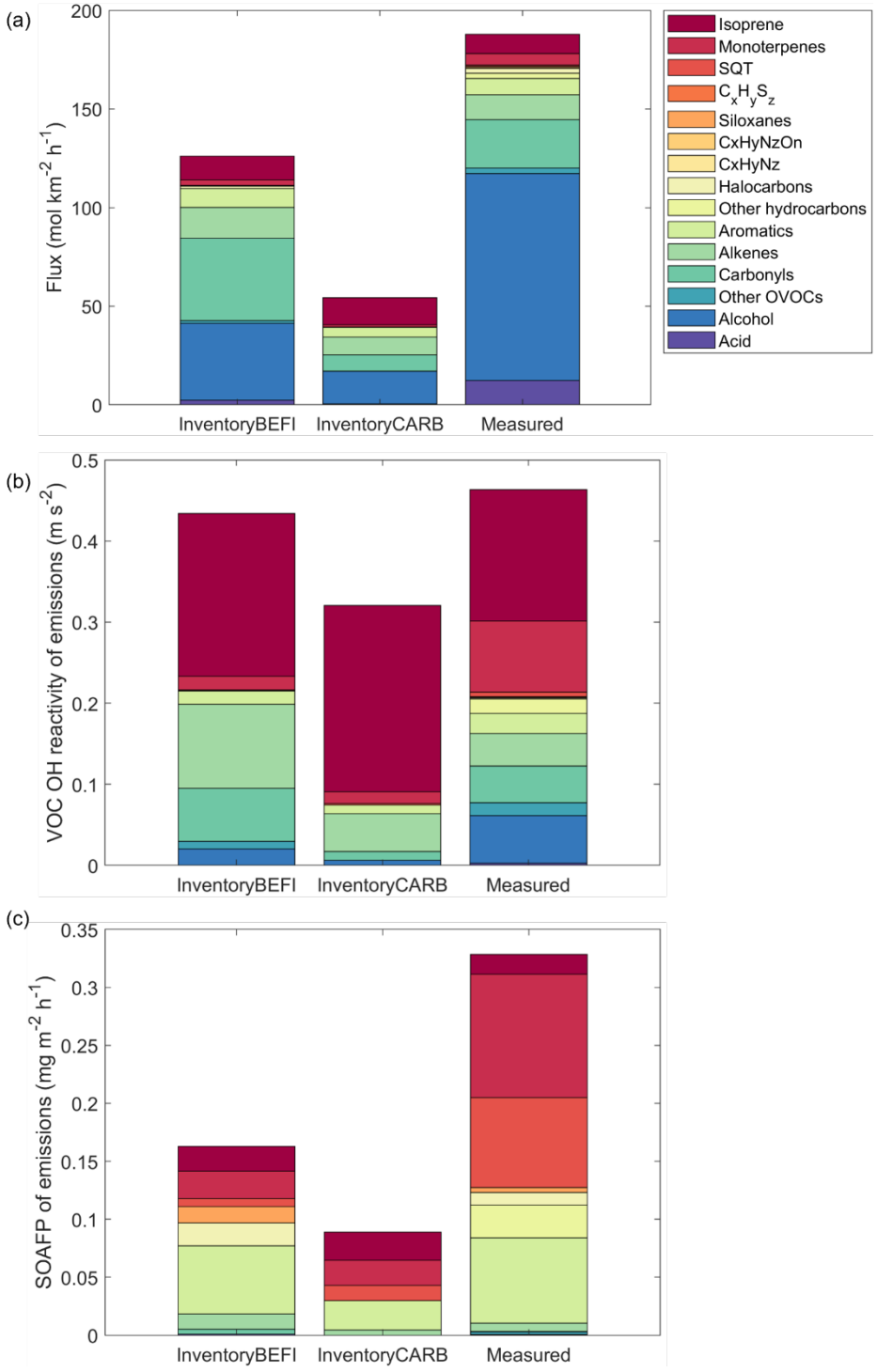

Figure 4.4. Comparison of a) molar flux, b) VOC OH reactivity, and c) SOA formation potential of emissions between BEIS+FIVE-VCP (BEFI) inventory, CARB inventory, and measurements by chemical family. Alkanes were not included in the comparison since they cannot be measured by PTR-MS. In both inventories, alkanes contributed ≈ 20 mol m^{-2} h^{-1} in emissions, 0.02 ms^{-2} in OH reactivity of emissions, and a negligible amount in SOA formation potential of emissions. Apart from alkanes, this comparison includes all VOCs available in the observations or in the inventories.

In Fig. 4.4b, the same data are shown in terms of OH reactivity, based on OH reaction rate constants listed in Supplementary Table 1. The OH reactivity emission sums are comparable between inventories and measurements. However, the inventories included more isoprene (but still within the measurement uncertainty) and substantially less monoterpene and alcohol emissions than the observations, leading to a similar sum based on a different composition than observed. Monoterpenes contributed 19% of the OH reactivity sum in the observations, much higher than in the inventories where they contributed only 4% (BEIS+FIVE-VCP) or 5% (CARB). The alcohol contribution was 13% in the observations, but only 5% (BEIS+FIVE-VCP) or 2% (CARB) in the inventories. The isoprene contribution to OH reactivity fluxes was 35% in the observations, but 46% (BEIS+FIVE-VCP) or 72% (CARB) in the inventories. We note that, since the PTR-MS method is not able to measure all VOCs (notably it is unable to ionize alkanes), there may be a significant missing OH reactivity source. Based on direct total OH reactivity observations performed in Los Angeles in 2010 (Hansen et al., 2021), and after comparison with species observed then, we estimate this missing OH reactivity source to be at maximum ~30%.

The SOA formation potentials of the emitted VOCs were estimated using the Statistical Oxidation Model (SOM), which is based on SOA yields from chamber studies and approximately accounts for multigenerational aging (Cappa and Wilson, 2012), combined with a one-dimensional volatility basis set for OVOCs (Robinson et al., 2007). The overall SOA formation potential of the emitted VOCs (Fig. 4.4c) was underestimated substantially (by a factor of 2-3) by both inventories. This discrepancy was mainly due to underestimated mono- and sesquiterpene emissions, which were on average at least a factor of 5 higher than in the inventories. This caused the fractional contribution of monoterpenes to SOA formation potential to be 33% in the observations, but just 15% (BEIS+FIVE-VCP) or 24% (CARB) in the inventories. On the other hand, the contribution of aromatic emissions was well represented by the FIVE-VCP inventory. The CARB inventory underestimated the aromatic contribution because, despite a good match for simple aromatics (Fig. 4.5), it underestimated heavier aromatic VOCs (see, e.g., naphthalene in Fig. 4.5). The summed SOA formation potential is likely underestimated by our observations, because long-chain alkanes, which were not detected in our measurements, are relevant SOA precursors (Gu et al., 2021). We estimate that including long-chain alkanes would increase the total SOA formation potential of emissions by maximum ~30% (uncorrected for trends since 2010).

A comparison of the median fluxes of individual VOC species (Fig. 4.5, Supplementary Table 1) provides a more detailed view of the similarities and differences between the two inventories and the measurements. Since the uncertainties of the observed VOC fluxes introduced through the necessary vertical divergence correction are on the order of a factor of 2, the agreement between measurements and inventories was considered reasonable within that range (Fig. 4.5). Note that this uncertainty is likely systematic, and a single scale factor for all measurements, so a better knowledge of it would not reduce the spread of agreement. The distribution of points shows that the CARB inventory has a general tendency towards underestimation for a subset of compounds (Fig. 4.5b), while the BEIS+FIVE-VCP inventory scatters more around the 1:1 line (Fig. 4.5a) both in the positive and the negative direction.

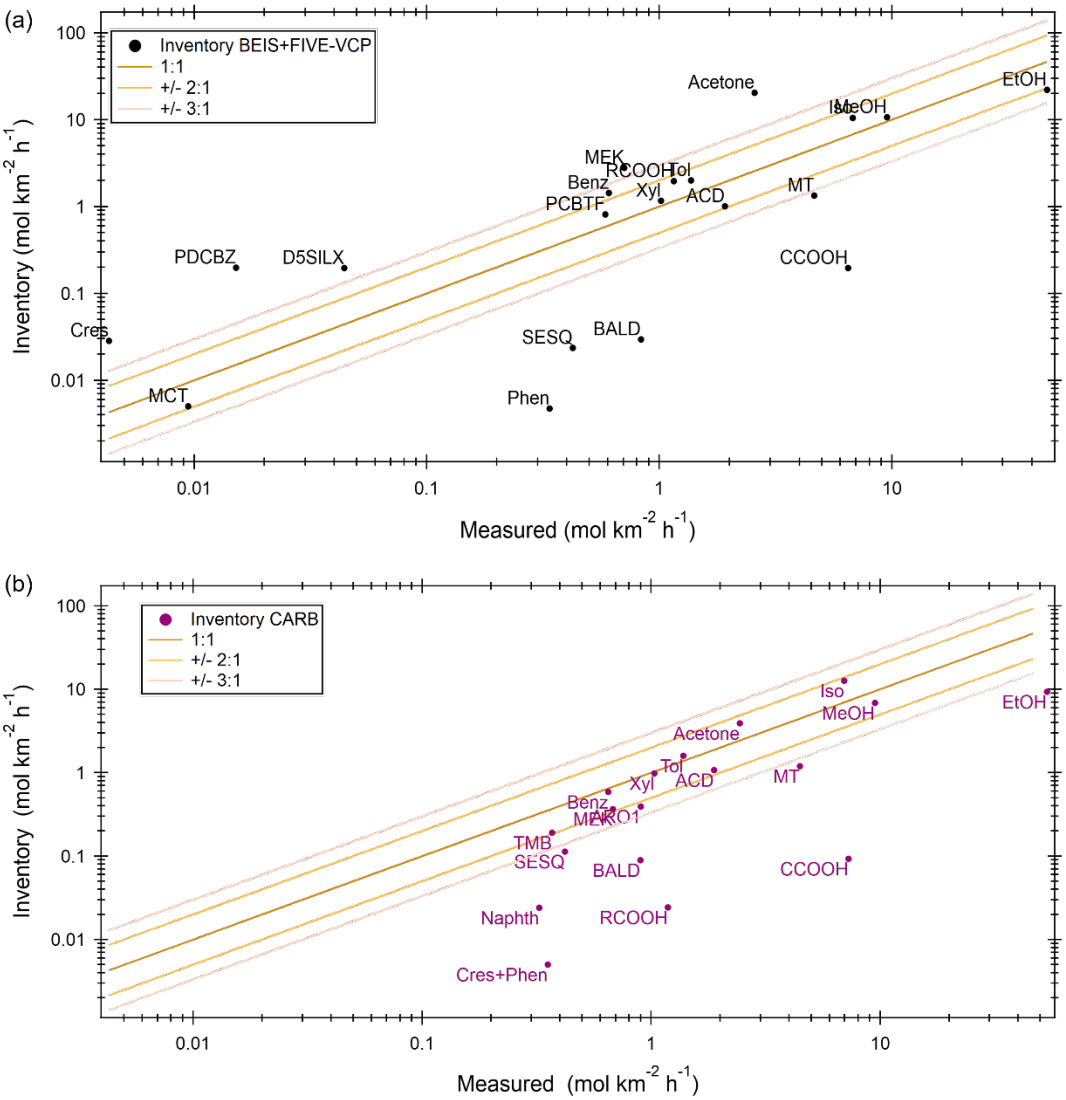

Figure 4.5. Comparison of median values between measured and inventory emissions of individual VOCs for (a) BEIS+FIVE-VCP and (b) CARB. Cres: Cresol, Phen: Phenol, MCT: Methanethiol, PDCBZ: Paradichlorobenzene, D5SILX: D5 siloxane, SESQ: sesquiterpenes, TMB: trimethylbenzene, BALD: benzaldehyde, Naphth: naphathalene, MEK: methyl ethyl ketone, Benz: benzene, PCBTF: para-chlorobenzotrifluoride, Xyl: Xylene, Tol: Toluene, MT: monoterpenes, Iso: isoprene, MeOH: methanol, EtOH, ethanol, CCOOH: acetic acid, ACD: acetaldehyde, RCOOH: Higher organic acids, ARO1: Other aromatics with kOH < $2x10^4$ ppm^{-1} min^{-1}. "Measured" values can slightly differ in comparison to each inventory because of a different distribution and coverage of inventory grid cells.

The agreement between measurements and CARB inventory was excellent for benzene, toluene, and xylene, while the BEIS+FIVE-VCP inventory was slightly higher than the observations for these species, but within a factor of 2 except for benzene. Also within a factor of 2 and thus within the uncertainty were (for both inventories) methanol, isoprene, acetaldehyde, and PCBTF (for BEIS+FIVE-VCP), as well as trimethylbenzene and acetone (for CARB). Larger discrepancies were observed for benzaldehyde, phenol, cresol, ethanol, acids, sesquiterpenes, dichlorobenzene, D5 siloxane, and methanethiol. Among these, benzaldehyde, ethanol, acids, and sesquiterpenes

were important contributors to OH reactivity and/or SOA formation potential (Fig. 4.3). Generally, there was better agreement between observations and inventories for aromatics than for OVOCs and other VCPs. This reflects the fact that routine measurements historically have been more focused on typical traffic emissions like aromatics, which are therefore much better understood.

On the contrary to that, OVOCs were not easily measurable with routine methods in the past. For example, even during an intense, state-of-the-art observation campaign like CalNex 2010 in Los Angeles, only nine OVOC species were observed (Hansen et al., 2021). With the airborne flux measurements in 2021, we observed significant fluxes of 93 different OVOCs thanks to more comprehensive state-of-the-art instrumentation. Eight of these OVOCs were among the 10 most important VOCs in terms of mass flux or OH reactivity flux (Fig. 4.3). The CARB inventory includes 19 and the BEIS+FIVE-VCP inventory 17 OVOCs, respectively (although including some lumped species). In the comparison of OVOCs it is important to be aware that our observations are net fluxes, which means that the median is decreased due to deposition fluxes. Emission inventories do not assume deposition, which is treated separately by another module in atmospheric modeling. This means that gross emission fluxes would be higher than the observation medians shown in Fig. 4.5 - in some cases (e.g., for acetone or ethanol) substantially, as can be seen in box charts of the fluxes that display large deposition fluxes (Fig. 4.8).

Notably, some relevant VOCs are only included in one of the inventories. For example, PCBTF, a solvent VOC that is included e.g. in coatings (Stockwell et al., 2020), is listed as carcinogenic (California Office of Environmental Health Hazard Assessment, 2022) and contributed a substantial amount to SOA formation potential (Fig. 4.3). However, PCBTF is missing from the CARB inventory and was only recently added to the FIVE-VCP inventory. Also missing from the CARB inventory and recently added to the FIVE-VCP inventory is dichlorobenzene ("PDCBZ" in Fig. 4.5), which is listed as carcinogenic (California Office of Environmental Health Hazard Assessment, 2022) and is widely used in pesticides.

Fig. 4.6 demonstrates the importance of the discrepancies between observations and inventories of the different VOC classes for the total mass flux, OH reactivity flux, and SOA formation potential flux. For the mass flux, the difference between observations and inventories was largest in alcohols (mainly ethanol), followed by other oxygenated VOC classes (carbonyls for CARB, acids for BEIS+FIVE-VCP). The largest missing sources of OH reactivity (and thus ozone formation potential) were monoterpenes and alcohols in both inventories. However, since this missing source was made up for by an overestimation of isoprene emissions (CARB) and/or alkene emissions (BEIS+FIVE-VCP), the summed OH reactivity source was very similar between observations and inventories (Fig. 4.4). The largest missing contributors to SOA formation potential were monoterpenes and sesquiterpenes in both inventories.

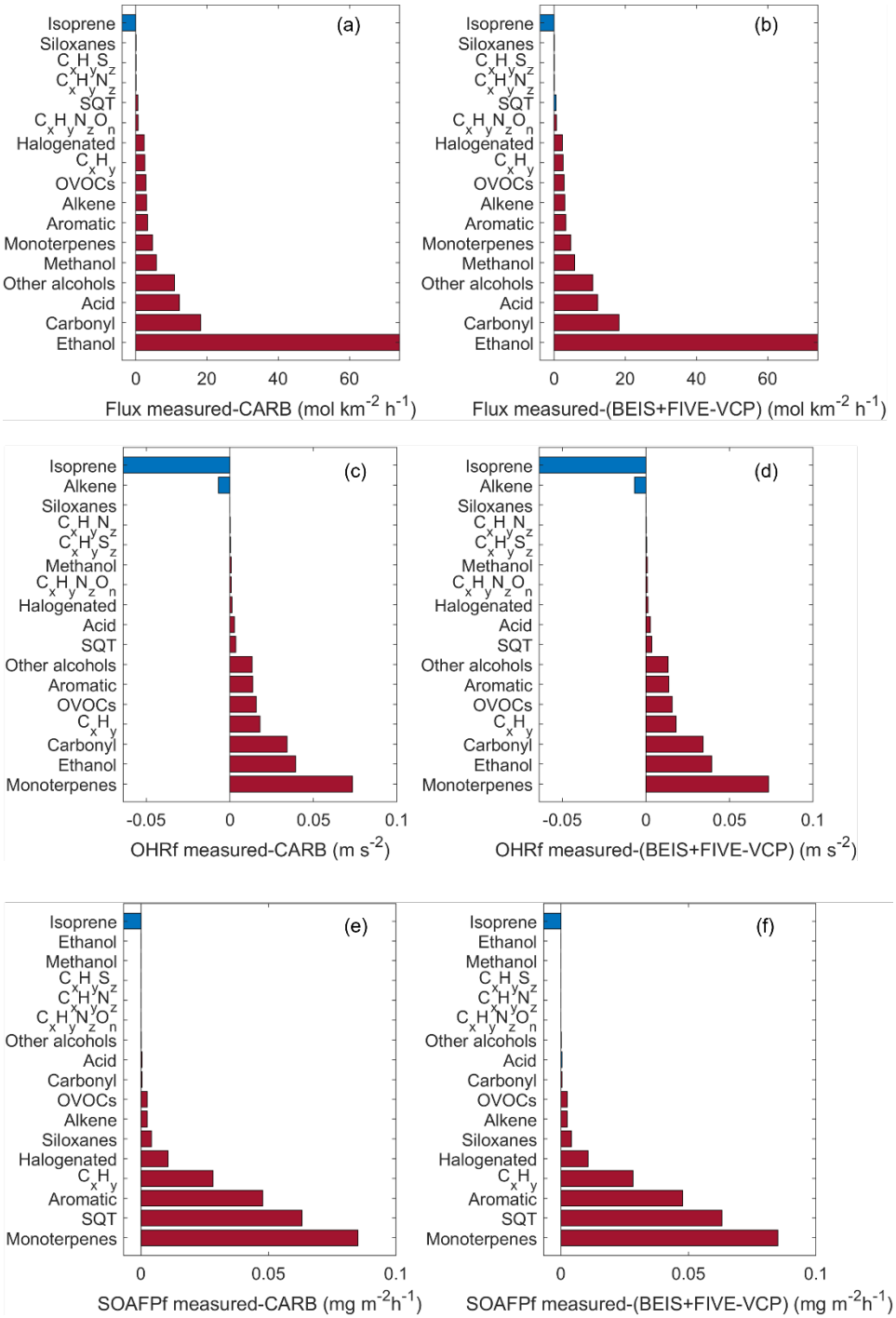

Figure 4.6. Relevance of the discrepancies between measurements and inventories for the total molar flux (a, b), the OH reactivity of the emissions (c, d), and the SOA formation potential of the emissions (e, f). The bars show the difference between measurements and inventories (a, c, e for CARB, and b, d, f for BEIS+ FIVE-VCP).

4.3. Regional, weekend and population density effects

While medians of the whole campaign (Fig. 4.5) can provide an overview validation of the inventories, spatially resolved airborne flux observations can be used more specifically to map regional agreements and disagreements with the emission inventories. Figure 4.7 shows the difference in flux units between inventories and measurements on a 4 km x 4 km grid scale for benzene, ethanol, isoprene, and monoterpene fluxes. The same data is shown in % (inventory emissions/measured emissions) in Fig. S4.1. For benzene, the differences between both inventories and measurements were small in the eastern San Bernardino Valley (around Rancho Cucamonga). However, in relative terms, this was the region where the inventories, especially CARB, underestimated the benzene emissions most clearly. The BEIS+FIVE-VCP inventory overestimated benzene emissions in the downtown and coastal areas. The CARB inventory mostly agreed better with the benzene measurements in the downtown and coastal regions. For ethanol, the spatial pattern of disagreement with the observations is almost the same between the two inventories. There appears to be a significant missing source of ethanol, which we suspect to be cooking and possibly other indoor to outdoor emissions, combined with point sources (e.g., breweries and food manufacturing). Isoprene emissions matched best with both inventories in the San Bernardino Valley, while the observations were lower than inventories in parts of the region between downtown and Santa Ana. For monoterpene emissions, there is almost no grid cell with a reasonable match between observations and inventories. The largest underestimation by the inventories (in absolute terms) occurred in an area that includes much of downtown Los Angeles. In relative terms, both inventories were more than a factor of 4 lower than the measurements also in the San Bernardino Valley and much of the Santa Ana region. Potential explanations for this mismatch are 1) a missing anthropogenic source of monoterpenes from fragrance use, and 2) a (probably larger) missing biogenic source induced by flowering and/or drought stress, as well as an unrealistic plant species composition and distribution in the inventories (see chapter 4.4). We provide more maps of the inventory and measurement values as well as the differences between both online (Pfannerstill et al., 2022), and tabular regional average comparisons in Supplementary Table 3.

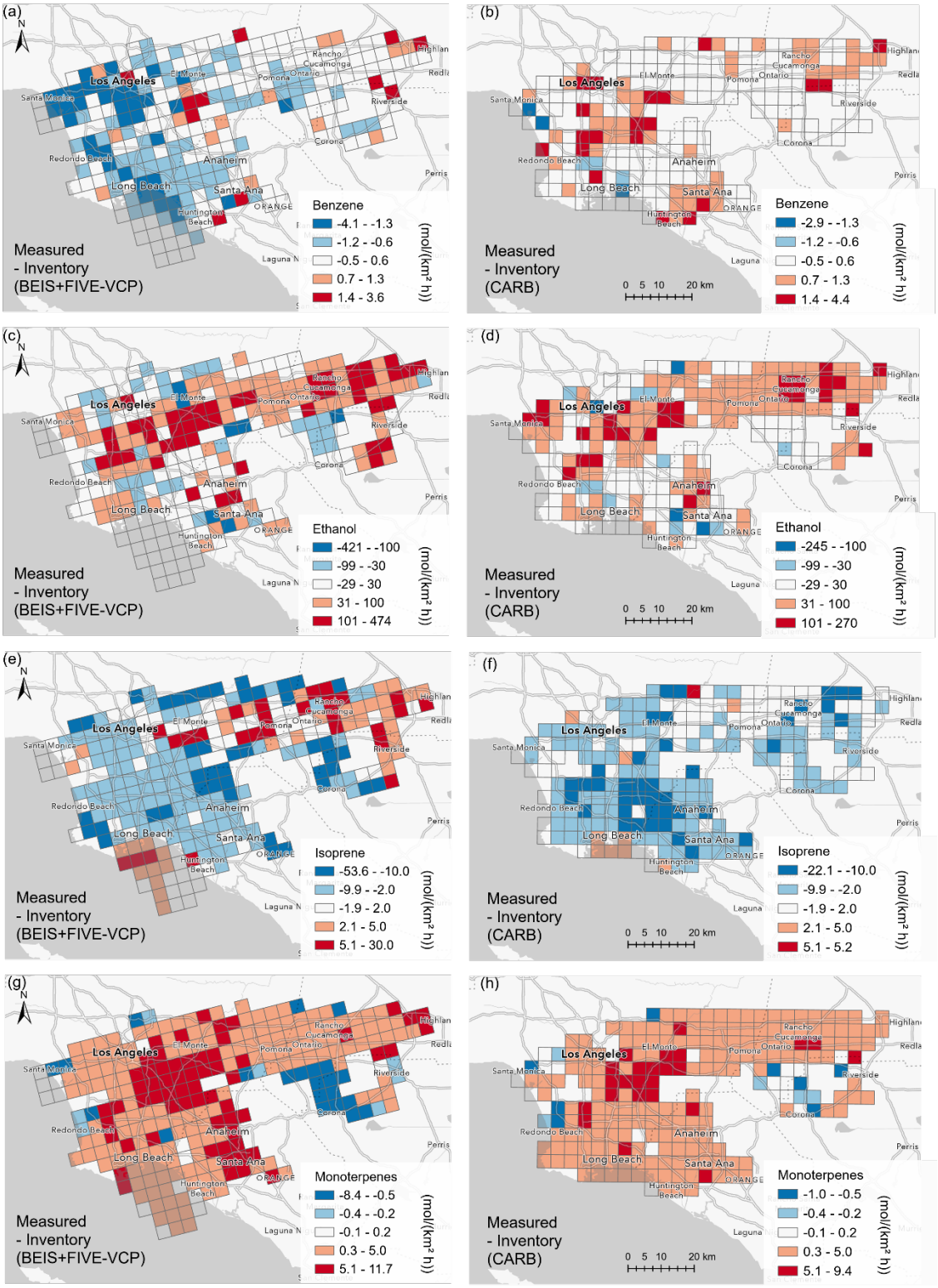

Figure 4.7. Difference of flux measured-inventory for a) BEIS+FIVE-VCP, benzene, b) CARB, benzene, c) BEIS+FIVE-VCP, ethanol, d) CARB, ethanol, e) BEIS+FIVE-VCP, isoprene, f) CARB, isoprene, g) BEIS+FIVE-VCP, monoterpenes, h) CARB, monoterpenes. Blue colors show that the measurements were lower than the inventory, red colors that the measurements were higher than the inventory. A comparison

by ratio instead of difference for the same VOCs is shown in Fig. S4.1. More comparison maps are available as an interactive online map (Pfannerstill et al., 2022).

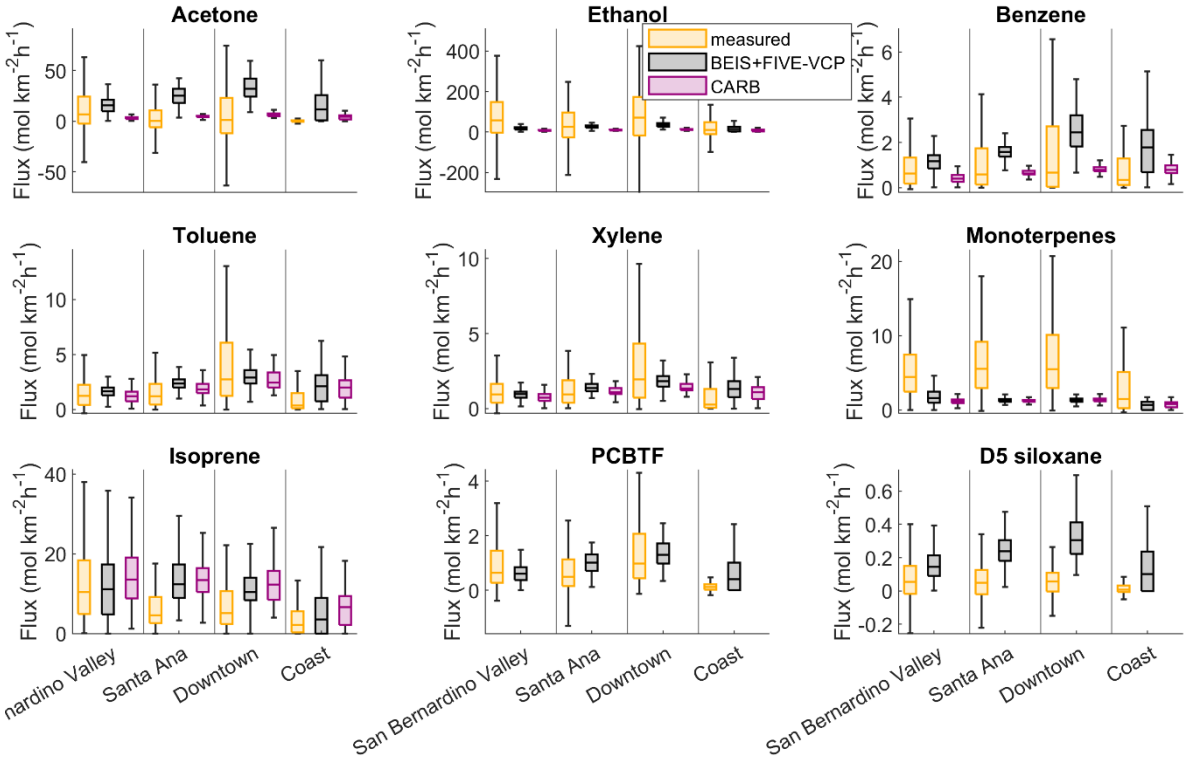

Figure 4.8. Regional fluxes shown for a selection of VOCs in comparison between measurements and the two inventories. The boxes represent the 25th-75th percentile of the data, the whiskers the 5th-95th percentile, and the horizontal line the median. PCBTF and D5 siloxane emissions are not reported in the CARB inventory.

The fact that observed fluxes matched better with the inventories in some regions than others is also illustrated in Fig. 4.8 and Supplementary Table 3. For example, isoprene fluxes agreed with the BEIS+FIVE-VCP inventory within 10% in the San Bernardino Valley, within 50% in at the coast, but only within a factor of 2 in Downtown and Santa Ana. Similarly, the CARB inventory agreed with the observations within 30% in the San Bernardino Valley, but only within a factor of 2-3 in the other regions. Observed benzene fluxes agreed with both inventories within 50% in the San Bernardino Valley, while the agreement decreased for the BEIS+FIVE-VCP inventory in the other regions. Notably, for many of the VOCs shown, the match was best in the San Bernardino Valley area. Potentially, this may be related to the fact that intense VOC observation campaigns in Los Angeles have so far usually been performed in Pasadena (Gouw et al., 2017; Warneke et al., 2013), which is located in the San Bernardino Valley. Inventories have been validated against those measurements. Another factor, likely contributing to mismatches in polar VOCs, is that our observations are net fluxes, while the inventories only consider emissions and not deposition. This means that some VOCs that are strongly deposited (e.g., acetone and other OVOCs, or D5 siloxane,

Fig. 4.8) have a reduced net flux as opposed to if only the emissions were considered. In addition to that, for D5 siloxane it is possible that the measurements somewhat underestimated the fluxes because siloxanes are relatively sticky in the inlet system, leading to a dampened covariance peak.

Some of the mismatch may be due to faulty assumptions of temperature dependence of emissions in the inventories (chapter 4.4), or to differences in temperature assumed in the inventories.

In order to investigate the effect of working days vs weekends on emissions, we performed three out of nine flights on weekends. Figure 4.9 shows comparisons between weekend and weekday fluxes for the measurements and the two inventories for a selection of VOCs. A tabular overview of weekend-weekday comparisons is given in Supplementary Table 4. Generally, there is a large overlap of the interquartile ranges between weekdays and weekends. Benzene, which mainly is emitted from vehicles, did not display any significant weekend effect. This observation agrees with the inventories and with previous studies that demonstrated no significant difference in gasoline-fueled vehicle activity between weekdays and weekends in California (Harley et al., 2005; Pollack et al., 2012). Isoprene, which as a biogenic emission is expected to be independent of workdays, also exhibits no weekend effect.

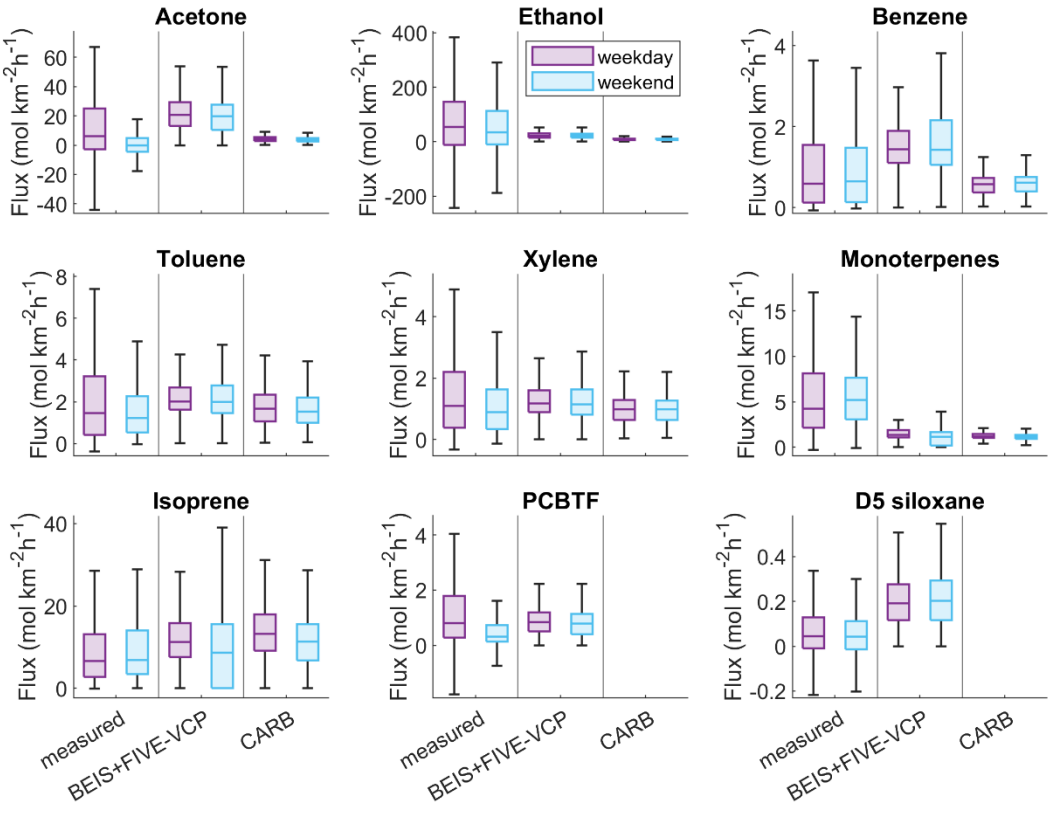

Figure 4.9. Weekday and weekend fluxes shown for a selection of VOCs in comparison between measurements and the two inventories. The boxes represent the 25th-75th percentile of the data, the whiskers the 5th-95th percentile, and the horizontal line the median. PCBTF and D5 siloxane are not reported in the CARB inventory. The plot only includes data from inventory grid cells that were sampled both on weekdays and weekends.

However, the median and top 50% fluxes of a number of other VOCs decreased on the weekend. This includes several of the more VCP- or solvent-related VOCs: acetone (94% decrease in median), ethanol (44% decrease), toluene (23% decrease), xylenes (26% decrease), and PCBTF (62% decrease). Since much solvent use is work/industry related (e.g., construction, printing, cleaning), this observed decrease in emissions on weekends seems plausible. It is also notable that the decreases in the aromatics xylene and toluene were smaller than in the purely solvent-sourced PCBTF, since part of the aromatic emissions are expected to come from gasoline vehicles and therefore not be affected as much by the weekend (see benzene). The inventories do not appear to consider a weekend effect on solvent emissions, with insignificant weekday-weekend differences (below 9%) in the medians for the above listed VOCs. This impacts OH reactivity and SOA projections.

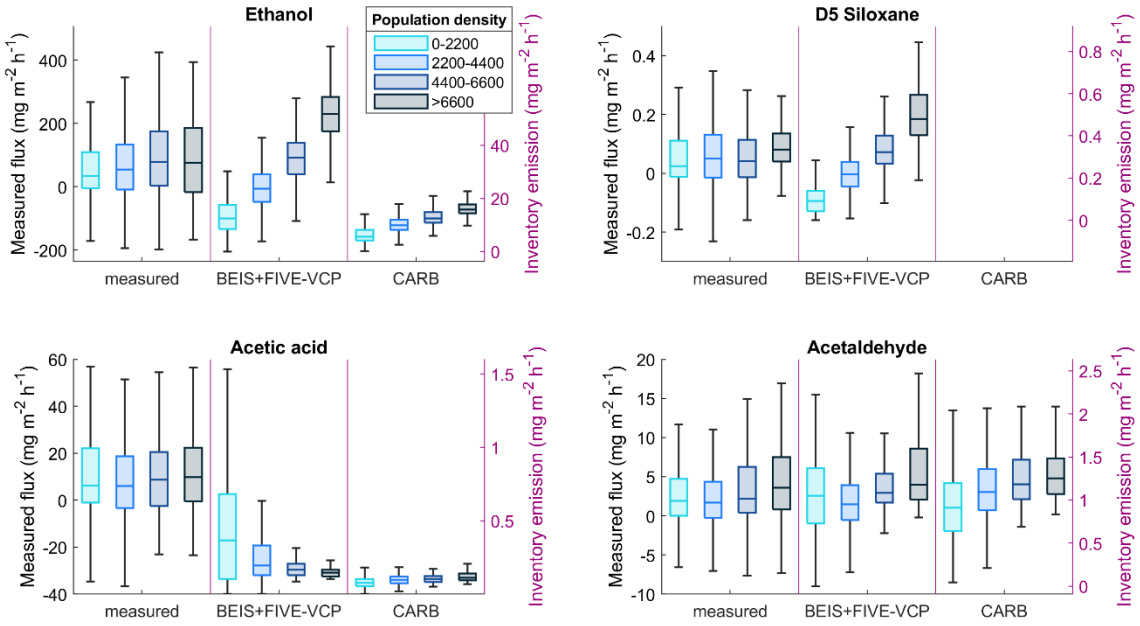

Figure 4.10. Fluxes of relevant indoor-to-outdoor emitted VOCs (Arata et al., in prep.) grouped as a function of population density. Population density is given in people per km². The left y axis corresponds to the measured data, the right y axis to the two inventories.

Figure 4.10 explores relationships between observed VOC emissions and population density for VOCs whose indoor-to-outdoor emission fraction is large (Arata et al., in prep.): ethanol, D5 siloxane, acetic acid, and acetaldehyde. These VOCs are expected to have other sources besides residences, e.g., acetaldehyde also comes from fuel combustion (Wang et al., 2022b) or solvent use (Wang et al., 2022c), and ethanol is also expected to be released from biogenic sources (Schade and Goldstein, 2002), fuel combustion or evaporation (Gouw et al., 2012), solvents (Gkatzelis et al., 2021b), restaurants and food/alcohol manufacturing point sources. Moreover, any population density effects are superimposed with weekend and/or temperature effects. This makes it reasonable that the emission relationship with population density shows a large scatter.

Nonetheless, our data demonstrate a tendency towards increasing emissions of these VOCs with population density. The significance of this tendency was investigated using linear regression through the median fluxes at each median population density for the four bins used in Fig. 4.10. The results of this analysis are shown in Table 4.1. Except for the monoterpenes, all listed VOCs possess a positive slope towards population density larger than the 1σ uncertainty of regression. The ratio of slope/uncertainty indicates the strength of the relationship. These results generally agree with a study that found a population density dependence of VOC mixing ratios for the VOCs listed (Gkatzelis et al., 2021b). The main difference is that our results indicate that monoterpene emissions in Los Angeles are dominated by biogenic sources and not VCPs. The slopes in Table 4.1 also provide estimates of the VOC emission per person and hour.

Table 4.1. Results of the linear regression (median flux vs. median population density) for the VOCs shown in Fig. 4.10 and further VOCs that were reported to increase with population density by Gkatzelis et al. (2021b). The ratio of the regression slope/uncertainty shows that all listed VOCs significantly increase with population density (within the 1σ uncertainty) except the monoterpenes, whose slope is therefore shown in brackets.

VOC	Slope (mg person^{-1} h^{-1})	1 σ uncertainty of slope	Ratio slope/ uncertainty
Ethanol	4170.0	3120.0	1.3
D5 siloxane	7.7	1.9	4.1
Acetic acid	419.0	86.0	4.9
Acetaldehyde	186.6	88.9	2.1
D4 siloxane	6.8	1.5	4.6
Dichlorobenzene	1.6	1.3	1.2
PCBTF	47.8	6.1	7.8
Monoterpenes	(40.0)	76.0	0.5

The BEIS+FIVE-VCP inventory shows a relatively larger increase in ethanol and D5 siloxane emissions with population density than the observations (Fig. 4.10), but a smaller relative increase in acetaldehyde emissions and none in acetic acid emissions. The CARB inventory reflects the observed relative ethanol emission increase well, while its increases in acetic acid and acetaldehyde emissions are somewhat smaller. Overall, the relative dependence of these VOC emissions on population density is mostly well reflected in the inventories. The absolute amounts emitted are a more important mismatch (see Fig. 4.5).

In conclusion, the overall underestimation of alcohol, monoterpene and sesquiterpene emissions by both inventories that we validated (CARB and BEIS+FIVE-VCP) is relevant for air quality predictions, since alcohols and monoterpenes contributed 13% and 19%, respectively, to OH reactivity (relevant for ozone formation), and sesquiterpenes and monoterpenes contributed 23% and 32%, respectively, to SOA formation potential. Our measurements indicate important missing sources of ethanol and terpenoids that should be added to current inventories. Traditionally better quantified typical traffic emissions such as aromatics matched better between the inventories and

measurements than OVOCs and terpenoids. Generally, the CARB inventory had a tendency towards underestimation of emissions for a subset of VOCs, while the BEIS+FIVE-VCP inventory underestimated some and overestimated other VOCs.

Apart from these general trends, there were regional trends in the mismatches. For many VOCs, the inventories agreed best with the observations in the inland region of the San Bernardino Valley, while downtown Los Angeles was more prone to emission underestimations, e.g., for ethanol and monoterpenes.

The interquartile ranges of weekend and weekday emissions mostly overlapped. Nevertheless, the observed weekend effect was stronger than predicted by the inventories, especially for solvent-related VOCs like PCBTF, acetone, and toluene. The relative increase of some VOC emissions with population density was reasonably well reflected in the inventories.

Seasonal and diel variability in emissions were not captured by our measurements, which are limited to daytime in June – however, a time period when air quality standard exceedance conditions typically occur.

Our results point to the necessity to improve inventory emissions of non-traditional VOC sources like VCPs, solvent use and cooking to obtain a comprehensive representation of relevant air pollutant precursors in urban areas. They also show the need for a better representation of urban biogenic VOC emissions in inventories, since these are highly important for ozone and SOA formation and not as accurately represented as transportation emissions.

4.4. Temperature-dependent VOC emissions dominate aerosol and ozone formation in Los Angeles

*A version of this chapter is under review at Science under the title "**Temperature-dependent emissions dominate aerosol and ozone formation in Los Angeles**", with the following authors: Eva Y. Pfannerstill, Caleb Arata, Qindan Zhu, Benjamin C. Schulze, Ryan Ward, Roy Woods, Colin Harkins, Rebecca H. Schwantes, John H. Seinfeld, Anthony Bucholtz, Ronald C. Cohen, and Allen H. Goldstein*

Ambient air pollution is the fourth ranking human health risk factor globally (Murray et al., 2020), leading to an estimated 4.2 million premature deaths per year (World Health Organization, 2022). Important pollutants causing cardiovascular and respiratory diseases are fine particulate matter ($PM_{2.5}$) and tropospheric ozone (World Health Organization, 2022). Volatile organic compounds (VOCs) are precursors to both: A large fraction of $PM_{2.5}$ is Secondary Organic Aerosol (SOA), formed through the oxidation of VOCs (Hayes et al., 2013b). In the presence of nitrogen oxides and sunlight, VOC oxidation leads to ozone formation.

99% of the world's population lives in places where the World Health Organization air quality guidelines are not met (World Health Organization, 2022). This includes the US megacity of Los Angeles, where ozone and $PM_{2.5}$ are frequently at unhealthy levels, especially in the summer (US EPA, 2016, 2020). As in many industrialized cities, technologies like efficient 3-way catalytic converters and efforts spurred by regulation led to a steep decrease in automotive VOC

emissions, and thus to a decades-long decrease of air pollutant concentrations (Warneke et al., 2012). However, concentrations of ozone and $PM_{2.5}$ particle pollution have stopped decreasing since ~2010 (Kim et al., 2022; Nussbaumer and Cohen, 2021). Recent studies indicate the increasing relative importance of volatile chemical products, which now contribute as much as half of urban fossil fuel VOC emissions in industrialized cities (McDonald et al., 2018; Coggon et al., 2021). The relative contribution of the biogenic VOC fraction must also have increased with declining transportation emissions. Following these changes in the emitted VOC mixture over the course of a few decades, the sources of secondary air pollution have been called into question. For example, model-observation comparisons have raised doubts on whether the models correctly reproduce the emission source mixture contributing to SOA (Hayes et al., 2015; Ma et al., 2017). The origin of SOA in Los Angeles is under debate – with some studies reporting a predominantly vehicular source (Zhao et al., 2022; Hayes et al., 2015), while a temperature-dependent analysis of $PM_{2.5}$ concentrations and isoprene concentrations indicated a major biogenic origin (Nussbaumer and Cohen, 2021). The percentage of days with $PM_{2.5}$ exceedances is below 10% at 20°C and more than 40% at 30°C, and reaches 70% at 40°C (Nussbaumer and Cohen, 2021). Similarly, the likelihood of ozone exceedances (≥ 70 ppb) is close to 0 at 20°C, and above 70% at temperatures ≥ 30°C, with temperature-dependent biogenic emissions of reactive terpenoids suggested as one of the driving factors (Nussbaumer and Cohen, 2020). However, concentration-based temperature dependencies may be influenced by meteorology instead of emissions, since hotter days tend to be more stagnant (Horton et al., 2014). This shows the need for direct emission observations. With climate change, an increase in the number of days with high temperatures is expected (Hulley et al., 2020; Pierce et al., 2013). Thus, it is important to understand how increasing temperatures affect VOC emission amounts, mixture, and what this means for secondary air pollutant formation, as well as regulation strategies.

4.4.1. Spatially resolved direct airborne measurements of VOC emission fluxes

Previous efforts to understand the magnitude and composition of VOC emissions in Los Angeles, as in other megacities, have relied on indirect methods – either using traditional bottom up emission inventories (Gu et al., 2021), or inferring emissions top down from concentration measurements via chemical transport models (Coggon et al., 2021). Both approaches are indirect and rely on a range of assumptions, and thus are subject to large uncertainties. To overcome these limitations, we performed airborne eddy covariance measurements in order to provide the first direct observations of spatially resolved VOC emissions in Los Angeles. Emission and deposition fluxes were calculated from 10 Hz concentration and vertical wind speed measurements using continuous wavelet transformation (Karl et al., 2013). State-of-the-art instrumentation (PTR-ToF-MS) provided an unprecedented comprehensiveness of VOC species for which spatially resolved urban fluxes were observed, including source specific tracers for biogenics, vehicle emissions, personal care products, solvents, etc. Nine flights were conducted in June 2021 between 11:00 and 17:00, with flight days selected to cover a temperature range as wide as possible (maps of flight tracks see fig. 2.1). Median flight temperatures ranged from 23°C to 31°C, with minima and maxima stretching from 15°C to 37°C, respectively.

Ozone formation in Los Angeles is still sensitive to VOCs, with recent analyses suggesting that current NO_x emissions need to be reduced substantially (more than 50%) to move to a NO_x sensitive ozone formation regime (Kim et al., 2022; Nussbaumer and Cohen, 2020). The contribution of VOCs to ozone formation is determined by the reaction frequency of each VOC species with the hydroxyl (OH) radical, the primary oxidant in the daytime troposphere. This reaction frequency is referred to as OH reactivity and is calculated for emissions as

$$OHR_F = k_{OH,VOC} * F_{VOC} \qquad \text{(eq. 4.1)},$$

where OHR_F is the OH reactivity of the flux in ms^{-2}, $k_{OH,VOC}$ is the reaction rate constant of a VOC with the OH radical in m^3 $molecules^{-1}$ s^{-1}, and F_{VOC} is the flux of the VOC in molecules m^{-2} s^{-1}. Since the daytime boundary layer over Los Angeles can be considered as a box which emissions are continuously added to, OH reactivity is a reasonable proxy for ozone formation here. If an air parcel moving out of the valley were considered, the contribution of highly reactive VOCs would decrease following oxidative loss. The contribution of VOCs to SOA formation is more complex to quantify. We estimated aerosol yields using the Statistical Oxidation Model (Robinson et al., 2007) combined with a one-dimensional volatility basis set for OVOCs (Cappa and Wilson, 2012). Ambient particle formation also depends on factors like ambient humidity (Gkatzelis et al., 2021a), pre-existing particle surface area (Holmes, 2007), and the mixture of VOCs present (McFiggans et al., 2019), which we have not considered here but are unlikely to substantially change the relative contribution of individual precursor classes to the SOA budget. Based on a back of the envelope calculation assuming 24 h aerosol lifetime (Nussbaumer and Cohen, 2021) and 800 m boundary layer height, the summed SOA potential of the measured VOC emissions (0.32 mg m^{-2} h^{-1}) yields 9.6 µg/m³ of SOA, which is ~80% of the afternoon OA observed during CalNex (Hayes et al., 2013a).

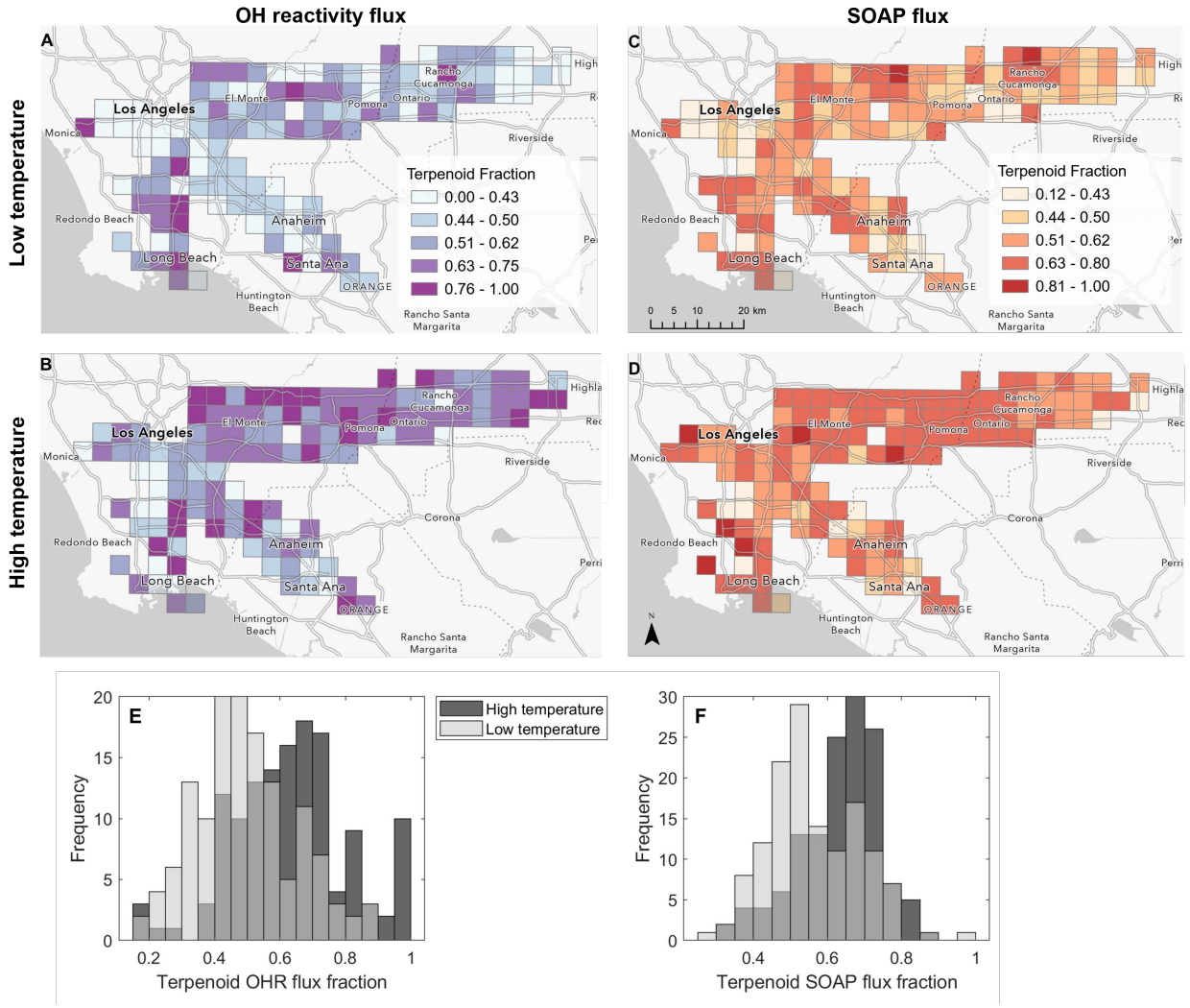

Fig. 4.11. Terpenoid fraction of OH reactivity and secondary organic aerosol formation potential (SOAP) of measured emissions at low vs high temperatures in Los Angeles. Maps show the terpenoid (isoprene (C_5H_8) + monoterpenes ($C_{10}H_{16}$, $C_{10}H_{16}O$, $C_{10}H_{18}O$) + sesquiterpenes ($C_{15}H_{24}$)) fraction in the summed OH reactivity flux (A) at low, (B) at high temperature, and in the summed SOA formation potential of VOC emissions (C) at low and (D) at high temperatures. For each 4x4 km² grid cell, "low temperature" was defined as an ambient temperature (2 m above ground) in the lowest 25% of all flux measurements (n ≥ 6) conducted over that grid cell, and "high temperature" was defined as an ambient temperature in the upper 25% of all flux measurements conducted over that grid cell. The frequency of grid cells' terpenoid fractions at low and high temperatures is shown in (E) and (F).

4.4.2. Temperature dependence of the VOC mixture contributing to secondary air pollutants

Mapped VOC emissions (Fig. 4.1) were attributed to footprint areas (Fig. 2.8) and averaged to 4 km x 4 km grid cells, and the OH reactivity and SOA formation potential were calculated for each of the observed 410 VOC species. The fraction of terpenoids (isoprene, monoterpenes, and sesquiterpenes, typically attributed to biogenic emissions) both in the summed OH reactivity and SOA formation potential was large even in the lowest temperature bin, and grew substantially

with temperature in most areas of Los Angeles (Fig. 4.11). In the lower 25th percentile of temperatures, OH reactivity in 45% of the grid cells, and SOA formation potential in 67% of the grid cells were dominated by terpenoids. This especially included regions at the less urbanized hillsides on the outskirts of the metropolitan area, e.g., north of El Monte. In the top 25th percentile, these values increased to 78% and 88%, respectively. Thus, at high temperatures, terpenoids became the main drivers for the formation of ozone and particles even in the downtown area (in Fig. 4.11 below and southeast of the label "Los Angeles") where traffic and consumer product emissions are expected to be largest based on current emission inventories.

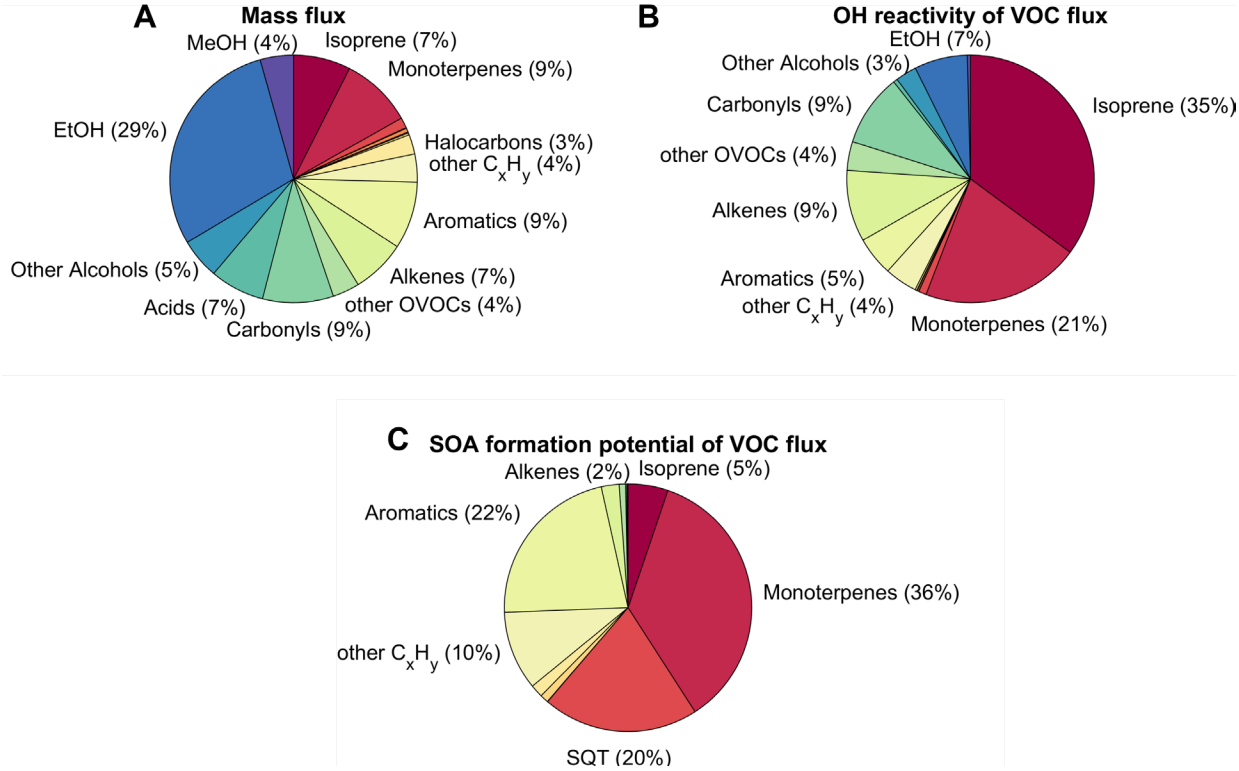

Fig. 4.12. Contribution of different VOC classes to **(A)** mass flux, **(B)** OH reactivity of VOC flux, and **(C)** secondary organic aerosol formation potential of VOC surface flux of all VOCs measured during the RECAP-CA flights in June 2021. The pie charts show the median composition over all flights. MeOH: methanol, EtOH: ethanol, SQT: sesquiterpenes. VOCs attributed to each group see Supplementary Table 1.

The composition of the observed average VOC emission mixture is shown in Fig. 4.12. Terpenoids contributed ~16% of the measured VOC mass flux. Due to the high reactivity of the terpenoids and the low volatility of their oxidation products, terpenoids accounted for 56% of the OH reactivity and 56% of the SOA formation potential. The OH reactivity contribution here is similar to the ~60% biogenic contribution to ozone in Berlin during a heatwave (Churkina et al., 2017). An inventory-based study also found ~60% contribution of biogenic terpenoids to ozone formation potential in Los Angeles, although with a higher isoprene and a lower monoterpene contribution (Gu et al., 2021). The same study predicted only 23% of the (annual average) SOA formation potential from terpenoids, but our value agrees well with a radiocarbon analysis of organic aerosol in summertime Los Angeles that attributed 58% ± 15% to non-fossil sources, of

which 44% ± 15% may be biogenic (Zotter et al., 2014). Ethanol, which was a major constituent of the VOC mass flux, is a low-reactivity VOC and thus only contributed ~5% of the OH reactivity. The terpenoid fraction here is higher than in our own (Fig. 4.13) and previously published concentration-based Los Angeles observations (Hansen et al., 2021). Since these VOCs react rapidly, the magnitude of their contribution to secondary products may be underestimated based on ambient concentrations alone.

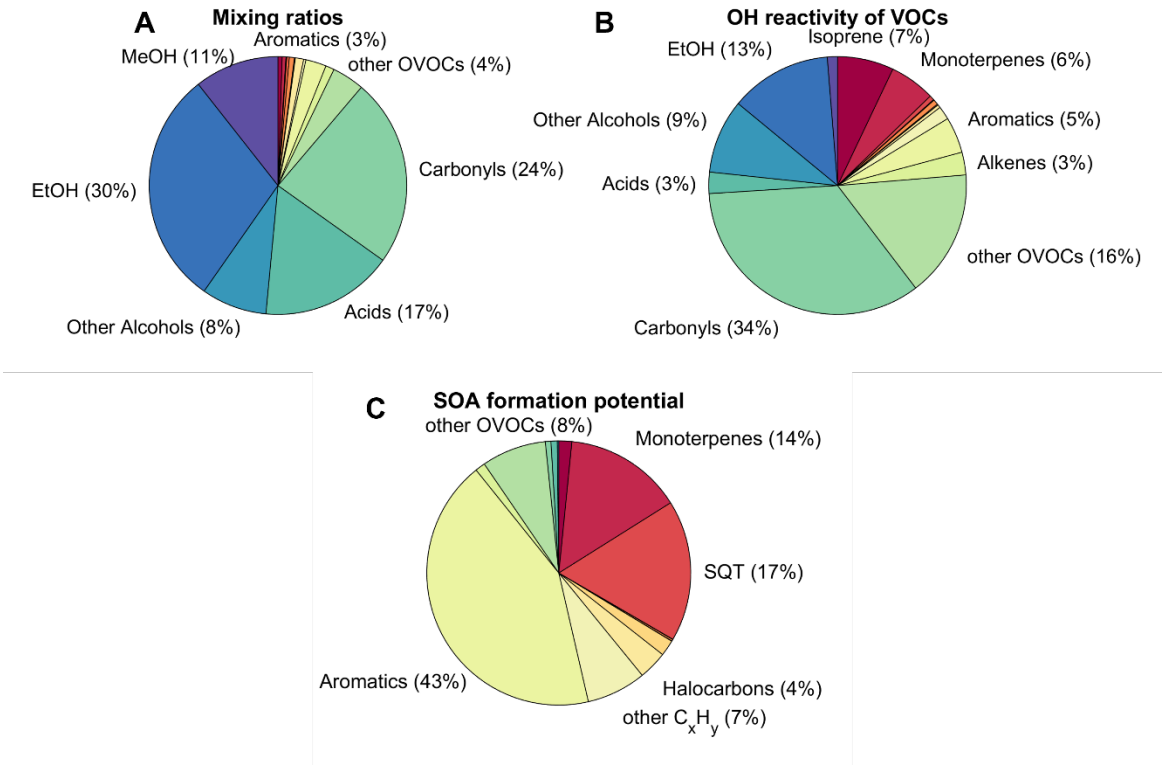

Fig. 4.13. Contribution of different VOC classes to **(A)** mixing ratios (ppbv), (**B)** OH reactivity of VOCs, and (**C)** secondary organic aerosol formation potential of VOCs during Los Angeles RECAP-CA flights. These charts are based on concentration-based values (different from primary emissions in Fig. 4.12). The pie charts show the median composition over all flights. MeOH: methanol, EtOH: ethanol, SQT: sesquiterpenes. VOCs attributed to each group see Supplementary Table 1.

We note that the VOC emission mixture observed here is incomplete, since the PTR method is not sensitive to alkanes. However, alkanes are a comparably minor and relatively unreactive fraction of total VOC, contributing only 4% of the measured mid-day VOC OH reactivity in Los Angeles in 2010 (Hansen et al., 2021). For SOA formation, long-chain alkanes are of higher significance (Gu et al., 2021). We estimate that including long-chain alkanes would reduce the relative terpenoid contribution to average summertime SOA formation by 25-30% of the fraction presented here. Seasonality and diel variability in emissions composition are not captured by our measurements, which are limited to daytime in June – however, a time period when air quality standard exceedance conditions typically occur.

The VOCs included in Fig. 4.14 were among the largest contributors to OH reactivity and/or SOA formation potential of the emissions, and they all increased with temperature. The observed increase of isoprene, monoterpene and sesquiterpene emissions with temperature is in accordance with the expectations for biogenic emissions (Guenther et al., 2012). Reflecting this state of knowledge, two current inventories (CARB/MEGAN and BEIS+FIVE-VCP) also predicted increases in emissions of these VOCs with temperature. However, the measured amount of monoterpene and sesquiterpene emissions was a factor of 2-3 higher than predicted by the inventories. The measured isoprene emission matched the inventories within the uncertainty of the fluxes.

Observed emissions of several anthropogenic VOCs also increased with temperature. This includes toluene (Fig. 4.14D), ethanol (Fig. 4.14E), and para-chlorobenzotrifluoride (PCBTF, Fig. 4.14F). The observed temperature dependences of ethanol and toluene emissions in the temperature range of 20-30°C approximately agree with their vapor pressure curves in this temperature range (National Institute of Standards and Technology, 2022). Toluene, ethanol and PCBTF can come from solvent-based sources, where evaporative volatilization could explain the temperature dependence. Moreover, evaporative losses from gasoline can become an important contributor to vehicle emissions at high temperatures (Rubin et al., 2006). The observed temperature dependence of these anthropogenic VOCs was not accurately predicted in either of the two inventories.

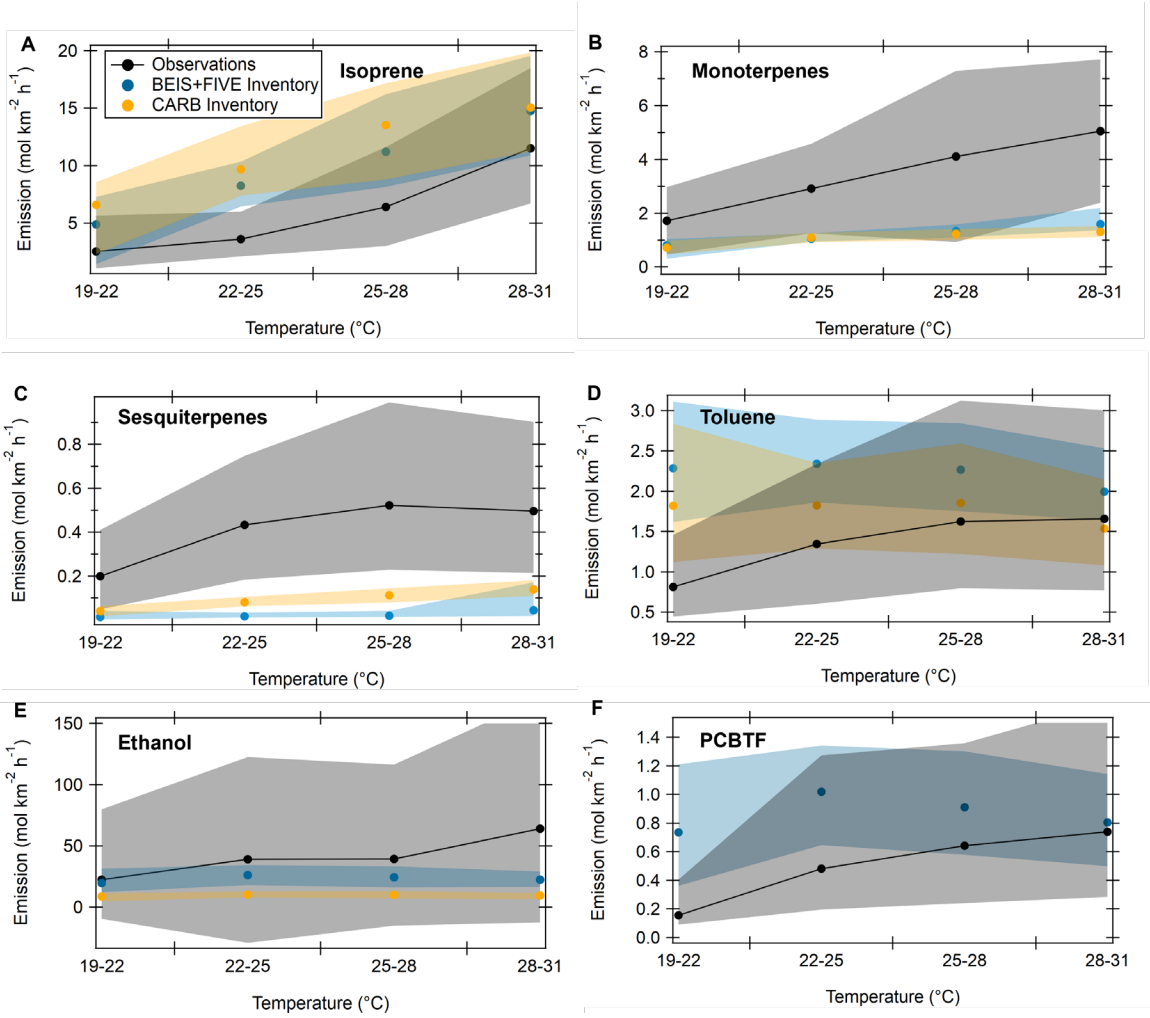

Fig. 4.14. Temperature dependence of emissions of individual VOC species in comparison with inventories. The VOC species shown here are among the largest contributors to SOA formation potential and OH reactivity in the measured VOC emissions. The circles represent medians of each temperature bin, and the shaded areas the 25th to 75th percentile of data. The temperature effect cannot be explained with regional emission differences that may co-occur with temperature differences (Fig. S4.3). Measurement uncertainties: 76%-96%. PCBTF (para-chlorobenzotrifluoride) is not included in the CARB inventory. Only temperature bins that include data from all regions (Fig. 4.1) are shown.

As a result of the increase of VOC emissions with temperature, the summed OH reactivity of the emissions, and thus the potential for ozone formation, increased 2- to 3-fold from 20°C to 30°C (Fig. 4.15A). This amounts to a 27% increase per 1°C (Fig. S4.4). Although there was an increase in both the emissions of terpenoids and all other VOCs, most of the overall increase was due to the terpenoid emissions alone, which increased more than 3-fold. The OH reactivity of non-terpenoid VOC emissions only doubled in the same temperature range. The terpenoid fraction in the sum of the OH reactivity of VOC emissions increased from ~40% at 20°C to ~60% at 30°C.

Similar to OH reactivity, the SOA formation potential of emitted VOCs increased 2- to 3-fold from 20°C to 30°C, or 13% per 1°C temperature increase (Fig. 4.15B, Fig. S4.4). The terpenoid

fraction was enhanced from 45% to 64% of the overall SOA formation from 20°C to 30°C, with the SOA-relevant terpenoid emissions approximately doubling in the same temperature range. The SOA-relevant non-terpenoid VOCs – mainly aromatics (Fig. 4.12) – barely increased with temperature (Fig. 4.15B). Although the emissions of the aromatic toluene were temperature dependent (Fig. 4.14) because it has a large solvent source, many other aromatics are mainly tailpipe emissions, which do not change with ambient temperature. We note that the SOA formation potential calculated here does not account for

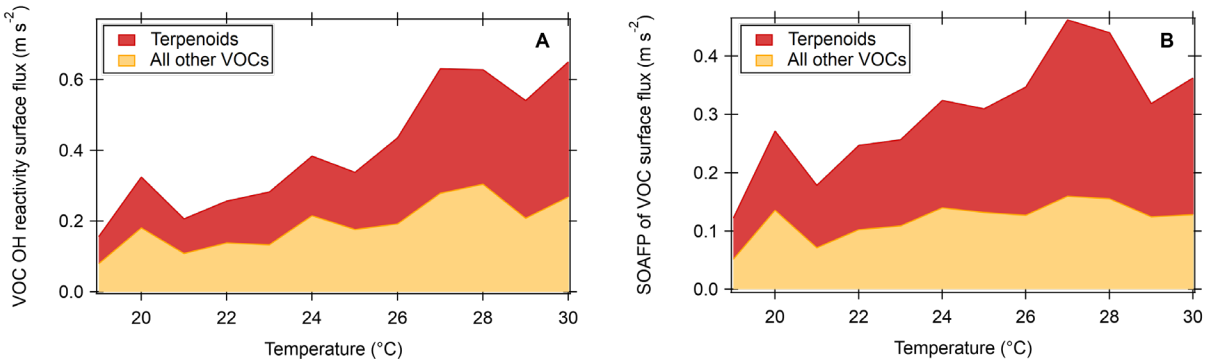

Fig. 4.15. Temperature dependence of the summed OH reactivity and SOA formation potential of the VOC emissions. The primary terpenoid contribution was separated from all other VOCs and is shown as the red fraction of the stacked plot. All measured fluxes were binned into 1°C temperature bins for this plot, where "temperature" is the ambient temperature at 2 m above ground level. To ensure that the dependence is not skewed by regional emission differences, only temperature bins that cover at least three regions were included.

4.4.3. Monoterpene sources: biogenic or anthropogenic?

Since monoterpenes are an especially relevant contributor to SOA formation and OH reactivity in Los Angeles, understanding whether their source is anthropogenic or biogenic is critical for air quality management. Recently, anthropogenic sources of urban monoterpenes, especially D-Limonene, have been reported (Gkatzelis et al., 2021b). Monoterpenes and sesquiterpenes are present in a variety of fragranced consumer products, e.g., cleaning or personal care products (Steinemann et al., 2011).

Our data suggest a dominant, but not sole, biogenic source for the monoterpenes. The biogenic dominance is indicated both by the temperature dependence (Fig. 4.14B, (Peng et al., 2022)), and by the correlation between monoterpenes and biogenic isoprene in fluxes measured in the downtown Los Angeles region (Fig. 4.16A). In the same region, we did not observe correlations between monoterpenes and any of the identified anthropogenic tracers, such as D5 siloxane (personal care product tracer, Fig. 4.16B), toluene, or ethanol (fig. S4.5). Since the sesquiterpene fluxes correlated well with the monoterpene fluxes (Fig. S4.5), a dominant biogenic source for the sesquiterpenes can be assumed, too. Monoterpene emissions did not scale with inventories of tree and shrub cover (Fig. S4.6, S4.7), likely because not all trees or shrubs are monoterpene emitters. Biogenic emission inventories like the ones included in our comparison (Fig. 4.14B) do

not consider the actual plant species variability within an urban area and therefore do not faithfully represent potential spatial differences in the composition and emission factors of biogenic emissions per tree. We observed regional differences in the isoprene/monoterpene emission ratio, which was ~3 in San Bernardino and ~1.5 in downtown, even though both regions have similar fractional tree coverage (Fig. S4.8). Likely, the species composition in the San Bernardino Valley with its hillside shrublands is different.

Nonetheless, there are indications for an anthropogenic influence on measured monoterpene emissions: Some high monoterpene emissions in downtown Los Angeles (Fig. 4.16A) were not correlated with isoprene. In New York in winter, i.e., where plant emissions are assumed to be low, monoterpenes scaled with population density (Gkatzelis et al., 2021b). However, in Los Angeles in summer, we did not observe a correlation between monoterpene emissions and population density in the flux footprint. (Different from the personal care product tracer D5 siloxane which did correlate with population density, see Fig. S4.6.) Due to this observation, we infer that a dominant anthropogenic monoterpene source is unlikely. A non-negative matrix factorization of monoterpene and other VOC fluxes with tree cover, temperature and population density assigned ~33% of the variability in monoterpenes fluxes to a factor dominated by population density, while the rest of the variability was explained by temperature, tree and shrub cover (Fig. S4.9). This is in good agreement with a source-apportionment study in Atlanta, Georgia, that attributed 26% of the monoterpenes to anthropogenic sources (Peng et al., 2022), and where anthropogenic monoterpenes did not correlate with temperature. Coggon et al. suggested an anthropogenic source of monoterpenes in New York of up to 860 mg person^{-1} day^{-1} (Coggon et al., 2021), which, applying the population density in our flux footprints, would amount to a median of 0.74 mol km^{-2} h^{-1} or 15% of observed total monoterpenes in Los Angeles.

The observed monoterpene and sesquiterpene emissions were significantly higher than predicted by the CARB and BEIS+FIVE-VCP inventories (Fig. 4.14). While this may indicate an anthropogenic source not incorporated in the inventories, the size of the mismatch suggests another missing source. Since the inventories only consider an average urban tree composition, specific local monoterpene emitters may be missing, e.g. eucalyptus trees that comprise 5% of Los Angeles tree population. Moreover, flowering emissions are not included in the inventories. For example, jacaranda (*jacaranda sp.*) trees, which are among the most abundant species in Los Angeles (McPherson et al., 2013), were in bloom during the aircraft observations. Monoterpene emissions during bloom can be up to an order of magnitude higher than usual (Fares et al., 2011; Baghi et al., 2012), and jacaranda flowers have been shown to emit a bouquet that includes monoterpenes and is rich in sesquiterpenes (Pontes et al., 2022; Guimarães et al., 2008). Another factor that can substantially increase biogenic terpenoid emissions and is not part of inventories is heat or drought stress (Holopainen et al., 2018; Werner et al., 2021). Long-term drought stress has been shown to increase sesquiterpene and monoterpene emissions while reducing isoprene emissions (Werner et al., 2021; Potosnak et al., 2014), which agrees with our observed inventory discrepancies. In California, 2021 was one of the driest and hottest years on record (California Department of Water Resources, 2021).

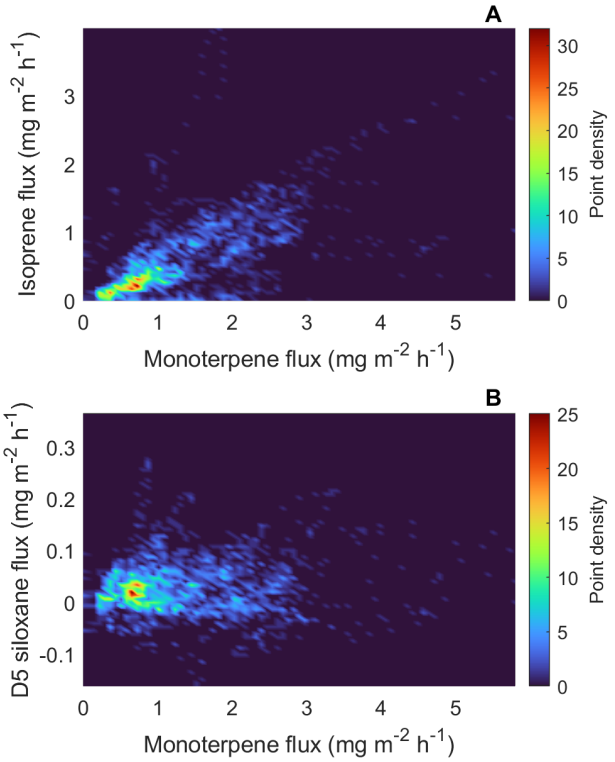

Fig. 4.16. Correlation of monoterpene emissions in downtown Los Angeles with other VOC fluxes, indicating biogenic origin of monoterpenes. (A) Density plot showing correlation (r = 0.7) between monoterpene fluxes and isoprene fluxes in the Los Angeles downtown region (definition of regions see Fig. 4.1). (B) No correlation (r = 0.25) of monoterpene fluxes with the fluxes of an anthropogenic tracer, D5 siloxane, in the downtown Los Angeles region.

4.4.4. Implications for urban air quality in a warming climate

Climate change is predicted to increase the number of hot days, with disproportionately large temperature increases in urban areas and in the summer (Hulley et al., 2020; Pierce et al., 2013). Average summer temperatures in the Los Angeles region are projected to increase by 3°C by the 2060s (Pierce et al., 2013). Our results imply that this would lead to a doubling in OH reactivity and a 40% increase in SOA formation potential of the VOCs represented here. These may even be underestimates as this calculation assumes a linear increase in OH reactivity and SOA formation potential with temperature, as observed in the limited temperature range covered in our study, while biogenic emissions are expected to increase exponentially with temperature (Guenther et al., 2012). Our data suggest that terpenoids dominate the SOA formation potential and ozone formation potential above 30°C. Historically, only 10% of July days in coastal Southern California exceeded 30°C. By the 2060s, this fraction is predicted to increase to 50% (Pierce et al., 2013). In inland Los Angeles regions, even currently July temperatures exceed 30°C (Pierce et al., 2013) nearly every day, and therefore biogenic sources likely already dominate SOA and ozone production.

Our findings underscore that climate change will lead to more high-ozone and high-$PM_{2.5}$ pollution events unless anthropogenic emissions are substantially reduced (Jacob and Winner, 2009; Schneidemesser et al., 2015; Wu et al., 2008). On high temperature days, it becomes even more important to reduce anthropogenic VOC emissions, since biogenic emissions cannot be regulated, and since anthropogenic SOA is thought to pose a higher health risk by mass than biogenic SOA (Lovett et al., 2018). A further reduction in NO_x emissions will also help alleviate the ozone burden after transitioning to a NO_x-limited ozone formation regime. Flowering and drought stress periods are expected to increase biogenic terpenoid emissions and may therefore be especially prone to high ozone and particle pollution events.

Even at lower summer temperatures, biogenic terpenoids dominate secondary air pollutant formation in many parts of Los Angeles. The inventory underestimation of mono- and sesquiterpene emissions caused a factor of ~2 underestimation of VOC SOA formation potential (Fig. 4.17) and may explain the gap between modeled and measured SOA (Pennington et al., 2021). This combined with the fact that inventories also did not capture the temperature dependence of anthropogenic VOCs has implications for the representation of the emission mixture in general, and for predicting how the composition and pollutant formation changes as temperatures increase.

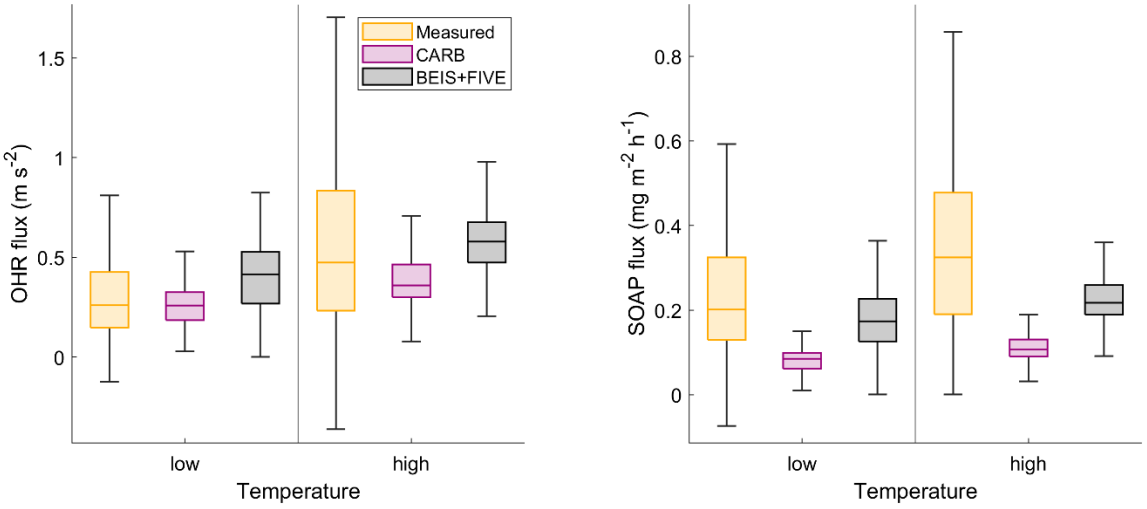

Fig. 4.17. Summed OH reactivity of flux for the lowest and highest 25% temperatures in each 4 km x 4 km grid cell, and summed SOA formation potential of flux for the lowest and highest 25% temperatures in each grid cell, shown for measurements, CARB and BEIS+FIVE-VCP inventories.

5. NO_x fluxes in the San Joaquin Valley

*A version of this chapter is under review in Atmospheric Chemistry and Physics under the title "**Direct observations of NOx emissions over the San Joaquin Valley using airborne flux measurements during RECAP-CA 2021 field campaign**", with the following authors: Qindan Zhu, Bryan Place, Eva Y. Pfannerstill, Sha Tong, Huanxin Jessie Zhang, Jun Wang, Clara M. Nussbaumer, Paul Wooldridge, Benjamin C. Schulze, Caleb Arata, Anthony Bucholtz, John H. Seinfeld, Allen H. Goldstein, Ronald C. Cohen (Zhu et al., 2023)*

5.1. Overview of observed NO_x fluxes

The overview of observed fluxes across 7 flights over San Joaquin Valley is illustrated in Fig. 5.1. It shows a distinct spatial heterogeneity (Figure 5.1 (a)). For instance, high NO_x flux signals are detected when the aircraft was flying above highway 99 between Bakersfield and Visalia. The transect of cities, such as Fresno, capture a substantial enhancement of NO_x fluxes. Fig. 5.1 (b) exhibits the distribution of airborne fluxes. 90% of the fluxes are positive, demonstrating that our airborne flux measurements are capable of detecting NO_x emissions over the study domain. We attribute the remaining 10% of negative fluxes to the uncertainties in the flux calculation. The distribution of observed fluxes is right-skewed; the mean and median observed flux over the SJV is 0.37 mg N m^{-2} h^{-1} and 0.25 mg m^{-2} h^{-1}, respectively. The interquantile range of flux is 0.11 mg N m^{-2} h^{-1} and 0.49 mg N m^{-2} h^{-1}. 1.2% of extremely high fluxes exceeding 2 mg N m^{-2} h^{-1} represents the long tail in the flux distribution, which are, like the negative fluxes, most likely caused by the incomplete sampling of the spectrum of eddies driving the fluxes.

As discussed in Sect. 2.5.6, we then calculate footprint for each flux observation during the RECAP field campaign. Figure 5.1 (a) shows the 90% footprint extent in grey. Fig. 5.1b illustrates that the 90% extent for the calculated footprints ranged from 0.16 to 12 km with a mean extent of 2.8 km. The KL04+2D footprint algorithm has been applied to airborne flux analysis over London and in that study the 90% footprint extents range from 3 km to 12 km from the measurement (Vaughan et al., 2021). While the largest footprint extent is comparable with those from Vaughan et al. (2021), our calculated footprints show a wider scatter towards smaller extent as 62% of the footprint extents are within 3 km. We attribute the small footprints to the stagnant weather conditions. Due to the valley geography, the SJV experiences more stagnant weather condition features with weaker horizontal wind advection compared to London. The mean wind speed was 2.9 m/s for the full observational data set and it reduces to 2.4 m/s for those data points with small footprint extents less than 3 km. The largest footprint extent corresponds to observations at the foothills, due to higher altitude relative to the boundary layer height and stronger horizontal wind advection.

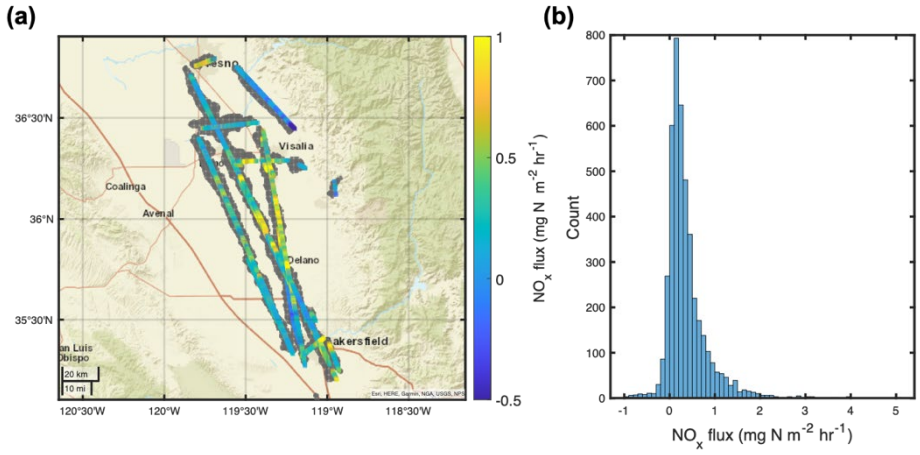

Fig 5.1. a) The map of observed airborne fluxes over 7 flights over the San Joaquin Valley. If the segment overlaps each other, the average flux is calculated. The grey shade represents the coverage of 90% footprint extents for all flux observations. b) The distribution of full data sets of observed airborne NO_x fluxes.

5.2. Component flux disaggregation

The region covered by the footprints is composed of mixed land cover types. We use the 2018 USDA CropScape database (2018) to describe the land cover types. The resolution has been degraded from the native 30m resolution to 500m. For each grid, the land cover type is assigned if a land type makes up more than 50\% of the 500m grid cell. We generalize a "soil" land cover type if the land cover type is identified as either cropland or grassland. The grids classified as "developed" in CropScape are dominated by anthropogenic activities including transportation and fuel combustion. We overlay the national highway network and categorize the grids containing highways as "highway" land types. The remaining grids are classified as "urban" and they correspond to the area with heavy populations in the absence of highways. The distinction between "highway" and "urban" land type is utilized to address on-road mobile sources. 37% of the flux observations include the highway land type in the 90% footprint extent, 23% of the observations include the urban land type and 96% of the observations include cultivated soil land type.

To disentangle the flux emanating from different land cover types, we apply the Disaggregation combining Footprint analysis and Multivariate Regression (DFMR) methodology described in Hutjes et al. (2010). The observed fluxes are treated as the weighted sum of component fluxes from each land cover type:

$$F_{obs} = \sum_{k=1}^{3} w_k F_k \qquad \text{(Eq. 5.1)}$$

where k_1 to k_3 denote highway, urban, and soil land types, w_k is the fractional area within the 90% footprint contour and F_k are the corresponding component fluxes from highway, urban and soil land types, respectively. The multi-linear regression is applied to observations from all flights, consisting of 4391 data points. We perform the Monte Carlo simulation to identify the

uncertainty of the multi-linear regression due to the flux uncertainty. The resulting statistical uncertainty is shown in Fig. 5.2. The highway land type yields the highest flux of 0.96 mg N m^{-2} h^{-1} with the standard deviation of 0.04 mg N m^{-2} h^{-1}. The areas classified as urban land type exhibit a flux of 0.43 (± 0.02) mg N m^{-2} h^{-1}, which is 50% of the highway flux.

Most likely the fluxes from highway are even higher than 0.95 mg N m^{-2} h^{-1}. Note that the land type map is at 500 m spatial scale, the grid classified as highway indeed includes both highway and areas near highway. If, for example, the highway is only 10% of the true area of the land cover pixel, then the fluxes on the highway could be as much as 10 times larger. the cultivated soil land type flux of 0.30 (± 0.01) mg N m^{-2} h^{-1} is large. It is about 1/4 the magnitude of the highway flux and half that of the urban flux. As the total area of soil pixels are much larger than the area of highway or urban pixels, integrated across the SJV soil NO_x emissions are a major factor.

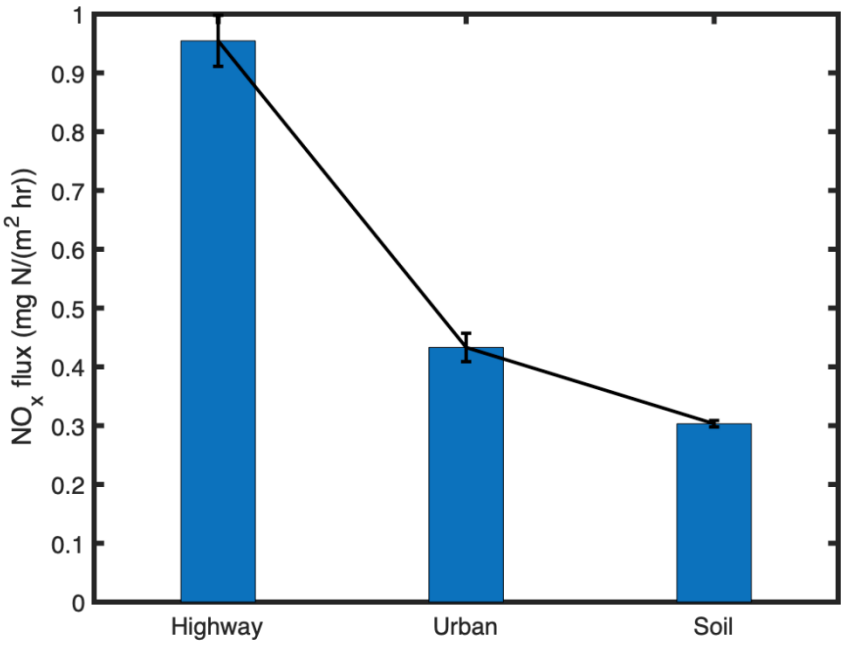

Fig. 5.2. Bootstrapped statistical results of multi-linear regression to resolve component fluxes from highway, urban and soil land types. Each bar represents the average component fluxes from each land type and the black line shows the standard deviation.

5.3. Estimate of NO_x emission map using airborne NO_x fluxes

While these separate component fluxes emphasize the distinction between individual land types at the spatial resolution of the land cover (500m), we utilize the NO_x fluxes to yield an estimate of NO_x emission at 4km. For each 4 km grid, we collect the observed fluxes whose 90% of the footprint overlaps with this grid area and define the weight r_k as the fractional area that the footprint covers. The emission, in a unit of mg N m^{-2} h^{-1}, is calculated by the weighted average of flux (Eqn. 5.2). Only grids measured by at least five flux observations are considered in order

to focus our attention on those pixels for which we have a statistically representative sample of the emissions.

$$Emis_i = \frac{\sum_{k=1}^{n\geq 5} r_k F_k}{\sum_{k=1}^{n\geq 5} r_k} \qquad \text{(Eq. 5.2)}$$

The emission is calculated based on the observations from six flights during weekdays(Fig. 5.3 (a)). The largest reported weekday emission was on June 03 when the median emission was 0.39 mg N m^{-2} h^{-1}. The lowest weekday emission was observed on June 15 with the median emission of 0.14 mg N m^{-2} h^{-1}. The large daily variation observed in estimated emissions during weekdays is partially due to the variation in flight routes and footprint coverage. This is illustrated by the daily estimated emission map shown in Fig. 5.3a.

As the emission inventories make a distinction between weekdays and weekends and do not account for the daily variation on different weekdays, we average over the six-weekday flights to yield the best estimate of emission maps over the San Joaquin Valley derived from flux measurements (Fig. 5.3 (b)). The median estimated weekday NO_x emission over the study domain is 0.26 mg N m^{-2} h^{-1}. with the interquantile range of 0.14 and 0.46 mg N m^{-2} h^{-1}. The observed emission map describes high NO_x emissions in the cities of Bakersfield (119° W, 35.3° N) and Fresno (119.8° W, 36.75° N) and along highway 99.

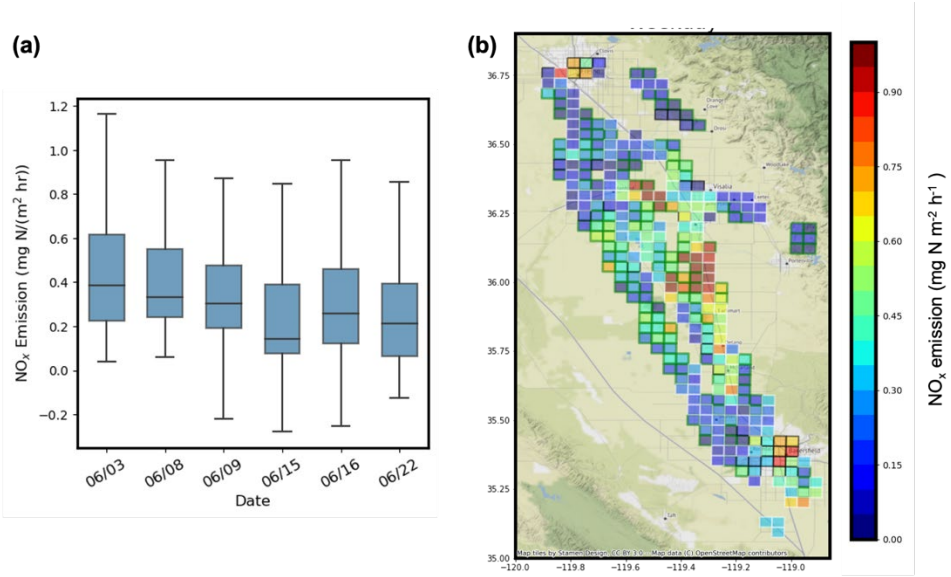

Fig. 5.3: a) The whisker box plot of observed emissions for each flight, aligned in the order of flight days. The box represents the interquartile ranges of observed emissions and the line represents the median emission. The whiskers show the maximum and minimum values. b) The spatial distribution of emission at 4 km over SJV derived from observed fluxes during weekdays. The patch color shows the observed NO_x emission. The edge color denotes the land cover type; the grid cells covering highways in white, those covering urban regions in black, and the rest of the grid cells that are categorized with cultivated soil land cover types in green.

5.4. Evaluation of anthropogenic NO_x emission inventories

For each grid cell categorized as anthropogenic emission dominant, we then match the emission inventories representing the weekday scenario to the same hour and grids of emissions derived from measured fluxes. The corresponding hour of this estimated emission is rounded to the closest hour of the observation times. Figure 5.4 shows the comparison of observed anthropogenic emissions against EMFAC and FIVE emission inventories. Over urban regions, the mean and median observed RECAP NO_x emission are 0.37 mg N m^{-2} h^{-1}, and the interquartile range is 0.14 and 0.58 mg N m^{-2} h^{-1}, Both EMFAC and FIVE yield a good agreement with our measurements; the mean urban NO_x emission are 0.40 and 0.43 mg N m^{-2} h^{-1}. However, the median urban NO_x emission in these inventories is 24% and 22% lower than the observation, respectively. The estimated NO_x emission on grid cells covering highways is more scattered. The median estimated NO_x emission is 0.24 mg N m^{-2} h^{-1}. It is lower than on urban grid cells due to spatial averaging and the fact that most of the highway length is outside the urban regions. The distribution of observed RECAP NO_x emissions from the highway is right-skewed, characterized by an interquartile range of 0.14 and 0.47 mg N m^{-2} h^{-1}. We also note that over Highway 99, the RECAP NO_x emission is a factor of 3 higher than average on grid cells near congestion, reflecting the variation of emission caused by real-time traffic conditions. Both EMFAC and FIVE provide lower NO_x emissions over highway grids, the median NO_x emissions are 37% and 50% of those from the RECAP observations. The highway pixels include a land cover that is mostly non-highway; typically, soil. If soil N emissions are substantially larger than in these inventories, it is possible that the measurements and bottom-up inventories for highways are in better agreement than indicated by the figure.

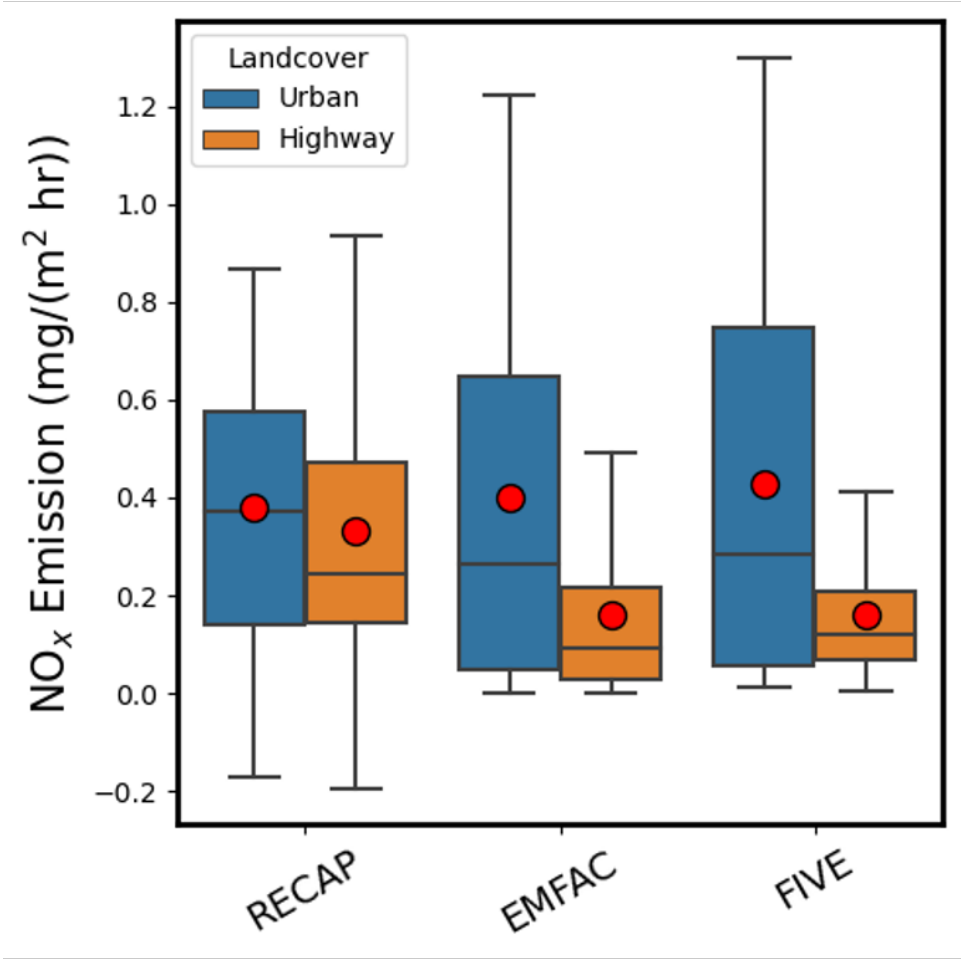

Fig. 5.4. Whisker box plot of observed RECAP anthropogenic NO_x emissions from transportation and fuel combustion as well as those from EMFAC and FIVE emission inventories, separated by highway and urban land cover types. The box is the interquartile range with the line of the median value. The maximum and minimum emissions are shown by whiskers and the mean emissions are shown in red dots.

5.5. Evaluation of soil NO_x scheme

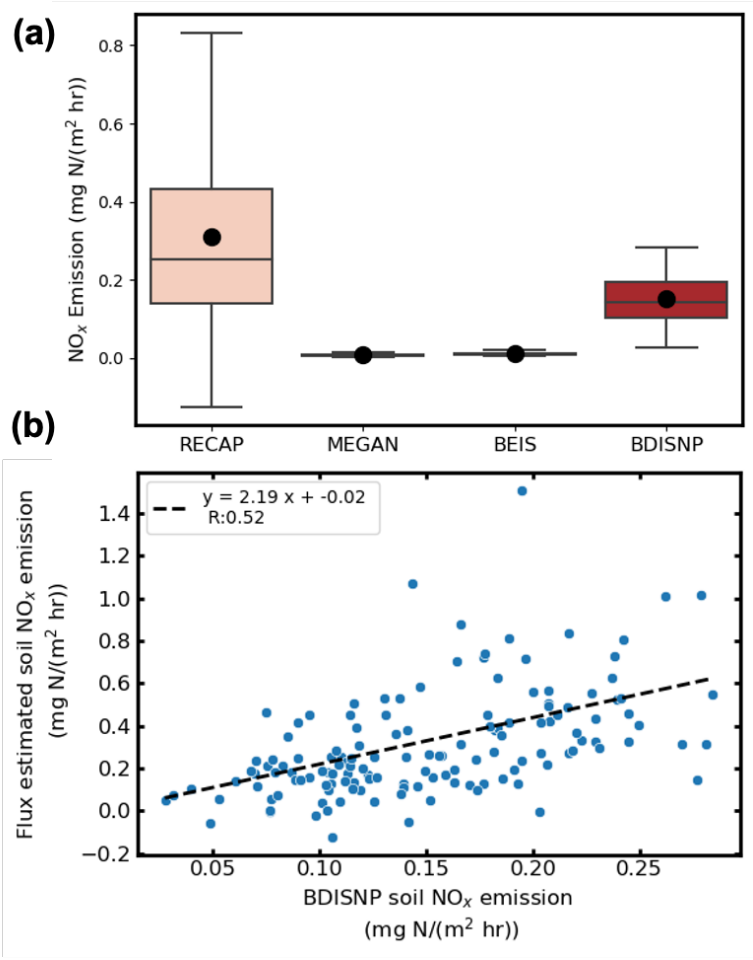

Figure. 5.5. a) Whisker box plot of estimated soil NO_x emissions and parameterized soil NO_x emissions from MEGAN, BEIS and BDISNP schemes. The mean soil NO_x emissions are shown in black dots. b) The scatter plot of soil NO_x emissions calculated from BDISNP scheme and from flux estimates. The dashed black is the least-square linear fit.

Figure. 5.5 (a) illustrates the range of soil N emissions derived from RECAP observations as compared to these three different soil NO_x schemes. The analysis of the observations exhibits a median cultivated soil NO_x emission of 0.26 mg N m^{-2} h^{-1}; the interquartile range of the inferred emission is 0.14 mg N m^{-2} h^{-1} and 0.45 mg N m^{-2} h^{-1}. MEGAN and BEIS both have an order of magnitude lower emissions with median soil NO_x emissions of 0.008, 0.011 mg N m^{-2} h^{-1}, respectively. The BDISNP soil NO_x scheme shows a median soil NO_x emission of 0.14 mg N m^{-2} h^{-1}. Figure. 5.5 (b) exhibits a point-by-point comparison of the observed RECAP and the BDISNP soil NO_x emissions showing that there is a correspondence between the two but the model is 2.2 times lower than the observations. Figure S5.4 (a) and (d) shows the spatial distribution of soil NO_x emissions from observation and BDISNP scheme. Both show higher soil NO_x emissions between 35.75° N and 36.25° N.

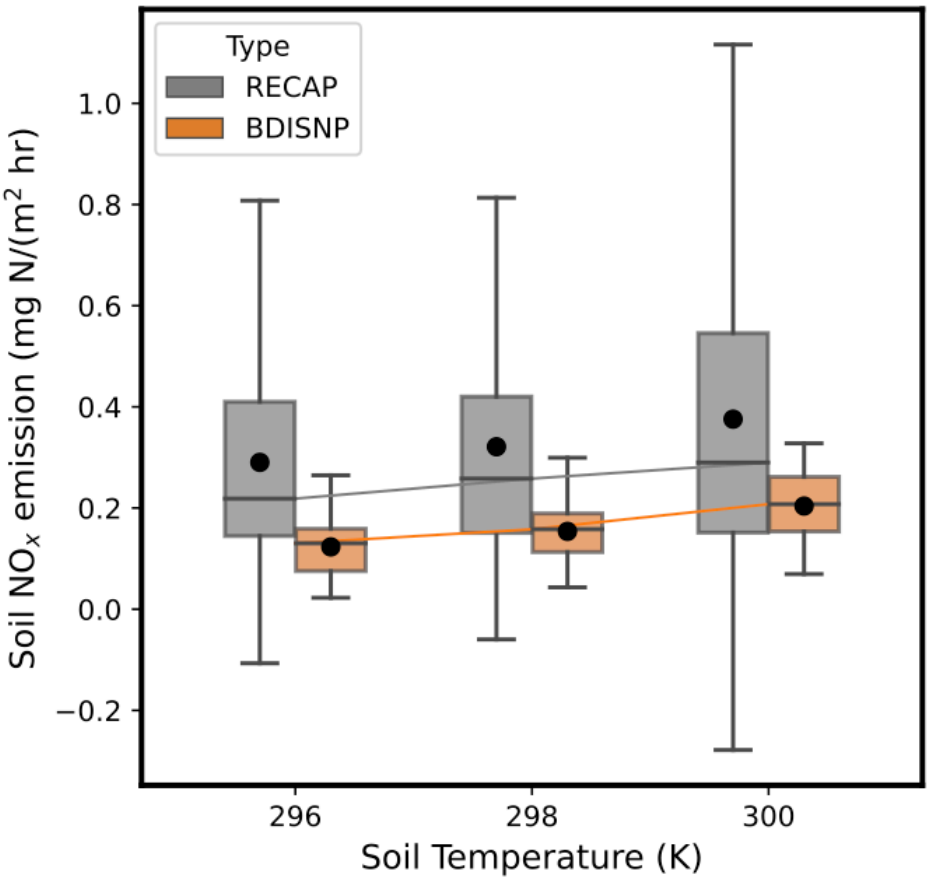

Figure. 5.6. The dependence of soil NO_x emissions on soil temperature from both flux measurements (gray) and BDISNP scheme (orange). Both observed and BDISNP soil NO_x emissions are binned based on mean soil temperature from WRF-Chem. Three soil temperature bins are described with 4k intervals. The whisker box shows the distribution and the black dot shows the mean within each bin, the line connects median soil NO_x emissions across three bins.

A distinct characteristic of soil NO_x emission is its temperature dependence. For instance, Oikawa et al. (2015) identified unusually high soil NO_x emissions in a high-temperature agricultural region based on in-situ observations. The temperature-driven increase in soil NO_x emission raises concerns in the future warmer climate, resulting in a larger contribution to O_3 pollution (Romer et al., 2018). Here we leverage our flux observations to probe this temperature dependence. We collect observed NO_x emissions for each flight and select the subset of NO_x emissions on grids categorized as cultivated soil land type. We also collect corresponding mean soil temperature from WRF-Chem and match them to observed NO_x emissions both in time and space. A range of soil temperature between 295K to 304K is observed. We then bin observed soil NO_x emissions to three soil temperature categories, each of which has 4K intervals. The median soil NO_x emissions increase from 0.22 mg N m^{-2} h^{-1} to 0.29 mg N m^{-2} h^{-1} with the median soil temperature increasing from 296 K to 300 K. As the response to soil temperature is incorporated in the BDISNP scheme, we also bin the BDISNP parameterized soil NO_x emissions into the

same soil temperature categories. Both the RECAP measured flux and the BDISNP modeled soil NO_x emissions exhibit an approximately 33% increase over the range of soil temperature shown.

5.6. Discussion of soil NO_x scheme

Soil NOx emissions in California have been studied in field experiments. Matson et al., 1997 measured soil NO_x emissions from nine dominant crop types in SJV and reported mean fluxes of 0.01-0.09 mg N m^{-2} h^{-1}. They also reported a large variation of measured NO_x flux among crops and among different fields of the same crop; the highest measured NO_x flux is 0.17 mg N m^{-2} h^{-1} due to the fertilizer application and soil moisture characteristics. Horwath et al., 2013 observed an average flux of 0.05-0.28 mg N m^{-2} h^{-1} at mid-days during summertime from five crops in California, and the highest NO_x flux is >4 mg N m^{-2} h^{-1} in systems receiving large N inputs resulting in high concentrations of ammonium. Oikawa et al., 2015 observed soil NO_x emissions in a high-temperature fertilized agricultural region of the Imperial Valley, CA, ranging between -0.02 and 3.2 mg N m^{-2} h^{-1}. They also conducted control experiments to investigate the soil NO_x emission responses to fertilization and irrigation. The highest soil NO_x flux was reported ~ 10 days after the fertilizer at the soil volumetric water content of 30% and the soil temperature of ~ 313K.

The mean soil NO_x flux, 0.32 mg N m^{-2} h^{-1}, derived in our flux measurements is higher than the mean fluxes reported in Matson et al., 1997 and Horwath et al., 2013, however, the range of estimated soil NO_x flux is within those in Horwath et al., 2013 and Oikawa et al., 2015. Fertilizer is likely the primary contributor to the higher mean soil NO_x flux in our study. The RECAP-CA field campaign was conducted in June, right after the month of peak fertilizer use in SJV (Guo et al., 2020). Shown in Oikawa et al., 2015, soil NO_x flux can increase up to 5-fold within 20 days of fertilizer. The higher mean soil NO_x flux is also contributed by higher soil temperature. In our study, the mean soil temperature is 299K with a range between 295K and 304K, whereas the observations in Horwath et al., 2013 and Oikawa et al., 2015 spread over a wider range of soil temperature, 288K-315K. Consistent with our study, the temperature dependence of soil NOX emission is observed in these field experiments. Horwath et al., 2013 reported a 2.5-3.5 fold increase in NOx fluxes with 10-degree increase in soil temperature. Oikawa et al., 2015 showed that the temperature dependence of soil NO_x emission is non-linear; a steeper increase in soil NO_x emission was observed with the soil temperature exceeding 295K.

It is worth noting the limitation of estimated soil NO_x emissions in our study. First of all, we are unable to investigate the dependence of soil NO_x emissions on meteorological drivers other than soil temperature, such as soil moisture, as modeled soil moisture presents very small variation during the field campaign. Second, as our measurements only cover limited cropland areas in SJV over a short time period and it is around the time of fertilizer use, we cannot scale the estimated soil NO_x emission to the whole year or to the total cropland areas in California. Last, in the absence of ozone and PM2.5 observations, we cannot investigate the impact of soil NO_x emission on air quality. However, as the SJV is in the NO_x limited regime (Pusede et al., 2014), we expect a model that captures the soil NO_x more accurately will produce higher ozone. Future work is needed to further advance our understanding of soil NO_x emission and its role in urban and rural air pollution.

6. VOC fluxes in the San Joaquin Valley

*A version of this chapter is under review at Atmospheric Chemistry and Physics under the title "**Volatile organic compound fluxes in the San Joaquin Valley – spatial distribution, source attribution, and inventory comparison**", with the following authors: Eva Y. Pfannerstill, Caleb Arata, Qindan Zhu, Benjamin C. Schulze, Roy Woods, Colin Harkins, Rebecca H. Schwantes, John H. Seinfeld, Anthony Bucholtz, Ronald C. Cohen, Allen H. Goldstein, https://doi.org/10.5194/egusphere-2023-723*

6.1. Overview of the VOC flux observations

VOC flux observations from seven flights on different days were spatially averaged to 1 km with the result shown in Fig. 6.1. As described in chapter 5.1 (Zhu et al., 2023) and shown in Fig. 2.9, the footprints were mostly close to the flight track and had an average extent of 2.6 km. The spatial distributions of the fluxes were clearly source-dependent (Fig. 6.1). Monoterpene emissions were highest (> 0.6 mg m^{-2} h^{-1}) in the areas where citrus orchards, citrus packaging and processing facilities are located, and moderate in the urban areas (mostly in the range of 0.3-0.6 mg m^{-2} h^{-1}), where both trees and anthropogenic sources like fragrance use may contribute to the monoterpene emissions (Peng et al., 2022). Aromatic emissions (example in Fig. 6.1: C3 benzenes, likely mainly trimethylbenzene) were highest (> 0.03 mg m^{-2} h^{-1} and up to 0.3 mg m^{-2} h^{-1} for C3 benzenes) in the urban areas and along the highway I-99. Isoprene emissions were negligible in the croplands, and high (0.6-3.8 mg m^{-2} h^{-1}) in the oak woodlands of the Sierra Nevada foothills (Sequoia National Forest), as previous airborne flux observations in the region have also shown (Misztal et al., 2014; Misztal et al., 2016). The isoprene emissions in the oak woodlands were in the same range as reported by Misztal et al., although visually up to 1/3 of the oaks appeared to be dead (Fig. S6.4), potentially from climate stress (Wang et al., 2022a) and/or Sudden Oak Death (Frankel, 2019). Enhanced isoprene emissions in Bakersfield (up to ~1 mg m^{-2} h^{-1}) may indicate isoprene-emitting urban trees. The negligible isoprene fluxes observed in the croplands confirm that crops are negligible isoprene emitters (Gentner et al., 2014b). The spatial distributions of methanol, ethanol, and cresol emissions were similar to each other (Fig. 6.1). They all resembled the distribution of dairy and cattle farms, which likely are their main sources. Like other oxygenated VOCs (OVOCs), methanol and ethanol were deposited in some parts of the study area, especially in the oak woodlands of the Sequoia National Forest. Maximum deposition fluxes reached -2.1, -7.0, and -0.08 mg m^{-2} h^{-1} for methanol, ethanol, and cresol, respectively.

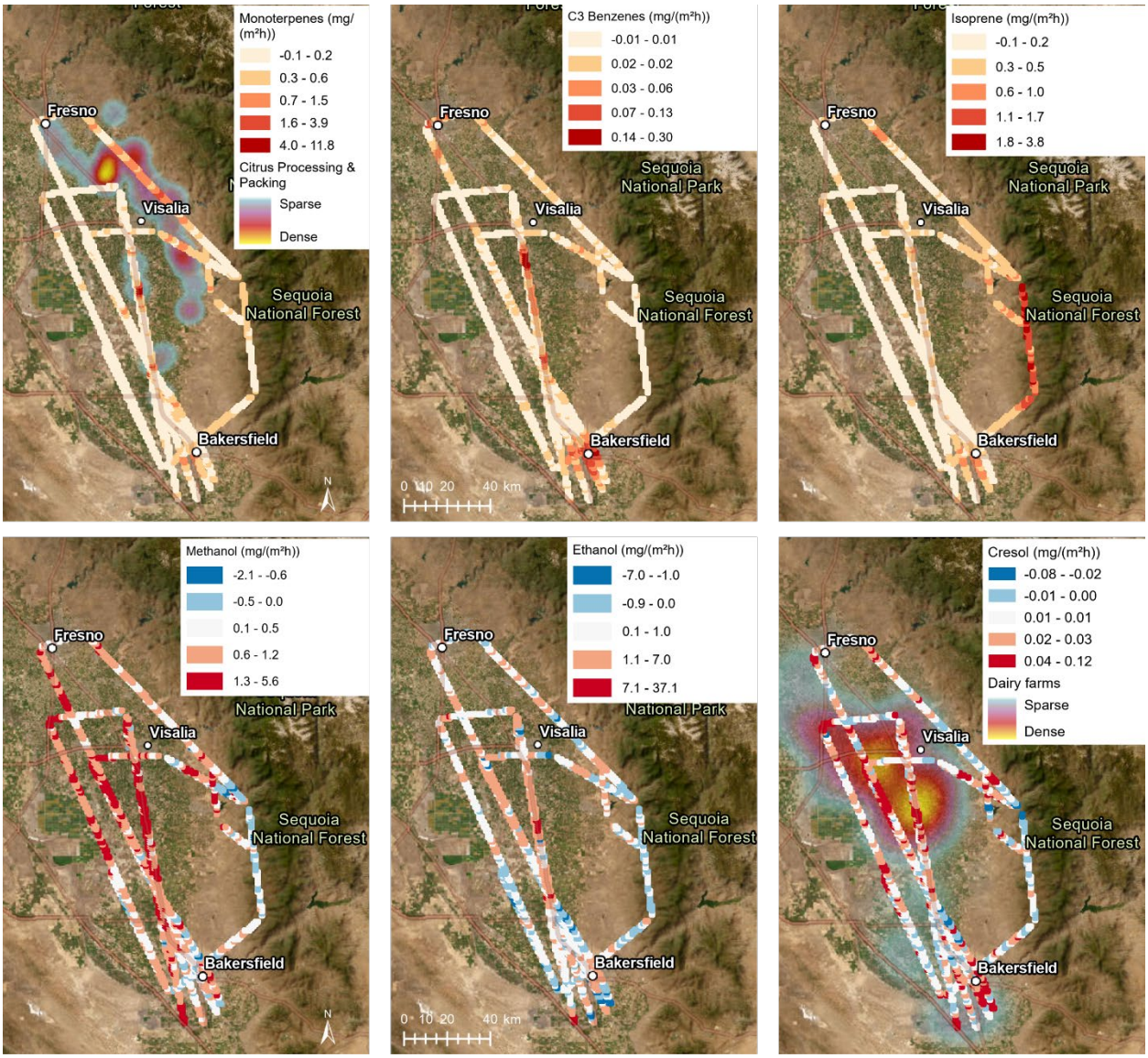

Figure 6.1: Fluxes in the San Joaquin Valley shown for 6 example VOCs. Values shown result from all flights, averaged to a 1 km grid (points enlarged for better visibility). Blue colors indicate deposition fluxes. The monoterpene emission distribution is shown together with a heat map of citrus packing and processing facilities. Methanol, ethanol and cresol emissions distributions are comparable to the distribution of dairy and cattle farms (shown as heat map in last panel). Satellite imagery map from ESRI ArcGIS Pro.

The mass flux measured in the San Joaquin Valley was overwhelmingly dominated by OVOCs (including alcohols, acids, carbonyls, and other OVOCs) with 81% of the total (Fig. 6.2). Alcohol emissions alone contributed almost half, mostly due to methanol (21%) and ethanol (18%). Acids (18%) and carbonyls (9%) also were relevant OVOC emissions. We attribute the dominance of OVOC emissions mainly to the abundance of dairy farms in the study area (see Fig. 6.1 and below), with 200 farms in the flux footprints and ≈1400 in the whole San Joaquin Valley (Hopkins et al., 2019). In an airborne study of VOC mixing ratios in the San Joaquin

Valley, OVOCs even accounted for 91% of the total (Liu et al., 2022). This reflects that a relevant fraction of the reactive VOCs is lost before it reaches the point of observation, which makes it difficult to determine primary emission contributions from concentration-based studies and underscores the value of direct flux measurements.

When the fluxes are scaled by OH reactivity (Fig. 6.2a), which is an indicator for the VOCs' relevance for ozone formation, the OVOCs contribute 42%, but now the terpenoids (isoprene, mono- and sesquiterpenes) contribute equally 42% of the total, mainly because of isoprene (32%) followed by monoterpenes (10%). This fraction is much higher than the concentration-based BVOC contribution to OH reactivity of 6% found in the SJV by Liu et al. (2022) or our own observation of 13% (Fig. 6.2b), since such observations are skewed towards long-lived species, depend on the transport and oxidation time between emission and observation, and do not reflect the primary emission contributions (see above). When considering the relative contributions shown in Fig. 6.2, it is important to note that the contribution of isoprene is almost entirely due to the flight leg performed in the Sierra Nevada foothills. Depending on the wind direction, it is possible that these emissions contribute less to air quality in the center of the San Joaquin Valley than Fig. 6.2 suggests.

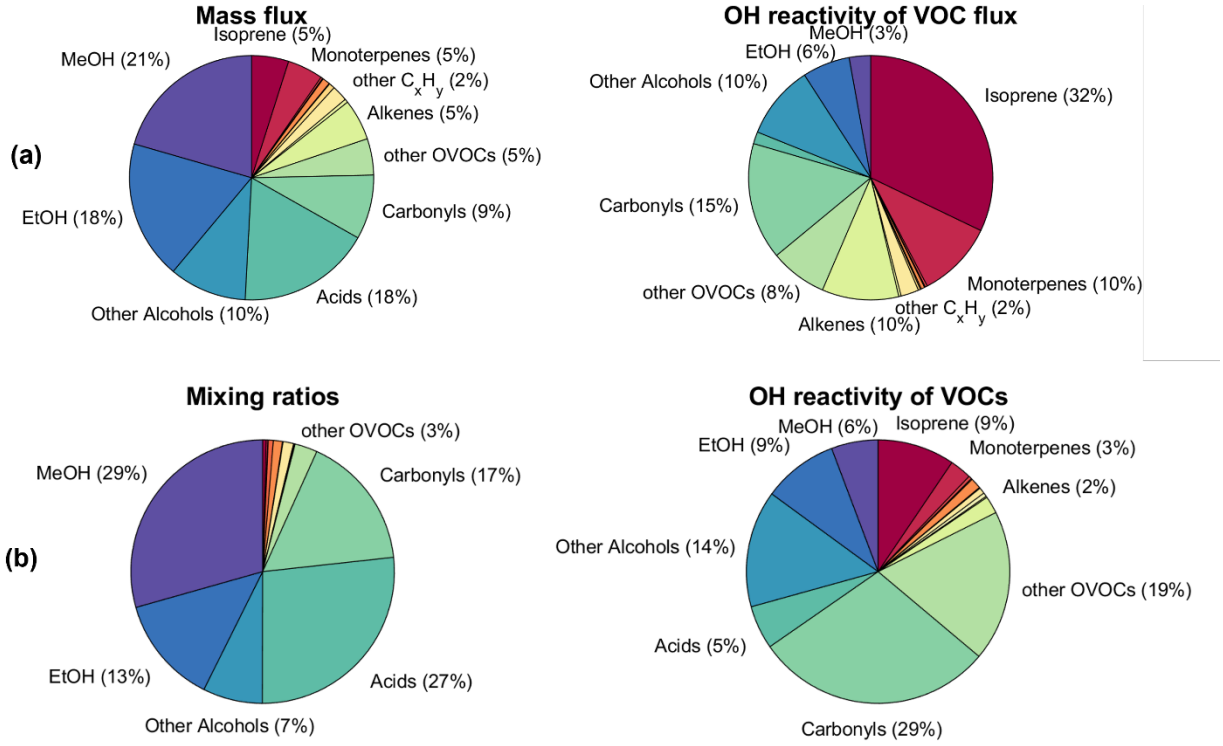

Figure 6.2: Pie charts showing the median composition of (a) flux-based quantities, with VOC group contribution to measured mass flux, and OH reactivity flux; and (b) concentration-based quantities, i.e., the contributions to the VOC mixing ratio and OH reactivity. The VOCs included in each group are listed in Supplementary Table 2. VOC classes contributing less than 2% of the total were not labeled. SQT: Sesquiterpenes.

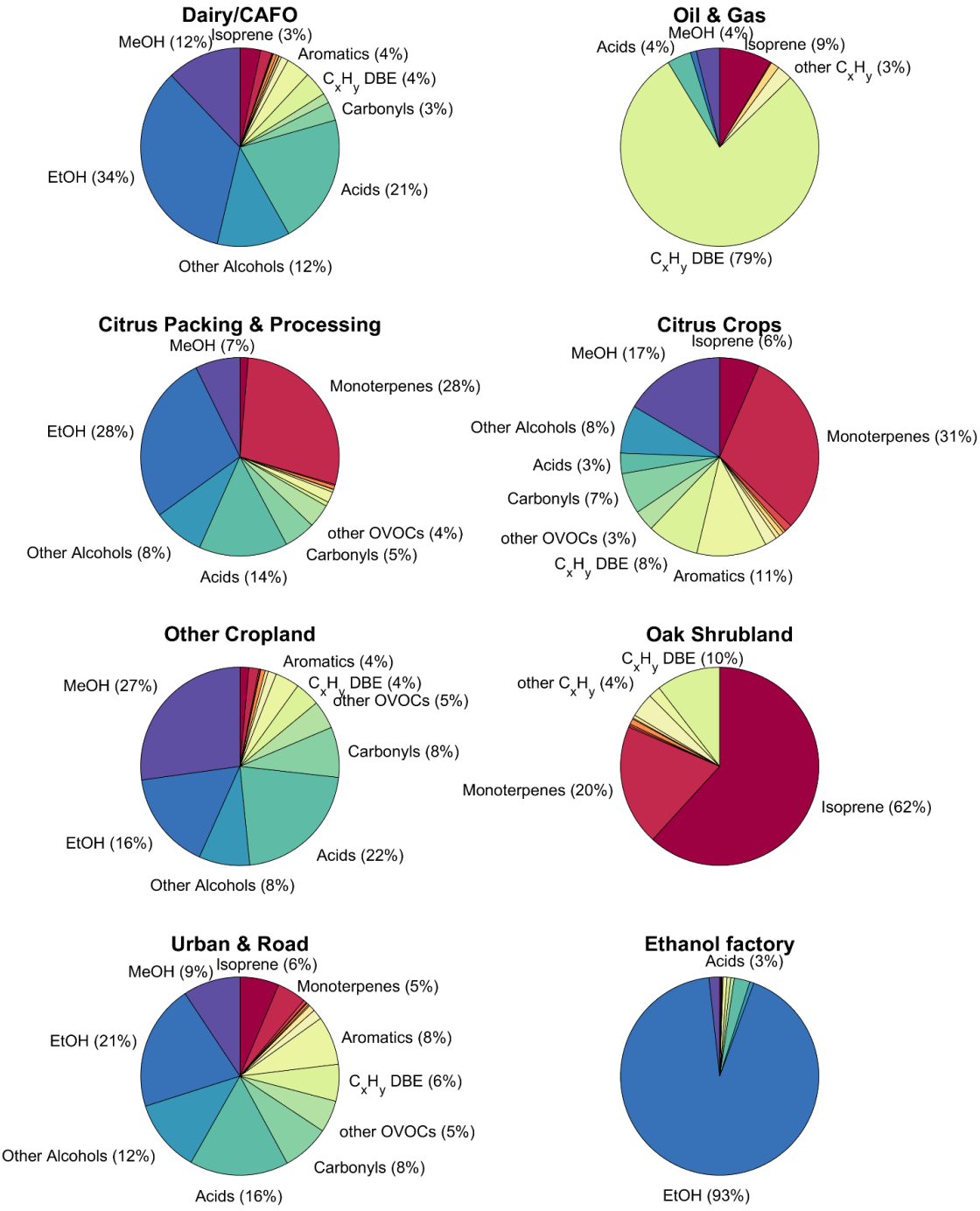

Figure 6.3: Pie charts showing the composition of the measured VOC emissions by mass from the footprint disaggregation result. CxHy DBE: Hydrocarbons with double bond equivalents (i.e., alkenes, cycloalkanes, and potentially unknown aromatics). For oil and gas sources, this category includes $C_{15}H_{24}$ (European Chemical Agency, 2006) and $C_{10}H_{16}$ (Gueneron et al., 2015) isomers that are sorted into the sesquiterpene and monoterpene categories, respectively, for other sources. Since the PTR-MS is blind to most alkanes, the VOC composition, especially of the oil & gas category, can be expected to be incomplete.

6.2. Source attribution

The San Joaquin Valley contains a multitude of potential VOC sources, with crop agriculture, dairy and cattle farms, major highways, oil and gas production, urban areas, and natural sources. In order to attribute VOC emissions to their sources, we used a footprint disaggregation method that applies multivariate linear regression of the measured fluxes using land cover information weighted by footprint density as predictors (Hutjes et al., 2010; Hannun et al., 2020). We compiled the spatial distribution of landcover types and point sources using CropScape for land cover (National Agricultural Statistics Service, 2018), Vista-CA for the locations of dairy and cattle farms, composting sites, digesters, landfills, and wastewater treatment plants (Hopkins et al., 2019), a business registry for ethanol biofuel manufacturing locations (SafeGraph, 2022), a registry of active oil and gas wells (CALGEM, 2022), and locations of citrus processing and packaging facilities collected from Google Maps which we uploaded to ArcGIS online (Pfannerstill, 2022). Using these sources as input, we first identified the crop types and Vista-CA sources that were present in at least 10 % of the footprints or covered at least 10 % of a footprint. The remaining source types were used as input for a multivariate linear regression for footprint disaggregation. The number of crop types was reduced further by performing a test with adding crop types in each regression loop. Only citrus crops (combining oranges and other citrus) and other tree fruit crops (combining cherries, nectarines, peaches, pomegranates, apples, pears) significantly improved the regression. All remaining crop types were summed up under a "cropland" category. The grasslands in the slopes of the Sierra Nevada were removed from the results since they are strongly impacted by the hillslope effect, which causes pollution from the valley to be transported up along the slopes and makes it appear as positive emission fluxes in the measurements, although it is not emitted by the grass itself. Grasslands are expected to be negligible VOC sources (Bamberger et al., 2010; Brunner et al., 2007) except immediately after cutting (Brilli et al., 2012; Davison et al., 2008). Figure 6.4 shows the relative composition of emissions attributed to eight relevant source types found in the San Joaquin Valley.

The footprint disaggregation results (Fig. 6.4) show reasonable emission compositions for the sources presented, although the separation of sources is not always complete. For example, the oil and gas category includes isoprene, since most of the oil and gas wells overflown were located in the Sierra Nevada foothills northeast of Bakersfield, close to the oak woodlands. Vice versa, the oak shrubland category includes hydrocarbons that may be stemming from the oil and gas production (but partly may be PTR-MS fragment ions from terpenoids emitted in the oak region (Kari et al., 2018; Tani, 2013)).

Apart from the overall composition of each source's emissions, we also identified tracer m/z for the sources (Table 6.1). These were m/z whose emissions in the disaggregation result were above 3x the overall median emission of that m/z, above 2x the standard deviation of emissions between the sources, and higher than in the disaggregation result of at least six other source categories.

The composition of the dairy/CAFO (concentrated animal feeding operation) category was dominated by fermentation-related VOCs, with a mass fraction of 12 % methanol (1.1 kg facility^{-1} h^{-1}), 34 % ethanol (3.0 kg facility^{-1} h^{-1}), 12 % other alcohols, and 21 % acids dominated

by acetic acid (1.8 kg facility^{-1} h^{-1}) (Fig. 6.4, Table 6.1). This composition is in agreement with direct measurements of dairy cattle VOC emissions (Gierschner et al., 2019; Oertel et al., 2018; Shaw et al., 2007; Stackhouse et al., 2011; Sun et al., 2008; Yuan et al., 2017), of silage, the fodder used for cows in industrial agriculture (Hafner et al., 2013; Malkina et al., 2011), and of manure (Hales et al., 2015; Sun et al., 2008), which all are rich in alcohols and acids. For example, Yuan et al. (2017) reported a mole fraction of 55-87 % alcohols and 4-32 % carboxylic acids from CAFO emissions. Less important in amount, but relevant "tracers" for dairy and cattle emissions (Table 6.1) in agreement with previous studies (Yuan et al., 2017; Borhan et al., 2012; Gierschner et al., 2019) also included strongly odor-active sulfur-containing VOCs (hydrogen sulfide, methane thiol, dimethyl sulfide or ethane thiol, benzothiazole), and phenolic species (phenol, cresols). The emission strengths can vary strongly between individual dairy farms (Gentner et al., 2014a; Yuan et al., 2017) based on feed composition (Hafner et al., 2013; Hales et al., 2015; Malkina et al., 2011), management practices, or animal age and state (Shaw et al., 2007; Gierschner et al., 2019; Stackhouse et al., 2011). This is confirmed by our observations, where e.g. methanol fluxes from dairy-dominated footprints had a variance of 2.2 mg m^{-2} h^{-1} associated with a median of 1.0 mg m^{-2} h^{-1}.

The oil and gas category mainly consisted of hydrocarbons (82%, Fig. 6.3). Since the PTR-MS method is blind to most alkanes, we can only report hydrocarbons with double bonds or longer-chain (cyclo)alkanes, and aromatics. Interestingly, two m/z that are usually attributed to biogenic emissions were significantly enhanced in the oil and gas emissions: $C_{15}H_{24}H^+$ (m/z 205.19) and $C_{10}H_{16}H^+$ (m/z 137.13; Table 6.1). In the oil and gas category, we attributed them to petroleum emissions and included them into the hydrocarbons with double bond equivalents category, since $C_{15}H_{24}$ can be a component of petroleum kerosine (European Chemical Agency, 2006) and $C_{10}H_{16}H^+$ here is likely a PTR-MS product of decahydronaphthalene (Gueneron et al., 2015). Tracers for this source category included C4-C17 hydrocarbons, covering almost the entire mass and volatility range that can be measured with the method used. Example m/z are $C_{14}H_{24}H^+$ (anthracene or phenantrene), and $C_8H_{15}^+$ and $C_9H_{17}^+$, which both are fragments of substituted cyclohexanes (Gueneron et al., 2015).

The citrus packing and processing category includes juice factories, fragrance extraction, and citrus packaging facilities. Emissions from these consist of 28% (8.75 kg facility^{-1} h^{-1}) monoterpene and 28% ethanol emissions as the largest contributors by mass (Fig. 6.3). While there were 45 citrus processing and packaging facilities identified in the study area, one of them stood out with extremely large emissions: A facility in Tipton, CA. In Fig. 6.1, this is shows up as the largest monoterpene source location, with 11.8 mg m^{-2} h^{-1} emitted on average in Tipton over all flights, while only a small fraction of the measurement footprint is covered by the facility. This facility does not only produce juices, but also extracts monoterpenes for the fragrance industry (Ventura Coastal, 2023). It is possible that ethanol is used as a solvent in the extraction process. Also, fruit juices contain significant amounts of ethanol (Gorgus et al., 2016). Since citrus fruits emit monoterpenes especially when they are being handled, and monoterpene emissions were enhanced around citrus packaging facilities, we conclude that citrus packing also contributes to the agroindustrial source of monoterpenes summed up in this category. Tracers

observed in the citrus processing and packing emissions (Table 6.1) were rich in $C_{10}H_{16}$ monoterpenes, but also included aromatic monoterpenes ($C_{10}H_{15}$), monoterpenoids (e.g. $C_{10}H_{18}O$, $C_9H_{14}O$, $C_9H_{14}O_2$, $C_{10}H_{18}O_2$), sesquiterpenes ($C_{15}H_{24}$), sesquiterpenoids ($C_{15}H_{22}$), diterpenes ($C_{20}H_{32}$), and the plant metabolite dodecane ($C_{12}H_{26}$).

The citrus crop emissions composition with mass fractions of 31% monoterpenes and 17% methanol agrees with a study performed on Californian citrus plants and in a San Joaquin Valley citrus plantation, where methanol and monoterpenes were the largest emissions, approximately equal in molar contributions (Fares et al., 2012; Fares et al., 2011). The aromatic fraction of the citrus crop emissions (11%) included aromatic monoterpenes ($C_{10}H_{15}$) and their fragments. Other aromatic emissions from citrus observed here (toluene, Table 6.1) have previously been reported as well (Misztal et al., 2015).

Emissions of the "other tree fruits" category (not shown in Fig. 6.3 for space reasons, see Fig. 6.4 and Table 6.1) were enhanced in monoterpene emissions compared to the other cropland, and exhibited a plant metabolite as a tracer: methyl salicylate, a methyl ester of a plant hormone that is considered to be a stress indicator (Niinemets and Monson, 2013). The monoterpene enhancement is in accordance with the literature, where fruit trees such as cherry and peach have been shown to be monoterpene emitters (e.g. Gentner et al., 2014b; Rapparini et al., 2001).

The emission mass fractions in the "other cropland" category look similar to the dairy emissions, which is likely because the dairy farms are usually located in the middle of cropland and cannot completely be separated out. However, in the cropland category, the methanol emission fraction is, at 27% of the total, much higher than in the dairy category (Fig. 6.3), which indicates that some actual crop emissions were captured by the disaggregation. Methanol has been reported to be emitted by many crops (König et al., 1995; Das et al., 2003; Gonzaga Gomez et al., 2019; Karl et al., 2001; Warneke, 2002; Gentner et al., 2014b; Loubet et al., 2022), including almonds (Gentner et al., 2014b), one of the major crops in the San Joaquin Valley. There were no specific tracer VOCs identified for the "other cropland" category.

The oak shrublands emissions were dominated by isoprene (62%, 0.73 mg m^{-2} h^{-1}) and monoterpenes (20%, Fig. 6.3). The oaks of the Sierra Nevada foothills are known isoprene emitters (Misztal et al., 2014). Tracer m/z identified for the oak shrubland emissions also included monoterpene alcohols ($C_{10}H_{18}O$) and sesquiterpene alcohols ($C_{15}H_{26}O$).

The emission composition of the urban & road category was similar to the composition of VOC emissions in Los Angeles (Pfannerstill et al., submitted), with a large ethanol contribution (21%, Fig. 6.3) and significant aromatics emissions (8%). Tracer species identified for this source category included chloramine (potentially from cleaning (Mattila et al., 2020)), several aromatics (styrene, C2 benzenes [e.g. xylene], C3 benzenes [e.g. trimethylbenzene]) indicative of traffic emissions, and para-chlorobenzotrifluoride, a coating solvent (Stockwell et al., 2020).

In Pixley, CA, the largest single ethanol source of the study area was observed: An ethanol biofuel factory, which according to the disaggregation emits 106 kg of ethanol per hour. The footprint disaggregation result of almost exclusively ethanol emissions (93%, Fig. 6.3) for this facility is reasonable.

Figure 6.4 shows quantitative results of the footprint disaggregation. Area fluxes per mass (Fig. 6.4a) were highest in the "developed" category (total of ~4.2 mg m^{-2} h^{-1}) which includes roads and urban areas, followed by cropland and citrus crop emissions of each ~3 mg m^{-2} h^{-1}. A notable result was the deposition of OVOCs (alcohols, acids, carbonyls) of in total -0.9 mg m^{-2} h^{-1} in the oak shrublands. With an emission flux of 1.1 mg m^{-2} h^{-1}, the resulting net mass flux of the oak shrublands was close to zero. Deposition of oxygenated VOCs on leaf surfaces and even uptake into leaves (Seco et al., 2007; Canaval et al., 2020) and soils (Rinnan and Albers, 2020) are known phenomena. Point source emissions (Fig. 6.4b) were highest from ethanol biofuel manufacturing (~115 kg h^{-1} $facility^{-1}$), followed by citrus processing/packing (~31 kg h^{-1} $facility^{-1}$), and dairy farms (~9 kg h^{-1} $facility^{-1}$).

Considering the OH reactivity instead of the mass of emissions by area (Fig. 6.4c) changes the order of source importance: The oaks were the largest source of OH reactivity per area (0.21 m s^{-2}) followed by citrus crops (0.17 m s^{-2}) and developed areas (0.16 m s^{-2}). Among the point sources, scaled by OH reactivity, the ethanol manufacturing factory (Fig. 6.4d) was still largest (0.59 m^3 s^{-2} $facility^{-1}$), and was closely followed by citrus processing (0.43 m^3 s^{-2} $facility^{-1}$). Dairy farms emitted an OH reactivity of 0.22 m^3 s^{-2} $facility^{-1}$.

The relevance of each of these sources for air quality in the San Joaquin Valley depends on their abundance in the region. It should be noted that there is only one ethanol biofuel factory in the valley, but ≈ 1400 dairy farms, 47 000 active oil or gas wells, and 45 citrus processing facilities. The areas of citrus crops, other tree fruits, other cropland, oak shrublands, and developed areas in the whole San Joaquin Valley are approximately 970, 1140, 17540, 3880, and 3960 km², respectively. (The oak area depends strongly on where the border of the valley is drawn.) Previous studies have reported that dairy farms are a major contributor to ozone formation in the San Joaquin Valley, only second to road transport (Howard et al., 2008) and predicted that traffic and dairies would contribute equally by 2020 (2012). We refrain from upscaling our results to the whole San Joaquin Valley for two reasons: The source separation resulting from the disaggregation is not perfect, and the contribution of the oak woodlands depends strongly on where along the slope of the Sierra Nevada the border of the valley is drawn. However, it becomes clear from our observations that citrus-related emissions – including crops and citrus processing or packing – are a previously disregarded source of highly reactive VOCs in the San Joaquin Valley with important ozone formation capabilities. Locally, in Pixley, ethanol biofuel manufacturing is a substantial VOC source with potential for secondary air pollution contribution.

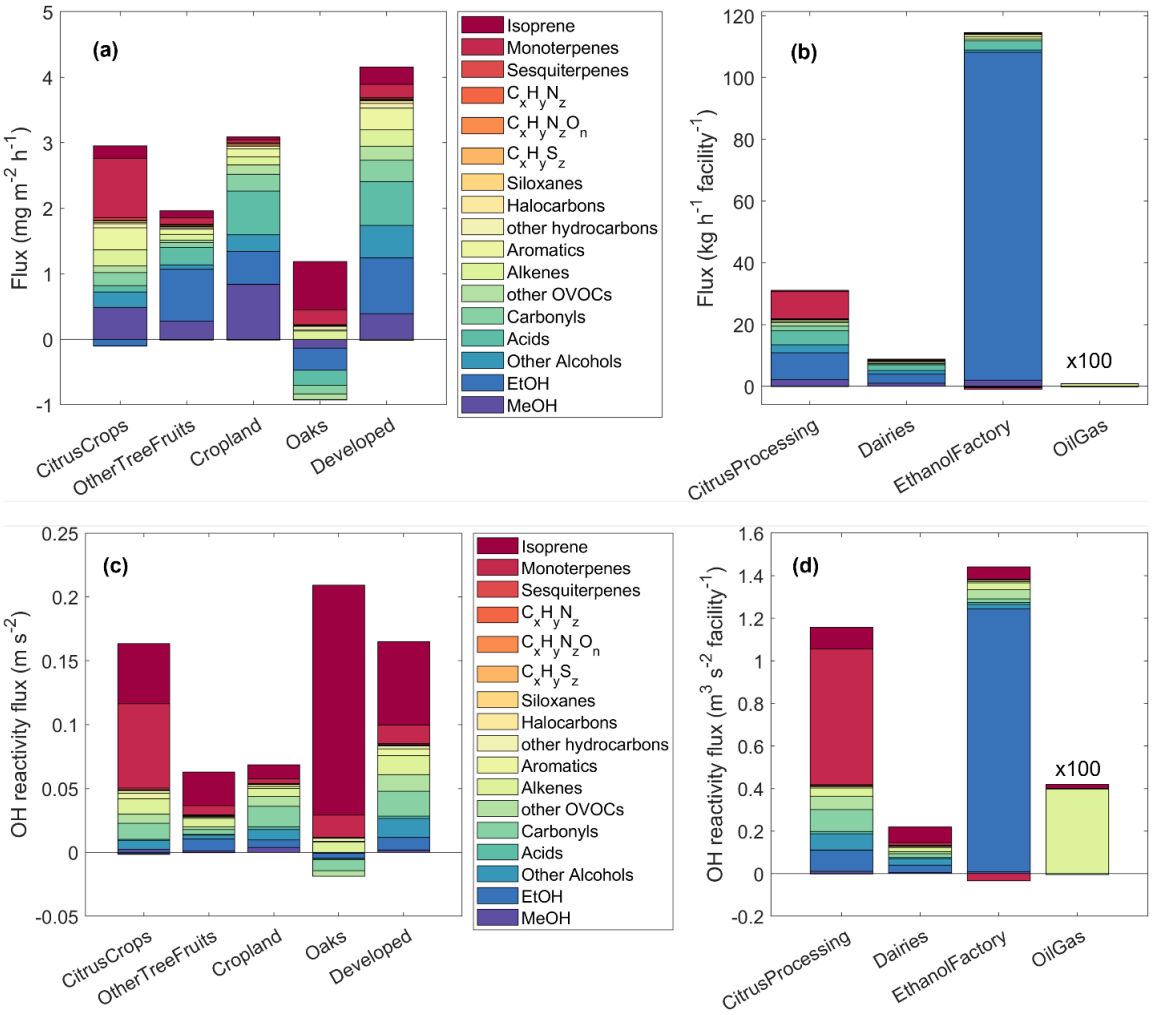

Figure 6.4: Quantitative footprint disaggregation results shown as mass fluxes (a, b) and OH reactivity fluxes (c, d). The fluxes for area sources were given per area (a, c), while point sources (b, d) are reported as fluxes per facility. Negative fluxes signify deposition. Note that the oil and gas well emissions were multiplied by 100 to become visible, and that their expectedly significant alkane emissions were not captured by the measurements. "Developed" includes urban areas and roads.

Table 6.1: *List of tracer m/z specific to the different sources, resulting from the footprint disaggregation. Point source emissions are given in kg facility^{-1} h^{-1}, and area source emissions in mg m^{-2} h^{-1}. The complete disaggregation results with emissions of each VOC attributed to each source are given in Supplementary Table 5. No specific tracers were found for the general cropland emissions.*

Source	Mass (amu, protonated)	Chemical Formula (protonated)	Potential ID	Source emission (kg facility^{-1} h^{-1})
Citrus Processing	93.055	$C_3H_9O_3$+	Glycerol, C_3 acid/ester water cluster	1.29E-01
	103.039	$C_4H_7O_3$+	Isoprene ox	5.81E-02

	103.075	$C_5H_{11}O_2$+	ethyl propionate, etc.	4.54E-02
	105.091	$C_5H_{13}O_2$+	Pentanediol	3.67E-02
	109.101	C_8H_{13}+	sesquiterpene fragment	1.07E-01
	133.050	$C_5H_9O_4$+	$C_5H_8O_4$	1.12E-01
	135.117	$C_{10}H_{15}$+	aromatic monoterpenes	5.04E-02
	137.132	$C_{10}H_{17}$+	monoterpene	8.75E+00
	139.112	$C_9H_{15}O$+	Nopinone etc	1.19E-02
	155.107	$C_9H_{15}O_2$+	norpinonaldehyde etc	1.21E-02
	155.143	$C_{10}H_{19}O$+	citronellal, monoterpene alcohols	1.01E-02
	159.138	$C_9H_{19}O_2$+	C_9 acid/ester	2.22E-02
	163.075	$C_{10}H_{11}O_2$+	Safrole, carbofuran	1.67E-02
	167.034	$C_8H_7O_4$+	Phthalic acid	2.66E-02
	171.065	$C_8H_{11}O_4$+	$C_8H_{10}O_4$	6.53E-03
	171.138	$C_{10}H_{19}O_2$+	Linalool oxide	4.72E-03
	171.211	$C_{12}H_{27}$+	Dodecane (plant metabolite)	4.90E-04
	175.060	$C_7H_{10}O_5H$+	Shikimic acid	6.28E-04
	203.179	$C_{15}H_{23}$+	Aromatic sesquiterpene, sesquiterpenoid	2.52E-03
	205.195	$C_{15}H_{25}$+	Sesquiterpenes	6.40E-02
	273.258	$C_{20}H_{32}H$+	Diterpenes	5.56E-04
Ethanol Biofuel Factory	47.049	C_2H_7O+	ethanol	106.14
Oil & Gas production	57.070	C_4H_9+	butene	9.79E-04
	71.086	C_5H_{11}+	pentene	4.45E-05
	83.086	C_6H_{11}+	cyclohexene, hexadiene	8.72E-04
	85.101	C_6H_{13}+	hexene, hexanol fragm	4.64E-05

	97.101	C_7H_{13}+	heptadiene, heptanal fragm	1.72E-04
	111.117	C_8H_{15}+	dimethylcyclohexane fragment	1.19E-04
	119.086	C_9H_{11}+	propenyl benzene, methyl styrene, indane	4.84E-05
	125.132	C_9H_{17}+	Trimethylcyclohexane fragment	3.81E-05
	129.164	C_9H_{21}+	C_9H_{20} hydrocarbons	1.85E-06
	133.101	$C_{10}H_{13}$+	Phenylbutene and isomers	4.68E-05
	135.117	$C_{10}H_{15}$+	tetramethyl benzene	1.64E-04
	137.132	$C_{10}H_{17}$+	Decahydronaphthalene	2.19E-03
	139.148	$C_{10}H_{19}$+	$C_{10}H_{18}$ hydrocarbons	2.14E-05
	146.976	$C_6Cl_2H_5$+	dichlorobenzene	4.41E-05
	151.148	$C_{11}H_{19}$+	methyl-caren	6.57E-05
	179.179	$C_{13}H_{23}$+	Heptylbenzene and isomers	6.91E-05
	193.195	$C_{14}H_{25}$+	anthracene, phenantrene	2.51E-05
	203.179	$C_{15}H_{23}$+	$C_{15}H_{22}$ petroleum hydrocarbons	7.83E-06
	205.195	$C_{15}H_{25}$+	$C_{15}H_{24}$ petroleum hydrocarbons	1.71E-04
	207.211	$C_{15}H_{27}$+	$C_{15}H_{26}$ petroleum hydrocarbons	5.75E-06
	221.226	$C_{16}H_{29}$+	C_{16} hydrocarbon, 3DBE	3.61E-06
	231.211	$C_{17}H_{27}$+	C_{17} hydrocarbon, 5 DBE	4.34E-06
	235.242	$C_{17}H_{31}$+	C_{17} hydrocarbon, 3 DBE	2.98E-06
Dairy & cattle farms	33.033	CH_5O+	methanol	1.08E+00
	34.995	H_3S+	Hydrogen sulfide	1.58E-03
	43.054	C_3H_7+	propanol fragment	7.06E-01

	44.049	C_2H_6N+	Vinylamine, acetaldimine	3.34E-03
	45.033	C_2H_5O+	acetaldehyde	2.06E-01
	47.049	C_2H_7O+	ethanol	3.03E+00
	49.011	CH_5S+	methane thiol	5.47E-03
	61.028	$C_2H_5O_2+$	acetic acid	1.78E+00
	63.026	C_2H_7S+	ethane thiol, dimethyl sulfide	2.30E-02
	63.944	S_2+	Sulfur	2.66E-03
	73.065	C_4H_9O+	methyl ethyl ketone	4.53E-02
	74.060	C_3H_7NOH+	Dimethylformamide	6.67E-03
	83.013	$C_4H_3O_2+$	fragment	5.68E-03
	87.080	$C_5H_{11}O+$	C_5 carbonyls	5.60E-03
	95.049	C_6H_7O+	phenol	2.83E-02
	103.075	$C_5H_{11}O_2+$	ethyl propionate, etc.	9.36E-03
	107.070	$C_4H_{11}O_3+$	C4-acid water cluster	2.56E-02
	109.065	C_7H_9O+	cresols, anisole	3.93E-02
	121.086	$C_5H_{10}O_2H_2OH+$	Valeric acid watercluster	9.85E-03
	129.127	$C_8H_{17}O+$	C_8 carbonyls	2.51E-03
	136.022	C_7H_6NS+	benzothiazole	6.03E-03
	141.055	$C_7H_9O_3+$	$C_7H_8O_3$	1.19E-02
	145.122	$C_8H_{17}O_2+$	C_8 acid	4.80E-03
	155.107	$C_9H_{15}O_2+$	C_9 acid/ester	3.07E-03
	173.044	$C_7H_9O_5+$	$C_7H_8O_4$	5.56E-03
	223.169	$C_{14}H_{23}O_2+$	$C_{14}H_{22}O_2$	7.25E-04

Source	**Mass (amu, protonated)**	**Chemical Formula (protonated)**	**Potential ID**	**Source emission (mg m^{-2} h^{-1})**
Citrus Crops	93.070	C_7H_9+	fragment of aromatic monoterpenes, toluene	0.076
	137.132	$C_{10}H_{17}+$	monoterpene	0.906

	151.112	$C_{10}H_{15}O+$	monoterpenoids - e.g. carvone, thymol	0.005
	205.195	$C_{15}H_{25}+$	sesquiterpene	0.036
Other Tree Fruits	137.132	$C_{10}H_{17}+$	monoterpene	0.095
	153.055	$C_8H_9O_3+$	Methyl salicylate (plant metabolite)	0.014
Developed (urban & road)	51.995	ClH_3N+	chloramine	0.005
	82.945	$CHCl_2+$	chlorinated fragment	0.007
	97.101	$C_7H_{13}+$	heptadiene, heptanal fragm	0.006
	105.070	C_8H_9+	styrene, cyclooctatetraene	0.028
	107.086	$C_8H_{11}+$	Xylene, C_2 benzenes	0.045
	121.101	$C_9H_{13}+$	trimethyl benzene, C_3 benzenes	0.022
	136.022	C_7H_6NS+	benzothiazole	0.007
	156.951	C_2H_6I+	Iodoethane	0.002
	181.003	$C_7H_4ClF_3H+$	Para-chlorobenzotrifluoride	0.006
Oak shrubland	38.015	C_3H_2+	alkyl fragment	0.010
	69.070	C_5H_9+	Isoprene	0.733
	155.143	$C_{10}H_{19}O+$	citronellal, monoterpene alcohols	0.003
	223.206	$C_{15}H_{27}O+$	Cadinol, farnesol, sesquiterpenoids	0.002

6.3. Inventory comparison

A comparison of observed median fluxes with the California Air Resources Board (CARB) Inventory and the combination of the BEIS (biogenic) and FIVE-VCP (anthropogenic)

Inventory, hereafter “BEIS + FIVE-VCP”, is given in Fig. 6.5. In both inventories, median isoprene emissions were strongly overestimated. In the CARB inventory (Fig. 6.5a), methanol, acetaldehyde and acetone emissions were relatively close to the observations (within a factor of 2). All other CARB VOCs included were underestimated in the medians, notably the aromatics and typical dairy emissions such as ethanol, acids, cresol and phenol.

While most CARB inventory VOC emissions were lower than observations, the BEIS + FIVE-VCP inventory emissions (Fig. 6.5b) scatter more around the 1:1 line with observations. Within a factor of 2 were methanol, ethanol, monoterpenes, long-chain acids, and acetaldehyde; within a factor of 3 toluene and xylene. The inventory underestimated the median emissions of cresol, phenol, benzaldehyde, benzene, and acetic acid, and overestimated acetone and potentially sesquiterpene emissions. The sesquiterpene emission observations are a lower limit because their speciation is unknown, and conservative reaction rates were assumed for the correction of ozone and OH loss between surface and flight altitude.

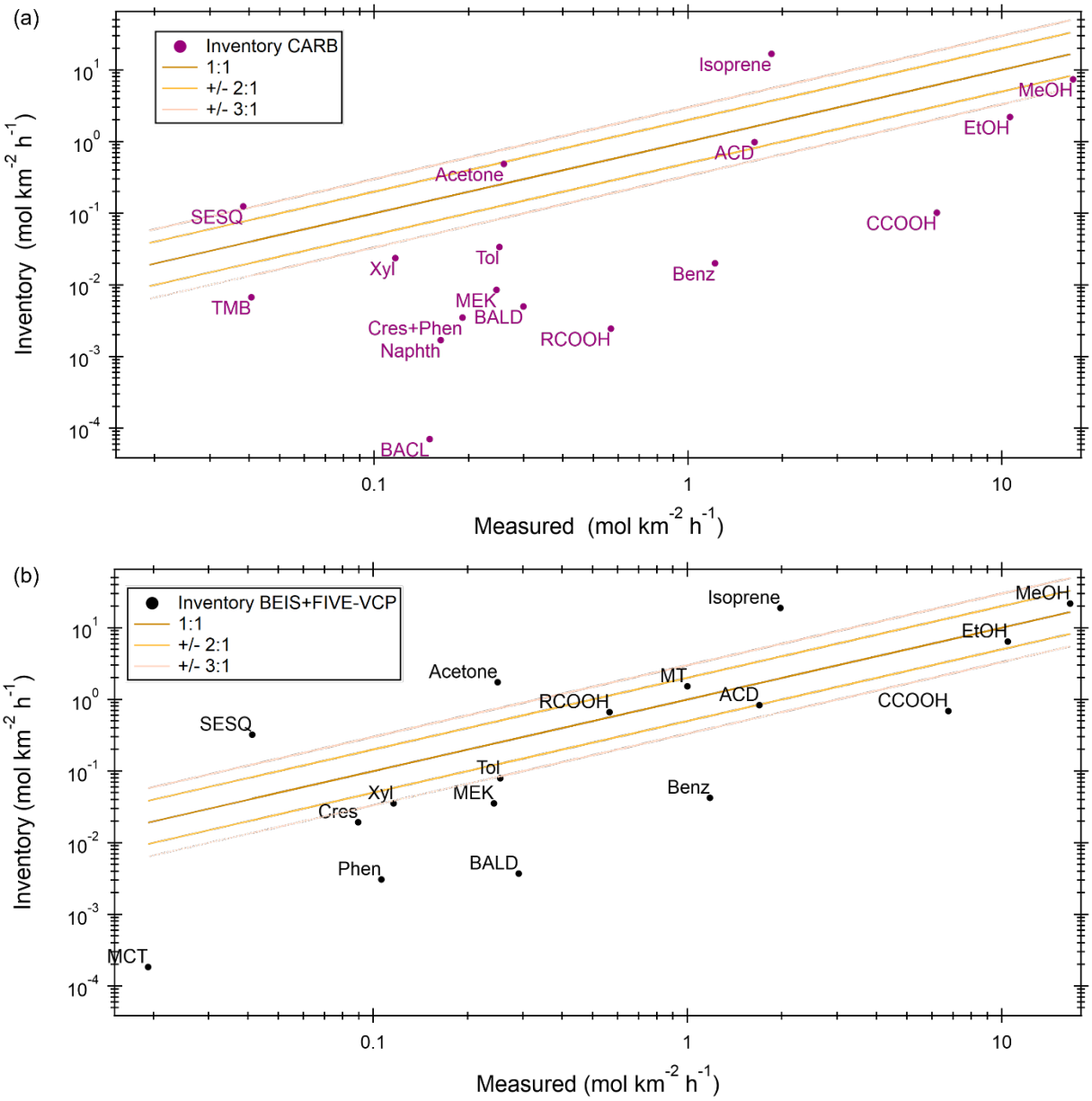

Figure 6.5: Comparison of median values between measured and inventory emissions of individual VOCs for (a) CARB and (b) BEIS+FIVE-VCP. Cres: Cresol, Phen: Phenol, MCT: Methanethiol, SESQ: sesquiterpenes, TMB: trimethylbenzene, BALD: benzaldehyde, BACL: Biacetyl, Naphth: naphathalene, MEK: methyl ethyl ketone, Benz: benzene, Xyl: Xylene, Tol: Toluene, TMB: Trimethylbenzene, MT: monoterpenes, MeOH: methanol, EtOH: ethanol, CCOOH: acetic acid, ACD: acetaldehyde, RCOOH: Higher organic acids, "Measured" values can slightly differ in comparison to each inventory because of a different distribution and coverage of inventory grid cells.

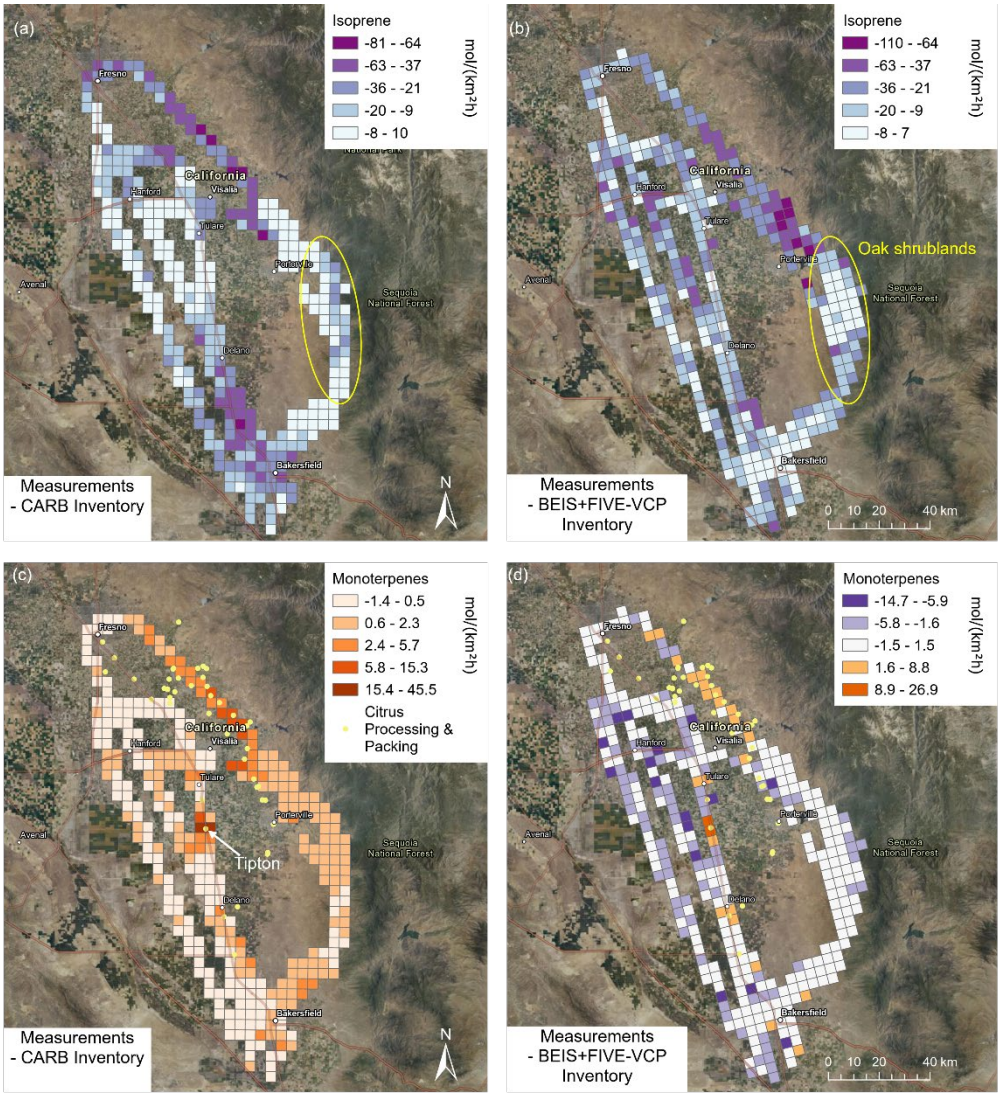

Figure 6.6: Differences between measurement and inventory emissions for terpenoids observed in the San Joaquin Valley. (a), (c): CARB Inventory, (b, d) BEIS+FIVE-VCP inventory. Orange colors designate observations > inventory emissions, purple colors the opposite. Color scales were chosen accordingly (diverging where there are both over- and underestimations in the inventory, orange where there are mainly underestimations, purple where there are mainly overestimations). Important sources are indicated in the maps (oak shrublands for isoprene, citrus processing and packing for monoterpenes, with Tipton highlighted as the place with a juice and fragrance extraction factory). Satellite maps from NAIP Imagery via ESRI ArcGIS Pro.

Since emissions are spatially highly variable within the San Joaquin Valley according to source distribution, spatial comparisons of observed emissions with the inventories provide additional information and can regionally differ from the median comparison shown in Fig. 6.5. Figure 6.6 shows the difference between measurements and inventory for isoprene and monoterpene emissions. Both inventories display similar patterns for isoprene (Fig. 6.6 a, b). Observations and inventories matched well in the oak shrublands, with only a slight tendency to overestimation especially in the BEIS inventory, potentially because of the reduced fraction of live oak trees

(see Fig. S6.6 and Sect. 6.1). Isoprene emissions were strongly overestimated by both inventories northeast of Visalia, in the region with intense citrus production (see Fig. 6.6d). The CARB inventory overestimated isoprene emissions in Bakersfield, while the BEIS + FIVE-VCP inventory matched relatively well there and instead showed a stronger overestimation in the dairy region around Hanford. For monoterpene emissions (Fig. 6.6 c, d), the two inventories were distinctly different. The CARB inventory underestimated monoterpene emissions almost throughout the study region, with especially strong underestimations in the regions with intense citrus processing. The monoterpene emission hotspots of the juice and fragrance factory in Tipton (and to a lesser extent of a juice factory in Delano) have clearly not been included in either of the two inventories. Contrary to the CARB inventory, the BEIS+FIVE-VCP inventory overestimated monoterpene emissions from large swaths of the croplands. However, it underestimated monoterpene emissions in the citrus regions similarly to the CARB inventory. An unrealistic land cover underlying the inventory is likely the reason for mismatches between observed and predicted isoprene and monoterpene emissions (Misztal et al., 2016).

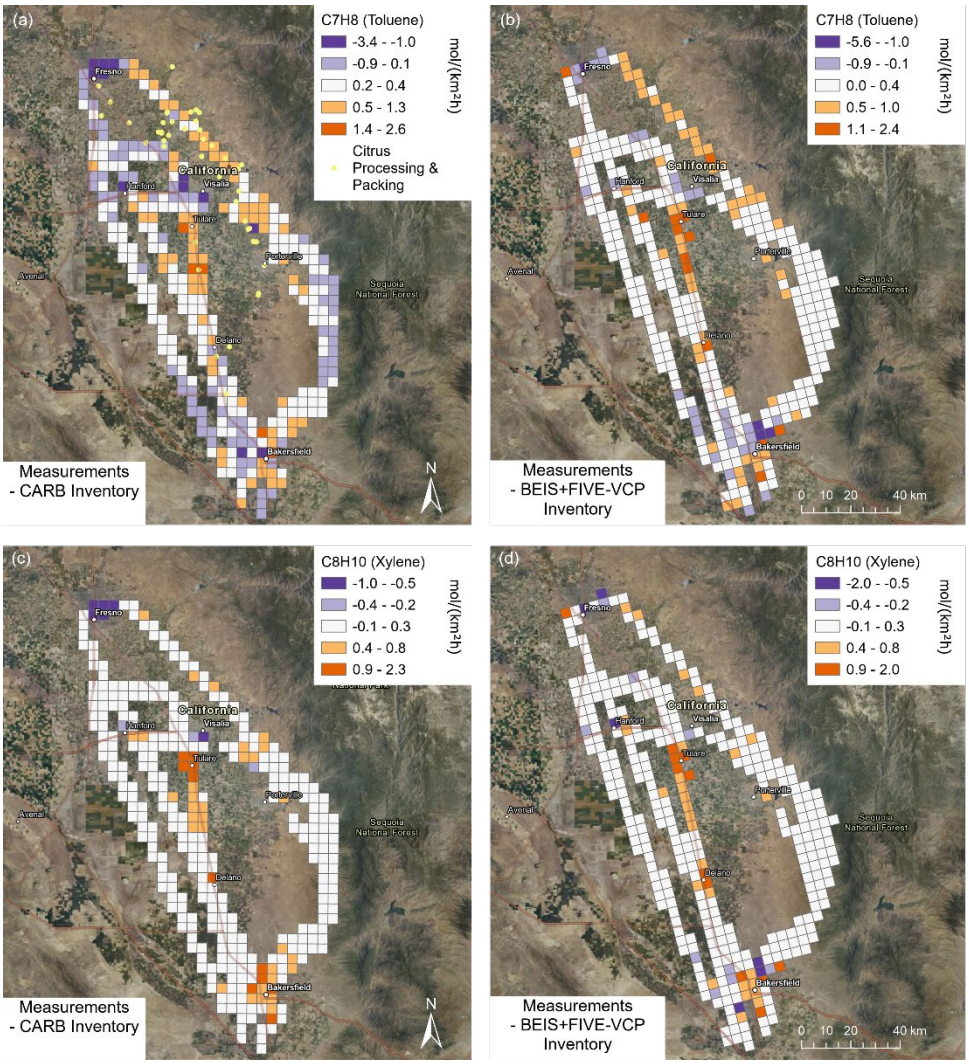

Figure 6.7: Differences between measurement and inventory emissions for two aromatic VOCs observed in the San Joaquin Valley. (a), (c): CARB Inventory, (b), (d) BEIS+FIVE-VCP inventory. Satellite maps from NAIP Imagery via ESRI ArcGIS Pro. Orange colors indicate where the inventory is underestimating emissions, purple colors where it is overestimating. The C_7H_8 signal potentially includes fragments of aromatic monoterpenes besides toluene.

The benzenoid emissions comparison (Fig. 6.7) showed distinct patterns where toluene and xylene were both underestimated by the inventories along the highway and in Bakersfield but overestimated in Fresno and Visalia. Toluene emissions were also underestimated in the citrus production regions northeast of Visalia, potentially because of citrus toluene emissions (Misztal et al., 2015), but this signal may be influenced by fragments of aromatic monoterpenes (Kari et al., 2018).

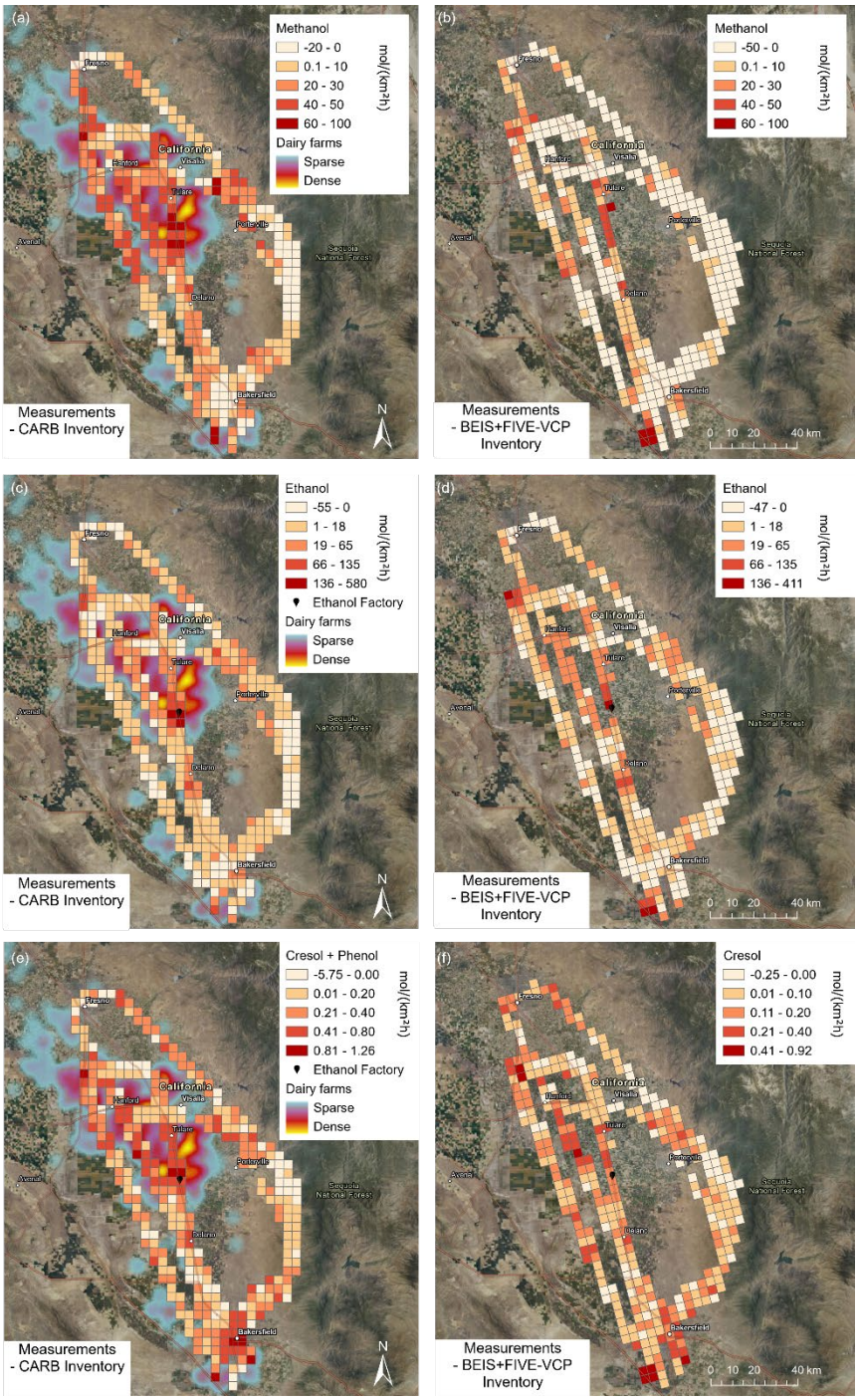

Figure 6.8: Differences between measurement and inventory emissions for some dairy and cattle farm VOC emissions observed in the San Joaquin Valley. (a), (c), (e): CARB Inventory, (b), (d), (f) BEIS+FIVE-VCP inventory. Important sources are indicated by the density of dairy farms and, for ethanol (c, d), by the ethanol biofuel factory location. The CARB inventory includes the sum of cresol and phenol (e), while cresol is shown separately for BEIS+FIVE-VCP. Satellite maps from NAIP Imagery via ESRI ArcGIS Pro.

Typical dairy VOC emissions are shown in comparison with the inventories in Fig. 6.8, and they all tend to be underestimated. Both inventories predicted lower than observed methanol emissions with especially strong differences in the dairy-intense regions (Fig. 6.8 a, b), while matching reasonably well in the urban areas of Bakersfield and Fresno. However, the differences were generally larger in the CARB inventory than in the BEIS+FIVE-VCP inventory. For ethanol emissions (Fig. 6.8 c, d), the ethanol biofuel factory was the location of the largest underestimation in both inventories. Both inventories also clearly underestimated ethanol emissions in the dairy-intense regions and matched better in the urban areas. Cresol and Phenol were underestimated by both inventories in the dairy regions, but also in the urban areas. For other dairy-relevant emissions not shown here (e.g. methanethiol and acetic acid), we find a similar result where the inventories underestimate these emissions. This may explain why a model based on the CARB inventory underestimates observed enhanced ozone near dairy farms (Cai et al., 2016).

This hypothesis is further explored in Fig. 6.9, which shows ratios of OH reactivity emissions (summed from all available VOC emissions, not including deposition fluxes) between inventories and observations. Because of the strong overestimation of highly reactive isoprene emissions almost throughout the study region (see Fig. 6.6), the emission of OH reactive species was overestimated by a factor of at least 2 by the two inventories almost everywhere (Fig. 6.9 a, b). However, the CARB inventory clearly shows some underestimation of OH reactive emissions (by a factor of 2-5) in the dairy-intense region, which also includes the two largest single sources of OH reactivity observed: the ethanol biofuel factory in Pixley and the citrus processing facility in Tipton, closely north of Pixley (see Fig. 6.6). These also were the locations where the BEIS+FIVE-VCP inventory underestimated the flux of OH reactive emissions. Since overestimated isoprene in the inventories was clearly dominant in causing the OH reactivity flux mismatch, we removed it from the sums in Fig. 6.9 c and d. Now it becomes apparent that the CARB inventory underestimated the remaining OH reactive emissions throughout the study region, usually by a factor of 3 and more. For BEIS+FIVE-VCP, the picture is different with underestimated OH reactive emissions of a factor of 3 and more in the oak shrublands (pointing at missing biogenic VOCs), underestimation at dairy farms at the south and northwest ends of the flight tracks and the abovementioned citrus and ethanol processing. In the urban areas, the BEIS+FIVE-VCP inventory had a tendency towards overestimating the OH reactivity source. In conclusion, our observations support the finding by Cai et al. (2016) that the dairy farm regions emit more ozone-relevant VOCs than predicted by the CARB inventory. However, some of this is not solely caused by dairy farms, because intense point sources of monoterpenes and ethanol contribute to the mismatch.

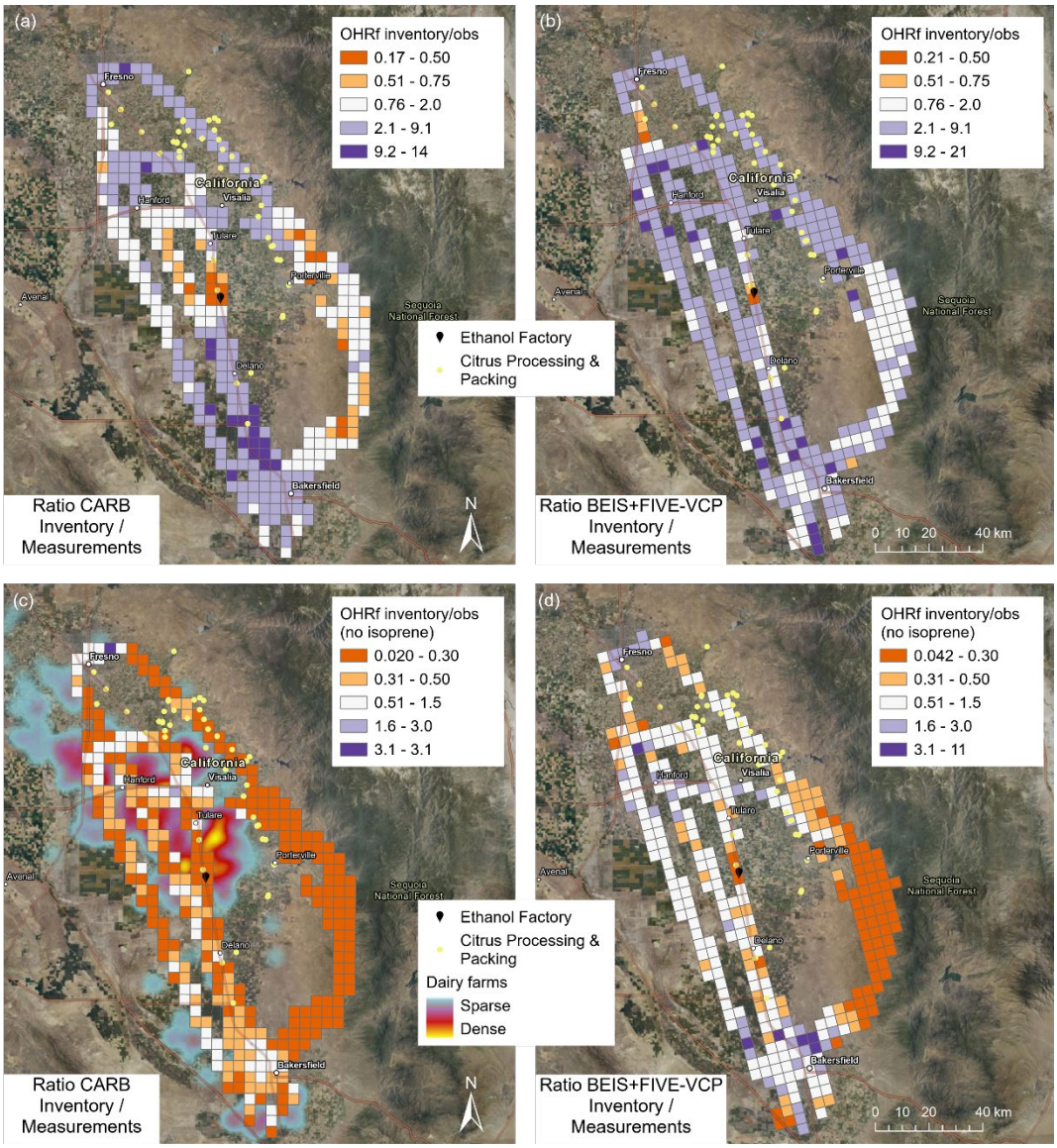

Figure 6.9: Inventory/observations ratio of OH reactivity emissions (OHRf) summed from all VOCs for a) CARB, b) BEIS + FIVE-VCP; and inventory/observations ratio of summed OH reactivity emissions without isoprene for c) CARB and D) BEIS+FIVE-VCP. Satellite maps from NAIP Imagery via ESRI ArcGIS Pro. Orange colors indicate where the inventory is underestimating emissions, purple colors where it is overestimating.

6.4. Temperature relationship of VOC emissions

The flight days were chosen so that measurements were conducted under a wide range of summer temperatures. Average flight temperatures ranged from 23 to 36°C (Table 2.2). In order to investigate measured and inventory fluxes dependence on temperature, the data were sorted into three different temperature bins. All data points in grid cells that were not covered in at least

6 out of 7 flights and in each temperature bin were removed. The non-temperature related point sources of the ethanol production and citrus extraction facilities were also removed from the temperature dependence analysis. Figure 6.10 shows a comparison of the observed fluxes with the two inventories grouped by those temperature bins.

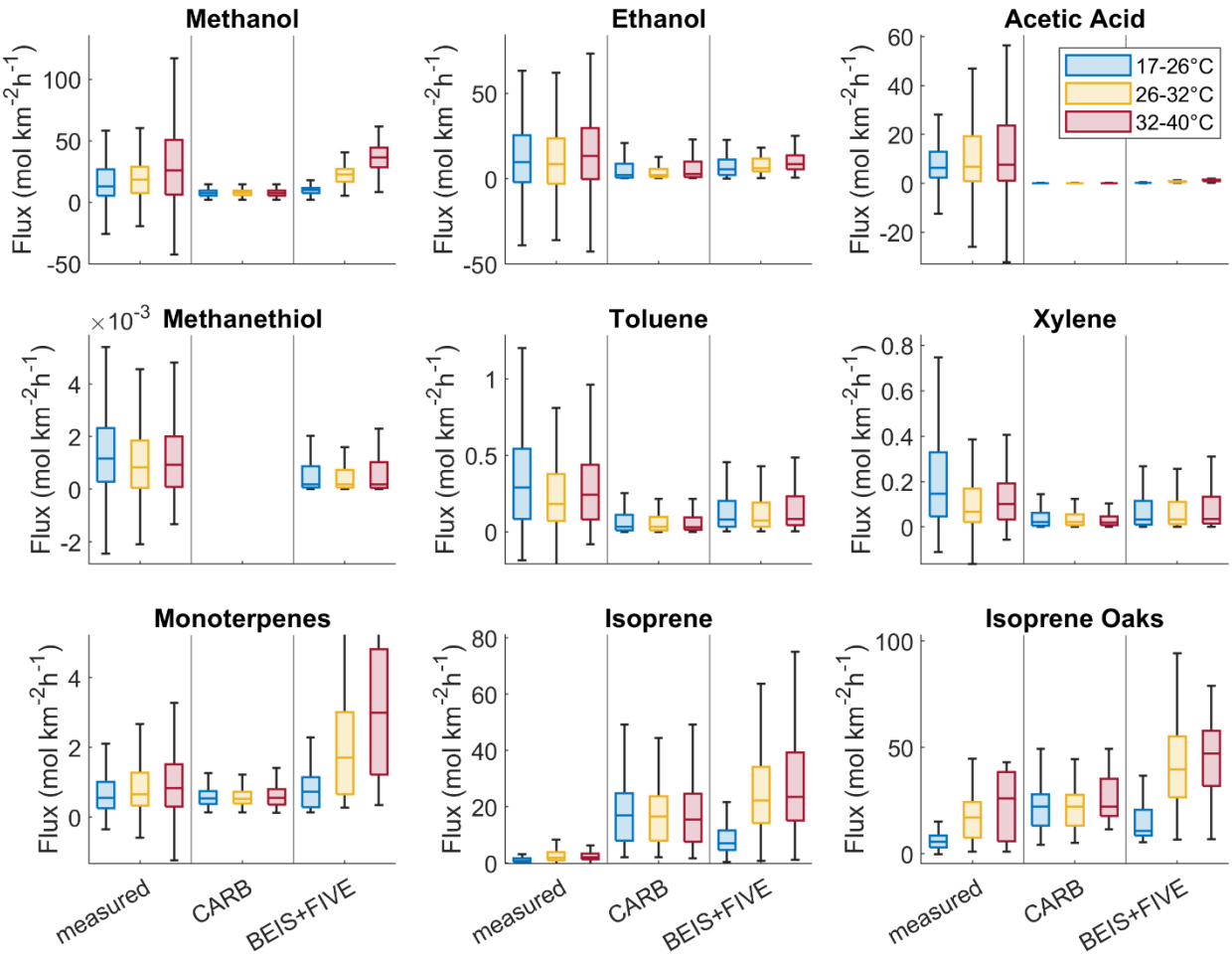

Figure 6.10: Fluxes of example VOCs grouped into three temperature bins, in comparison between measurements, CARB, and BEIS+FIVE-VCP inventories. All data points in grid cells that were not covered in at least 6 out of 7 flights and in each temperature bin were removed. Each of the temperature bins includes 310-366 data points (except the subset of oak shrubland data with 20-60 data points)

Some of the VOC emissions increased with temperature, while others did not appear to have temperature relationships (Fig. 6.10). Methanol, ethanol, and acetic acid showed overall increased emissions with temperature in agreement with a study that reported increasing contributions of small oxygenated VOCs to OH reactivity in the San Joaquin Valley with increasing temperature (Pusede et al., 2015). This may be related to the main source of alcohols and acids here, dairy farms (Table 6.1), and specifically silage (Hafner et al., 2013), whose VOC emissions can volatilize more at higher temperatures as has been shown in experiments (Hafner et al., 2012). However, wind speed (Hafner et al., 2012) and management practices such as

opening silage plastic covers (Heguy et al., 2016) play a role in this volatilization, which may explain why the temperature dependence is not more prominent in our observations. For methanol, the temperature dependence of agricultural crop emissions is a contributing factor, too (Gonzaga Gomez et al., 2019; Loubet et al., 2022). The CARB inventory did not reflect the observed emission increases of these OVOCs with temperature, while the BEIS+FIVE-VCP did better (although underestimating acetic acid emissions significantly).

Methanethiol also is a dairy farm emission, but it does not come from silage (Hafner et al., 2013). Its main source is expected to be the cows themselves (Shaw et al., 2007; Gierschner et al., 2019), and it was not temperature dependent (Fig. 6.10). Toluene and xylene did not display temperature-related patterns, potentially because their main source in the study region was traffic. When toluene emissions are mostly solvent-related, they do increase with temperature (Pfannerstill et al., submitted).

The biogenic VOC emissions – monoterpenes and isoprene – were clearly temperature related, as is known (Guenther et al., 2012). The observed monoterpene emission increase with temperature was not as strong as predicted by the BEIS + FIVE-VCP inventory, but stronger than in the CARB inventory. The isoprene emissions were clearly temperature related in the oak shrublands, where the observed flux range was in between the CARB and BEIS+FIVE-VCP predictions. There were no significant isoprene emissions observed in the rest of the study region, especially not in the croplands (see Fig. 6.1). Therefore, the overall isoprene emission medians were low. The overall isoprene emissions predicted by the inventories, with a clear temperature increase in BEIS+FIVE-VCP, suggest an unrealistic biogenic emission source assumed as a basis of both the inventories.

7. Summary and Conclusions

We performed airborne NO_x and VOC flux measurements during the RECAP-CA field campaign over the San Joaquin Valley and Los Angeles region (South Coast Air Basin) in June 2021. We calculated the fluxes using continuous wavelet transformation.

Nine flights were conducted over the Los Angeles region. VOC flux comparisons with emission inventories revealed an overall underestimation of alcohol, monoterpene and sesquiterpene emissions by both inventories that we validated (CARB and BEIS+FIVE-VCP). This is relevant for air quality predictions, since alcohols and monoterpenes contributed 13% and 19%, respectively, to OH reactivity (relevant for ozone formation), and sesquiterpenes and monoterpenes contributed 23% and 32%, respectively, to SOA formation potential. Our measurements indicate important missing sources of ethanol and terpenoids that should be added to current inventories. Not surprisingly, because of the more extensive history of observations, we found that the observed traffic emissions, for example aromatic compounds, were described more accurately by the inventories than other classes of emissions. Generally, the CARB inventory had a tendency towards underestimation of emissions for a subset of VOCs, while the BEIS+FIVE-VCP inventory underestimated some and overestimated other VOCs. Apart from these general trends, there were regional trends in the mismatches. For many VOCs, the

inventories agreed best with the observations in the inland region of the San Bernardino Valley, while downtown Los Angeles was more prone to emission underestimations, e.g., for ethanol and monoterpenes. Our results point to the necessity to improve inventory emissions of non-traditional VOC sources like VCPs, solvent use and cooking to obtain a comprehensive representation of relevant air pollutant precursors in urban areas. They also show the need for a better representation of urban biogenic VOC emissions in inventories, since these are highly important for ozone and SOA formation and not as accurately represented as transportation emissions.

Our findings on temperature-dependent VOC emissions in Los Angeles (chapter 4.3) underscore that climate change will lead to more high-ozone and high-$PM_{2.5}$ pollution events unless anthropogenic emissions are substantially reduced. On high temperature days, it becomes even more important to reduce anthropogenic VOC emissions, since biogenic emissions cannot be regulated (except by changing the tree and plant species), and since anthropogenic SOA is thought to pose a higher health risk by mass than biogenic SOA (Lovett et al., 2018). A further reduction in NO_x emissions will also help alleviate the ozone burden after transitioning to a NO_x-limited ozone formation regime. Flowering and drought stress periods are expected to increase biogenic terpenoid emissions and may therefore be especially prone to high ozone and particle pollution events.

Even at lower summer temperatures, biogenic terpenoids dominate secondary air pollutant formation in many parts of Los Angeles. The inventory underestimation of mono- and sesquiterpene emissions caused a factor of ~2 underestimation of VOC SOA formation potential and may explain the gap between modeled and measured SOA (Pennington et al., 2021). This combined with the fact that inventories also did not capture the temperature dependence of anthropogenic VOCs has implications for the representation of the emission mixture in general, and for predicting how the composition and pollutant formation changes as temperatures increase.

Seven flights were made over the San Joaquin Valley. When combined with footprint and land cover information, we resolve spatial heterogeneity in landscape flux. The component fluxes are estimated based on the multi-linear regression and exhibit statistically significant differences. The component fluxes are the highest from highways at 0.96 mg N m^{-2} h^{-1}. Cultivated soil land types emit a non-negligible flux of 0.30 mg N m^{-2} h^{-1}. The airborne flux observations are projected to a 4 km grid spacing to yield an estimated emission map over the SJV. We utilize this map to evaluate emission inventories commonly used in photochemical modeling. The anthropogenic emission inventories, EMFAC and FIVE, agree well with estimated mean NO_x emissions over urban regions. However, the widely used, but not biogeochemical process-based, models for soil NO_x emissions underestimate emissions by an order of magnitude or more in the SJV, leading to a poor assessment of the relative roles of mobile and agriculture sources of NO_x in the region. The BDISNP model as adapted by Sha et al., 2021 results in a better comparison with the observations. Even though it is still lower by a factor of 2.2, we show it yields a similar spatial pattern and soil temperature dependence as observed. Variations of this model are embedded in CMAQ (Rasool et al., 2019) and GEOS-CHEM (Wang et al., 2021) and have been

implemented in WRF-CHEM by Sha et al., 2021. Studies, where soil NO_x is potentially important, should make use of these codes, all of which are more consistent with observations at multiple scales.

The VOC flux measurements in the San Joaquin Valley provide unprecedented insight into the sources and sinks of volatile organic compounds in the region, including their spatial distribution and their contribution to OH reactivity. Using a landcover-informed footprint disaggregation method, we were able to attribute and quantify emissions of various sources, and to identify tracer compounds for distinct source types.

We found that developed areas, dairies, and citrus (including citrus crops and packing or processing) are important sources of anthropogenic VOCs and reactivity in the San Joaquin Valley. Citrus processing and biofuel manufacturing sources were apparently not included in the two commonly used inventories that we compared with, CARB and BEIS+FIVE-VCP. Spatially resolved differences in inventory mismatches showed that the inventories generally underestimated dairy, citrus, and highway traffic emissions, but strongly overestimated isoprene emissions in the cropland regions. The oak woodlands in the Sierra Nevada foothills were a significant sink for oxygenated VOCs. Apart from the expected temperature dependence of biogenic VOC emissions, we also observed evidence for temperature-dependent dairy silage VOC emissions.

8. Recommendations for CARB inventory

Based on our flux measurements over the San Joaquin Valley and South Coast Air Basin, and comparison to emission inventories, we recommend the following:

To represent the agricultural NO_x emissions faithfully, BDISNP or another model that is tested against ecosystem scale parameters should be implemented. To improve the representation of the temperature dependence of ozone and SOA in the Los Angeles region, the biogenic emissions and especially monoterpenes should be better described in the inventories. The landcover information responsible for biogenic emissions in both the San Joaquin Valley and Los Angeles region should be improved to better represent the major sources, especially in the croplands, where isoprene was strongly overestimated. The representation of the temperature dependence of solvent emissions should be improved. PCBTF emissions should be added to the CARB inventory, since we observed high fluxes of it in Los Angeles, it is carcinogenic, and may have a high SOA formation potential. Cooking and other not traditionally included emissions should be added to improve the representation of OVOCs, especially ethanol. Dairy emissions in the San Joaquin Valley need to be increased to match the observed fluxes. Several additional sources such as the warehouses in the eastern San Bernardino Valley (causing added truck traffic emissions of NOx and benzene), citrus processing and ethanol manufacturing in the San Joaquin Valley should be included.

We also recommend repeating the flux measurements in both the San Joaquin Valley and South Coast Air Basin to establish seasonal patterns and longer-term trends in VOC and NO_x fluxes. Care should be taken when choosing the season for flux measurements in the South Coast Air Basin to maximize the boundary layer height and reduce the necessity for vertical flux divergence correction.

It would be beneficial to explore establishing long term flux towers in a few key locations (San Bernardino Valley, downtown Los Angeles, close to dairy farms in San Joaquin Valley, Bakersfield, …) to supplement existing concentration measurement networks, and to prepare to make routine and rapid use of the satellite remote sensing observations of NO_x, H_2CO and aerosol that will soon be available from TEMPO. Emission rates and source contributions will likely continue to evolve with climate change, the transformation of the vehicle fleet towards electric power, and other controls that may be implemented on anthropogenic sources. Thus, future measurements of fluxes both at fixed tower sites and through airborne measurements at regular intervals are needed for documenting future VOC and NO_x emissions in these evolving polluted regions.

9. References

Acton, W. J. F., et al.: Surface–atmosphere fluxes of volatile organic compounds in Beijing, Atmos. Chem. Phys., 20, 15101–15125, https://doi.org/10.5194/acp-20-15101-2020, 2020.

Ahmadov, R., McKeen, S. A., Robinson, A. L., Bahreini, R., Middlebrook, A. M., Gouw, J. A. de, Meagher, J., Hsie, E.-Y., Edgerton, E., Shaw, S., and Trainer, M.: A volatility basis set model for summertime secondary organic aerosols over the eastern United States in 2006, J. Geophys. Res., 117, n/a-n/a, https://doi.org/10.1029/2011JD016831, 2012.

Ampollini, L., Katz, E. F., Bourne, S., Tian, Y., Novoselac, A., Goldstein, A. H., Lucic, G., Waring, M. S., and DeCarlo, P. F.: Observations and Contributions of Real-Time Indoor Ammonia Concentrations during HOMEChem, Environmental science & technology, 53, 8591–8598, https://doi.org/10.1021/acs.est.9b02157, 2019.

Arata, C., Zarzana, K. J., Misztal, P. K., Liu, Y., Brown, S. S., Nazaroff, W. W., and Goldstein, A. H.: Measurement of NO 3 and N 2 O 5 in a Residential Kitchen, Environ. Sci. Technol. Lett., 5, 595–599, https://doi.org/10.1021/acs.estlett.8b00415, 2018.

Baghi, R., Helmig, D., Guenther, A., Duhl, T., and Daly, R.: Contribution of flowering trees to urban atmospheric biogenic volatile organic compound emissions, Biogeosciences, 9, 3777–3785, https://doi.org/10.5194/bg-9-3777-2012, 2012.

Bamberger, I., Hortnagl, L., Schnitzhofer, R., Graus, M., Ruuskanen, T. M., Muller, M., Dunkl, J., Wohlfahrt, G., and Hansel, A.: BVOC fluxes above mountain grassland, Biogeosciences Discussions, 7, https://doi.org/10.5194/bg-7-1413-2010, 2010.

Borhan, M. S., Capareda, S., Mukhtar, S., Faulkner, W. B., McGee, R., and Parnell, C. B.: Comparison of seasonal phenol and p-cresol emissions from ground-level area sources in a dairy operation in central Texas, Journal of the Air & Waste Management Association (1995), 62, 381–392, https://doi.org/10.1080/10473289.2011.646050, 2012.

Bouvier-Brown, N. C., Schade, G. W., Misson, L., Lee, A., McKay, M., and Goldstein, A. H.: Contributions of biogenic volatile organic compounds to net ecosystem carbon flux in a ponderosa pine plantation, ATMOSPHERIC ENVIRONMENT, 60, 527–533, https://doi.org/10.1016/j.atmosenv.2012.06.070, 2012.

Brilli, F., Hörtnagl, L., Bamberger, I., Schnitzhofer, R., Ruuskanen, T. M., Hansel, A., Loreto, F., and Wohlfahrt, G.: Qualitative and quantitative characterization of volatile organic compound emissions from cut grass, Environmental science & technology, 46, 3859–3865, https://doi.org/10.1021/es204025y, 2012.

Browne, E. C., Wooldridge, P. J., Min, K.-E., and Cohen, R. C.: On the role of monoterpene chemistry in the remote continental boundary layer, Atmos. Chem. Phys., 14, 1225–1238, https://doi.org/10.5194/acp-14-1225-2014, 2014.

Brunner, A., Ammann, C., Neftel, A., and Spirig, C.: Methanol exchange between grassland and the atmosphere, Biogeosciences, 4, 395–410, https://doi.org/10.5194/bg-4-395-2007, 2007.

Buhr, K., van Ruth, S., and Delahunty, C.: Analysis of volatile flavour compounds by Proton Transfer Reaction-Mass Spectrometry: fragmentation patterns and discrimination between isobaric and isomeric compounds, International Journal of Mass Spectrometry, 221, 1–7, https://doi.org/10.1016/S1387-3806(02)00896-5, available at: https://www.sciencedirect.com/science/article/pii/S1387380602008965, 2002.

Burian, S. J., Brown, M. J., and Velugubantla, S. P.: Roughness Length and Displacement Height Derived from Building Databases, American Meteorological Society, Norfolk, VA, 2002, 2002.

Cai, C., et al.: Simulating reactive nitrogen, carbon monoxide, and ozone in California during ARCTAS-CARB 2008 with high wildfire activity, ATMOSPHERIC ENVIRONMENT, 128, 28–44, https://doi.org/10.1016/J.ATMOSENV.2015.12.031, 2016.

CALGEM: California Active Well Sites, https://arcg.is/1X9KvH, 2022.

California Department of Transportation: State Highways (Segments), https://purl.stanford.edu/xc453kn9742, last access: 27-Mar-23, 2015.

California Department of Water Resources: Water Year 2021: An Extreme Year, 2021.
California Office of Environmental Health Hazard Assessment: p-Chloro-α,α,α-trifluorotoluene (para-Chlorobenzotrifluoride, PCBTF), Government of California, https://www.p65warnings.ca.gov/fact-sheets/p-chloro-aaa-trifluorotoluene-para-chlorobenzotrifluoride-pcbtf, last access: 18-Nov-22, 2022.
Canaval, E., Millet, D. B., Zimmer, I., Nosenko, T., Georgii, E., Partoll, E. M., Fischer, L., Alwe, H. D., Kulmala, M., Karl, T., Schnitzler, J.-P., and Hansel, A.: Rapid conversion of isoprene photooxidation products in terrestrial plants, Commun Earth Environ, 1, 44, https://doi.org/10.1038/s43247-020-00041-2, 2020.
Cappa, C. D. and Wilson, K. R.: Multi-generation gas-phase oxidation, equilibrium partitioning, and the formation and evolution of secondary organic aerosol, Atmos. Chem. Phys., 12, 9505–9528, https://doi.org/10.5194/acp-12-9505-2012, 2012.
Churkina, G., Kuik, F., Bonn, B., Lauer, A., Grote, R., Tomiak, K., and Butler, T. M.: Effect of VOC Emissions from Vegetation on Air Quality in Berlin during a Heatwave, Environmental science & technology, 51, 6120–6130, https://doi.org/10.1021/acs.est.6b06514, 2017.
Coggon, M. M., et al.: Volatile chemical product emissions enhance ozone and modulate urban chemistry, PNAS, 118, https://doi.org/10.1073/pnas.2026653118, 2021.
Coggon, M. M., McDonald, B. C., Vlasenko, A., Veres, P. R., Bernard, F., Koss, A. R., Yuan, B., Gilman, J. B., Peischl, J., Aikin, K. C., DuRant, J., Warneke, C., Li, S.-M., and Gouw, J. A. de: Diurnal Variability and Emission Pattern of Decamethylcyclopentasiloxane (D5) from the Application of Personal Care Products in Two North American Cities, Environmental science & technology, 52, 5610–5618, https://doi.org/10.1021/acs.est.8b00506, 2018.
Da Day, Wooldridge, P. J., Dillon, M. B., Thornton, J. A., and Cohen, R. C.: A thermal dissociation laser-induced fluorescence instrument for in situ detection of NO2, peroxy nitrates, alkyl nitrates, and HNO3, Geophys Res Atmos, 107, ACH-4, 2002.
Das, M., Kang, D., Aneja, V. P., Lonneman, W., Cook, D. R., and Wesely, M. L.: Measurements of hydrocarbon air–surface exchange rates over maize, ATMOSPHERIC ENVIRONMENT, 37, 2269–2277, https://doi.org/10.1016/S1352-2310(03)00076-1, 2003.
Davison, B., Brunner, A., Ammann, C., Spirig, C., Jocher, M., and Neftel, A.: Cut-induced VOC emissions from agricultural grasslands, Plant biology (Stuttgart, Germany), 10, 76–85, https://doi.org/10.1055/s-2007-965043, 2008.
Delaria, E. R. and Cohen, R. C.: A model-based analysis of foliar NO_x deposition, Atmos. Chem. Phys., 20, 2123–2141, https://doi.org/10.5194/acp-20-2123-2020, 2020.
Delaria, E. R., Vieira, M., Cremieux, J., and Cohen, R. C.: Measurements of NO and NO_2 exchange between the atmosphere and Quercus agrifolia, Atmos. Chem. Phys., 18, 14161–14173, https://doi.org/10.5194/acp-18-14161-2018, 2018.
Drozd, G. T., Zhao, Y., Saliba, G., Frodin, B., Maddox, C., Oliver Chang, M.-C., Maldonado, H., Sardar, S., Weber, R. J., Robinson, A. L., and Goldstein, A. H.: Detailed Speciation of Intermediate Volatility and Semivolatile Organic Compound Emissions from Gasoline Vehicles: Effects of Cold-Starts and Implications for Secondary Organic Aerosol Formation, Environmental science & technology, 53, 1706–1714, https://doi.org/10.1021/acs.est.8b05600, 2019.
Drozd, G. T., Zhao, Y., Saliba, G., Frodin, B., Maddox, C., Weber, R. J., Chang, M.-C. O., Maldonado, H., Sardar, S., Robinson, A. L., and Goldstein, A. H.: Time Resolved Measurements of Speciated Tailpipe Emissions from Motor Vehicles: Trends with Emission Control Technology, Cold Start Effects, and Speciation, Environmental science & technology, 50, 13592–13599, https://doi.org/10.1021/acs.est.6b04513, 2016.

Druilhet, A. and Durand, P.: Etude de la couche limite convective sahelienne en presence de brumes seches (Exprience ECLATS), Boundary-Layer Meteorol, 28, 51–77, https://doi.org/10.1007/BF00119456, 1984.

Drysdale, W. S., Vaughan, A. R., Squires, F. A., Cliff, S. J., Metzger, S., Durden, D., Pingintha-Durden, N., Helfter, C., Nemitz, E., Grimmond, C. S. B., and others: Eddy Covariance Measurements Highlight Sources of Nitrogen Oxide Emissions Missing from Inventories for Central London, Atmos. Chem. Phys. Discuss., 1–35, 2022.

European Chemical Agency: Kerosine (petroleum), https://echa.europa.eu/registration-dossier/-/registered-dossier/15567/11/?documentUUID=8bcc8b52-7801-40dd-a85d-c9feb8ed0f9d, last access: 10-Feb-23, 2006.

Fares, S., Park, J.-H., Gentner, D. R., Weber, R., Ormeño, E., Karlik, J., and Goldstein, A. H.: Seasonal cycles of biogenic volatile organic compound fluxes and concentrations in a California citrus orchard, Atmos. Chem. Phys., 12, 9865–9880, https://doi.org/10.5194/acp-12-9865-2012, 2012.

Fares, S., Gentner, D. R., Park, J.-H., Ormeno, E., Karlik, J., and Goldstein, A. H.: Biogenic emissions from Citrus species in California, ATMOSPHERIC ENVIRONMENT, 45, 4557–4568, https://doi.org/10.1016/j.atmosenv.2011.05.066, 2011.

Farmer, D. K., et al.: Overview of HOMEChem: House Observations of Microbial and Environmental Chemistry, Environmental science. Processes & impacts, 21, 1280–1300, https://doi.org/10.1039/c9em00228f, 2019.

Frankel, S. J.: Proceedings of the Seventh Sudden Oak Death Science and Management Symposium: Healthy Plants in a World With Phytophthora, San Francisco, 134 pp., 2019.

Gentner, D. R., et al.: Emissions of organic carbon and methane from petroleum and dairy operations in California's San Joaquin Valley, Atmos. Chem. Phys., 14, 4955–4978, https://doi.org/10.5194/acp-14-4955-2014, 2014a.

Gentner, D. R., Ormeño, E., Fares, S., Ford, T. B., Weber, R., Park, J.-H., Brioude, J., Angevine, W. M., Karlik, J. F., and Goldstein, A. H.: Emissions of terpenoids, benzenoids, and other biogenic gas-phase organic compounds from agricultural crops and their potential implications for air quality, Atmos. Chem. Phys., 14, 5393–5413, https://doi.org/10.5194/acp-14-5393-2014, 2014b.

Gierschner, P., Küntzel, A., Reinhold, P., Köhler, H., Schubert, J. K., and Miekisch, W.: Crowd monitoring in dairy cattle-real-time VOC profiling by direct mass spectrometry, Journal of breath research, 13, 46006, https://doi.org/10.1088/1752-7163/ab269f, 2019.

Gkatzelis, G. I., et al.: Uptake of Water-soluble Gas-phase Oxidation Products Drives Organic Particulate Pollution in Beijing, Geophysical Research Letters, 48, https://doi.org/10.1029/2020GL091351, 2021a.

Gkatzelis, G. I., Coggon, M. M., McDonald, B. C., Peischl, J., Aikin, K. C., Gilman, J. B., Trainer, M., and Warneke, C.: Identifying Volatile Chemical Product Tracer Compounds in U.S. Cities, Environmental science & technology, 55, 188–199, https://doi.org/10.1021/acs.est.0c05467, 2021b.

Goldstein, A. H., Robinson, A. L., Drozd, G. T., Zhao, Y., Saliba, G., Saleh, R., and Presto, A. A.: Investigating Semi-Volatile Organic Compound Emissions from Light-Duty Vehicles: Final Report, 2017.

Goldstein, A. H. and Galbally, I. E.: Known and Unexplored Organic Constituents in the Earth's Atmosphere, Environ. Sci. Technol., 41, 1514–1521, https://doi.org/10.1021/es072476p, 2007.

Goliff, W. S., Stockwell, W. R., and Lawson, C. V.: The regional atmospheric chemistry mechanism, version 2, ATMOSPHERIC ENVIRONMENT, 68, 174–185, https://doi.org/10.1016/j.atmosenv.2012.11.038, available at: https://www.sciencedirect.com/science/article/pii/S1352231012011065, 2013.

Gonzaga Gomez, L., et al.: Comparative study of biogenic volatile organic compounds fluxes by wheat, maize and rapeseed with dynamic chambers over a short period in northern France, ATMOSPHERIC ENVIRONMENT, 214, 116855, https://doi.org/10.1016/j.atmosenv.2019.116855, 2019.
Gorgus, E., Hittinger, M., and Schrenk, D.: Estimates of Ethanol Exposure in Children from Food not Labeled as Alcohol-Containing, Journal of analytical toxicology, 40, 537–542, https://doi.org/10.1093/jat/bkw046, 2016.
Gouw, J. A. de, Gilman, J. B., Kim, S.-W., Lerner, B. M., Isaacman-VanWertz, G., McDonald, B. C., Warneke, C., Kuster, W. C., Lefer, B. L., Griffith, S. M., Dusanter, S., Stevens, P. S., and Stutz, J.: Chemistry of Volatile Organic Compounds in the Los Angeles basin: Nighttime Removal of Alkenes and Determination of Emission Ratios, Journal of Geophysical Research. Atmospheres, 122, 11,843-11,861, https://doi.org/10.1002/2017JD027459, 2017.
Gouw, J. A. de, Gilman, J. B., Borbon, A., Warneke, C., Kuster, W. C., Goldan, P. D., Holloway, J. S., Peischl, J., Ryerson, T. B., Parrish, D. D., Gentner, D. R., Goldstein, A. H., and Harley, R. A.: Increasing atmospheric burden of ethanol in the United States, Geophys. Res. Lett., 39, https://doi.org/10.1029/2012GL052109, 2012.
Griffith, S. M., et al.: Measurements of hydroxyl and hydroperoxy radicals during CalNex-LA: Model comparisons and radical budgets, Geophys Res Atmos, 121, 4211–4232, https://doi.org/10.1002/2015JD024358, 2016.
Gu, S., Guenther, A., and Faiola, C.: Effects of Anthropogenic and Biogenic Volatile Organic Compounds on Los Angeles Air Quality, Environmental science & technology, https://doi.org/10.1021/acs.est.1c01481, 2021.
Gueneron, M., Erickson, M. H., VanderSchelden, G. S., and Jobson, B. T.: PTR-MS fragmentation patterns of gasoline hydrocarbons, International Journal of Mass Spectrometry, 379, 97–109, https://doi.org/10.1016/j.ijms.2015.01.001, 2015.
Guenther, A. B., Jiang, X., Heald, C. L., Sakulyanontvittaya, T., Duhl, T., Emmons, L. K., and Wang, X.: The Model of Emissions of Gases and Aerosols from Nature version 2.1 (MEGAN2.1): An extended and updated framework for modeling biogenic emissions, Geosci. Model Dev., 5, 1471–1492, https://doi.org/10.5194/gmd-5-1471-2012, 2012.
Guimarães, E., Di Stasi, L. C., and Maimoni-Rodella, R. d. C. S.: Pollination biology of Jacaranda oxyphylla with an emphasis on staminode function, Annals of botany, 102, 699–711, https://doi.org/10.1093/aob/mcn152, 2008.
Hafner, S. D., Howard, C., Muck, R. E., Franco, R. B., Montes, F., Green, P. G., Mitloehner, F., Trabue, S. L., and Rotz, C. A.: Emission of volatile organic compounds from silage: Compounds, sources, and implications, ATMOSPHERIC ENVIRONMENT, 77, 827–839, https://doi.org/10.1016/J.ATMOSENV.2013.04.076, 2013.
Hafner, S. D., Montes, F., and Rotz, C. A.: A mass transfer model for VOC emission from silage, ATMOSPHERIC ENVIRONMENT, 54, 134–140, https://doi.org/10.1016/j.atmosenv.2012.03.005, 2012.
Hales, K., Parker, D. B., and Cole, N.: Volatile organic compound flux from manure of cattle fed diets differing in grain processing method and co-product inclusion, ATMOSPHERIC ENVIRONMENT, 100, 20–24, https://doi.org/10.1016/j.atmosenv.2014.10.037, 2015.
Hannun, R. A., et al.: Spatial heterogeneity in CO 2 CH 4 and energy fluxes: insights from airborne eddy covariance measurements over the Mid-Atlantic region, Environ. Res. Lett., 15, 35008, https://doi.org/10.1088/1748-9326/ab7391, 2020.
Hansen, R. F., et al.: Measurements of Total OH Reactivity During CalNex-LA, Journal of Geophysical Research. Atmospheres, 126, https://doi.org/10.1029/2020JD032988, 2021.

Harkins, C., McDonald, B. C., Henze, D. K., and Wiedinmyer, C.: A fuel-based method for updating mobile source emissions during the COVID-19 pandemic, Environ. Res. Lett., 16, 65018, 2021.
Harley, R. A., Marr, L. C., Lehner, J. K., and Giddings, S. N.: Changes in Motor Vehicle Emissions on Diurnal to Decadal Time Scales and Effects on Atmospheric Composition, Environ. Sci. Technol., 39, 5356–5362, https://doi.org/10.1021/es048172, available at: https://doi.org/10.1021/es048172+, 2005.
Hayes, P. L., et al.: Modeling the formation and aging of secondary organic aerosols in Los Angeles during CalNex 2010, Atmos. Chem. Phys., 15, 5773–5801, https://doi.org/10.5194/acp-15-5773-2015, 2015.
Hayes, P. L., et al.: Organic aerosol composition and sources in Pasadena, California, during the 2010 CalNex campaign, Geophys Res Atmos, 118, 9233–9257, https://doi.org/10.1002/jgrd.50530, 2013a.
Hayes, P. L., et al.: Organic aerosol composition and sources in Pasadena, California, during the 2010 CalNex campaign, Geophys Res Atmos, 118, 9233–9257, https://doi.org/10.1002/jgrd.50530, available at: https://agupubs.onlinelibrary.wiley.com/doi/full/10.1002/jgrd.50530, 2013b.
Hegg, D. A., Covert, D. S., Jonsson, H., and Covert, P. A.: Determination of the Transmission Efficiency of an Aircraft Aerosol Inlet, Aerosol Science and Technology, 39, 966–971, https://doi.org/10.1080/02786820500377814, 2005.
Heguy, J. M., Meyer, D., and Silva-Del-Río, N.: A survey of silage management practices on California dairies, Journal of dairy science, 99, 1649–1654, https://doi.org/10.3168/jds.2015-10058, 2016.
Holmes, N. S.: A review of particle formation events and growth in the atmosphere in the various environments and discussion of mechanistic implications, ATMOSPHERIC ENVIRONMENT, 41, 2183–2201, https://doi.org/10.1016/j.atmosenv.2006.10.058, 2007.
Holopainen, J. K., Virjamo, V., Ghimire, R. P., Blande, J. D., Julkunen-Tiitto, R., and Kivimäenpää, M.: Climate Change Effects on Secondary Compounds of Forest Trees in the Northern Hemisphere, Frontiers in plant science, 9, 1445, https://doi.org/10.3389/fpls.2018.01445, 2018.
Holzinger, R., Acton, W. J. F., Bloss, W. J., Breitenlechner, M., Crilley, L. R., Dusanter, S., Gonin, M., Gros, V., Keutsch, F. N., Kiendler-Scharr, A., Kramer, L. J., Krechmer, J. E., Languille, B., Locoge, N., Lopez-Hilfiker, F., Materić, D., Moreno, S., Nemitz, E., Quéléver, L. L. J., Sarda Esteve, R., Sauvage, S., Schallhart, S., Sommariva, R., Tillmann, R., Wedel, S., Worton, D. R., Xu, K., and Zaytsev, A.: Validity and limitations of simple reaction kinetics to calculate concentrations of organic compounds from ion counts in PTR-MS, Atmos. Meas. Tech., 12, 6193–6208, https://doi.org/10.5194/amt-12-6193-2019, 2019.
Hopkins, F. M., Rafiq, T., and Duren, R. M.: Sources of Methane Emissions (Vista-CA), State of California, USA, doi.org/ 10.3334/ORNLDAAC/1726, 2019.
Horton, D. E., Skinner, C. B., Singh, D., and Diffenbaugh, N. S.: Occurrence and persistence of future atmospheric stagnation events, Nature climate change, 4, 698–703, https://doi.org/10.1038/nclimate2272, 2014.
Howard, C. J., Yang, W., Green, P. G., Mitloehner, F., Malkina, I. L., Flocchini, R. G., and Kleeman, M. J.: Direct measurements of the ozone formation potential from dairy cattle emissions using a transportable smog chamber, ATMOSPHERIC ENVIRONMENT, 42, 5267–5277, https://doi.org/10.1016/j.atmosenv.2008.02.064, 2008.
Hu, J., Howard, C. J., Mitloehner, F., Green, P. G., and Kleeman, M. J.: Mobile source and livestock feed contributions to regional ozone formation in Central California, Environmental science & technology, 46, 2781–2789, https://doi.org/10.1021/es203369p, 2012.
Hudman, R. C., Moore, N. E., Mebust, A. K., Martin, R. V., Russell, A. R., Valin, L. C., and Cohen, R. C.: Steps towards a mechanistic model of global soil nitric oxide emissions: implementation and space based-constraints, Atmos. Chem. Phys., 12, 7779–7795, 2012.

Hulley, G. C., Dousset, B., and Kahn, B. H.: Rising Trends in Heatwave Metrics Across Southern California, Earth's Future, 8, https://doi.org/10.1029/2020EF001480, 2020.
Hutjes, R., Vellinga, O. S., Gioli, B., and Miglietta, F.: Dis-aggregation of airborne flux measurements using footprint analysis, Agricultural and Forest Meteorology, 150, 966–983, https://doi.org/10.1016/j.agrformet.2010.03.004, 2010.
Jacob, D. J. and Winner, D. A.: Effect of climate change on air quality, ATMOSPHERIC ENVIRONMENT, 43, 51–63, https://doi.org/10.1016/j.atmosenv.2008.09.051, 2009.
Kari, E., Miettinen, P., Yli-Pirilä, P., Virtanen, A., and Faiola, C. L.: PTR-ToF-MS product ion distributions and humidity-dependence of biogenic volatile organic compounds, International Journal of Mass Spectrometry, 430, 87–97, https://doi.org/10.1016/j.ijms.2018.05.003, available at: http://www.sciencedirect.com/science/article/pii/S1387380617304943, 2018.
Karl, T., Striednig, M., Graus, M., Hammerle, A., and Wohlfahrt, G.: Urban flux measurements reveal a large pool of oxygenated volatile organic compound emissions, Proceedings of the National Academy of Sciences of the United States of America, 115, 1186–1191, https://doi.org/10.1073/pnas.1714715115, 2018.
Karl, T., Misztal, P. K., Jonsson, H. H., Shertz, S., Goldstein, A. H., and Guenther, A. B.: Airborne Flux Measurements of BVOCs above Californian Oak Forests: Experimental Investigation of Surface and Entrainment Fluxes, OH Densities, and Damköhler Numbers, J. Atmos. Sci., 70, 3277–3287, https://doi.org/10.1175/JAS-D-13-054.1, 2013.
Karl, T., Guenther, A., Lindinger, C., Jordan, A., Fall, R., and Lindinger, W.: Eddy covariance measurements of oxygenated volatile organic compound fluxes from crop harvesting using a redesigned proton-transfer-reaction mass spectrometer, J. Geophys. Res., 106, 24157–24167, https://doi.org/10.1029/2000JD000112, 2001.
Khare, P. and Gentner, D. R.: Considering the future of anthropogenic gas-phase organic compound emissions and the increasing influence of non-combustion sources on urban air quality, Atmos. Chem. Phys., 18, 5391–5413, https://doi.org/10.5194/acp-18-5391-2018, 2018.
Kim, S.-W., McDonald, B. C., Seo, S., Kim, K.-M., and Trainer, M.: Understanding the Paths of Surface Ozone Abatement in the Los Angeles Basin, Geophys Res Atmos, 127, https://doi.org/10.1029/2021JD035606, 2022.
Kljun, N., Calanca, P., Rotach, M. W., and Schmid, H. P.: A simple two-dimensional parameterisation for Flux Footprint Prediction (FFP), Geosci. Model Dev., 8, 3695–3713, https://doi.org/10.5194/gmd-8-3695-2015, 2015.
Kljun, N., Calanca, P., Rotach, M. W., and Schmid, H. P.: A simple parameterisation for flux footprint predictions, Boundary-Layer Meteorol, 112, 503–523, 2004.
König, G., Brunda, M., Puxbaum, H., Hewitt, C. N., and Duckham, S. C.: Relative contribution of oxygenated hydrocarbons to the total biogenic VOC emissions of selected mid-European agricultural and natural plant species, ATMOSPHERIC ENVIRONMENT, 29, 861–874, https://doi.org/10.1016/1352-2310(95)00026-U, 1995.
Krechmer, J., Lopez-Hilfiker, F., Koss, A., Hutterli, M., Stoermer, C., Deming, B., Kimmel, J., Warneke, C., Holzinger, R., Jayne, J., Worsnop, D., Fuhrer, K., Gonin, M., and Gouw, J. de: Evaluation of a New Reagent-Ion Source and Focusing Ion-Molecule Reactor for Use in Proton-Transfer-Reaction Mass Spectrometry, Analytical chemistry, 90, 12011–12018, https://doi.org/10.1021/acs.analchem.8b02641, 2018.
Kristensen, K., Lunderberg, D. M., Liu, Y., Misztal, P. K., Tian, Y., Arata, C., Nazaroff, W. W., and Goldstein, A. H.: Sources and dynamics of semivolatile organic compounds in a single-family residence in northern California, Indoor air, 29, 645–655, https://doi.org/10.1111/ina.12561, 2019.

Langford, B., Acton, W., Ammann, C., Valach, A., and Nemitz, E.: Eddy-covariance data with low signal-to-noise ratio: time-lag determination, uncertainties and limit of detection, Atmos. Meas. Tech., 8, 4197–4213, https://doi.org/10.5194/AMT-8-4197-2015, 2015.

Langford, B., Nemitz, E., House, E., Phillips, G. J., d. Famulari, Davison, B., Hopkins, J. R., Lewis, A. C., and Hewitt, C. N.: Fluxes and concentrations of volatile organic compounds above central London, UK, Atmos. Chem. Phys., 10, 627–645, https://doi.org/10.5194/acp-10-627-2010, 2010.

Langford, B., Davison, B., Nemitz, E., and Hewitt, C. N.: Mixing ratios and eddy covariance flux measurements of volatile organic compounds from an urban canopy (Manchester, UK), Atmos. Chem. Phys., 9, 1971–1987, https://doi.org/10.5194/acp-9-1971-2009, 2009.

Laughner, J. L. and Cohen, R. C.: Direct observation of changing NO x lifetime in North American cities, Science, 366, 723–727, https://doi.org/10.1126/science.aax6832, 2019.

Lee, X., Massman, W. J., and Law, B. E. (Eds.): Handbook of Micrometeorology, Springer, Dordrecht, Netherlands, 2005.

Lenschow, D. H., Mann, J., and Kristensen, L.: How Long Is Long Enough When Measuring Fluxes and Other Turbulence Statistics?, J. Atmos. Oceanic Technol., 11, 661–673, https://doi.org/10.1175/1520-0426(1994)011<0661:HLILEW>2.0.CO;2, 1994.

Lenschow, D. H.: Aircraft Measurements in the Boundary Layer, in: Probing the Atmospheric Boundary Layer, edited by: Lenschow, D. H., American Meteorological Society, Boston, MA, 39–55, https://doi.org/10.1007/978-1-944970-14-7_5, 1986.

Li, M., McDonald, B. C., McKeen, S. A., Eskes, H., Levelt, P., Francoeur, C., Harkins, C., He, J., Barth, M., Henze, D. K., Bela, M. M., Trainer, M., Gouw, J. A., and Frost, G. J.: Assessment of Updated Fuel-Based Emissions Inventories Over the Contiguous United States Using TROPOMI NO 2 Retrievals, Geophys Res Atmos, 126, https://doi.org/10.1029/2021JD035484, 2021.

Liu, S., et al.: Composition and Reactivity of Volatile Organic Compounds in the South Coast Air Basin and San Joaquin Valley of California, Atmos. Chem. Phys., https://doi.org/10.5194/acp-2022-399, 2022.

Liu, Y., Misztal, P. K., Xiong, J., Tian, Y., Arata, C., Weber, R. J., Nazaroff, W. W., and Goldstein, A. H.: Characterizing sources and emissions of volatile organic compounds in a northern California residence using space- and time-resolved measurements, Indoor air, 29, 630–644, https://doi.org/10.1111/ina.12562, 2019.

Loubet, B., et al.: Volatile organic compound fluxes over a winter wheat field by PTR-Qi-TOF-MS and eddy covariance, Atmos. Chem. Phys., 22, 2817–2842, https://doi.org/10.5194/acp-22-2817-2022, 2022.

Lovett, C., Baasiri, M., Atwi, K., Sowlat, M. H., Shirmohammadi, F., Shihadeh, A. L., and Sioutas, C.: Comparison of the oxidative potential of primary (POA) and secondary (SOA) organic aerosols derived from α-pinene and gasoline engine exhaust precursors, F1000Research, 7, 1031, https://doi.org/10.12688/f1000research.15445.2, available at: https://www.ncbi.nlm.nih.gov/pmc/articles/PMC6392154/, 2018.

Lunderberg, D. M., Kristensen, K., Liu, Y., Misztal, P. K., Tian, Y., Arata, C., Wernis, R., Kreisberg, N., Nazaroff, W. W., and Goldstein, A. H.: Characterizing Airborne Phthalate Concentrations and Dynamics in a Normally Occupied Residence, Environmental science & technology, 53, 7337–7346, https://doi.org/10.1021/acs.est.9b02123, 2019.

Ma, P. K., Zhao, Y., Robinson, A. L., Worton, D. R., Goldstein, A. H., Ortega, A. M., Jimenez, J. L., Zotter, P., Prévôt, A. S. H., Szidat, S., and Hayes, P. L.: Evaluating the impact of new observational constraints on P-S/IVOC emissions, multi-generation oxidation, and chamber wall losses on SOA modeling for Los Angeles, CA, Atmos. Chem. Phys., 17, 9237–9259, https://doi.org/10.5194/acp-17-9237-2017, 2017.

Malkina, I. L., Kumar, A., Green, P. G., and Mitloehner, F. M.: Identification and quantitation of volatile organic compounds emitted from dairy silages and other feedstuffs, Journal of environmental quality, 40, 28–36, https://doi.org/10.2134/jeq2010.0302, 2011.
Massman, J, W., and Clement, R.: Uncertainty in eddy covariance flux estimates resulting from spectral attenuation [Chapter 4]: A Guide to Surface Flux Measurements, in: Handbook of Micrometeorology, edited by: Lee, X., Massman, W. J., and Law, B. E., Springer, Dordrecht, Netherlands, 39–71, 2005.
Mattila, J. M., et al.: Multiphase Chemistry Controls Inorganic Chlorinated and Nitrogenated Compounds in Indoor Air during Bleach Cleaning, Environmental science & technology, 54, 1730–1739, https://doi.org/10.1021/acs.est.9b05767, 2020.
McDonald, B. C., et al.: Volatile chemical products emerging as largest petrochemical source of urban organic emissions, Science (New York, N.Y.), 359, 760–764, https://doi.org/10.1126/science.aaq0524, 2018.
McDonald, B. C., Dallmann, T. R., Martin, E. W., and Harley, R. A.: Long-term trends in nitrogen oxide emissions from motor vehicles at national, state, and air basin scales, Geophys Res Atmos, 117, 2012.
McFiggans, G., et al.: Secondary organic aerosol reduced by mixture of atmospheric vapours, Nature, 565, 587–593, https://doi.org/10.1038/s41586-018-0871-y, 2019.
McPherson, E. G., Xiao, Q., and Aguaron, E.: A new approach to quantify and map carbon stored, sequestered and emissions avoided by urban forests, Landscape and Urban Planning, 120, 70–84, https://doi.org/10.1016/j.landurbplan.2013.08.005, 2013.
Metzger, S., Junkermann, W., Mauder, M., Butterbach-Bahl, K., Trancón y Widemann, B., Neidl, F., Schäfer, K., Wieneke, S., Zheng, X. H., Schmid, H. P., and Foken, T.: Spatially explicit regionalization of airborne flux measurements using environmental response functions, Biogeosciences, 10, 2193–2217, https://doi.org/10.5194/BG-10-2193-2013, 2013.
Metzger, S., Junkermann, W., Mauder, M., Beyrich, F., Butterbach-Bahl, K., Schmid, H. P., and Foken, T.: Eddy-covariance flux measurements with a weight-shift microlight aircraft, Atmos. Meas. Tech., 5, 1699–1717, https://doi.org/10.5194/amt-5-1699-2012, 2012.
Metzger, S., Durden, D., Sturtevant, C., Luo, H., Pingintha-Durden, N., Sachs, T., Serafimovich, A., Hartmann, J., Li, J., Xu, K., and Desai, A. R.: eddy4R 0.2.0: a DevOps model for community-extensible processing and analysis of eddy-covariance data based on R, Git, Docker, and HDF5, Geosci. Model Dev., 10, 3189–3206, https://doi.org/10.5194/gmd-10-3189-2017, 2017.
Misztal, P. K., et al.: Atmospheric benzenoid emissions from plants rival those from fossil fuels, Scientific reports, 5, 12064, https://doi.org/10.1038/srep12064, 2015.
Misztal, P. K., Karl, T., Weber, R., Jonsson, H. H., Guenther, A. B., and Goldstein, A. H.: Airborne flux measurements of biogenic isoprene over California, Atmos. Chem. Phys., 14, 10631–10647, https://doi.org/10.5194/acp-14-10631-2014, 2014.
Misztal, P. K., Avise, J. C., Karl, T., Scott, K., Jonsson, H. H., Guenther, A. B., and Goldstein, A. H.: Evaluation of regional isoprene emission factors and modeled fluxes in California, Atmos. Chem. Phys., 16, 9611–9628, https://doi.org/10.5194/acp-16-9611-2016, 2016.
Multi-Resolution Land Characteristics (MRLC) Consortium: National Land Cover Database, https://www.mrlc.gov/, last access: 28 September 2022, 2019.
Murray, C. J. L., et al.: Global burden of 87 risk factors in 204 countries and territories, 1990–2019: a systematic analysis for the Global Burden of Disease Study 2019, The Lancet, 396, 1223–1249, https://doi.org/10.1016/S0140-6736(20)30752-2, 2020.
National Agricultural Statistics Service: CropScape - NASS CDL Program, https://nassgeodata.gmu.edu/CropScape/, last access: 28 September 2022, 2018.
National Institute of Standards and Technology: NIST Webbook, https://webbook.nist.gov/chemistry/form-ser/, last access: 20-Nov-22, 2022.

Niinemets, Ü. and Monson, R. K.: Biology, controls and models of tree volatile organic compound emissions, Tree physiology, 5, Springer, Dordrecht, New York, xv, 547, 2013.
Niinemets, Ü., Fares, S., Harley, P., and Jardine, K. J.: Bidirectional exchange of biogenic volatiles with vegetation: Emission sources, reactions, breakdown and deposition, Plant, cell & environment, 37, 1790–1809, https://doi.org/10.1111/pce.12322, 2014.
Nussbaumer, C. M. and Cohen, R. C.: Impact of OA on the Temperature Dependence of PM 2.5 in the Los Angeles Basin, Environmental science & technology, 55, 3549–3558, https://doi.org/10.1021/acs.est.0c07144, 2021.
Nussbaumer, C. M. and Cohen, R. C.: The Role of Temperature and NOx in Ozone Trends in the Los Angeles Basin, Environ. Sci. Technol., https://doi.org/10.1021/acs.est.0c04910, 2020.
Oertel, P., Küntzel, A., Reinhold, P., Köhler, H., Schubert, J. K., Kolb, J., and Miekisch, W.: Continuous real-time breath analysis in ruminants: effect of eructation on exhaled VOC profiles, Journal of breath research, 12, 36014, https://doi.org/10.1088/1752-7163/aabdaf, 2018.
Oikawa, P. Y., Ge, C., Wang, J., Eberwein, JR, Liang, L. L., La Allsman, Da Grantz, and Jenerette, G. D.: Unusually high soil nitrogen oxide emissions influence air quality in a high-temperature agricultural region, Nat Commun, 6, 1–10, 2015.
Park, C., Schade, G. W., and Boedeker, I.: Flux measurements of volatile organic compounds by the relaxed eddy accumulation method combined with a GC-FID system in urban Houston, Texas, ATMOSPHERIC ENVIRONMENT, 44, 2605–2614, https://doi.org/10.1016/j.atmosenv.2010.04.016, 2010.
Peng, Y., Mouat, A. P., Hu, Y., Li, M., McDonald, B. C., and Kaiser, J.: Source appointment of volatile organic compounds and evaluation of anthropogenic monoterpene emission estimates in Atlanta, Georgia, ATMOSPHERIC ENVIRONMENT, 288, 119324, https://doi.org/10.1016/j.atmosenv.2022.119324, available at: https://www.sciencedirect.com/science/article/pii/S1352231022003892, 2022.
Pennington, E. A., Seltzer, K. M., Murphy, B. N., Qin, M., Seinfeld, J. H., and Pye, H. O. T.: Modeling secondary organic aerosol formation from volatile chemical products, Atmospheric Chemistry and Physics Discussions, 21, 18247–18261, https://doi.org/10.5194/acp-21-18247-2021, 2021.
Pfannerstill, E. Y., Arata, C., Zhu, Q., Schulze, B., Place, B., Ward, R., Woods, R., Seinfeld, J. H., Bucholtz, A., Cohen, R. C., and Goldstein, A. H.: RECAP_VOCflux_Inventory_Comparison, https://arcg.is/ryDOK, last access: 28-Nov-22, 2022.
Pfannerstill, E. Y.: Citrus processing and ethanol manufacturing locations southern San Joaquin Valley, https://arcg.is/1iCnXu0, last access: 28-Nov-2022, 2022.
Pfannerstill, E. Y., et al.: Shipborne measurements of total OH reactivity around the Arabian Peninsula and its role in ozone chemistry, Atmospheric Chemistry and Physics, 19, 11501–11523, https://doi.org/10.5194/acp-19-11501-2019, available at: https://www.atmos-chem-phys.net/19/11501/2019/acp-19-11501-2019.pdf, 2019.
Pierce, D. W., Das, T., Cayan, D. R., Maurer, E. P., Miller, N. L., Bao, Y., Kanamitsu, M., Yoshimura, K., Snyder, M. A., Sloan, L. C., Franco, G., and Tyree, M.: Probabilistic estimates of future changes in California temperature and precipitation using statistical and dynamical downscaling, Clim Dyn, 40, 839–856, https://doi.org/10.1007/s00382-012-1337-9, 2013.
Pigeon, G., Lemonsu, A., Grimmond, C. S. B., Durand, P., Thouron, O., and Masson, V.: Divergence of turbulent fluxes in the surface layer: case of a coastal city, Boundary-Layer Meteorol, 124, 269–290, https://doi.org/10.1007/s10546-007-9160-2, 2007.
Pollack, I. B., et al.: Airborne and ground-based observations of a weekend effect in ozone, precursors, and oxidation products in the California South Coast Air Basin, J. Geophys. Res., 117, n/a-n/a, https://doi.org/10.1029/2011JD016772, 2012.

Pontes, C. A. d. S., Domingos-Melo, A., Milet-Pinheiro, P., Navarro, D. M. d. A. F., Lima Nadia, T., and Machado, I. C.: Staminode of Jacaranda rugosa A.H. Gentry (Bignoniaceae) promotes functional specialization by ensuring signaling and mechanical fit to medium-sized bees, Org Divers Evol, 22, 527–541, https://doi.org/10.1007/s13127-022-00558-8, 2022.

Potosnak, M. J., LeStourgeon, L., Pallardy, S. G., Hosman, K. P., Gu, L., Karl, T., Geron, C., and Guenther, A. B.: Observed and modeled ecosystem isoprene fluxes from an oak-dominated temperate forest and the influence of drought stress, ATMOSPHERIC ENVIRONMENT, 84, 314–322, https://doi.org/10.1016/j.atmosenv.2013.11.055, 2014.

Pusede, S. E., Steiner, A. L., and Cohen, R. C.: Temperature and recent trends in the chemistry of continental surface ozone, Chemical reviews, 115, 3898–3918, https://doi.org/10.1021/cr5006815, 2015.

Rabaud, N. E., Ebeler, S. E., Ashbaugh, L. L., and Flocchini, R. G.: Characterization and quantification of odorous and non-odorous volatile organic compounds near a commercial dairy in California, ATMOSPHERIC ENVIRONMENT, 37, 933–940, https://doi.org/10.1016/S1352-2310(02)00970-6, available at: https://www.sciencedirect.com/science/article/pii/S1352231002009706, 2003.

Rantala, P., Järvi, L., Taipale, R., Laurila, T. K., Patokoski, J., Kajos, M. K., Kurppa, M., Haapanala, S., Siivola, E., Petäjä, T., Ruuskanen, T. M., and Rinne, J.: Anthropogenic and biogenic influence on VOC fluxes at an urban background site in Helsinki, Finland, Atmos. Chem. Phys., 16, 7981–8007, https://doi.org/10.5194/acp-16-7981-2016, 2016.

Rapparini, F., Baraldi, R., and Facini, O.: Seasonal variation of monoterpene emission from Malus domestica and Prunus avium, Phytochemistry, 57, 681–687, https://doi.org/10.1016/S0031-9422(01)00124-8, 2001.

Rinnan, R. and Albers, C. N.: Soil Uptake of Volatile Organic Compounds: Ubiquitous and Underestimated?, J. Geophys. Res. Biogeosci., 125, https://doi.org/10.1029/2020JG005773, 2020.

Robinson, A. L., Donahue, N. M., Shrivastava, M. K., Weitkamp, E. A., Sage, A. M., Grieshop, A. P., Lane, T. E., Pierce, J. R., and Pandis, S. N.: Rethinking organic aerosols: semivolatile emissions and photochemical aging, Science, 315, 1259–1262, https://doi.org/10.1126/science.1133061, 2007.

Rubin, J. I., Kean, A. J., Harley, R. A., Millet, D. B., and Goldstein, A. H.: Temperature dependence of volatile organic compound evaporative emissions from motor vehicles, J. Geophys. Res., 111, https://doi.org/10.1029/2005JD006458, 2006.

SafeGraph: Places Data Curated for Accurate Geospatial Analytics, https://www.safegraph.com/, last access: 28 September 2022, 2022.

Saliba, G., Saleh, R., Zhao, Y., Presto, A. A., Lambe, A. T., Frodin, B., Sardar, S., Maldonado, H., Maddox, C., May, A. A., Drozd, G. T., Goldstein, A. H., Russell, L. M., Hagen, F., and Robinson, A. L.: Comparison of Gasoline Direct-Injection (GDI) and Port Fuel Injection (PFI) Vehicle Emissions: Emission Certification Standards, Cold-Start, Secondary Organic Aerosol Formation Potential, and Potential Climate Impacts, Environmental science & technology, 51, 6542–6552, https://doi.org/10.1021/acs.est.6b06509, 2017.

Schade, G. W. and Goldstein, A. H.: Plant physiological influences on the fluxes of oxygenated volatile organic compounds from ponderosa pine trees, J. Geophys. Res., 107, ACH 2-1-ACH 2-8, https://doi.org/10.1029/2001JD000532, 2002.

Schneidemesser, E. von, Monks, P. S., Allan, J. D., Bruhwiler, L., Forster, P., Fowler, D., Lauer, A., Morgan, W. T., Paasonen, P., Righi, M., Sindelarova, K., and Sutton, M. A.: Chemistry and the Linkages between Air Quality and Climate Change, Chemical reviews, 115, 3856–3897, https://doi.org/10.1021/acs.chemrev.5b00089, 2015.

Schorung, M. and Lecourt, T.: Analysis of the spatial logics of Amazon warehouses following a multiscalar and temporal approach. For a geography of Amazon's logistics system in the United States., 2021.
Scott, K. I. and Benjamin, M. T.: Development of a biogenic volatile organic compounds emission inventory for the SCOS97-NARSTO domain, ATMOSPHERIC ENVIRONMENT, 37, 39–49, https://doi.org/10.1016/S1352-2310(03)00381-9, 2003.
Seco, R., Peñuelas, J., and Filella, I.: Short-chain oxygenated VOCs: Emission and uptake by plants and atmospheric sources, sinks, and concentrations, ATMOSPHERIC ENVIRONMENT, 41, 2477–2499, https://doi.org/10.1016/j.atmosenv.2006.11.029, 2007.
Sha, T., Ma, X., Zhang, H., Janechek, N., Wang, Y., Wang, Y., Castro García, L., Jenerette, G. D., and Wang, J.: Impacts of Soil NO x Emission on O3 Air Quality in Rural California, Environ. Sci. Technol., 55, 7113–7122, 2021.
Shaw, S. L., Mitloehner, F. M., Jackson, W., Depeters, E. J., Fadel, J. G., Robinson, P. H., Holzinger, R., and Goldstein, A. H.: Volatile organic compound emissions from dairy cows and their waste as measured by proton-transfer-reaction mass spectrometry, Environ. Sci. Technol., 41, 1310–1316, https://doi.org/10.1021/es061475e, 2007.
Stackhouse, K. R., Pan, Y., Zhao, Y., and Mitloehner, F. M.: Greenhouse gas and alcohol emissions from feedlot steers and calves, Journal of environmental quality, 40, 899–906, https://doi.org/10.2134/jeq2010.0354, 2011.
Statista: Amazon annual net sales 2022, https://www.statista.com/statistics/266282/annual-net-revenue-of-amazoncom/, last access: 27-Mar-23, 2022a.
Statista: Amazon Logistics: package volume in the U.S., https://www.statista.com/statistics/1178979/amazon-logistics-package-volume-united-states/, last access: 27-Mar-23, 2022b.
Steinemann, A. C., MacGregor, I. C., Gordon, S. M., Gallagher, L. G., Davis, A. L., Ribeiro, D. S., and Wallace, L. A.: Fragranced consumer products: Chemicals emitted, ingredients unlisted, Environmental Impact Assessment Review, 31, 328–333, https://doi.org/10.1016/j.eiar.2010.08.002, 2011.
Stockwell, C. E., Coggon, M. M., Gkatzelis, G. I., Ortega, J., McDonald, B. C., Peischl, J., Aikin, K., Gilman, J. B., Trainer, M., and Warneke, C.: Volatile organic compound emissions from solvent- and water-borne coatings: compositional differences and tracer compound identifications, https://doi.org/10.5194/acp-2020-1078, 2020.
Sun, H., Trabue, S. L., Scoggin, K., Jackson, W. A., Pan, Y., Zhao, Y., Malkina, I. L., Koziel, J. A., and Mitloehner, F. M.: Alcohol, volatile fatty acid, phenol, and methane emissions from dairy cows and fresh manure, Journal of environmental quality, 37, 615–622, https://doi.org/10.2134/jeq2007.0357, 2008.
Taipale, R., Ruuskanen, T. M., and Rinne, J.: Lag time determination in DEC measurements with PTR-MS, Atmos. Meas. Tech., 3, 853–862, https://doi.org/10.5194/amt-3-853-2010, 2010.
Tang, X., Misztal, P. K., Nazaroff, W. W., and Goldstein, A. H.: Volatile Organic Compound Emissions from Humans Indoors, Environmental science & technology, 50, 12686–12694, https://doi.org/10.1021/acs.est.6b04415, 2016.
Tang, X., Misztal, P. K., Nazaroff, W. W., and Goldstein, A. H.: Siloxanes Are the Most Abundant Volatile Organic Compound Emitted from Engineering Students in a Classroom, Environ. Sci. Technol. Lett., 2, 303–307, https://doi.org/10.1021/acs.estlett.5b00256, 2015.
Tani, A.: Fragmentation and Reaction Rate Constants of Terpenoids Determined by Proton Transfer Reaction-mass Spectrometry, Environmental Control in Biology, 51, 23–29, https://doi.org/10.2525/ecb.51.23, 2013.

Thornton, J. A., Wooldridge, P. J., and Cohen, R. C.: Atmospheric NO2: In situ laser-induced fluorescence detection at parts per trillion mixing ratios, Anal. Chem., 72, 528–539, 2000.
Torrence, C. and Compo, G. P.: A Practical Guide to Wavelet Analysis, Bull. Amer. Meteor. Soc., 79, 61–78, https://doi.org/10.1175/1520-0477(1998)079<0061:APGTWA>2.0.CO;2, 1998.
U. S. Census Bureau: Census Bureau Data, https://data.census.gov/cedsci/, last access: 04-Nov-22, 2020.
Uranga, R.: Warehouses replace farms as big rigs fill Inland Empire, Los Angeles Times, 2023, available at: https://www.latimes.com/california/story/2023-02-05/warehouses-big-rigs-fill-inland-empire-streets?utm_id=85748&sfmc_id=1882085, last access: 27-Mar-23, 2023.
US EPA: Air Data - Daily Air Quality Tracker | US EPA, https://www.epa.gov/outdoor-air-quality-data/air-data-daily-air-quality-tracker, last access: 03-Nov-22, 2020.
US EPA: Air Data - Ozone Exceedances | US EPA, https://www.epa.gov/outdoor-air-quality-data/air-data-ozone-exceedances, last access: 03-Nov-22, 2016.
Valach, A. C., Langford, B., Nemitz, E., MacKenzie, A. R., and Hewitt, C. N.: Seasonal and diurnal trends in concentrations and fluxes of volatile organic compounds in central London, Atmos. Chem. Phys., 15, 7777–7796, https://doi.org/10.5194/acp-15-7777-2015, 2015.
van Rooy, P., Tasnia, A., Barletta, B., Buenconsejo, R., Crounse, J. D., Kenseth, C. M., Meinardi, S., Murphy, S., Parker, H., Schulze, B., Seinfeld, J. H., Wennberg, P. O., Blake, D. R., and Barsanti, K. C.: Observations of Volatile Organic Compounds in the Los Angeles Basin during COVID-19, ACS Earth Space Chem., 5, 3045–3055, https://doi.org/10.1021/acsearthspacechem.1c00248, 2021.
Vaughan, A. R., Lee, J. D., Metzger, S., Durden, D., Lewis, A. C., Shaw, M. D., Drysdale, W. S., Purvis, R. M., Davison, B., and Hewitt, C. N.: Spatially and temporally resolved measurements of NO_x fluxes by airborne eddy covariance over Greater London, Atmos. Chem. Phys., 21, 15283–15298, https://doi.org/10.5194/acp-21-15283-2021, 2021.
Vaughan, A. R., Lee, J. D., Misztal, P. K., Metzger, S., Shaw, M. D., Lewis, A. C., Purvis, R. M., Carslaw, D. C., Goldstein, A. H., Hewitt, C. N., Davison, B., Beevers, S. D., and Karl, T. G.: Spatially resolved flux measurements of NOx from London suggest significantly higher emissions than predicted by inventories, Faraday Discuss., 189, 455–472, https://doi.org/10.1039/c5fd00170f, 2016.
Velasco, E., Pressley, S., Grivicke, R., Allwine, E., Coons, T., Foster, W., Jobson, B. T., Westberg, H., Ramos, R., Hernández, F., Molina, L. T., and Lamb, B.: Eddy covariance flux measurements of pollutant gases in urban Mexico City, Atmos. Chem. Phys., 9, 7325–7342, https://doi.org/10.5194/acp-9-7325-2009, 2009.
Ventura Coastal: Operating Plants, https://www.venturacoastal.com/operating-plants, last access: 17-Feb-23, 2023.
Wang, C., Collins, D. B., Arata, C., Goldstein, A. H., Mattila, J. M., Farmer, D. K., Ampollini, L., DeCarlo, P. F., Novoselac, A., Vance, M. E., Nazaroff, W. W., and Abbatt, J. P. D.: Surface reservoirs dominate dynamic gas-surface partitioning of many indoor air constituents, Science advances, 6, eaay8973, https://doi.org/10.1126/sciadv.aay8973, 2020.
Wang, J. A., Randerson, J. T., Goulden, M. L., Knight, C. A., and Battles, J. J.: Losses of Tree Cover in California Driven by Increasing Fire Disturbance and Climate Stress, AGU Advances, 3, https://doi.org/10.1029/2021AV000654, 2022a.
Wang, S., et al.: Oxygenated volatile organic compounds (VOCs) as significant but varied contributors to VOC emissions from vehicles, Atmos. Chem. Phys., 22, 9703–9720, https://doi.org/10.5194/acp-22-9703-2022, available at: https://acp.copernicus.org/articles/22/9703/2022/, 2022b.
Wang, W., Yan, Y., Fang, H., Li, J., Zha, S., and Wu, T.: Volatile organic compound emissions from typical industries: Implications for the importance of oxygenated volatile organic compounds, Atmospheric Pollution Research, 101640, https://doi.org/10.1016/j.apr.2022.101640, 2022c.

Warneke, C.: Disjunct eddy covariance measurements of oxygenated volatile organic compounds fluxes from an alfalfa field before and after cutting, J. Geophys. Res., 107, https://doi.org/10.1029/2001JD000594, 2002.
Warneke, C., et al.: Photochemical aging of volatile organic compounds in the Los Angeles basin: Weekday-weekend effect, Geophys Res Atmos, 118, 5018–5028, https://doi.org/10.1002/jgrd.50423, 2013.
Warneke, C., Gouw, J. A. de, Holloway, J. S., Peischl, J., Ryerson, T. B., Atlas, E., Blake, D., Trainer, M., and Parrish, D. D.: Multiyear trends in volatile organic compounds in Los Angeles, California: Five decades of decreasing emissions, J. Geophys. Res., 117, n/a-n/a, https://doi.org/10.1029/2012JD017899, 2012.
Weil, J. C. and Horst, T. W.: Footprint estimates for atmospheric flux measurements in the convective boundary layer, in: Precipitation scavenging and atmosphere surface exchange: Proceedings of the Fifth International Conference on Precipitation Scavenging and Atmosphere Surface Exchange Processes, Richland, Washington, 15 - 19 July 1991, edited by: Schwartz, S. E., Hemisphere Publ. Co, Washington, 717–728, 1992.
Werner, C., et al.: Ecosystem fluxes during drought and recovery in an experimental forest, Science, 374, 1514–1518, https://doi.org/10.1126/science.abj6789, 2021.
Wolfe, G. M., et al.: The NASA Carbon Airborne Flux Experiment (CARAFE): instrumentation and methodology, Atmos. Meas. Tech., 11, 1757–1776, https://doi.org/10.5194/AMT-11-1757-2018, 2018.
Wooldridge, P. J., Perring, A. E., Bertram, T. H., Flocke, F. M., Roberts, J. M., Singh, H. B., Huey, L. G., Thornton, J. A., Wolfe, G. M., Murphy, J. G., and others: Total Peroxy Nitrates (\SigmaPNs) in the atmosphere: the Thermal Dissociation-Laser Induced Fluorescence (TD-LIF) technique and comparisons to speciated PAN measurements, Atmos. Meas. Tech., 3, 593–607, 2010.
World Health Organization: World Health Statistics 2022: Monitoring health for the SDGs, sustainable development goals, 131 pp., 2022.
Wu, S., Mickley, L. J., Leibensperger, E. M., Jacob, D. J., Rind, D., and Streets, D. G.: Effects of 2000–2050 global change on ozone air quality in the United States, J. Geophys. Res., 113, https://doi.org/10.1029/2007JD008917, 2008.
Xiong, J., He, Z., Tang, X., Misztal, P. K., and Goldstein, A. H.: Modeling the Time-Dependent Concentrations of Primary and Secondary Reaction Products of Ozone with Squalene in a University Classroom, Environmental science & technology, 53, 8262–8270, https://doi.org/10.1021/acs.est.9b02302, 2019.
Yuan, B., Coggon, M. M., Koss, A. R., Warneke, C., Eilerman, S., Peischl, J., Aikin, K. C., Ryerson, T. B., and Gouw, J. A. de: Emissions of volatile organic compounds (VOCs) from concentrated animal feeding operations (CAFOs): chemical compositions and separation of sources, Atmos. Chem. Phys., 17, 4945–4956, https://doi.org/10.5194/acp-17-4945-2017, 2017.
Yuan, B., Koss, A. R., Warneke, C., Coggon, M., Sekimoto, K., and Gouw, J. A. de: Proton-Transfer-Reaction Mass Spectrometry: Applications in Atmospheric Sciences, Chemical reviews, 117, 13187–13229, https://doi.org/10.1021/acs.chemrev.7b00325, 2017.
Zare, A., Romer, P. S., Nguyen, T., Keutsch, F. N., Skog, K., and Cohen, R. C.: A comprehensive organic nitrate chemistry: insights into the lifetime of atmospheric organic nitrates, Atmos. Chem. Phys., 18, 15419–15436, https://doi.org/10.5194/acp-18-15419-2018, 2018.
Zhao, Y., Tkacik, D. S., May, A. A., Donahue, N. M., and Robinson, A. L.: Mobile Sources Are Still an Important Source of Secondary Organic Aerosol and Fine Particulate Matter in the Los Angeles Region, Environmental science & technology, https://doi.org/10.1021/acs.est.2c03317, 2022.

Zhao, Y., Saleh, R., Saliba, G., Presto, A. A., Gordon, T. D., Drozd, G. T., Goldstein, A. H., Donahue, N. M., and Robinson, A. L.: Reducing secondary organic aerosol formation from gasoline vehicle exhaust, PNAS, 114, 6984–6989, https://doi.org/10.1073/pnas.1620911114, 2017.

Zhu, Q. and Pfannerstill, E. Y.: FLUX/calc_footprint_KL04.m, https://github.com/qdzhu/FLUX/blob/main/calc_footprint_KL04.m, last access: 28 September 2022, 2022.

Zhu, Q., Place, B., Pfannerstill, E. Y., Tong, S., Zhang, H., Wang, J., Nussbaumer, C. M., Wooldridge, P., Schulze, B. C., Arata, C., Bucholtz, A., Seinfeld, J. H., Goldstein, A. H., and Cohen, R. C.: Direct observations of NO x emissions over the San Joaquin Valley using airborne flux measurements during RECAP-CA 2021 field campaign, Atmos. Chem. Phys. Discuss., https://doi.org/10.5194/acp-2023-3, 2023.

Zotter, P., et al.: Diurnal cycle of fossil and nonfossil carbon using radiocarbon analyses during CalNex, Geophys Res Atmos, 119, 6818–6835, https://doi.org/10.1002/2013JD021114, 2014.

Appendix

Appendix 1: Supplementary Tables

See separate xlsx and csv files: Supplementary Tables 1-5.

Appendix 2: Supplementary Figures

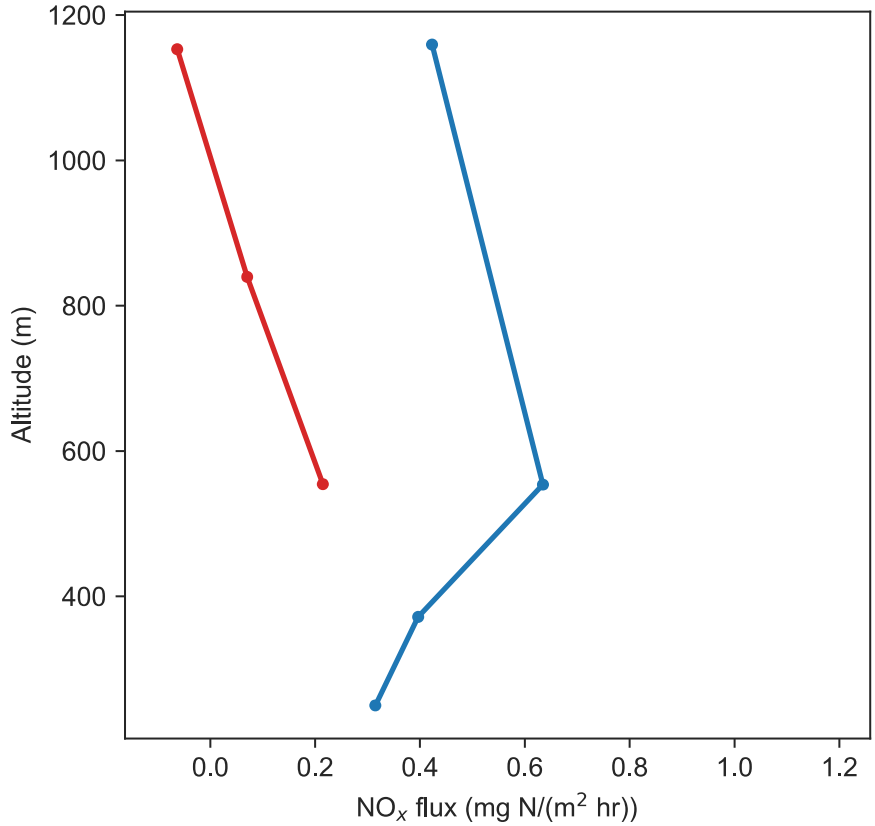

Figure S2.1: Vertical distribution of observed flux during racetrack, separated by the west patch (red) and east patch (east). The dot represents the median flux and the shade refers to the interquantile range.

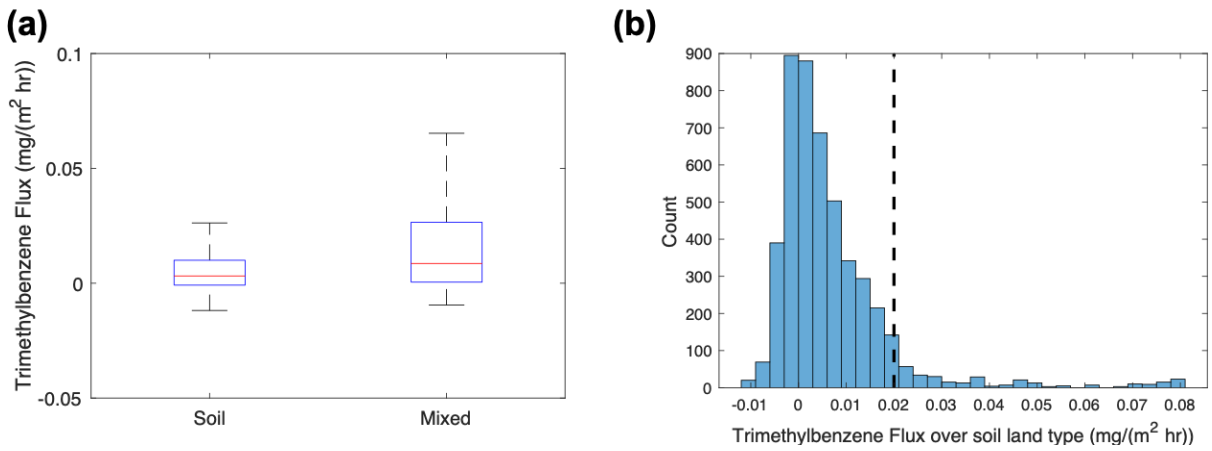

Figure S2.2: a) the comparison of trimethylbenzene fluxes with footprints exclusively covering soil land cover type and those with footprints covering mixed land cover types. b) The distribution of trimethylbenzene fluxes with footprints exclusively covering soil land cover type. The dashed line denotes a trimethylbenzene flux of 0.02 mg m^{-2} h^{-1}.

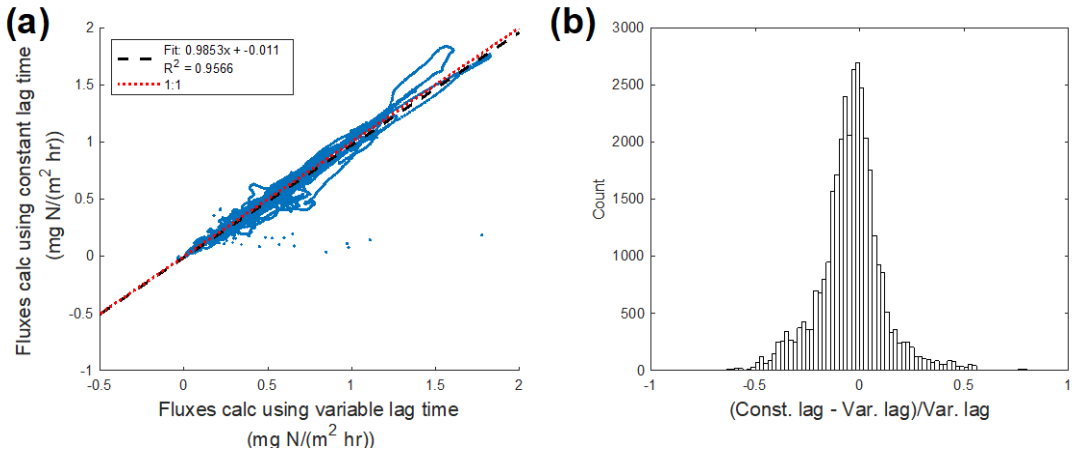

Figure S2.3: a) the comparison of calculated fluxes using various and constant lag time. b) corresponds the relative difference of fluxes.

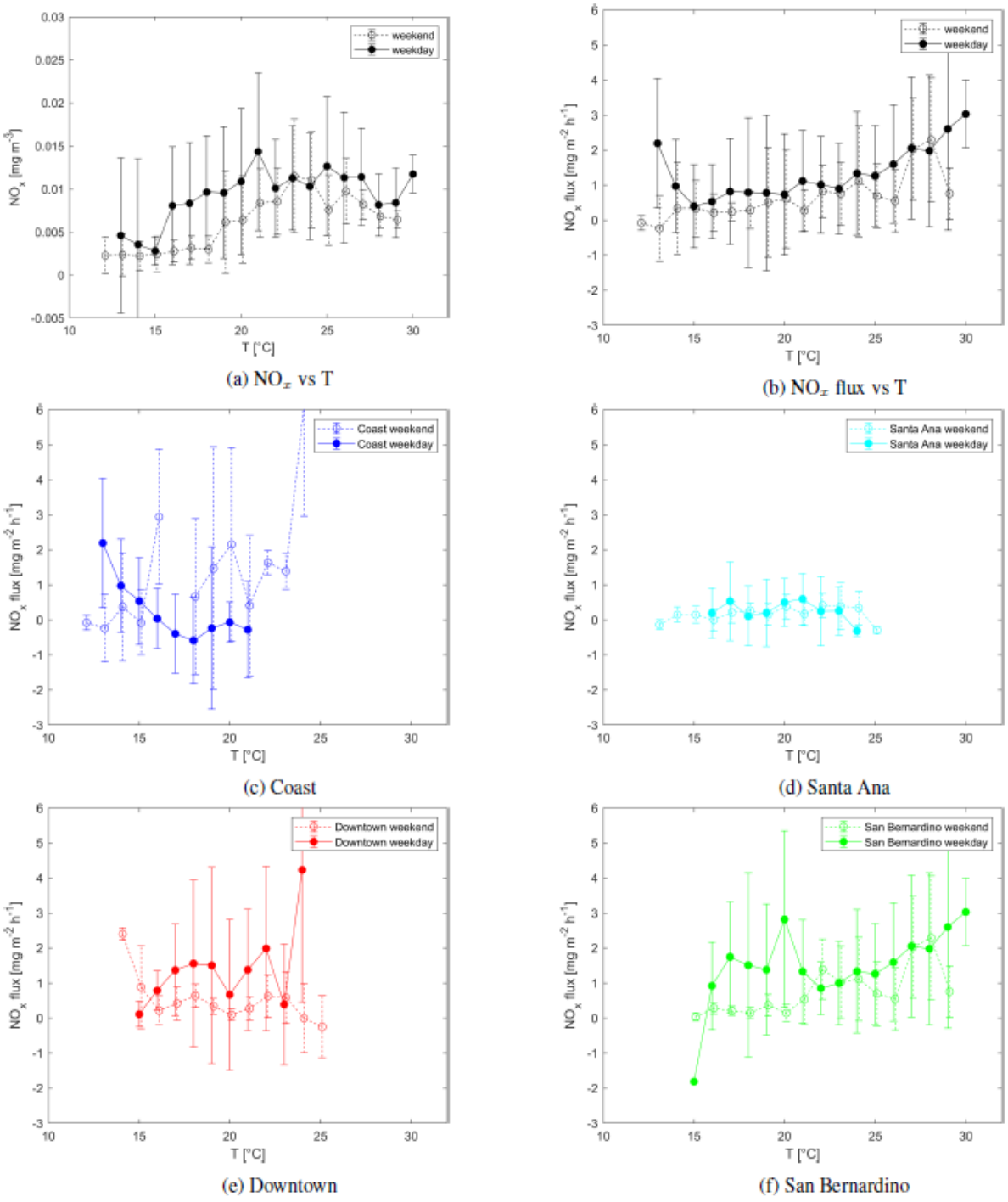

Figure S3.1. Temperature correlation of NOx concentrations and NOx fluxes for all data points ((a)&(b)) and separated into the four regions ((c)-(f)).

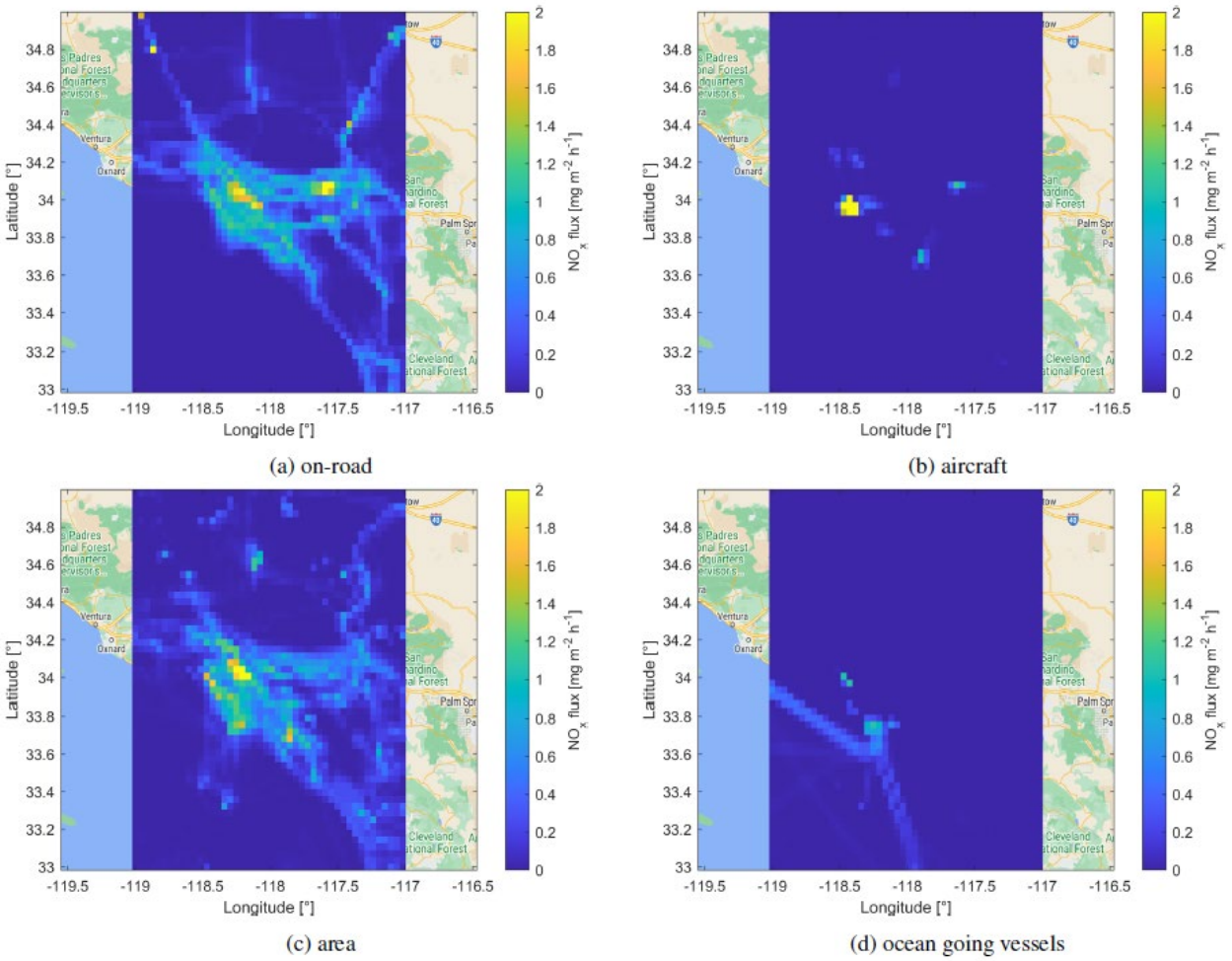

Fig. S3.2. CARB NO_x emission inventory for Los Angeles, separated into different sectors.

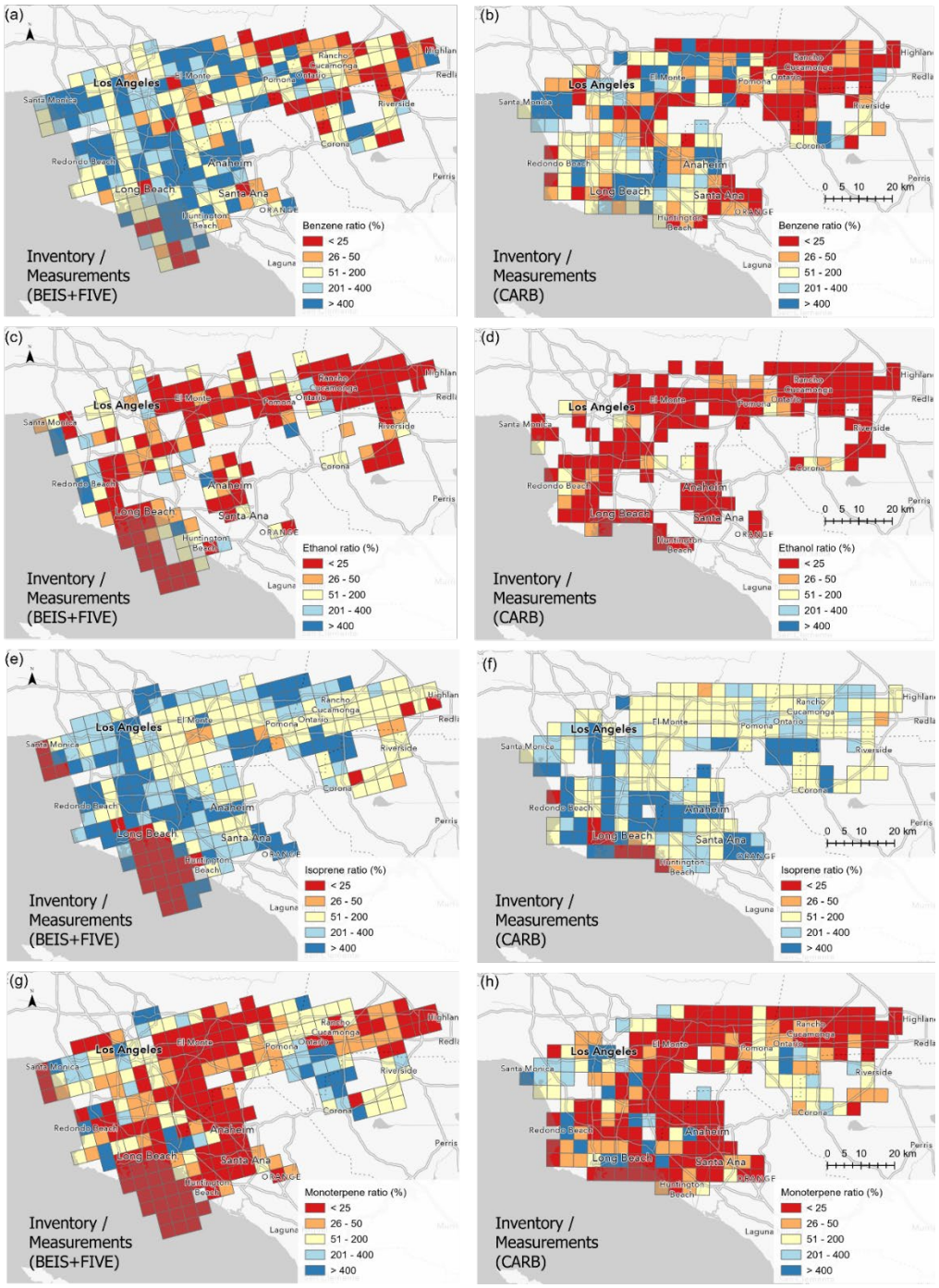

Figure S4.1. Ratio of inventory/measured flux in % for a) BEIS+FIVE-VCP, benzene, b) CARB, benzene, c) BEIS+FIVE-VCP, ethanol, d) CARB, ethanol, e) BEIS+FIVE-VCP, isoprene, f) CARB, isoprene, g) BEIS+FIVE-VCP, monoterpenes, h) CARB, monoterpenes. Blue colors show that the measurements were lower than the inventory, red colors that the measurements were higher than the inventory.

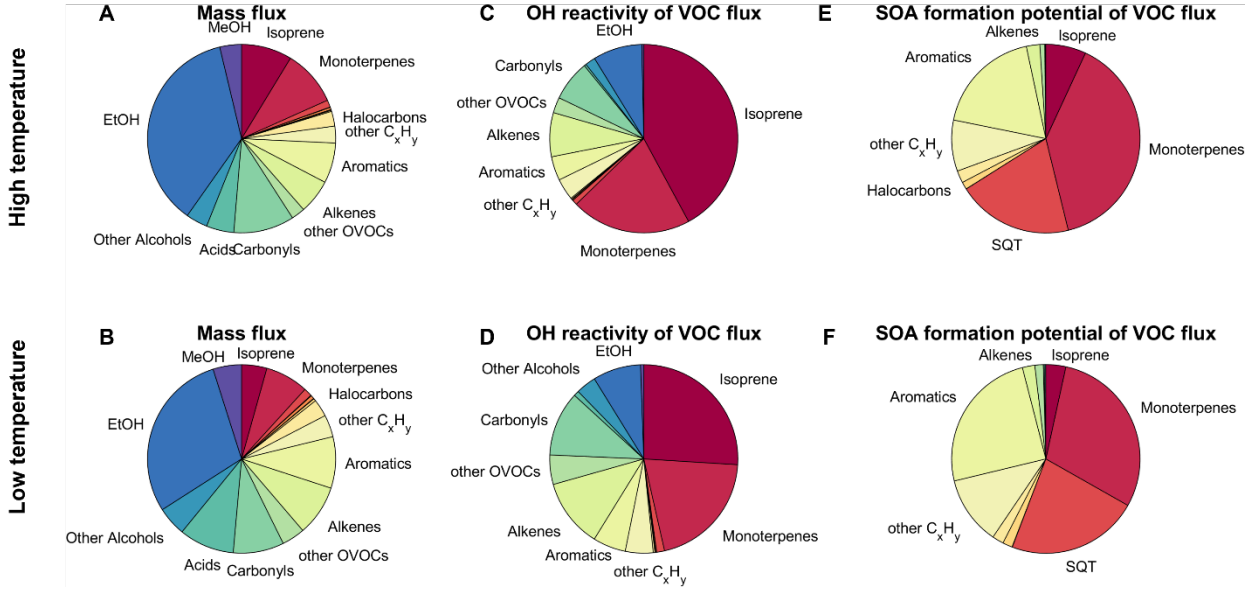

Fig. S4.2. Contribution of different VOC classes at high and low temperature to **(A)** mass flux, (**B)** OH reactivity of VOC flux, and (**C)** secondary organic aerosol formation potential of VOC surface flux of all VOCs measured during the RECAP-CA flights in June 2021. The pie charts show the median composition in the low/high temperature bin (regional lowest/highest 25% temperatures). MeOH: methanol, EtOH: ethanol, SQT: sesquiterpenes.

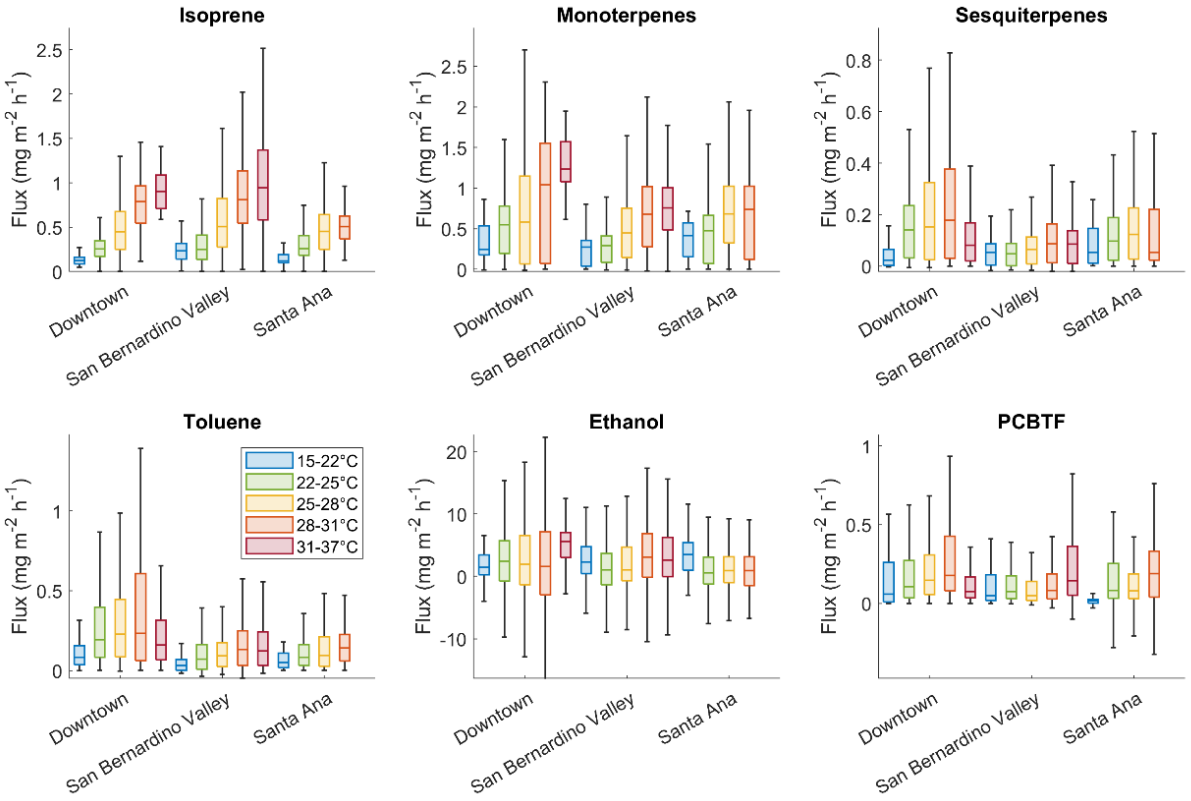

Fig. S4.3. Box charts of the temperature dependence of VOC fluxes separated by region in Los Angeles. This shows that emission ranges may differ by region due to a different source distribution, but emissions of these VOCs increase with temperature almost everywhere. The coastal region is not shown because of low coverage.

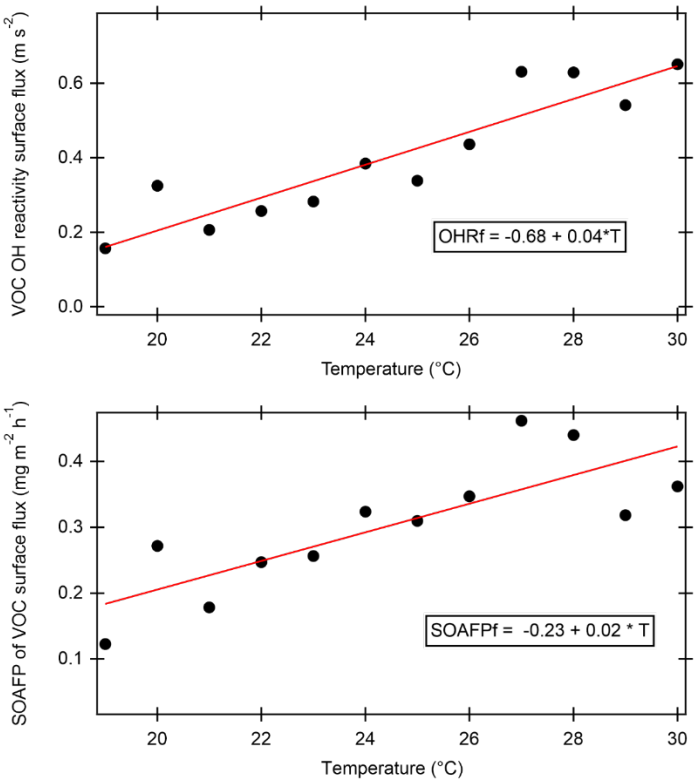

Fig. S4.4. Summed OH reactivity of VOC emissions ($r^2 = 0.71$) and SOA formation potential of VOC emissions ($r^2 = 0.72$) as a function of temperature. The linear fit equations are shown in the figures.

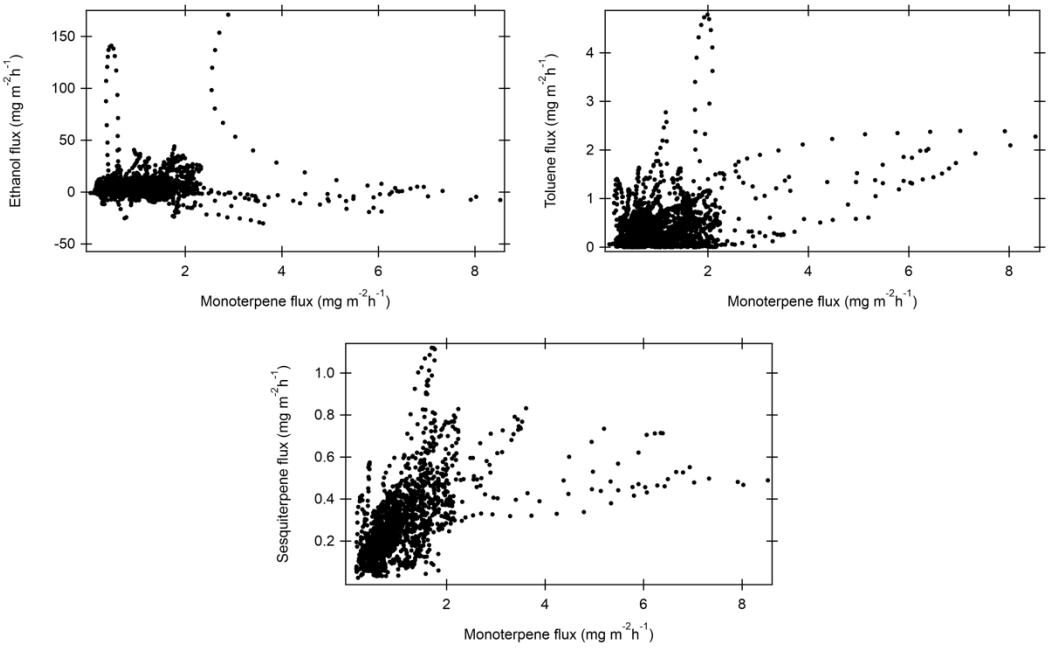

Fig. S4.5. No correlation of monoterpene fluxes in downtown Los Angeles with anthropogenic tracer VOCs, indicating biogenic origin of monoterpenes. (A) Monoterpenes vs. ethanol. (B) Monoterpenes vs. toluene. (C) Monoterpenes vs. sesquiterpenes – the relatively good correlation suggests a common source.

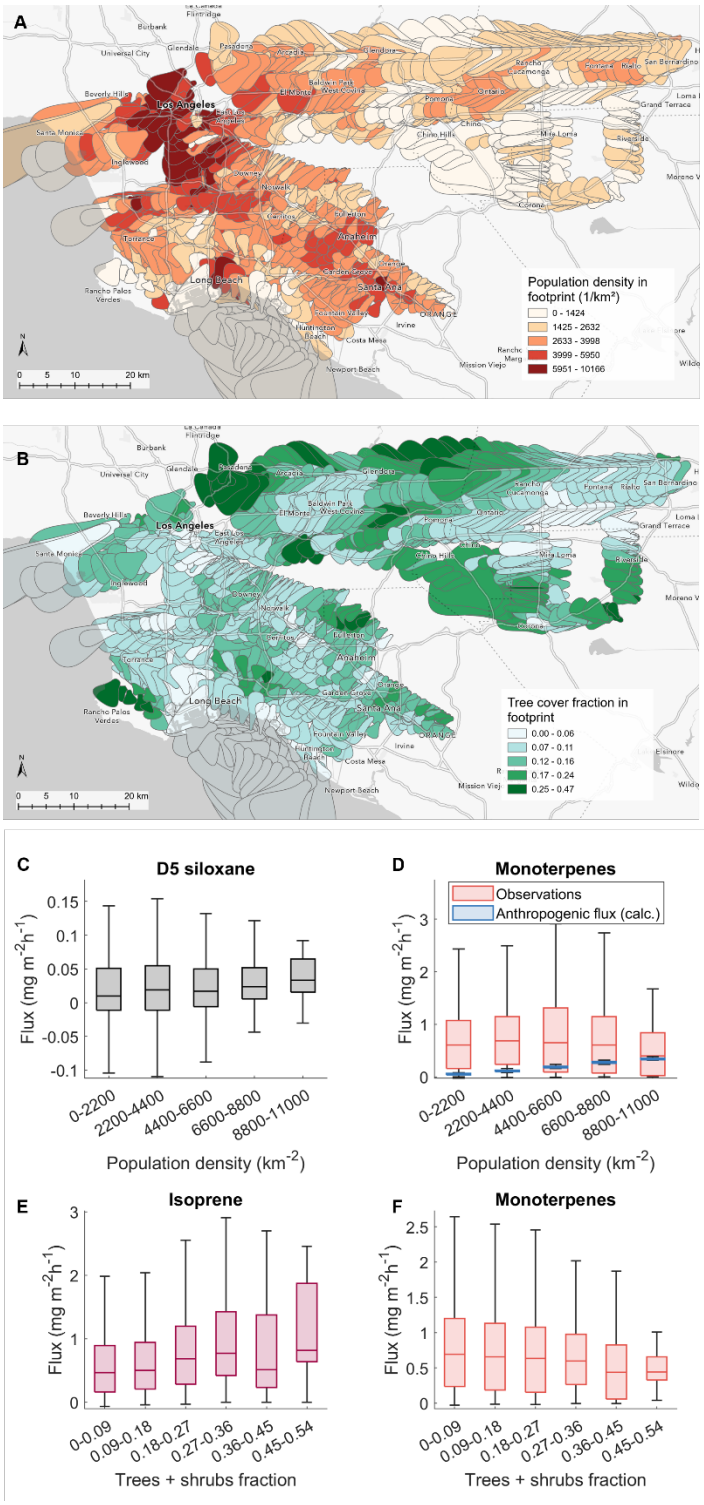

Fig. S4.6. (A) Population density in the flux footprints and tree cover in the flux footprints, (B) Fluxes of D5 siloxane and monoterpenes vs. binned population density, (C) fluxes of D5 siloxane vs population density, (D) fluxes of monoterpenes vs population density (observations and calculated following the emission factor from Coggon et al.), (E) isoprene fluxes vs. tree and shrub cover, (F) monoterpene fluxes vs tree and shrub cover in the footprint. The boxes represent the interquartile range, the horizontal lines the median, and the whiskers the 5th-95th percentile range.

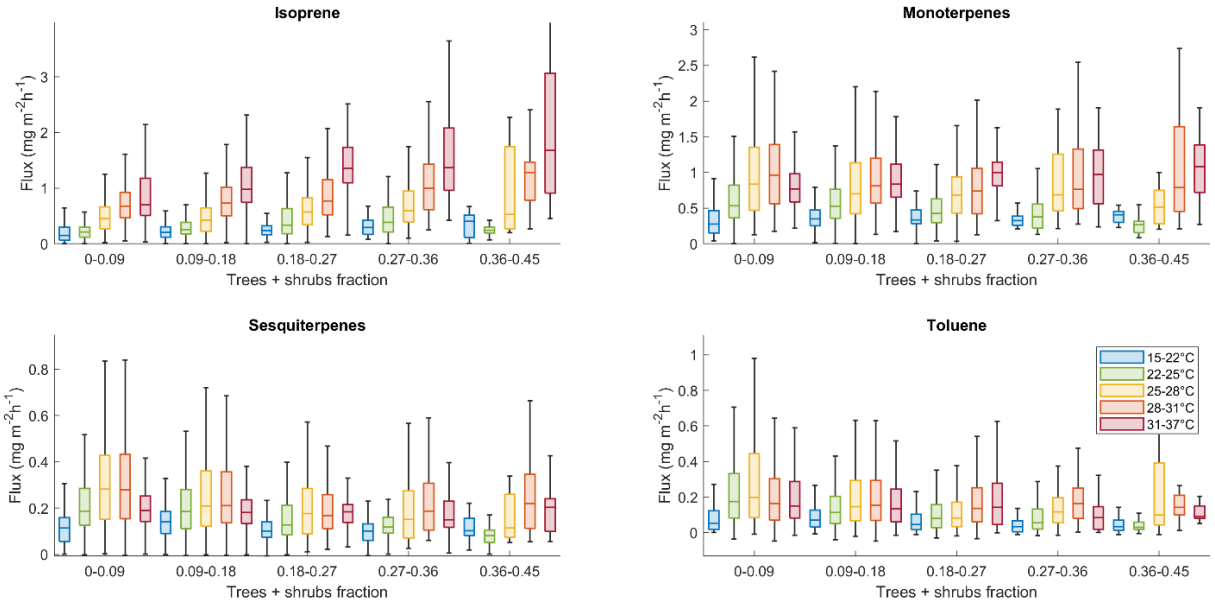

Fig. S4.7. Isoprene, monoterpene, sesquiterpene and toluene fluxes plotted as box plots in five bins of tree and shrub cover in the flux footprint, separated by temperature.

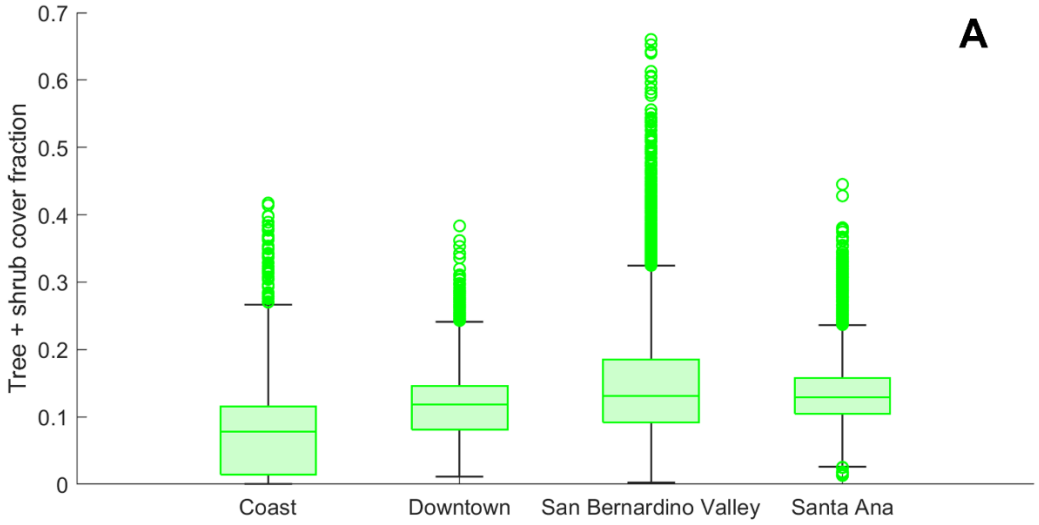

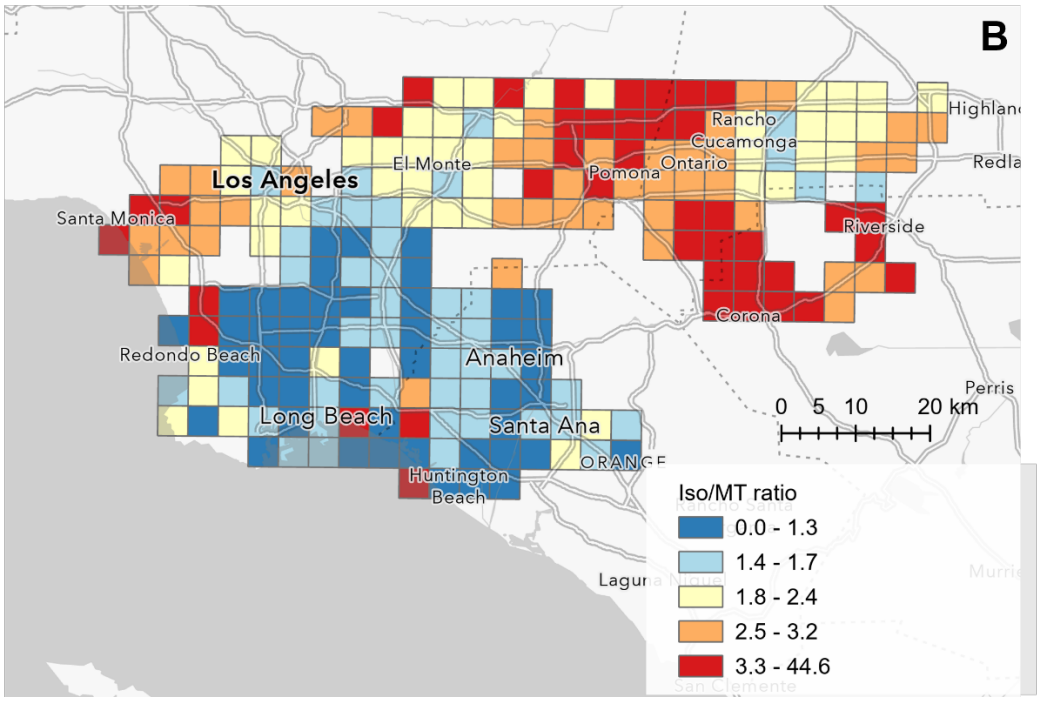

Fig. S4.8. (A) Combined tree and shrub cover fraction in the flux footprints by region (region definition see fig. S1). The boxes show the interquartile range, the horizontal line the median, and the whiskers the 1.5x interquartile range. Points outside the interquartile range are shown as circles. (B) Ratio of measured isoprene (Iso) fluxes vs. monoterpene (MT) fluxes on a 4 km x 4 km grid.

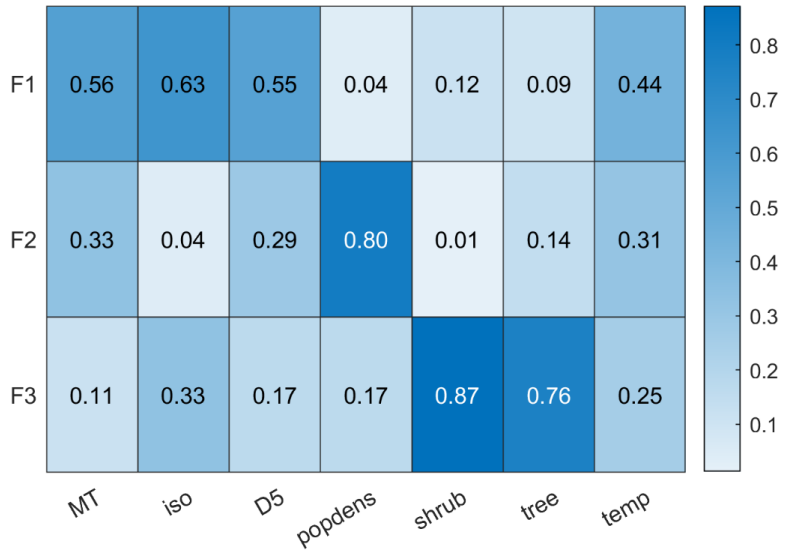

Fig. S4.9.

Non-negative matrix factorization result of monterpene (MT), isoprene (iso) and D5 siloxane (D5) fluxes with population density (popdens), shrub and tree cover, and temperature (temp). F1-F3 are factors resulting from the non-negative matrix factorization that together explain the time series of the respective variables. Values shown are fractions of the variability of each variable explained by the respective factor (F1-F3). The “nnmf” function in Matlab with “mult” algorithm was used.

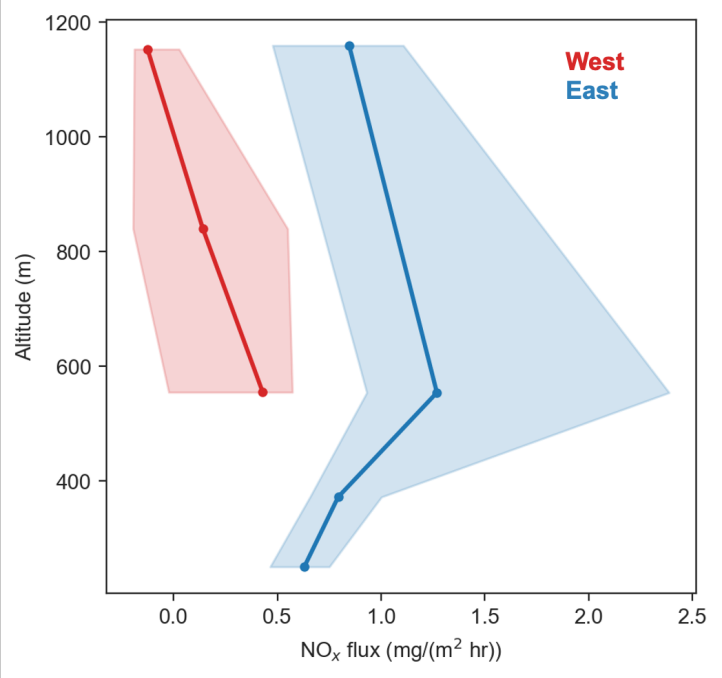

Figure S5.1. Vertical distribution of observed flux during racetrack, separated by the west patch and east patch. The dot represents the median flux and the shade refers to the interquantile range.

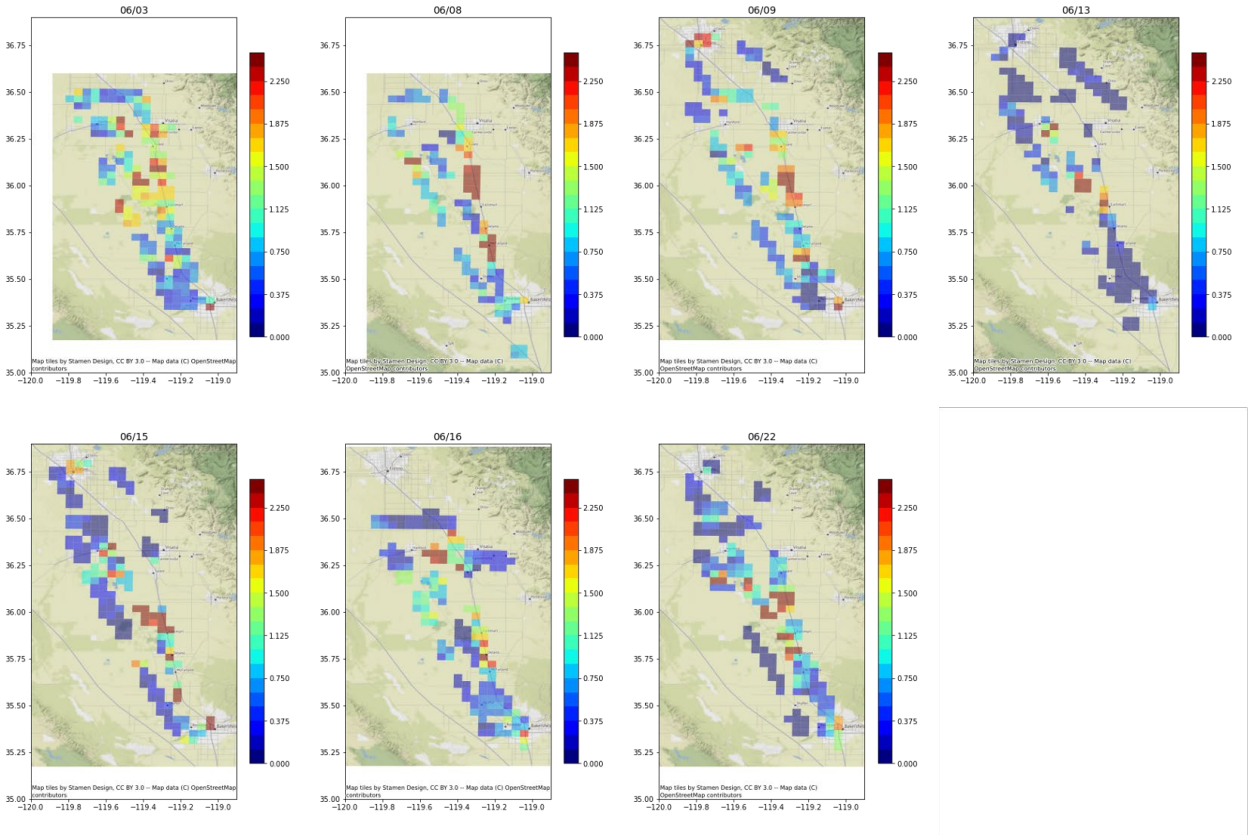

Figure. S5.2. The estimated gridded emission map for each flight, aligned in the order of flight days.

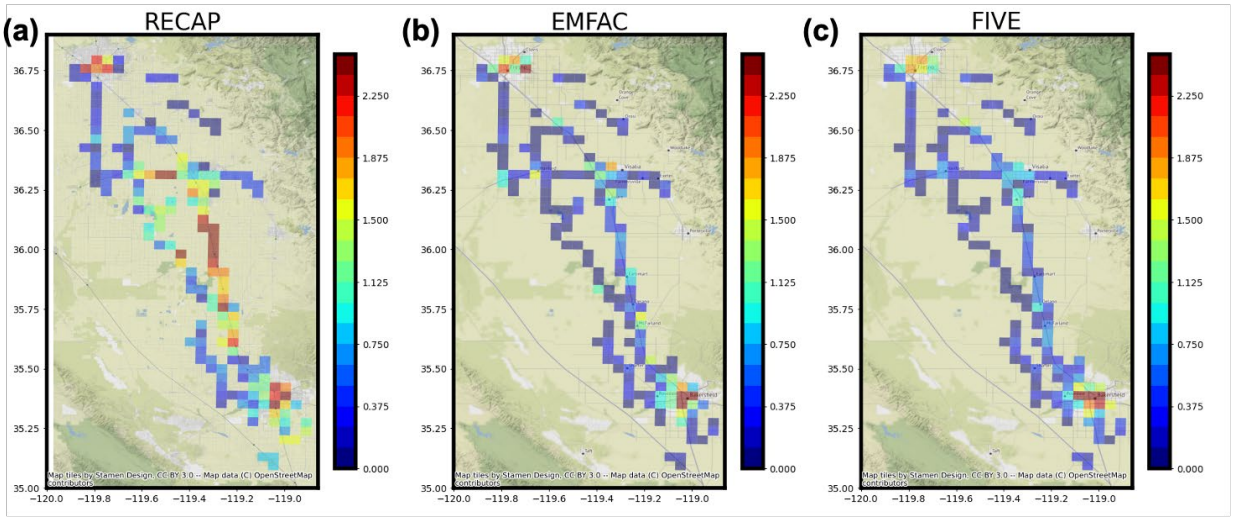

Figure S5.3. a) The estimated anthropogenic NOx emission map at 4 km resolution during weekday. b) and c) are EMFAC and FIVE-VCP anthropogenic emission inventories matched both in time and space, respectively.

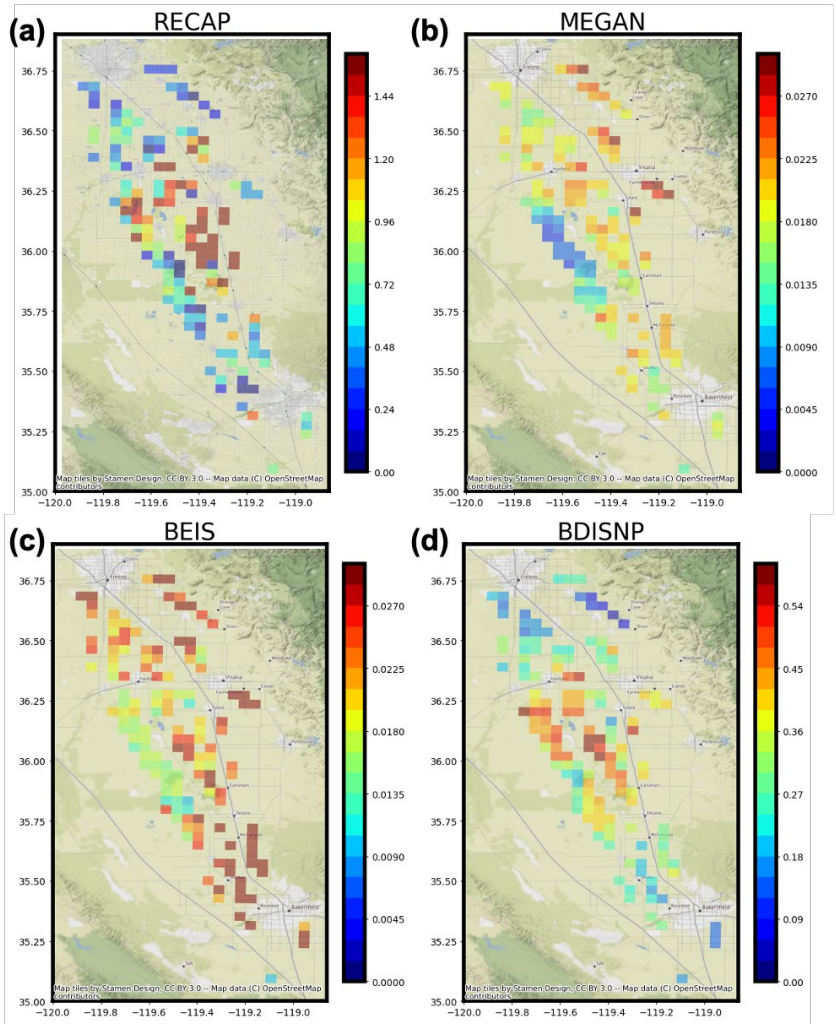

Figure S5.4. a) The estimated soil NO_x emission map at 4km during weekday. b), c), d) are made from soil NOx schemes matched both in time and space, including MEGAN, BEIS and BDISNP.

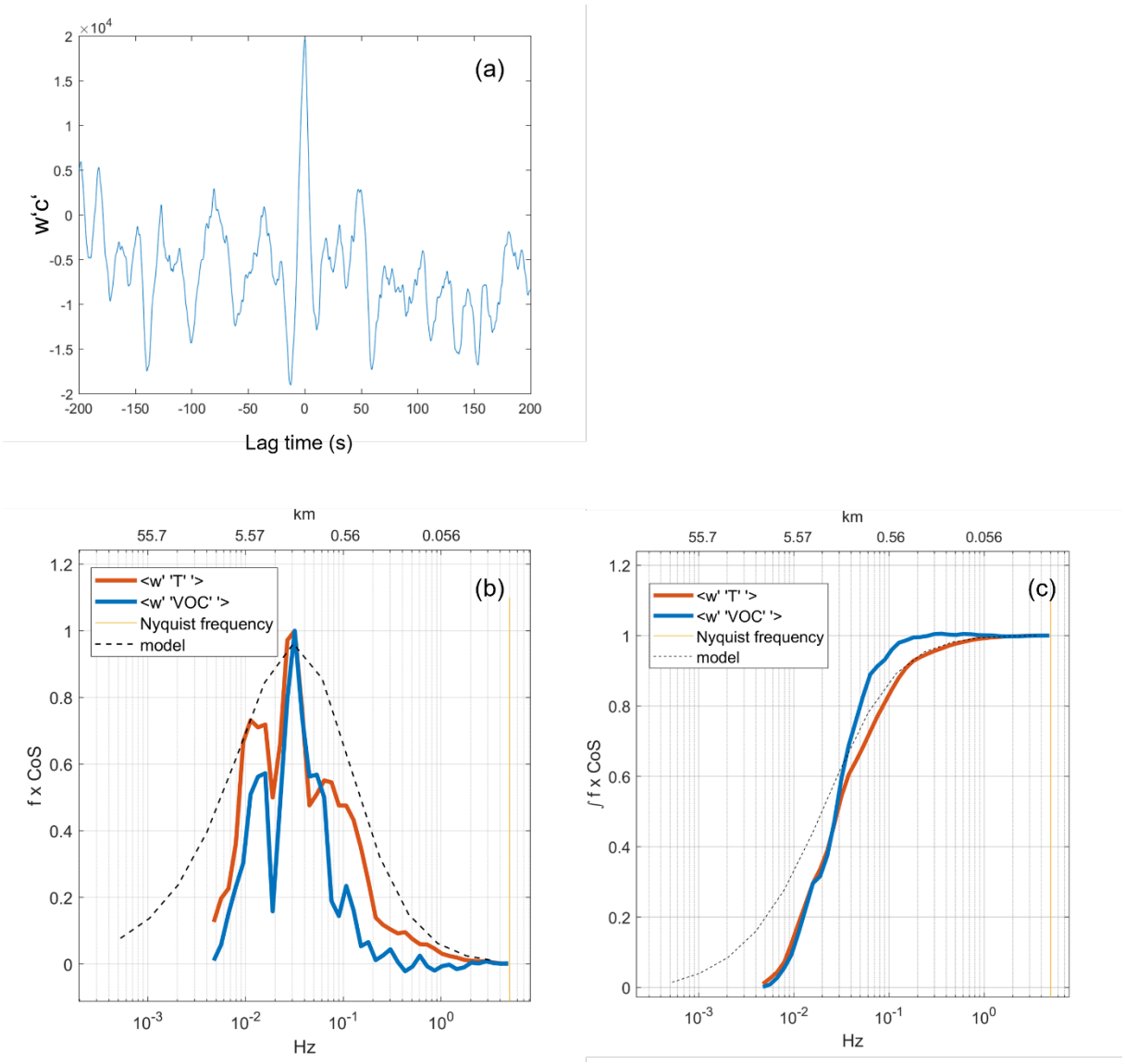

Figure S6.1. Spectral quality control for SJV VOCs. (a) Covariance peak for methanol (as an example for a sticky VOC) for one flight segment. (b) Cospectra for wind and temperature (w'T''), wind and C_3-benzenes (w'VOC''), and from a cospectral model (Massman et al., 2005). The Nyquist frequency is half the sampling frequency. (c) Same as in b), but cumulative cospectra.

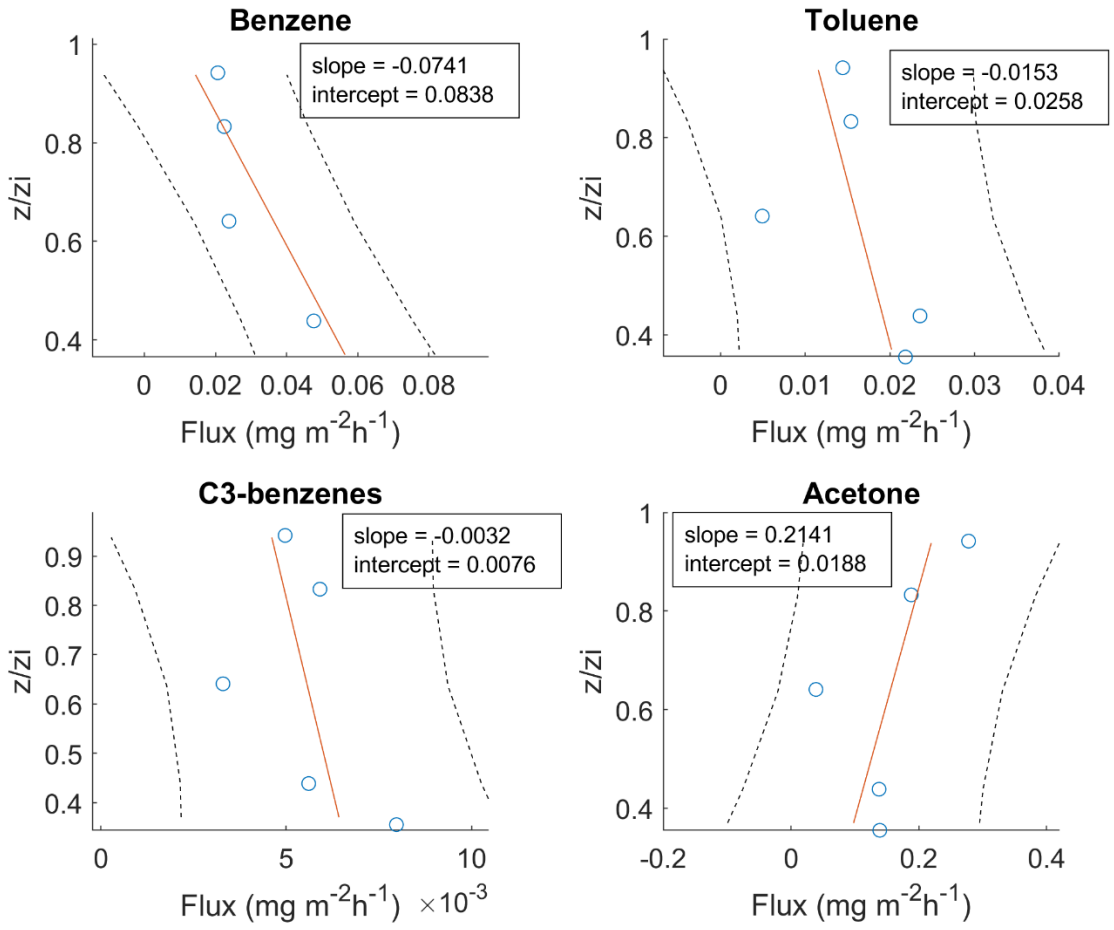

Figure S6.2. Physical vertical flux divergence for a selection of VOCs in the San Joaquin Valley.

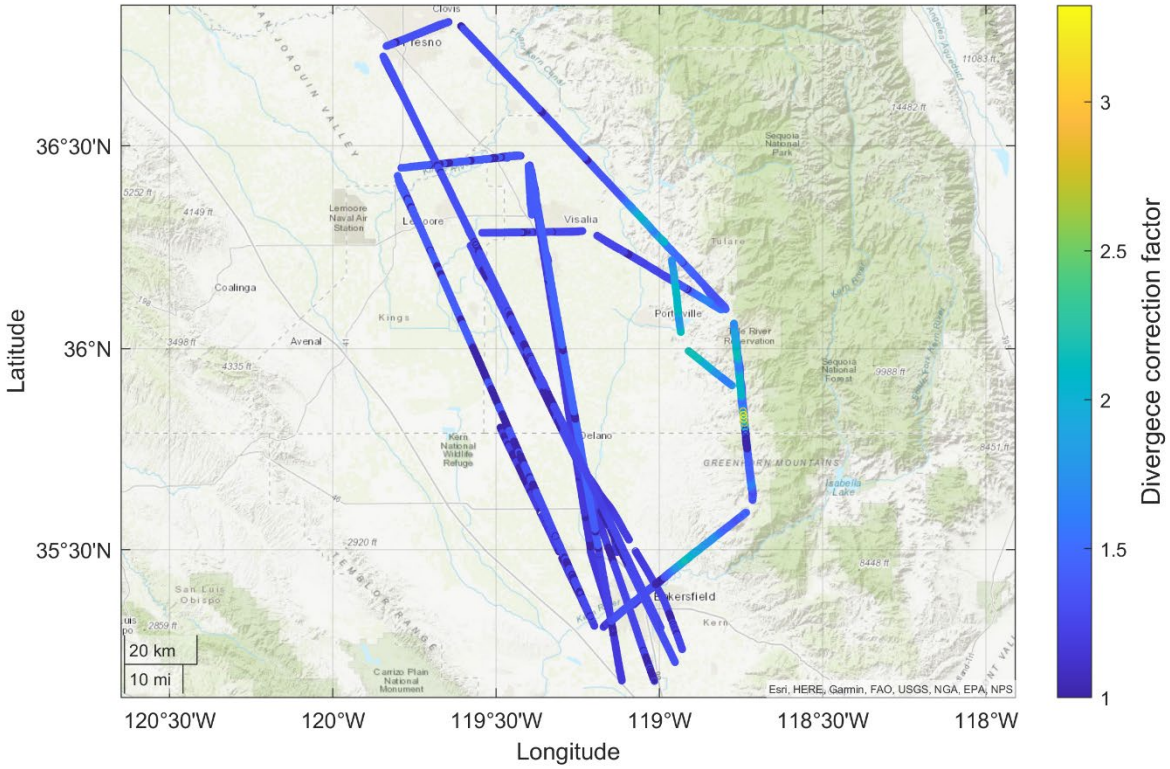

Figure S6.3. Size of the isoprene physical vertical divergence correction along the flight tracks.

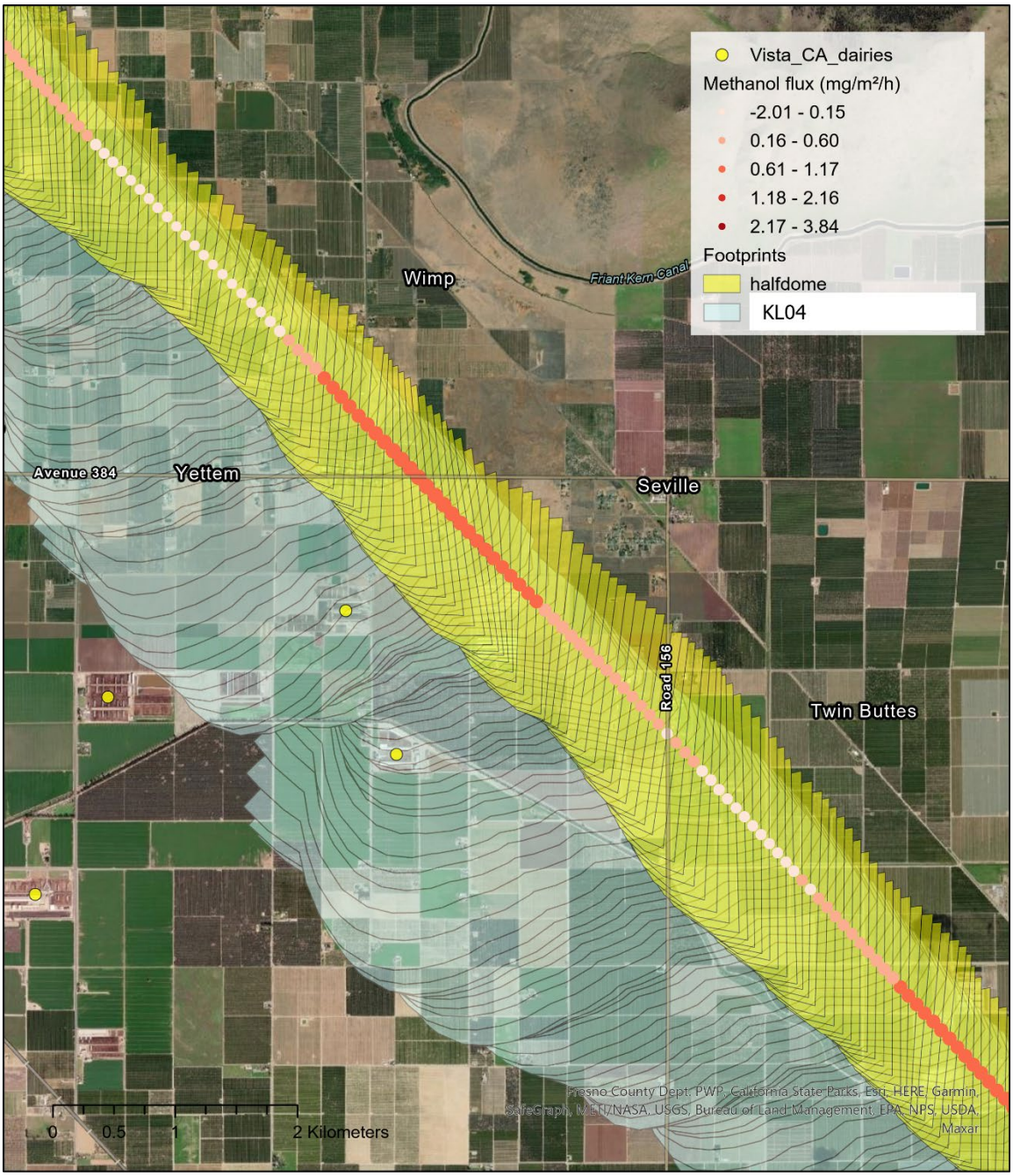

Figure S6.4. Footprint model comparison between KL04+2D and the half dome footprints (Weil and Horst, 1992). 90th percentile footprints calculated from both models shown. The increase in methanol flux seen in the flux measurements cannot be explained by the smaller half dome footprints (yellow), which do not contain the dairy farms. The KL04+ footprints (blue) contain the dairy farms which are most likely responsible for the methanol emission enhancement observed. Vista_CA_dairies: Dairy farm locations from Vista-CA inventory.

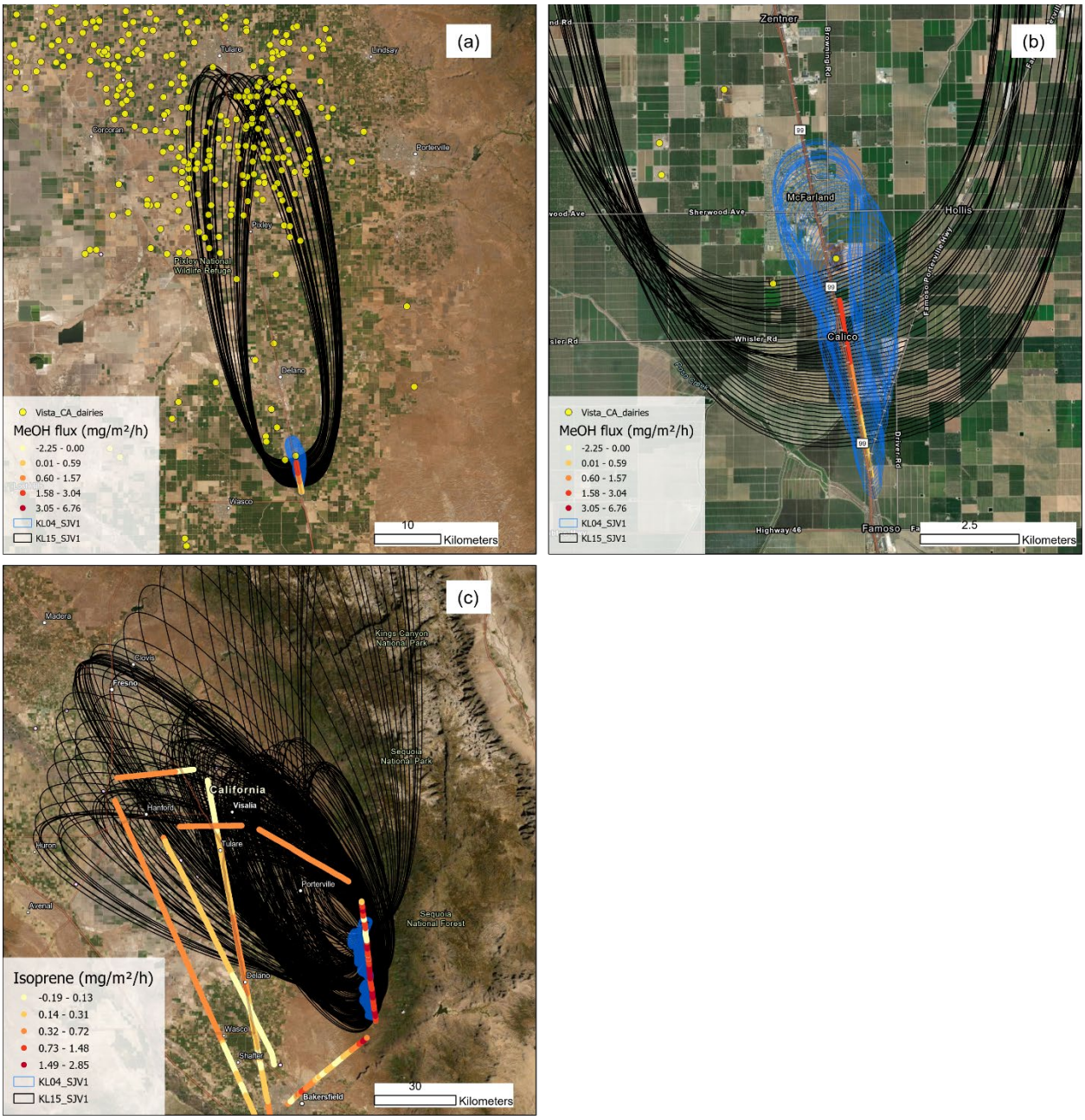

Figure S6.5. Footprint model comparison between KL04+2D and KL15. 90th percentile footprint contours shown. (a) The KL15 footprints (black) are extremely large, encompassing almost the entire study area, due to a bias that increases the footprint size strongly when the point of observation is close to the top of the boundary layer. (b) shows a zoom into the southern part of (a). The methanol emission increase observed can not be explained by the KL15 footprints, which always include the dairy farms, but the KL04+ footprints (blue) explain the flux increase well. (c) The strong isoprene fluxes observed in the Sierra Nevada foothills are explained well by the size of the KL04+ footprints, which contain almost exclusively the oak woodlands in the area with strong isoprene fluxes. The KL15 footprints are too large to explain the isoprene emissions observed. Vista_CA_dairies: Dairy farm locations from Vista CA inventory.

Figure S6.6. Swaths of dead oak trees in the Sierra Nevada foothills.